KU LEUVEN

ARENBERG DOCTORAL SCHOOL
Faculty of Engineering Science

High Speed MRAM with Voltage Control of Magnetic Anisotropy Effect

Yueh Chang (Jackson) Wu

Supervisors:
Prof. dr. ir. Guido Groeseneken
Prof. dr. ir. Jan Van Houdt

Dissertation presented in partial fulfillment of the requirements for the degree of Doctor of Engineering Science (PhD): Electrical Engineering

February 2021

High Speed MRAM with Voltage Control of Magnetic Anisotropy Effect

Yueh Chang (Jackson) WU

Examination committee:
Prof. dr. ir. Paul Sas, chair
Prof. dr. ir. Guido Groeseneken, supervisor
Prof. dr. ir. Jan Van Houdt, supervisor
Dr. Woojin Kim
Prof. dr. Kristiaan Temst
Prof. dr. ir. Wim Dehaene
Prof. dr. Thibaut Devolder
(Université Paris-Sud, France)
Dr. ir. Koen Martens
(imec, Belgium)

Dissertation presented in partial fulfillment of the requirements for the degree of Doctor of Engineering Science (PhD): Electrical Engineering

February 2021

Acknowledgment

By the time writing this thesis, it has been six years since I came to Leuven, including the two-year master program and the four-year PhD research. My life in Belgium is fantastic thanks to all my sincere friends, excellent colleagues, and interesting peers. Especially, 2020 was not easy for everyone, but together we got through and created wonderful memories. With this chance, I would like to express my gratitude to all of you.

I would like to give my first thanks to my parents Shu-Chen Lin and Meng-Feng Wu, my brother Yueh-Ta Wu, and Wen-Chi Han. They always give me full support. During my PhD life, there were so many challenges, and the most difficult time was definitely the second year. Without your backs, I could have given up pursuing this degree.

Next, I would like to thank Prof. Guido Groeseneken and Prof. Jan Van Houdt, my PhD promotors, for selecting me to join imec to experience a very special time studying and working together with people all around the world. Their guidance and insights on memory devices make this research continue smoothly in the right direction.

It is of equivalent importance to give my gratitude to my daily advisor Dr. Woojin Kim. Promoting a new topic in the MRAM program from the beginning is tough, but it would even be impossible if you were not there. We breakthrough several challenges, and in the end these efforts have accomplished several journal papers, patent, and conference proceedings. Meanwhile, I must also highlight the contributions from Dr. Bart Vermeulen, who also supervise me a lot since my master thesis. His patience, research attitude, and dedication to VCMA are definitely worthy of respect and learning. With this outstanding VCMA team, we successfully integrate VCMA into the MRAM program together.

I am also grateful to all my PhD jury members. Prof. Kristiaan Temst and Prof. Wim Dehaene, my assessors: thanks for giving valuable feedback during the annual examinations, approving the reports and presentations, and the

agreements on the continuation of this research. Prof. Thibaut Devolder (Univ. Paris-Sud): It was really my pleasure to learn the time-resolved measurement techniques from you, the week in your lab was especially substantial. Also, your suggestions significantly improve the quality of this dissertation. Dr. Koen Martens (imec): my thanks to you should be dated back to the master thesis time when you brought and guided the VCMA studies. I felt very lucky to join you because VCMA is so interesting that I even chose it as my PhD topic.

The important help from the MRAM program members should also be acknowledged and highlighted. I particularly appreciate Dr. Arnaud Furnemont, Dr. Gouri Sankar Kar, Dr. Ludovic Goux, and Dr. Davide Crotti for providing the resources to make the VCMA research possible. Great thanks to Dr. Kevin Garello, for his endless guidance on the device physics and characterization techniques; to Dr. Siddarth Rao and Dr. Simon Van Beek, for always being supportive on measurement tools and paper corrections; to Dr. Johan Swerts, Dr. Sebastien Couet, Dr. Robert Carpenter, and Dr. Enlong Liu, for erudite discussions on the magnetic materials and deposition techniques.

Some great friends who I admire all the time should also be emphasized. It is my pleasure to meet Prof. Tian-Li Wu, Dr. Chao-Yang (Michael) Chen, Dr. Min-Hsiang (Mark) Hsu, and Dr. Kai-Hsin (Kent) Chuang, you all set excellent examples of what a good PhD student should be.

PhD life can be stressful sometimes, for this I must also give my special thanks to Meerdaal table tennis club where I can release my pressure with great players. While pursuing a PhD degree, we also pursue higher team/personal rankings in the Flemish league. Thanks to all the club members and especially my teammates of all time, Mr. Stanislas Denauw and Kenny Becker.

Last but not least, I would like to thank all my friends and colleagues whoever made my life in Leuven joyful: Stanley Nee and Jason Chen, for yearly warm gathering in America; Yu Fang, Yun-Ching Chien, Thomas Tsau, Hung-Chieh Tsai, and Yun-Tzu Chang, for the conference on empire development; Dr. Ting-Wei Liao, Dr. Yao-Teng Chuang, and Sheng-Kai Wang, for the bicycle tours; Dr. Ren-Jie Chang (ASM), Dr. Yee-Chaung See (TSMC), Dr. Chung-Te Lin (TSMC), Dr. Tsann Lin (TSMC), Kuang-Wei Cheng (TSMC), Shu-Chi Sheu (ASML), Yi-Cheng Lai (AUO), Dr. Shih-Huang Chen, Prof. Kuo-Hsing (Frank) Kao, Dr. Tung Huei Ke, Ally Wang, Wen-Chieh Chen, Wei-Ming Wu, Cheng-Hsien Wu, Chien-Yu Lin, Brent Hsu, Yun-An Huang, Yu-Ting Ling, Wei-Ling Liao, Li-Hsin Li, Kenny Wu, Tsang-Hsuan Wang, Ya-Te Chen, for sharing your time with me in the past years.

Yueh Chang (Jackson) Wu
Leuven, Belgium, February 2021

Abstract

Magnetic random access memory (MRAM) is gaining intensive interest for embedded and stand-alone memory applications. Its inherent non-volatility is believed to address the large stand-by energy consumption issues in the present memory hierarchy. In recent years, the spin-transfer torque (STT)-MRAM has gradually matured and started to appear in the market. Typically, STT writing of perpendicular magnetic tunnel junction (pMTJ) is limited to a few nanoseconds. Because STT is collinear with intrinsic damping of the free-layer (FL), the FL needs to wait for the thermal fluctuation to tilt its magnetization to gain a finite torque. Further, it requires a large enough STT current to overcome the damping torque, which consumes a great amount of writing energy.

One can overcome these issues by using different writing mechanisms that do not directly compete with the intrinsic damping. Among several proposals, the most attractive ones are the voltage control of magnetic anisotropy (VCMA) and the spin-orbit torques (SOT). In particular, VCMA promises low power operation of MRAM as it allows modification of the FL perpendicular magnetic anisotropy (PMA), a parameter directly linked to the writing current/energy. In this thesis, we will study VCMA both as the writing mechanism and as the assisting mechanism to SOT.

First, we study the conventional VCMA write mechanism. Under a constantly applied in-plane field, a voltage pulse across the MTJ stack instantly changes the equilibrium magnetization direction from perpendicular to in-plane, thereby inducing high angle precessional switching. This writing mechanism is demonstrated to be 10x faster (0.5-1ns) and 100x lower energy (10-40fJ) when compared to the STT devices of the same diameter.

Next, we solve the technological challenges of the conventional scheme: 1) integration of an in-plane field generator and 2) prolonged write duration due to pre-read operation. Challenge 1 is solved by using the magnetic-hard-mask (MHM) design, and we demonstrate that the MHM cell can implement field-free

VCMA switching while maintaining the same write error rate as the standard devices. To solve challenge 2, we propose a deterministic writing scheme, with which the parallel (P) state is written by a single-pulse and the anti-parallel state is achieved by a double-pulse. This scheme manifests energy consumption similar to the conventional scheme while removing the long pre-read duration.

Furthermore, the temperature dependences of VCMA device properties are investigated. We observe a high decreasing rate of the critical VCMA switching voltage (36.6mV/K) due to the large decrease in PMA and minor variation in the VCMA coefficient (ξ). On the other hand, the decreasing rate of the breakdown voltage is 3.8mV/K. From the application point of view, the MTJ has a larger write-to-breakdown margin at elevated temperatures, which can mitigate the risk of MTJ degradation.

In the last part, VCMA is implemented as an assisting effect to improve SOT-MRAM, forming the voltage-gate assisted spin-orbit torque (VGSOT)-MRAM. With the present ξ = 15fJ/Vm, we demonstrate a 25% reduction in SOT switching current, corresponding to total switching energy of 30fJ at 0.4ns for 80nm devices. Based on the experimental results, we further project the device parameters required at 30nm pMTJ. We show that VGSOT-MRAM with improved ξ = 300fJ/Vm and θ_{SH} = 0.45 is enough to suit both high-density and high-performance embedded memory applications. Notice that these values are much lower than the requirements in VCMA-MRAM ($\xi >$ 800fJ/Vm) and SOT-MRAM ($\theta_{SH} > 2$).

Beknopte samenvatting

Magnetische werkgeheugen (MRAM) wint aan belang voor verschillende ingebedde en alleenstaande geheugen toepassingen. Door zijn inherente niet-vluchtigheid kan hij de grote stand-by energieconsumptie problemen oplossen die in de huidige geheugen hiërarchie aanwezig zijn. Recent is spin-transfer torque (STT)-MRAM geleidelijk aan verbeterd en is nu beschikbaar. Schrijven in perpendicular magnetic tunnel junctions (pMTJ) gebeurd met STT en is gelimiteerd tot een paar nanoseconden. Omdat STT collineair is met de intrinsieke demping van de free-layer (FL), kost het tijd voordat er in de FL, op basis van thermische fluctuatie van de magnetisatie, voldoende koppel ontwikkelt door de STT elektrische stroom. Daarenboven vereist het een grote STT stroom om het demping koppel te overwinnen. Dit zorgt voor een groot energie verbruik tijdens het schrijven van het geheugen.

Deze problemen kunnen echter opgelost worden door een ander schrijfmechanisme te gebruiken dat niet in directe competitie is met de intrinsieke demping. Van verschillende voorstellen lijken de voltage control of magnetic anisotropy (VCMA) en de spin-orbit torques (SOT) de grote kanshebbers. VCMA zorgt voor een lage vermogen werking van MRAM aangezien het de perpendicular magnetic anisotropy (PMA) van de FL kan aanpassen. PMA is gelinkt aan de vereiste stroom/energie voor een schrijfopdracht. In deze thesis, zullen we VCMA bestuderen, zowel als schrijfmechanisme alsook als een assisterend mechanisme tot schrijven met een SOT stroom.

Allereerst, bestuderen we het conventionele VCMA schrijf mechanisme. Tijdens een constant aangelegd evenwijdig magnetisch veld, kan een spanningspuls over de MTJ ogenblikkelijke veranderingen in het magnetisatie evenwicht aanbrengen van loodrecht op het vlak naar in het vlak. Deze verandering veroorzaakt schakelen door een precessie onder grote hoek. Het is aangetoond dat dit schrijfmechanisme 10x zo snel is (0.5-1ns) en met een 100x lagere energie (10-40fJ) dan schrijven met STT in apparaten van dezelfde grootte.

Vervolgens, zoeken we oplossingen voor de technologische uitdagingen van het conventionele schrijfschema: 1) integratie van een evenwijdig met het vlak magnetisch veldgenerator en 2) een langdurige schrijftijd door de vooraf leesoperatie. Uitdaging 1) is opgelost door gebruik te maken van een magnetic-hard-mask (MHM) in het design. Zo een MHM zorgt voor VCMA schrijven zonder magnetisch veld, maar nog steeds met dezelfde schrijffout proportie. Voor uitdaging 2) stellen we een deterministisch schrijfschema voor: de parallel (P) toestand wordt geschreven door een enkele spanningspuls en de anti-parallel (AP) toestand met een dubbele spanningspuls. De schrijfenergie met dit schrijfschema is nog steeds vergelijkbaar met het conventionele schema, maar de langdurige pre-leesopdracht is niet meer nodig.

Daarnaast, bestuderen we de temperatuur afhankelijkheid van verschillende eigenschappen in VCMA apparaten. We zien enerzijds een snelle daling in de kritische VCMA schakelspanning (36.6mV/K), doordat er een grote daling in PMA en een kleine variatie in de VCMA coëfficiënt (ξ). Anderzijds, is de snelheid van doorslagspanning slechts 3.8mV/K. Vanuit een applicatie oogpunt zal een grotere schrijf-tot-doorslag marge van de MTJ bij hogere temperaturen zorgen een verlaagd risico op MTJ degradatie.

In het laatste deel wordt VCMA geïmplementeerd om SOT-MRAM te assisteren, namelijk een voltage-gate assisted spin-orbit torque (VGSOT)-MRAM. Met de huidige $\xi = 15$fJ/Vm, verlagen we de SOT schakelstroom met 25%. Dit komt overeen met een schakelenergie van 30 fJ tijdens een 0.4 ns schrijfpuls in een 80 nm apparaat. Op basis van experimentele resultaten maken we een projectie van de apparaat eigenschappen die nodig zijn voor een 30 nm grote pMTJ. Wij tonen aan dat VGSOT-MRAM met een betere $\xi = 300$fJ/Vm en $\theta_{SH} = 0.45$ genoeg is om zowel voor hoge densiteit en hoge performante ingebedde geheugenapplicaties te dienen. Deze waarden zijn bovendien veel lager dan de vereisten in VCMA-MRAM ($\xi > 800$fJ/Vm) en SOT-MRAM ($\theta_{SH} > 2$).

List of Abbreviations

AC Alternating Current.

AP Anti-Parallel state.

BCC Body-Centerred-Cubic.

BE Bottom Electrode.

BP Bottom-Pinned.

CBRAM Conductive Bridge Random Access Memory.

CMOS Complementary Metal Oxide Semiconductor.

CPU Central Processing Unit.

DC Direct Current.

DMM Digitized Multi-Meter.

DOS Density Of States.

DRAM Dynamic Random Access Memory.

DUT Device Under Test.

DW Domain Wall.

eCD Electrical Critical Dimension.

eDRAM Embedded Dynamic Random Access Memory.

FeRAM Ferroelectric Random Access Memory.

FET Field-Effect-Transistor.

FFCS Field-Free Conventional Switch.

FIT Failures In Time.

FL Free-Layer.

FM Ferromagnet.

FMR Ferromagnetic Resonance.

HDD Hard-Disk-Drive.

HL Hard-Layer.

HM Heavy Metal.

HRS High Resistance State.

IBE Ion Beam Etch.

IC Integrated Circuit.

ICT Information and Communication Technology.

IEC Interlayer Exchange Coupling.

IoT Internet of Things.

iPMA Interfacial Perpendicular Magnetic Anisotropy.

ipMTJ In-plane Magnetic Tunnel Junction.

IPP In-Plane Polarizer.

IT Information Technology.

LRS Low Resistance State.

MCA Magneto-Crystalline Anisotropy.

MCU Micro Control Unit.

MDL Magnetic Dead Layer.

MEA Magneto-Elastic Anisotropy.

MHM Magnetic Hard Mask.

MOKE Magneto-Optical Kerr Effect.

MOS Metal-Oxide-Semiconductor.

MRAM Magnetic Random Access Memory.

MS Macro-Spin.

MTJ Magnetic Tunnel Junction.

OOMMF Object-Oriented Micro-Magnetic Framework.

OxRAM Oxide Random Access Memory.

P Parallel state.

PCRAM Phase Change Random Access Memory.

PG Pulse Generator.

pMTJ Perpendicular Magnetic Tunnel Junction.

RA Resistance-Area product.

RL Reference-Layer.

RRAM Resistive Random Access Memory.

RVS Ramped Voltage Stress.

SAF Synthetic Anti-Ferromagnet.

SCM Storage Class Memory.

SHE Spin Hall Effect.

SIA Structural Inversion Asymmetry.

SMU Source Measure Unit.

SOC Spin-Orbit Coupling.

SOT Spin-Orbit Torque.

SRAM Static Random Access Memory.

STT Spin-Transfer Torque.

TE Top Electrode.

TEM Tunneling Electron Microscopy.

TI Topological Insulator.

TMR Tunneling Magneto-Resistance.

TP Top-Pinned.

VCMA Voltage Control of Magnetic Anisotropy.

VGSOT Voltage-Gate assisted Spin-Orbit Torque.

VSM Vibrating Sample Magnetometer.

List of Symbols

α	Gilbert damping constant
$\vec{\boldsymbol{l}}$	Angular momentum
Δ	Thermal stability factor
η	Spin-transfer torque efficiency
γ	Gyromagnetic ratio
$\hbar$	Reduced Planck constant
μ_0	Vacuum permeability
μ_B	Bohr magneton
ω	Angular frequency
τ_0	Inverse of the attempt rate
θ_R	Rashba coefficient
θ_{SH}	Spin Hall angle
$\vec{L}$	Total orbital angular momentum
$\vec{S}$	Total spin angular momentum
ξ	VCMA coefficient
A_{ex}	Exchange stiffness
B_C	Coercive field
B_{eff}	Effective field

B_{ext} External magnetic field

$B_{k,eff}$ Effective anisotropy field

$B_{thermal}$ Thermal fluctuation field

$B_{x,IPP}$ In-plane field generated by the in-plane polarizer

$B_{x,MHM}$ In-plane field generated by the magnetic-hard-mask

B_x Applied magnetic field in x direction

B_y Applied magnetic field in y direction

$B_{z,FL}$ Perpendicular field generated by the free-layer

B_z Applied magnetic field in z direction

D Junction diameter

d_w Domain nucleation width

E_b Energy barrier

E_F Fermi energy

E_{sw} Switching energy

f_p Precession frequency

f_s Switching speed

G Conductance

g g-factor

G_{AP} Conductance of the anti-parallel state

G_P Conductance of the parallel state

h Planck constant

I Electric current

I_c^{SOT} Critical spin-orbit torque switching current

I_c^{STT} Critical spin-transfer torque switching current

J_{ex} Exchange integral

k_B Boltzmann constant

K_d	Shape anisotropy
K_{eff}	Effective anisotropy
K_i	Interfacial anisotropy
K_{mc}	Magneto-crystalline anisotropy
K_{me}	Magneto-elastic anisotropy
m	Magnetic moment
M^{area}	Area magnetization
m_e	Electron mass
m_L	Orbital magnetic moment
m_l	Magnetic quantum number
M_S	Saturation magnetization
m_S	Spin magnetic moment
m_s	Spin quantum number
P	Electron polarization
P_{sw}	Switching probability
R_{AP}	Resistance of anti-parallel state
R_P	Resistance of parallel state
S	Area of circulating electric current loop
T	Operating Temperature
T_C	Curie temperature
t_{eff}	Effective thickness
t_{inter}	Inter-time between a double-pulse
t_{MDL}	Magnetic dead layer thickness
t_p	Pulse duration
V	Volume

Contents

List of Figures

List of Tables

Chapter 1

Introduction

Since ancient time, humans record information in the forms of symbols, characters, and texts on visible items to the naked eye such as slabs, planks, and papers. In 1947, the first germanium point-contact transistor [1] was invented, and later the well-known metal-oxide-semiconductor field-effect-transistor (MOSFET) [2] made significant changes to our lifestyles. The industry rapidly entered the information revolution bringing our lives into the digital age, a period of information technology (IT). Since then, integrated circuits (IC) and semiconductor devices have vigorously progressed. Moore's law [3] predicts the number of transistors on an IC chip doubling every two years, and the reality surprisingly obeys it over the past half-century. All these events allow us to calculate and memorize a huge amount of data on today's information and communications technology (ICT) systems.

The modern computers are designed with the architecture based on the report firstly proposed by John von Neumann in 1945, in which the input/output mechanisms and how the central processing unit (CPU) worked with the main memory were described [4]. This Von Neumann architecture later reached a bottleneck mainly due to the tremendous increase in the speed of the CPU and the size of the memory without a corresponding increase in the data transferring rate. This has led to today's memory hierarchy to mitigate the latency problems. The advancement of the memory technologies is therefore said to be the enabler for high computer performance [5].

1.1 Memory Hierarchy: Present and Future

In the ordinary computer systems, the performance is boosted by combining different types of memory technologies in order to improve the computational speed and maintain the data storage capacity, so-called memory hierarchy. Generally, there are three components: cache memory, main memory, and storage memory, as shown in Figure 1.1. The commercialized technologies responsible for the corresponding parts are: static random access memory (SRAM), dynamic random access memory (DRAM), and Flash memory/Hard-disk-drive (HDD). In the following, the fundamental working principles of these semiconductor memory technologies are briefly reviewed.

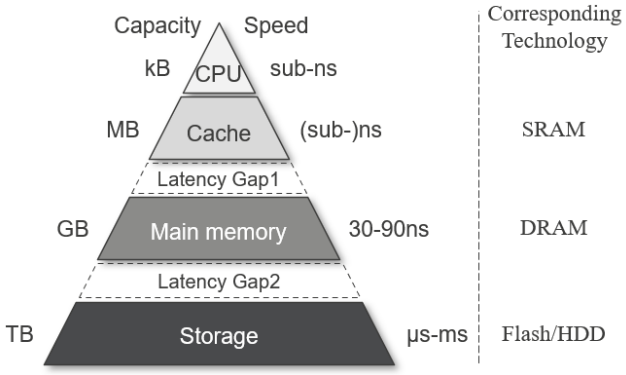

Figure 1.1: *A general memory hierarchy on the computer. Adapted from [5, 6, 7].*

Static Random Access Memory (SRAM): SRAM is a volatile memory that is typically composed of six transistors (6T), as shown in Figure 1.2(a). The two cross-coupled inverters formed by the four transistors in the middle are for storage, and the two access transistors on the sides are for writing and reading. SRAM is the fastest memory technology to date, for which the access time is in the range of (sub-)nanosecond [5]. Since it merely consists of silicon based transistors, it is integrated as embedded cache memory next to the CPU. On the other hand, as a volatile memory, SRAM retains its bit only when the power is supplied, which consumes stand-by power. Its 6T feature also makes it expensive and remarkably area consuming. Therefore, SRAM is suitable as cache memory only, and the computer requires other technologies to make up the deficiency of capacity.

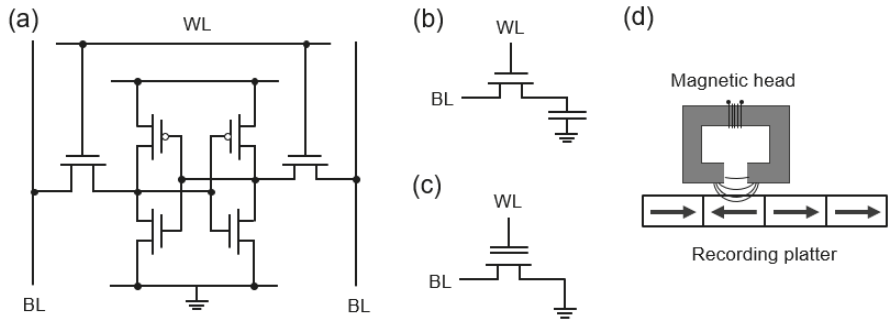

Figure 1.2: *Schematics of (a) SRAM with six transistors, (b) DRAM with one transistor and one capacitor, (c) Flash memory with one transistor and one floating gate, and (d) HDD with a magnetic head and a magnetic recording platter.*

Dynamic Random Access Memory (DRAM): DRAM is made up of one transistor and one capacitor (1T1C), as shown in Figure 1.2(b). It writes/stores the data through charging and discharging the capacitor. Due to the latency in charging the capacitor, the access time is in the range of few tens of nanoseconds. Since the capacitor (oxide) is leaky, DRAM needs to be refreshed intermittently, typically every 64ms. The term 'dynamic' refers to the need for this refresh operation. Once the power is turned off, the stored charges flow out. For these reasons, DRAM consumes larger energy than SRAM. On the other hand, DRAM's simple structure allows it to be densely integrated to compensate for the area disadvantage of SRAM.

Flash Memory: Flash memory is a type of non-volatile memory that serves as a storage medium. Each memory cell resembles a typical MOSFET, except there are two gates: control gate and floating gate [Figure 1.2(c)]. The control gate is on top of the floating gate. When programming, a positive voltage is applied to the control gate to induce electrons being injected from the channel to the floating gate. These electrons are trapped in the floating gate and cause electric field screening, leading to a shift in MOSFET's threshold voltage [8]. To erase the charges, a negative voltage is applied to the control gate to repel them away from the floating gate. These operations, however, require 20V stress which degrades the oxide layer gradually. Hence, the endurance is limited to the order of 10^5 cycles. In NAND Flash architecture, the cells are connected in series. When reading, the data needs to be accessed sequentially which increases the read latency. Overall, the characteristics of NAND Flash make it suitable

for massive data storage.

Hard-Disk-Drive (HDD): HDD uses a rotating platter that is coated with ferromagnetic materials for recording. The magnetization of the ferromagnet (FM) represents the binary logic states. A magnetic head, placed on an actuator, is on top of the platter for reading and writing, as sketched in Figure 1.2(d). The operating speed of HDD is specified by the time required to move the head to a track and the physical rotational speed of the platter. Hence, the average latency is long among conventional memory technologies. The advantages of HDD are low fabrication cost and large capacity.

To summarize the commercialized memory devices, Table 1.1 compares the performance metrics for these technologies.

Table 1.1: *Performance metrics for the commercialized memory technologies. Data collected based on Ref. [7, 9, 10].*

Parameters	SRAM	DRAM	NAND Flash	HDD
Cell size (F^2)*	>150	6-10	< 4	2-3
Read latency (ns)	< 1	30-50	10^3	$5 - 8 \times 10^5$
Write latency (ns)	< 1	30-90	10^5	$5 - 8 \times 10^5$
Endurance (cycles)	$>10^{15}$	$>10^{15}$	10^5	10^4
Retention	volatile	volatile	>10 years	>10 years

*F: feature size, the minimum printable size in a technology node.

1.1.1 Challenges in Modern Memory Hierarchy

As Moore's law persistently proceeds, ICT systems with conventional memory hierarchy (Figure 1.1) are facing three challenges. The first challenge regards the overall performance. There are two major latency gaps in the modern hierarchy, one lies between the cache memory and the main memory (Gap1), and another one lies between the main memory and the storage memory (Gap2). Gap1 is ascribed to the speed limit of DRAM. Due to its operating principle, the access time of DRAM is typically in the range of tens of nanoseconds, whereas cache SRAM can be as fast as sub-nanosecond [7, 12]. Gap2 stems from the latency of massive data storage technologies whose speeds are in the range of hundred-microseconds to milliseconds. Although, in the modern hierarchy [Figure 1.3(a)], these latency gaps are somewhat fetched up by the introductions of embedded DRAM (eDRAM) to Gap1 and storage class memory (SCM) to

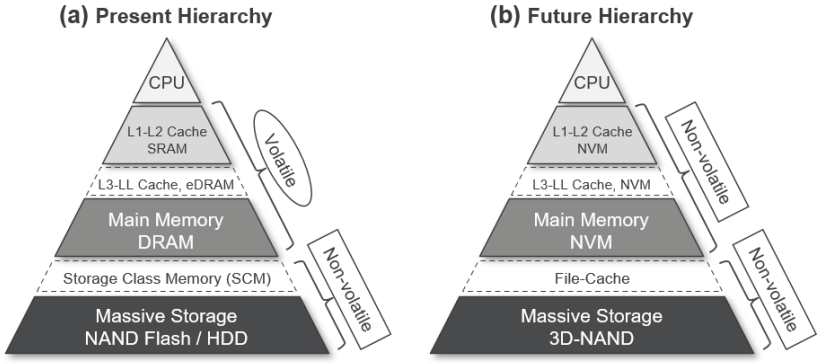

Figure 1.3: *Memory hierarchy (a) at present and (b) in the future. Adapted from Ref. [7, 11].*

Gap2, advancing in the technology node brings up the second challenge: power consumption.

The rapid increase in power consumption is primarily due to the scaling characteristic of the transistors and the increased memory density. Particularly, the simultaneous refresh of a large DRAM array to retain the cell information has to account for the extensive raise in the stand-by power. Such stand-by energy becomes comparable to the dynamic operating power consumption [7, 13].

Last but not least, despite stacking the memory layers based on speed and capacity enables better computing performance, this design leads to a slow start-up, long idle times, and low power efficiency. Because of the volatile nature of cache memory and main memory, during system booting and shutting down these devices have to transfer their data to the storage level, causing redundant time for system backup [11]. Design of a new memory architecture which made up completely with non-volatile memory technologies [Figure 1.3(b)] is believed to address the large stand-by power issue and additionally allows instant resuming to the state prior to interruption [7, 11].

Apart from the above-cited challenges, there are new concepts and applications, e.g. neuromorphic computing, Internet of Things (IoT), and machine learning, that requires alternative memory technologies whose performances are more suitable than the commercialized ones. In search of alternatives, several technologies are being intensively studied as the enablers, these are termed as "Emerging Memory Technologies".

1.1.2 Emerging Memory Technologies

As discussed in the previous section, various new technologies are being studied as the enablers for new applications and opportunities. Among many different concepts, resistive RAM (RRAM), phase change RAM (PCRAM), ferroelectric RAM (FeRAM) and magnetic RAM (MRAM) are of great interest. In the following, the basic working principle and the potential applications for these emerging memory devices are discussed.

RRAM: RRAM is a collective name referring to a group of memory technologies that can be switched between low resistance state (LRS) and high resistance state (HRS) by a reduction-oxidation reaction. Based on the materials used, it can be categorized into conductive bridge RAM (CBRAM) and oxide RAM (OxRAM), as shown in Figure 1.4(a) and (b). By applying voltage pulses, metal cations (CBRAM) or oxygen ions (OxRAM) migrate in the oxide layer to form/eliminate the conducting filament and achieve resistive switching [14, 15]. The filament formation mechanism relies mostly on the materials used and is less dependent on the physical size of the cell; therefore, these devices have good scalability in write performance. RRAM is also fascinating for its simple three-layered stack structure and low fabrication cost. RRAM cell is a simple 2-terminal device. Figure 1.4(c) shows the schematic of a RRAM cell which is made up with one transistor and one resistor (1T1R). Considering RRAM's overall characteristics, it can potentially target the SCM applications and also more recently by replacing Flash in the field of micro control unit (MCU) [7, 8].

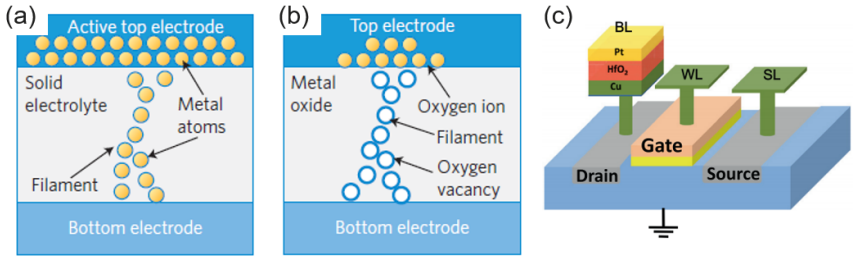

Figure 1.4: *Schematics of (a) the RRAM unit cell and the working principle for (b) CBRAM and (c) OxRAM. Reproduced from Refs. [5, 16].*

PCRAM: In PCRAM, a phase change material, such as chalcogenide glass, is connected to the top electrode on one side, and on another side first to a resistive heater then to the bottom electrode [5]. Figure 1.5 shows a schematic of a PCRAM unit cell. The basic working principle is to alter the phase between amorphous and crystalline upon heating and cooling. Such heat is generated by applying a current through the heater to induce Joule heating. The two phases, amorphous and crystalline, have different resistances, high and low, that can represent the two logic states. The advantage of PCRAM is its small unit cell size, it is therefore suitable for application in storage class memory [7].

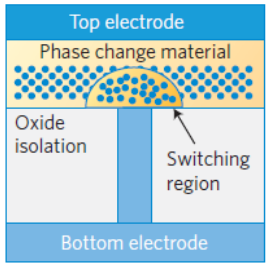

Figure 1.5: *(a) Schematic of a PCRAM unit cell showing the amorphous and crystalline phases in the programming region. Reproduced from Refs. [5].*

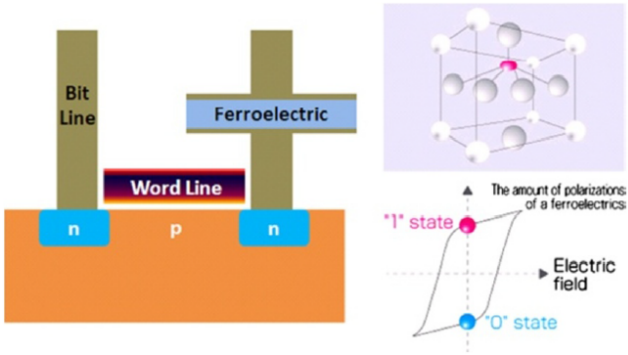

Figure 1.6: *(Left) FeRAM unit cell. (Right-top) The crystal structure of a ferroelectric material and (right-bottom) the ferroelectric hysteresis curve. Reprinted from Ref. [8].*

FeRAM: FeRAM is a non-volatile RAM that combines a ferroelectric capacitor and a transistor as shown in Figure 1.6 [8]. The cell is accessed

via the transistor, which enables the switching of the ferroelectric state in the capacitor. The typical capacitor material is lead zirconate titanate (PZT), which can be polarized up and down upon electric field application. Its polarization state retains without external electric field applied. More recently, hafnium oxide (HfO_2) has gained a great deal of attention as it is a common material in CMOS techonology, and it exhibits ferroelectric properties through engineering with dopants [17]. The ferroelectric HfO_2 possesses better coercivity than the traditional PZT, making it better in data stability. However, the major challenge in FeRAM is the endurance. Operation of FeRAM requires the electric field that is close to the breakdown value. In addition, read cycles are also counted as to the total number of endurance cycles. Due to the endurance limitation, despite FeRAM having faster write/read speed, its applications may be somewhat limited to MCU with small storage capacity [7].

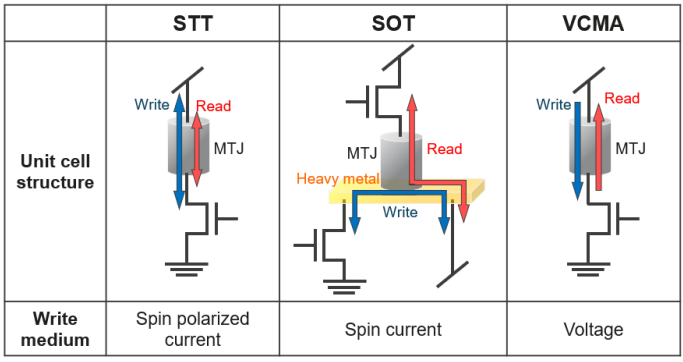

Figure 1.7: *MRAM cell structure for different write mechanisms: spin-transfer torque, spin-orbit torque, and voltage control of magnetic anisotropy.*

MRAM: MRAM is a class of memory technology that exploits magnetic materials for reading, data storage, and writing. By its writing mechanisms, MRAM can be subdivided into spin-transfer torque (STT), spin-orbit torque (SOT), and voltage control of magnetic anisotropy (VCMA). The unit cell structures of these devices are shown in Figure 1.7. Both STT and SOT use current for writing, whereas VCMA writing is voltage-mediated. The working principle of MRAM will be discussed in more detail in the next section (Section 1.2). Among the emerging memory technologies, MRAM has advantages of fast write/read speed, small cell size, long retention, low power, and ideally unlimited endurance. With these merits, MRAM is highly potential for a wide range of applications such as cache memory, main memory, MCU, and Internet of Things (IoT) [18, 19, 20].

To summarize, Table 1.2 compares the performance metrics of different emerging memory technologies.

Table 1.2: *Performance metrics for emerging memory technologies. Data collected based on Ref. [7, 21, 22].*

Parameters	**RRAM**	**PCRAM**	**FeRAM**	**MRAM**
Cell size (F^2)	6-10	4-19	15-35	6-14
Read latency (ns)	<10	<10	<10	<10
Write latency (ns)	100	100	30	0.1-10*
Write power (J/s)	10^{-4}	10^{-4}	10^{-6}	10^{-4}-10^{-6}*
Endurance (cycles)	10^{9}	10^{9}	10^{13}	10^{15}
Retention	>10 years	>10 years	>10 years	>10 years

*Differ by write mechanisms (see Section 1.2.4).

1.2 Magnetic Random Access Memory: Device Design and Operation

In the previous section, it was pointed out that MRAM shows great potential for future applications in many fields. In this section, more details in the MRAM system will be discussed from the aspects of stack design and working principle.

The basic operations of a memory technology include reading, retention of data storage, and writing. In MRAM, these operations are enabled by the combination of a transistor and a magnetic tunnel junction (MTJ). The development of the MTJ structure can be dated back to the first discovery of the tunneling effect by M. Julliere in 1975 in a Fe/Ge/Fe stack [23]. Two distinct resistances are observed in accordance with the orientations of the two ferromagnets, parallel (P) and anti-parallel (AP), which provide the prototype of reading operation as '1' or '0' for the logic states. As an intrinsic nature of a ferromagnet (FM), the magnetic anisotropy brings an energy barrier between the two states, enabling non-volatile data storage. To switch between the two states, the write mechanism has evolved from magnetic field switch in the old days to spin-transfer torque (STT) of today, and to spin-orbit torque (SOT) and voltage control of magnetic anisotropy (VCMA) in the future. In the following discussions, the state-of-the-art MTJ and the fundamentals of the operation principles are reviewed.

1.2.1 Perpendicular Magnetic Tunnel Junction

In the early stage of MTJ development, research focused on the in-plane magnetized magnetic tunnel junction (ipMTJ). However, on the basis of device scaling and power reduction, MRAM has evolved into today's perpendicular magnetized magnetic tunnel junction (pMTJ). The current pMTJ can be categorized into bottom-pinned (BP) and top-pinned (TP) stacks, as shown in Figure 1.8. Both stacks are assembled with some common components.

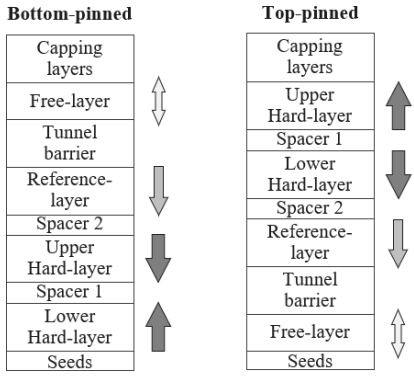

Figure 1.8: *The state-of-the-art stacks for bottom-pinned (left) and top-pinned (right) magnetic tunnel junctions.*

Seeds: Seed layers serve as the crystalline/amorphous template to provide the layers above with a specific texture. Difference seed layers are observed to impact the physical properties such as crystalline structure and orientation of the layers grown above. Modification in these physical properties can vary the magnetic [24, 25] and transport properties [26, 27, 28].

Hard-layers and Spacer 1: Both lower hard-layer (HL) and upper hard-layer are magnetically hard compared to the reference-layer (RL) and the free-layer (FL), and they are antiferromagnetically coupled by a non-magnetic spacer (Spacer 1) through interlayer exchange coupling (IEC) to form so-called the synthetic anti-ferromagnet (SAF). The purpose is to imitate the antiferromagnet used in the older generations of MRAM technology (with ipMTJ) that pins the direction of the RL. Typical materials used for the HLs are $[Co/Pt]_x$ [29, 30, 31] and $[Co/Pd]_x$ multilayers [32, 33]. Each Co/Pt and Co/Pd interface provides a strong interfacial perpendicular magnetic anisotropy through spin-orbit coupling,

making the hard-layer insensitive to any disturbance. In the advanced pMTJ, the upper HL in the BP stack (or the lower one in the TP stack) is reduced or removed, with only a thin Co layer remaining which subtracts the entire thickness of the MTJ without paying penalties on the magnetic and transport properties [34].

Spacer 2: A second spacer (Spacer 2) is adopted to couple the RL ferromagnetically to the adjacent SAF. Through IEC, the RL is pinned and becomes robust against disturbances such as external magnetic field and spin torques.

Reference-layer: The RL is placed at the opposite side of the tunnel barrier against the FL, forming the key FM/barrier/FM structure for pMTJ operation. Recent studies focus on using FeB and CoFeB as the RL since these materials are lattice-matched with MgO barriers. In addition, they provide high spin polarization [35, 36] and tunneling magneto-resistance ratio (TMR) when combined with the MgO barrier [37, 38].

Tunnel barrier: The tunnel barrier is typically an oxide layer which filters the Bloch state of the tunneling spins, resulting in TMR effect. In the early stage of MRAM development, Al_2O_3 was used as the barrier [39, 40] material. Later, MgO was discovered to outperform Al_2O_3 [38, 41] in all aspects. Intensive studies are performed on MgO thereafter, and to date, no other oxide can surpass the performance of MgO based devices.

Free-layer: For the FL, CoFeB and FeB are the top research objects not only due to high TMR, but also low damping constants [42] which makes the writing of MTJ devices more efficient. In addition, it is important that the FL possesses high thermal stability in order to have long data retention. This recently led to the design of double-MgO FL, e.g. MgO/CoFeB/Ta/CoFeB/MgO structure [43, 44]. The Ta layer in the middle couples the two CoFeB layers ferromagnetically such that they behave as a single magnetic recording layer. By doing so, there are two additional interfaces contributing interfacial perpendicular magnetic anisotropy, and the total volume of the FL can be almost doubled. Since data retention is exponentially proportional to the volume and anisotropy, double-MgO FLs often have retention much longer than conventional single MgO FL [43].

Capping layers: Capping layers are crucial to the properties of the adjacent ferromagnets. Especially in the BP stacks, capping layers can effectively modify the thermal budget [45], damping constant [46], perpendicular magnetic anisotropy [47] and other magnetic properties [48] of the FL.

1.2.2 Read mechanism

In order to identify '1' and '0', any memory cell must offer two distinguishable states. In MRAM, this is accomplished by the tunneling magneto-resistance (TMR) effect which gives two distinct resistances in an MTJ. The key components include two FMs and a sandwiched oxide, i.e. FM/oxide/FM structure. The oxide layer, MgO, is thin enough to allow electrons tunneling through. A general picture of the concept is given in Figure 1.9. When electrons pass through a ferromagnet, they are polarized based on the orientation of the magnetization, and the amount of polarization depends on the spin-dependent density of states (DOS) at the Fermi-level:

$$P = \frac{D_{\uparrow}(E_F) - D_{\downarrow}(E_F)}{D_{\uparrow}(E_F) + D_{\downarrow}(E_F)} \tag{1.1}$$

with $D_{\uparrow}$ and $D_{\downarrow}$ being the DOS of the up- and down-spin electrons, respectively. When there is a potential difference, the conductance (G) of the junction is dependent on the orientation of the two ferromagnets. To be more specific, the DOS of the first FM and the DOS of the second FM define the tunneling probability:

$$G_P \propto D_{\uparrow,1}(E_F)D_{\uparrow,2}(E_F) + D_{\downarrow,1}(E_F)D_{\downarrow,2}(E_F) \tag{1.2}$$

$$G_{AP} \propto D_{\uparrow,1}(E_F)D_{\downarrow,2}(E_F) + D_{\downarrow,1}(E_F)D_{\uparrow,2}(E_F) \tag{1.3}$$

Here, G_P and G_{AP} denote the conductance in the P state and in the AP state, respectively. Then, the TMR ratio can be derived:

$$TMR = \frac{2P_1P_2}{1 - P_1P_2} = \frac{G_P - G_{AP}}{G_{AP}} = \frac{R_{AP} - R_P}{R_P} \quad [\%] \tag{1.4}$$

Up to here, the general picture of the TMR effect is explained using the Julliere's model which, however, fails to explain the high TMR phenomena in the crystalline MgO based MTJs [37, 41]. In fact, for crystalline MgO combined with body-centered-cubic(001) (BCC) FMs, e.g. CoFeB and FeB, the electrons with different band symmetries have dissimilar tunneling probabilities. Especially, it correlates with the thickness of the MgO barrier. Electrons with different symmetries are subjected to different decay rates, resulting in a spin-filtering effect and giant TMR [50, 51].

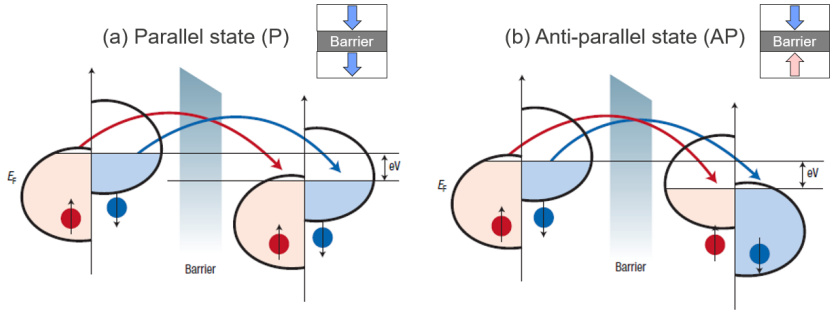

Figure 1.9: *Schematics of the tunneling magneto-resistance effect in the magnetic tunnel junction formed by a tunnel barrier and two ferromagnets: (a) the parallel state in which the two ferromagnets orient in the same direction, and (b) the anti-parallel state in which the two ferromagnets orient in opposite directions. Reproduced from Ref. [49].*

1.2.3 Retention of Data Storage

The non-volatile nature of MRAM cell is attributed to the magnetic anisotropy in the ferromagnet. The sources of the anisotropy include magneto-crystalline anisotropy (MCA), interfacial perpendicular magnetic anisotropy (iPMA), shape anisotropy and magneto-elastic anisotropy (MEA). These will be discussed in Chapter 2. Overall, the effective magnetic anisotropy provides the magnetization of the FL with an energetically favorable axis, so-called the easy axis. In pMTJs, this corresponds to the out-of-plane axis (z-axis). The two directions, $+z$ and $-z$, are energetically equivalent in an ideal case, i.e. no external forces to make them asymmetric. In presence of such anisotropy, an energy barrier exists in between the two directions, allowing the FL to stably point in one of the directions even within small disturbance like thermal fluctuation. An ordinary energy profile for a magnetic anisotropic system is shown in Figure 1.10(a).

For pMTJ devices, the energy barrier (E_b) and the thermal stability factor Δ can be expressed as [52]:

$$E_b = K_{eff}V = \frac{1}{2}\mu_0 M_S B_{k,eff} V_{FL} \quad [J] \tag{1.5}$$

$$\Delta = \frac{E_b}{k_B T} \tag{1.6}$$

where K_{eff} is the effective magnetic anisotropy energy density, V_{FL} is the volume of the FL, μ_0 is the vacuum permeability, M_S is the saturation magnetization, $B_{k,eff}$ is effective anisotropy field, k_B is the Boltzmann's constant and T is the

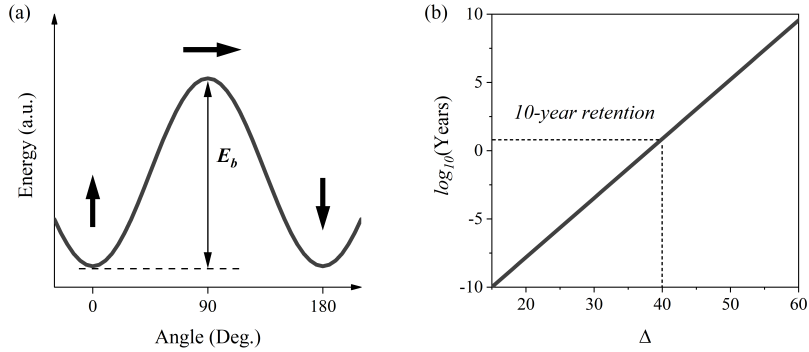

Figure 1.10: *(a) Data storage mechanism, showing two magnetically stable states separated by an energy barrier. (b) Retention as a function of thermal stability factor (Δ) for a single cell.*

ambient temperature in Kelvin. The thermal excitation rate for a single cell can be estimated with the Arrhenius equation:

$$f = f_0 \exp(-\Delta) \quad [s] \tag{1.7}$$

with f_0 being the attempt rate, typically 1 GHz. As shown in Figure 1.10(b), the required Δ to achieve 10 years retention is approximately 40 for a single cell, and it should be higher ($\Delta > 60$) to meet the required number of failures in time (FIT) for memory arrays > 1Mbits [52].

1.2.4 Write mechanisms

For MRAM technologies, data writing refers to the mechanisms that can rotate the magnetization of the FL to obtain the magnetic states at will. In the early stage of MRAM development, the magnetic states were switched by the magnetic field. However, to generate a large enough magnetic field, the required current flowing through the metal line is enormously increased in the scaled devices since it is inversely proportional to the volume of the storage layer. This is because when the device size is reduced, one must increase the magnetic anisotropy to overcome the loss of volume in order to maintain its retention (Equation 1.5). Therefore, magnetic-field-driven MRAM devices cannot be scaled beyond 90nm node [53]. So at a certain time, MRAM technology was believed not to be a feasible solution. It was not until the proposal of spin-transfer torque MRAM [54] that the research interest revived, though spin-transfer torque had been

predicted for a decade [55, 56]. Following upon the heels of STT-MRAM, spin-orbit torque (SOT) [57] and voltage control of magnetic anisotropy (VCMA) MRAMs [58, 59] were proposed and attracting great attention. In the following, these writing mechanisms are introduced.

Spin-Transfer Torque (STT)

Spin-transfer torque refers to the transfer of angular momentum of the spin polarized current to the ferromagnet. It has been used to switch the FL magnetization in spin-valve (SV) and magnetic tunnel junction (MTJ). To explain the STT effect, we consider the relatively simple structure: two ferromagnets and a metal sandwich (Figure 1.11). Notice that this SV device has giant magnetoresistance (GMR) instead of TMR, yet it yields good explanation on the phenomenon. The situation in MTJ devices is more complex which depends on several factors [60]. When electrons passing through one ferromagnetic layer, they are polarized in the direction of the magnetization producing the majority spin. Within the spin diffusion length, the polarization of the polarized electrons is preserved and is able to exert a torque on another ferromagnet. In the case of writing the parallel state (P), electrons are injected from the pinned layer to the free layer. The majority electrons, said up-spin, tunneling through the barrier and transfer their angular momentum to the free layer, resulting in the parallel orientation as shown in Figure 1.11(a). In the contrary, to achieve an antiparallel (AP) configuration, electrons are injected from the free layer side to the pinned layer. The majority electrons will pass through the interface while the minority electrons are scattered back to the free layer. These reflected electrons exert a torque to force the free layer aligning antiparallelly to the pinned layer, as shown in Figure 1.11(b). Since the pinned layer is stabilized by the adjacent antiferromagnet or the synthetic antiferromagnet, it is more robust compared to the free layer, and its magnetization remains stable during the write operation.

In SV devices, switching occurs upon reaching the critical current, or in pMTJ devices it occurs at the critical voltage [62]:

$$I_{c,SV}^{STT} \sim \frac{2e\alpha\mu_0 M_S B_{k,eff} V}{\eta\hbar} \tag{1.8}$$

$$V_{c,MTJ}^{STT} \sim \frac{2e\alpha\mu_0 M_S B_{k,eff} V R_{\perp}}{\eta\hbar} \tag{1.9}$$

where α is the Gilbert damping constant which represents the relaxation rate of the magnetization to its equilibrium position and $R_{\perp}$ is the median resistance of AP and P states. The STT efficiency η is a parameter related to the spin

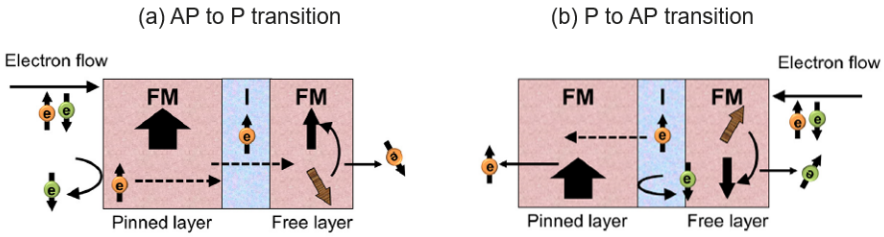

Figure 1.11: *Illustration of STT effect in a spin-valve. (a) The AP to P transition. Electrons are injected from the pinned layer side. The majority spin exerts a torque on the FL to reverse it. Before switching the electrons also receive torques from the free layer so that it is reversed at the initial switching state. (b) The P to AP transition. Electrons are injected from the free layer side. The majority electrons pass through the barrier, while the minority electrons reflect at the interface to exert torques on the free layer itself. Reproduced from Ref. [61].*

polarization. Intuitively from both equations, to reduce the write current/voltage of STT-MRAM, decreasing damping constant, and enhancing STT efficiency are the primary targets.

Spin-Orbit Torque (SOT)

Spin-orbit torque refers to the torque applied on the magnetization by the spin current which is generated from the spin-orbit coupling (SOC) effect (see Chapter 2), contrary to STT whose torque is applied by spin-polarized current induced from polarization. In recent MRAM research, SOT attracts a great deal of attention as it offers an alternative write mechanism with faster switching and lower energy than the STT mechanism [57, 63]. The physics behind SOT includes the spin Hall effect (SHE) and the Rashba effect [64].

The *Spin-Hall effect* (SHE) is a spin-orbit interaction phenomenon that converts a charge current into spin current due to different spin-dependent scattering mechanisms. When a charge current travels in a heavy metal layer, the SOC effect leads to the deflection of electrons of different spins in different directions, shown as the green arrow in Figure 1.12(a). Currents with pure spin directions are then produced transversely to the applied charge current [65, 66]. As an example, if the charge current is traveling along $+x$ direction, the electrons deflected in $+z$ ($-z$) direction contains spin in $+y$ ($-y$) direction. Different from the spin-polarized current in STT mechanism, the spin current generated

by SHE contains equal amount of electrons with contrary spin directions at the opposite surface (interface). The number of electrons in the charge current being converted into the spin current by SHE is characterized by the spin Hall angle θ_{SH}, the ratio of the spin current to the charge current.

$$\theta_{SH} = \frac{I_{SH}}{I} \tag{1.10}$$

Considering a simple system with a heavy metal(HM)/FM structure, the critical current to induce magnetization switching is characterized as [67]:

$$I_c^{SOT} \sim \frac{2eM_S t_{FL}}{\hbar\theta_{SH}} \left(\frac{B_{k,eff}}{2} - \frac{B_x}{2} \right) t_{SOT} w_{SOT} \tag{1.11}$$

where B_x is the applied in-plane magnetic field in the x direction, t_{SOT} is the thickness of the SOT layer, and w_{SOT} is the width of the SOT track. It can be clearly seen that a larger θ_{SH} is responsible for lowering the switching current.

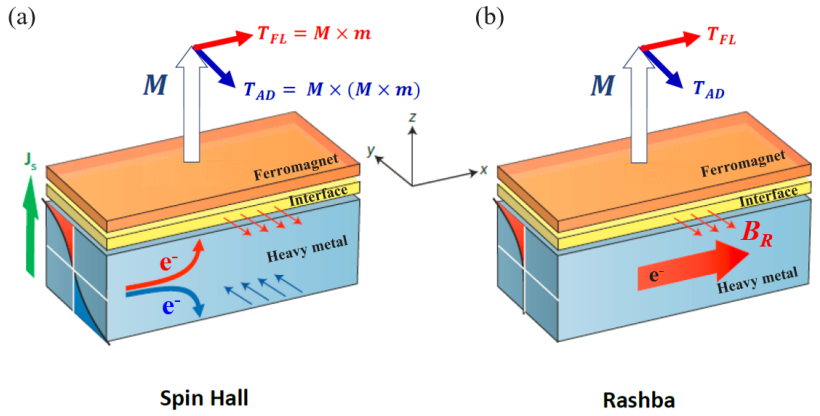

Figure 1.12: *Illustration of spin-orbit torques. (a) The spin-Hall effect. Electrons with opposite spin directions $+y$ and $-y$ flowing in the $+x$ direction are deflected in $-z$ and $+z$ directions, creating a spin current with pure spin (green arrow) at the top and bottom interfaces. The electrons at the heavy metal/ferromagnet interface (red arrow) electrons with spin in $-y$ direction will then apply anti-damping torque (T_{AD}) and field-like torque (T_{FL}) on the ferromagnet. (b) The Rashba effect. Electrons traveling at the interface with strong spin-orbit coupling and structural inversion asymmetry induce a Rashba magnetic field (B_R) in the plane. Reproduced from Ref. [68].*

The *Rashba effect* occurs when electrons travel at the interface with strong spin-orbit coupling and structural inversion asymmetry (SIA). With SIA, an

electric field perpendicular to the interface is created due to the difference in crystal electric fields above and below. Electrons flowing at such interface induce a Rashba magnetic field (B_R) in the direction of $k \times E$ [69], with k and E being the direction of the electron flow and the electric field, respectively. For the same electron flow as we discussed in the spin Hall effect, the resultant Rashba magnetic field is in the same direction as the anti-damping torque to accelerate SOT switching, as shown in Figure 1.12(b).

SOT-MRAM shows great potential in cache memory applications, as SOT enables ultra-fast, energy efficient and MTJ degradation-free writing of MRAM devices. However, to generate the spin current, SOT-MRAM requires a three-terminal structure as shown in Figure 1.7, which enlarges the unit cell size. To breakthrough this physical limitation, a modified cell structure that exploits a hybrid switching mechanism (VCMA and SOT) has been proposed [70]. Studies on such VCMA-SOT induced switching will be discussed in Chapter 6.

Voltage Control of Magnetic Anisotropy (VCMA)

VCMA, as its name suggests, allows controlling of the magnetic anisotropy and magnetization reversal with voltage (electric field) applied instead of current. It was first experimentally observed in 2007 in a liquid electrolyte system [71] and first realized in 2009 in a solid-state system [58]. When a FM/oxide interface is charged/discharged, the interfacial perpendicular magnetic anisotropy (iPMA) is reduced/enhanced, corresponding to the reduction/increase in the energy barrier as shown in Figure 1.13(a). The physical background behind the VCMA properties will be introduced in Chapter 2. If the anisotropy of the ferromagnet is initially close to the transition between perpendicular and in-plane, applying corresponding voltages to the system can effectively alter its anisotropy and the equilibrium effective field ($\vec{B}_{eff}^{eq}$) [72]. As shown in Figure 1.13(b), when $\vec{B}_{eff}^{eq}$ is switched from perpendicular to in-plane by voltage, the magnetization will precess about the new $\vec{B}_{eff}^{eq}$ to induce precessional switching [59]. The required time to switch from up to down corresponds to the period of a half precession. More details regarding the VCMA induced switching mechanisms will be studied in Chapter 3-4.

VCMA effect in the recent MRAM research is attractive and important. On one hand, as a write mechanism, VCMA enables switching of the magnetization with power consumption several orders lower than that of all other emerging memory technologies [73], expect for FeRAM. On the other hand, as an assisting effect, VCMA can effectively reduce the switching energy of STT-/SOT-MRAMs at a shorter write duration [70, 74]. Moreover, since the electric current is not required, the MgO barrier can be made much thicker than in STT/SOT

devices to suppress the writing energy. Hence, VCMA devices are more adapted to advanced usages such as neuromorphic computing and machine learning, which require intensive writing with extremely low energy consumption, than STT/SOT devices.

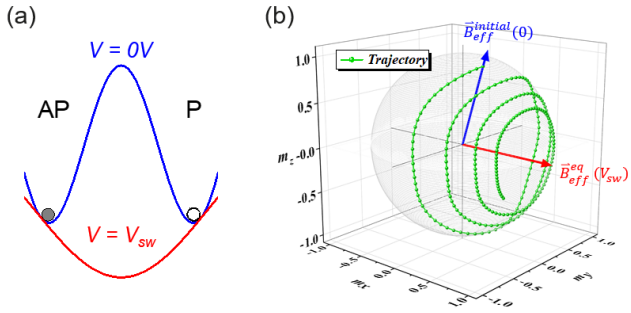

Figure 1.13: *(a) Reduction of the energy barrier when a voltage is applied. (b) VCMA induced precessional switching. The effective field direction can be manipulated by voltages to change the FL precessional axis.*

1.3 Summary

In this introductory chapter, we reviewed the ordinary memory technologies (SRAM, DRAM, Flash, and HDD) that are commercialized in the modern ICT systems. The challenges in the modern hierarchy were pointed out, which becomes the driving force for developing faster speed and lower power memory devices for new memory architecture and applications. We also briefly introduced the fundamentals of emerging memory technologies. For applications such as storage class memory and microcontroller, RRAM, PCRAM and FeRAM are the top choices. As for the non-volatile cache and main memory applications, MRAM is believed to be the most suitable one among them. As scaling and improvement of ordinary memory devices continue, the study of new memory technologies aims at overcoming the bottlenecks of the ordinary ones to make new applications available.

1.4 Thesis Objectives

Around the time this thesis is written, STT-MRAM has reached maturity for mass production. Many major foundries have announced their prototype

products. However, power consumption and reliability issues will always come back when programming STT-MRAM at GHz speed due to the long incubation delays and large current injection. In the road to advance MRAM applications toward ultra-low power and faster speeds, the VCMA effect is of considerable importance. This Ph.D work will focus on implementation of VCMA effect in the novel MRAM devices, where the VCMA effect acts either as a main writing mechanism or as an assisting effect. For the former case, we further propose and study the solutions to the challenges in the conventional VCMA write scheme, namely in-plane field integration and pre-read operation issues. In the latter case, we combine VCMA to SOT effect, aiming to develop and benchmark a writing scheme that will suit non-volatile sub-30nm devices.

1.4.1 Thesis Outline

To conduct the studies on MRAM writing properties with VCMA effect, this thesis is organized as follow:

Chapter 2 - Voltage Control of Magnetic Anisotropy: Physics and Usages. In this chapter, we will review the necessary knowledge relevant to this dissertation. We will start with the physical origins of the ferromagnetism and various contributions to the magnetic anisotropy. Based on the different origins of magnetic anisotropy, numerous voltage control of anisotropy (VCMA) effects are introduced. From the perspectives of memory applications, the electronic based VCMA effect is emphasized and adopted for writing the MRAM devices. To assist understanding the general pictures of the magnetization energy and dynamics, two modeling domains (energy and time) in two different perspectives (macro-spin and micro-magnetic) are also introduced. In the end, the concept of precessional switching is reviewed as the background of conventional VCMA write mechanism.

Chapter 3 - VCMA Write Mechanism: Conventional Scheme. In search of alternative MRAM writing mechanisms beyond spin-transfer torque, VCMA promises ultra-low power and GHz writing speed. In this chapter, we will discuss the variations of the switching properties by changing the intrinsic (MgO barrier thickness) and extrinsic (amplitude of operating voltage and in-plane field) parameters. Further, by performing simulations, we correlate the experimental results to the modelings. Finally, the merits and challenges are stated, where the solutions to the challenges will be discussed in Chapter 4.

Chapter 4 - External-Field-Free and Deterministic Solutions to Conventional VCMA Write. After pointing out the challenges in the conventional VCMA operation scheme, we propose and demonstrate the novel solutions to the two fundamental operation challenges: **Challenge 1: In-**

plane field generator to manage field free operation and **Challenge 2: Deterministic switching to remove the pre-read operation**. For Challenge 1, two methods are investigated: in-plane polarizer (IPP) and magnetic-hard-mask (MHM). We first study them with micro-magnetic simulation, and we will find out the pros and cons of each methods. For demonstrations, we will use the MHM concept and show that it is a credible solution for device integration and scaling. For Challenge 2, we propose a new switching scheme that utilizing an asymmetric stability in both states. It will be demonstrated that the pre-read operation is not necessary, while 100% switching probability is achievable without knowing the initial state.

Chapter 5 - Operating Temperature: Impact on Magnetic and VCMA Writing Properties. Commercial devices should be able to sustain higher operating temperatures, e.g. 85°C, in order to adapt the variation in ambient temperature. In Chapter 5, we will study impact of temperature on both the magnetic and switching properties of the VCMA devices.

Chapter 6 - Hybrid MRAM: VCMA-Gate assisted Spin-Orbit Torque. Besides the challenges stated in Chapter 4, how to improve the VCMA efficiency to avoid compensating retention at sub-30nm MTJ size is still vague. A similar issue happens in SOT-MRAMs. The spin-Hall angle will be insufficient for scaled MTJ to maintain its data retention. Fortunately, VCMA and SOT effects occurs at two different interfaces, making a hybrid switching mechanism possible, so-called Voltage-Gate assisted Spin-Orbit Torque (VGSOT). In this chapter, we will discuss the properties of VGSOT writing. Based on the experimental results and the macro-spin model, we also study the criteria for implementation of VGSOT as the credible solution for the next MRAM generation.

Chapter 7: Conclusion and Outlook. Results and learnings in this work are concluded. In the perspective of long term development, the challenges remained in the VCMA- and VGSOT-MRAM technologies are also highlighted.

Chapter 2

Voltage Control of Magnetic Anisotropy: Physics and Origins

2.1 Introduction

As pointed out in Chapter 1, voltage control of magnetic anisotropy (VCMA) has become research of great importance and has the potential to bring MRAM technologies to a new era. In fact, intensive studies on the VCMA effects started merely a decade ago, and the physics behind them are just progressively established. This chapter provides the reader with the fundamental background of the VCMA effect which can serve as the basis to understand this thesis work. We first briefly introduce the fundamental of magnetic phenomena specifically for ferromagnetic materials in Section 2.2. As the prerequisite for the VCMA effects, various sources of magnetic anisotropy contributions are discussed in Section 2.3. Recognizing these magnetic anisotropy contributions leads us to the field of the VCMA mechanism. Various types of VCMA effect will be presented in Section 2.4. Section 2.5 presents the methods to calculate the magnetic energy and the magnetization dynamics, these methods will also be used in the experimental chapters. Finally, Section 2.6 reviews the preceding works on the understanding of precession switching mechanism. The knowledge gained from those studies is helpful for comprehending how VCMA writes the MRAM devices.

2.2 Magnetic Phenomena in Ferromagnet

2.2.1 Magnetic Moment

The magnetic moment refers to the object that produces a magnetic field. In a classical view, it is explained by Ampere's circuital law which relates the magnetic field to the circulating electric current loop, as shown in Fig 2.1. The magnitude of the magnetic moment (m) of an electric current (I) loop with an area (S) is given by:

$$|m| = IS \quad [J/T] \tag{2.1}$$

In a magnetic material, the magnetic moment is generated by the orbital

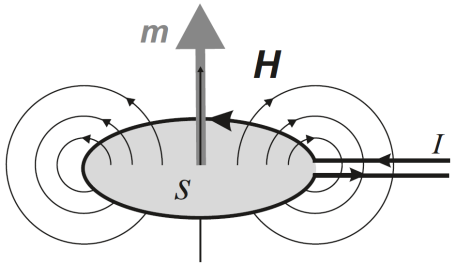

Figure 2.1: *Magnetic moment (m) and magnetic field (H) of an electric current (I) loop with area S. Reprinted from Ref. [75]*

angular momentum and spin angular momentum of the electrons. The orbital angular momentum is associated with the motion that an electron orbits around the nucleus. An electron possesses a charge $q = -e$, and its orbital motion creates a current loop $I = -e\omega/2\pi$, where ω is the angular frequency of the orbiting electron. The area of the orbital motion is πr^2, with r being the distance between the electron and the nucleus. Then, the classical form of the orbital magnetic moment (m_L) derived from Equation 2.1 is:

$$m_L = \frac{-e\omega r^2}{2} \tag{2.2}$$

The electron angular momentum ($\boldsymbol{l}$) can be expressed as $\boldsymbol{l} = m_e \omega r^2$, where m_e is the mass of the electron. Combining with Equation 2.2, we obtain an expression:

$$\vec{m}_L = -\frac{e}{2m_e}\vec{\boldsymbol{l}} \tag{2.3}$$

In a quantum mechanical view, the orbital angular momentum is quantized. The orbital quantum number, denoted as l (here the symbol is in light type

to avoid confusing with the classical angular momentum $\boldsymbol{l}$), has non-negative integer: 0, 1, 2, 3, etc. These orbital quantum numbers correspond to the electron orbits s, p, d, f, and so on. For each orbit, the magnitude of the quantized orbital magnetic moment is:

$$m_L = -\frac{e\hbar}{2m_e} m_l \tag{2.4}$$

where m_l is the magnetic quantum number which can take the integers: $-l$, $-l{+}1$, $\cdots\, l-1$, l. In this equation, the quantity $e\hbar/2m_e$ is defined as the Bohr magneton $\mu_B = 9.274 \times 10^{-24}$ $[J/T]$, a physical constant for expressing the magnetic moment of an electron caused by orbital or spin angular momentum.

In addition to the orbital angular momentum, the spin angular momentum of an electron also contributes to the magnetic moment. Electron by its nature has an intrinsic spin angular momentum, whose spin quantum number m_s takes the value of either $+\frac{1}{2}$ or $-\frac{1}{2}$. The spin magnetic moment associated with the spin angular momentum along the quantization axis is expressed as:

$$m_S = -g\mu_B m_s \tag{2.5}$$

where $g \simeq 2$ is called the g-factor.

In the case of a multi-electron atom, the orbital angular momenta of individual electrons are combined to get the total orbital angular momentum $\vec{L} = \Sigma \vec{m}_L$. Likewise, the total spin angular momentum is $\vec{S} = \Sigma \vec{m}_S$. Subsequent calculation of the total magnetic moment follows the Hund's rules and Pauli exclusion principle to maximize both L and S. Further derivation of the total magnetic moment is out of the scope of this thesis, but it is worth noting that only the valence electrons in the partially filled outer shell contribute to the magnetic moment since both L and S are zero for the full shells and sub-shells.

2.2.2 Spin-Orbit Coupling

So far, the magnetic moment is discussed from the aspect of considering the nucleus as the frame of reference. However, motion is relative, from the frame of reference of an electron it appears that the positively charged nucleus is also circulating the electron, and thus generating a magnetic field on the electron. A general picture for the concept of SOC is shown in Figure 2.2. The phenomenon that the magnetic field generated by the orbital motion of the nucleus ($\vec{B}_{SOC}$) interacts with the spin angular momentum is known as the spin-orbit coupling (SOC). In general, the energy of SOC is expressed as:

$$E_{SOC} = \lambda \vec{L} \cdot \vec{S} \tag{2.6}$$

where $\vec{L}$ and $\vec{S}$ are, respectively, the total orbital angular momentum and total spin angular momentum, and λ characterizes the strength of the interaction which is proportional to Z^4 (atomic number) [76]. Indeed, due to quenching of the electron orbital momentum, the orbital moment is small, but in heavy metals (HM) the SOC strength is largely increased and has strong impacts on the magnetic anisotropy. We will see later in Section 2.3 that SOC is of key importance for the interpretation of magnetic anisotropy.

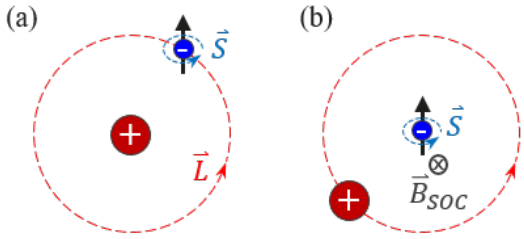

Figure 2.2: *Illustration of the concept of spin-orbit interaction. (a) From the nucleus frame of reference, the electron circulates the nucleus to create orbital angular momentum $\vec{L}$. (b) From the electron's frame of reference, the nucleus revolves around the electron generating a magnetic field ($\vec{B}_{SOC}$) acting on the electron spin ($\vec{S}$).*

2.2.3 Exchange Interaction in Ferromagnet

In previous sections, we have discussed that both orbital and spin angular momenta of the electrons contribute to the magnetic moment in response to the external magnetic field. However, it is known that ferromagnetic materials have a net magnetic moment even without magnetic field applied, so-called spontaneous magnetization. Such an appearance of an ordered spin alignment is a consequence of exchange interaction, which arises from the Coulomb interactions between electrons in combination with the Pauli exclusion principle [77]. To be more specific, it is the spin-spin direct exchange interaction that couples the spin moments together. For two spins with angular momenta $\vec{S}_a$ and $\vec{S}_b$, the exchange energy between them is:

$$E_{Ex} = -2J_{ex}\vec{S}_a \cdot \vec{S}_b \tag{2.7}$$

where J_{ex} is the exchange integral. If $J_{ex} > 0$, the electron spins are aligned in parallel resulting in a ferromagnetic ordering, whereas $J_{ex} < 0$ leads to an

anti-ferromagnetic ordering. The sign of J_{ex} is related to the inter-distance of the spins [78].

2.3 Magnetic Anisotropy

In the previous section, the exchange interaction aligns the spins either in parallel or in anti-parallel configuration. In a macroscopic view, such interaction is isotropic meaning there is no preferential direction for the aligned spins. However, in a ferromagnetic material, the spontaneous magnetization usually points in some favorable axes, namely the easy axes. These easy axes arise as a consequence of the magnetic anisotropy. Magnetization pointing along the easy axes are in the states with local energy minima. In contrast, those directions along the local energy maxima are called the hard axes. In general, four distinct contributions constitute the effective magnetic anisotropy: magneto-crystalline anisotropy, interfacial anisotropy, shape anisotropy, and magneto-elastic anisotropy. These contributions are discussed in the following sections. We will also exemplify the applications of these anisotropies in MRAM technologies.

2.3.1 Magneto-Crystalline Anisotropy

Magnetic crystalline anisotropy (MCA), denoted as K_{mc}, arises primarily from the spin-orbit interaction [79]. Although calculation of MCA is rather complicated mainly due to its small amplitude in light elements compared to the exchange interaction [80], theoretical calculations of MCA were carried out [80, 81, 82] on the basis of SOC. Since SOC couples the spin moment to the orbital moment and the orbital moment in the crystalline material is bonded to the crystal lattice through crystal field, the spin moment is therefore indirectly coupled to the lattice. This is where the MCA originates from, and the easy axis (axes) provided by MCA is (are) related to the crystal structure. The Bruno model [81] relates the MCA to the difference in the orbital magnetic moments along the easy and hard axes:

$$\Delta E_{SOC} = \frac{\lambda}{4\mu_B}(m_L^{easy} - m_L^{hard}) > 0 \tag{2.8}$$

where m_L^{easy} and m_L^{hard} are the orbital magnetic moment along the easy and hard axis, respectively. This equation states that the orbital moment is larger along the easy magnetization direction, and MCA is proportional to the difference between the orbital moments along the easy and hard directions. Generally,

MCA can be characterized by uni-axial and cubic anisotropy. Typical easy axis/axes for the uni-axial anisotropy is the *c*-axis for hexagonal systems, and for the cubic anisotropy are the principal axes <100>.

In the state-of-the-art pMTJ stack, the magnetic materials used are typically $3d$ transition metals (Co and Fe). The bulk MCAs of these layers are weak and can often be neglected [83]. However, in thin film layered systems, another important contribution arises significantly: the interfacial anisotropy.

2.3.2 Interfacial Anisotropy

In 1954, L. Néel [84] first proposed the concept of magneto-crystalline surface anisotropy which could originate from lacking of neighboring atoms. Later, P. Bruno [85] extended the theoretical calculations that included spin-orbit coupling and orbital magnetic moment to derive the anisotropy at the surface. Additionally, his model can be applied not only to the surface but also to the interface with broken symmetry. The anisotropy associated with the surface or interface is denoted as K_s or K_i. More recently, Y. Suzuki and S. Miwa [86] completed the expression of interfacial perpendicular magnetic anisotropy which took into account Bruno's model [85] and the intra-atomic magnetic dipole operator [87, 88]. Here, we briefly discuss these two contributions.

Bruno's model treats the anisotropy with SOC energy, which is then directly related to the orbital magnetic moment (Equation 2.8). The microscopic origin of the surface anisotropy can be qualitatively explained using the ligand field model [75]. To illustrate this concept, a model with a free d atom presented in the middle of the other four ions in a planar geometry is considered, as shown in Figure 2.3. The four neighboring ions can be either negatively or positively charged. An external magnetic field is applied along the $+z$ direction such that the orbital angular momentum is quantized, and m_l can take the values of $-2 \leq m_l \leq 2$. Noted that here m_l represents the same meaning as L_z used in Figure 2.3 and in Ref. [75]: the magnetic quantum number. In such configuration, the electron suffers from the effects of Coulomb repulsion or attraction depending on the sign of its neighboring charges. Now the in-plane d orbits, d_{xy} and $d_{x^2-y^2}$, are degenerated. The corresponding orbital moments perpendicular to the plane are quenched. On the other hand, the orbital motion perpendicular to the plane is less perturbed due to the lack of neighboring ions, and the corresponding in-plane orbital moment remains unquenched. For this 'free monolayer' system, the orbital moment is predicted to be larger in the plane than perpendicular to the plane, resulting in an in-plane surface anisotropy.

To this point, the ligand field model qualitatively explains Bruno's model that the magneto-crystalline surface anisotropy is related to the anisotropic orbital

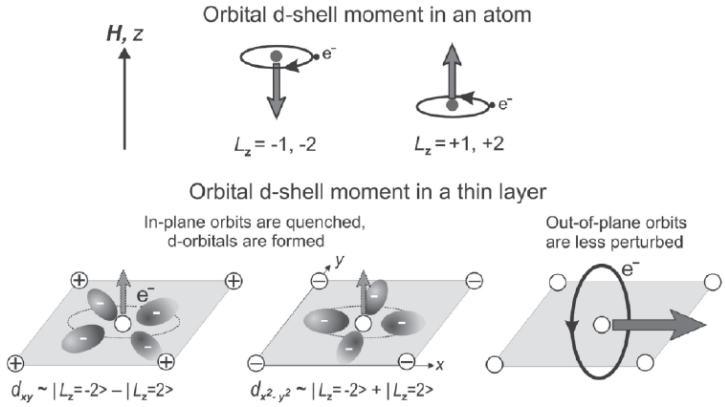

Figure 2.3: *Illustration of the directional quenching of the d orbital moments of an atom in a free thin film by the ligand field effects. The magnetic field (H) is applied in z direction and the magnetic quantum number takes the values of $-2 \leq L_z \leq 2$. Two in-plane d orbits, d_{xy} and $d_{x^2-y^2}$, are quenched by the four neighboring charges such that their corresponding orbital moments perpendicular to the plane are zero. The remaining perpendicular orbits create in-plane magnetic moments and in-plane surface anisotropy. Reprinted from Ref. [75]*

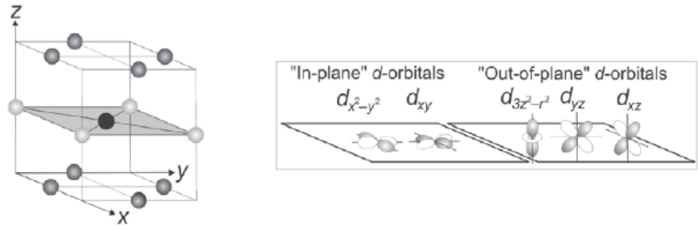

Figure 2.4: *Illustration of the anisotropic bonding in a sandwiched system that generates interfacial anisotropy. The atom(s) in black, light gray, and dark gray represents the center atom, in-plane neighboring atoms of the same type, and out-of-plane neighboring atoms of different types, respectively. Bonding of these ions forms five 3d orbits. Reproduced from Ref. [75]*

moments. In more realistic cases, we consider a magnetic monolayer sandwiched by two layers other than the one being sandwiched, as shown in Figure 2.4. Now the center atom is bonded to different ions above and below to form three additional perpendicular orbits: d_{yz}, d_{xz} and $d_{3z^2-r^2}$. Then, the interfacial

anisotropy direction is determined by the strength of the in-plane and out-of-plane bondings. For example, assuming the in-plane Co-Co bonding strength is normalized to 1, for out-of-plane Co-X bonding strength < 1 the resulting anisotropy is in the in-plane direction. This occurs when X = Cu and Ag [89]. On the contrary, for X = Au, Pt, Pd, and Ta, the out-of-plane Co-X bonding strength is larger than 1 [75], resulting in an interfacial perpendicular magnetic anisotropy (iPMA).

Although Bruno's model allows qualitative prediction for the anisotropy axis, it remains illustrative and is too simple to estimate the MCA energy. As pointed out by C. Andersson [90], the MCA is not directly proportional to the orbital moment in the case of Co in conjunction with heavy metals whose spin-orbit interactions are strong. This leads to the discussion of another contribution to the interfacial anisotropy other than Bruno's orbital contribution: the magnetic dipole operator T [87, 88]. The major difference is that the orbital term considers only the orbital moment, whereas the magnetic dipole operator term takes into account the orbital moment acting on the spin moment (both up-spin $\uparrow$ and down-spin $\downarrow$). Hence, the magnetic dipole operator is related to the quadrupole moment when SOC is strong. S. Miwa modeled the charge density in a MgO/Pt monolayer/Fe structure [91]. Since the dielectric/metal interface has an atomically inhomogeneous electric field due to strong electrostatic screening effect in metals, the anisotropic charge distribution causes anisotropy in the spin moment. As a consequence, an interfacial anisotropy is added in addition to Bruno's model. These two contributions, orbital moment (L) and magnetic dipole operator ($T^{'}$), yields the expression for the anisotropy energy [86]:

$$\Delta E \approx -\frac{\lambda}{4\hbar}(\langle \Delta L_{\zeta,\Uparrow} \rangle + \langle \Delta L_{\zeta,\Downarrow} \rangle) + \frac{7\lambda}{2\hbar}(\langle \Delta T^{'}_{\zeta,\downarrow\uparrow} \rangle + \langle \Delta T^{'}_{\zeta,\uparrow\downarrow} \rangle) \tag{2.9}$$

where $\langle \Delta L_{\zeta} \rangle \equiv \langle \Delta L_z \rangle - \langle \Delta L_x \rangle$ ($\langle \Delta T^{'}_{\zeta} \rangle \equiv \langle \Delta T^{'}_z \rangle - \langle \Delta T^{'}_x \rangle$) is the difference between angular momentum along z direction and x direction for the orbital (magnetic dipole) term. For materials with weak SOC, such as Fe and Co without contacting Pt, the orbital magnetic moment is then:

$$\Delta m_L \equiv m_{L,\perp} - m_{L,//} = -\frac{\mu_B}{\hbar}(\langle \Delta L_{\zeta,\Uparrow} \rangle + \langle \Delta L_{\zeta,\Downarrow} \rangle) \tag{2.10}$$

where $m_{L,\perp}$ and $m_{L,//}$ are the orbital moments perpendicular to the plane and in the plane, respectively. Combining Equation 2.9 and 2.10 with magnetic dipole terms being neglected yields $\Delta E = \frac{\lambda}{4\mu_B}\Delta m_L$, the same expression as Equation 2.8 (Bruno's model). In summary, for the light elements, Equation 2.8 yields a satisfactory explanation for the interfacial anisotropy, while for the heavy metals such as proximity magnetized Pt, treating both orbital and magnetic dipole contributions is required [86].

In MTJ stacks, there are two types of interface that induce interfacial perpendicular magnetic anisotropy (iPMA): ferromagnet/oxide and ferromagnet/heavy metal. The first one can be seen on the two sides of the MgO barrier, such as MgO/CoFe and MgO/Fe interfaces. Their iPMA arises from the hybridization between Fe (Co) $3d$ orbitals and oxygen $2p$ orbitals [92, 93]. The other type of iPMA is employed in the HL, which is typically composed of $[Co/Pt]_x$ or $[Co/Pd]_x$ multilayers. Each Co/Pt (Co/Pd) interface has a strong iPMA through SOC [94] making the HL invulnerable against disturbance.

2.3.3 Shape Anisotropy

The shape anisotropy (K_d) is linked to the geometry of the ferromagnet. It originates from the dipole-dipole interaction between spin moments in the ferromagnet. Considering a thin film ferromagnet with uniformly magnetized magnetic moments, a magnetization perpendicular to the film will leave magnetic poles spreading across a large area. This leads to a demagnetizing field to force the magnetization aligning along the longest axis to reduce total magnetic energy. Generally, the shape anisotropy for a homogeneously magnetized thin film ferromagnet can be expressed as:

$$K_d = -\frac{1}{2}\mu_0 M_S^2 (D_z - D_{x,y}) \tag{2.11}$$

where M_S is the saturation magnetization of the ferromagnet and $D_{x,y,z}$ is the demagnetization factor. Depending on the dimensions, the demagnetization factors have been numerically calculated for ellipsoids [95, 96], rectangular prisms [96], and circular cylinders [97].

The shape anisotropy was applied in the older generations of MRAM technology, whose MTJ stacks were in-plane magnetized. Both P and AP states were stabilized by patterning the MTJ pillar into an ellipsoidal shape. Research on in-plane MTJ has become less interesting as it limits the density of memory arrays. This has led to the use of pMTJ stacks, whose cylindrical shape allows densely packed arrays. In fact, a circular ferromagnetic thin film has an easy plane shape anisotropy, since the directions in the plane are isotropic. However, if such film is in conjunction with oxides and heavy metals, e.g. oxide/FM/HM, the interfacial perpendicular anisotropy is sufficiently strong to overcome the shape anisotropy, resulting in perpendicularly magnetized FL and pMTJ.

2.3.4 Magneto-Elastic Anisotropy

The magneto-elastic anisotropy (K_{me}), also referred to as the strain anisotropy, is an additional anisotropy when a ferromagnet is subjected to mechanical stresses. In the previous sections, we have discussed that the fundamental origins of the magneto-crystalline anisotropy are the spin-orbit interaction and the crystal field. If the lattice is deformed by a stress, change in the interatomic distance modifies the strength of the MCA, so-called the magneto-elastic anisotropy. Such strain can be induced by various sources, such as thermal stress associated with differences in thermal expansion coefficients, intrinsic stress brought about by the nature of the deposition process, and stress due to lattice mismatch between the adjacent layers [85, 98, 99]. The determination of magneto-elastic anisotropy is experimentally difficult due to its various origins. In fact, in most of the calculations for the magnetic properties of the sputter-deposited MTJ stacks, the magneto-elastic anisotropy is negligible since the shape anisotropy and the interfacial anisotropy dominate in the evaluation of the effective magnetic anisotropy [83, 100].

2.3.5 Exchange Anisotropy

When a ferromagnet is in conjunction with an antiferromagnet, the surface ions of the antiferromagnet tend to align the magnetization of the ferromagnet to its direction through exchange interaction, hence it was termed as the exchange anisotropy [101, 102]. Unlike other anisotropy contributions, exchange anisotropy provides the FM with an easy direction instead of an easy axis. As a consequence, the magnetic hysteresis loop of the FM is shifted, as shown in Figure 2.5. The amount of shift is called the exchange bias shift B_b. Since AFM has a net zero magnetization, it is robust against external disturbance, and the adjacent FM is pinned. Application of the exchange anisotropy can be seen in the MRAM technologies. In the in-plane MTJ generations, the RL was typically pinned by the antiferromagnet IrMn [103], whereas in the perpendicular MTJ generations it is pinned by the SAF structures $[\mathrm{Co/Pt}]_{\mathrm{x}}/\mathrm{Ru}/[\mathrm{Co/Pt}]_{\mathrm{x}}$ [20] or $[\mathrm{Co/Pd}]_{\mathrm{x}}/\mathrm{Ru}/[\mathrm{Co/Pd}]_{\mathrm{x}}$ [32].

2.3.6 Effective magnetic anisotropy

Since those five anisotropy components mentioned above do not necessarily provide the ferromagnet with the same easy axis, the overall anisotropy is determined by their sum, so-called the effective magnetic anisotropy (K_{eff}). As an example, we consider a general system compatible with the free-layer

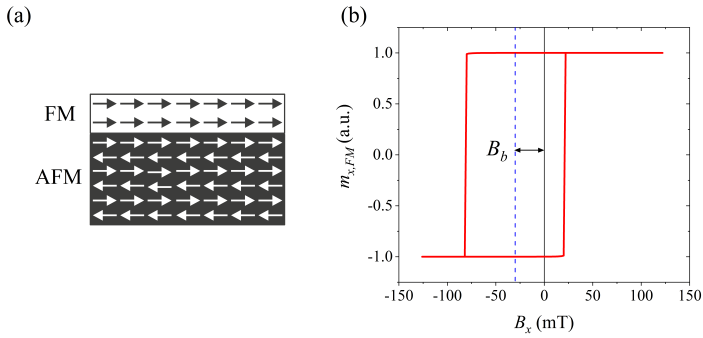

Figure 2.5: *(a) Schematic of a coupled FM/AFM system. (b) Hysteresis loop of the ferromagnet, showing a unidirectional bias shift B_b due to exchange interaction.*

(FL) of the pMTJ stacks: MgO/CoFeB/Ta, the effective anisotropy K_{eff} can be evaluated as:

$$K_{eff}\ [J/m^3] = K_{mc} + K_d + K_{me} + \frac{K_{i,MgO/CoFeB}}{t_{FL}} + \frac{K_{i,CoFeB/Ta}}{t_{FL}} \tag{2.12}$$

$$= K_V + \frac{K_i}{t_{FL}} \tag{2.13}$$

where t_{FL} is the thickness of the CoFeB FL. Here, K_V describes the total volume anisotropy contribution including the magneto-crystalline anisotropy, shape anisotropy, and strain anisotropy, while K_i indicates the total interfacial contributions from both MgO/CoFeB and CoFeB/Ta interfaces. The exchange anisotropy is not included as it will provide an easy direction which is not preferable for the FL.

For such MgO/CoFeB/Ta system, K_d is negative producing an in-plane anisotropy, while K_i is positive as discussed in Section 2.3.2. Below a critical FL thickness, K_{eff} is positive such that the system has an effective perpendicular magnetic anisotropy (PMA); or if the FL is above the critical thickness, K_{eff} is negative then the system exhibits an effective in-plane magnetic anisotropy (IPA).

2.4 Voltage Control of Magnetic Anisotropy

Voltage control of magnetic anisotropy refers to any direct/indirect voltage-mediated modulation of magnetic anisotropy. The first demonstration on voltage actuation of magnetic properties was carried out on a ferromagnetic semiconducting system [104]. However, it did not attract much attention from MRAM researchers. The potential applications of the magnetic semiconducting systems were somewhat limited because the Curie temperature (above which the ferromagnetism disappears) of these materials are typically much lower than room temperature (< 50K). Research interests on the VCMA effects were ignited only after the experimental results from M. Weisheit [71] in 2007 and T. Maruyama [58] in 2009. M. Weisheit presented a 1% change in the coercive field of a Fe/Pt stack which was immersed in a liquid electrolyte for gating, and T. Maruyama reported an 8.8kJ/m^3 change in magnetic anisotropy energy density under an electric field of 45mV/nm on the MgO barrier. Their experiments and key results are shown in Figure 2.6.

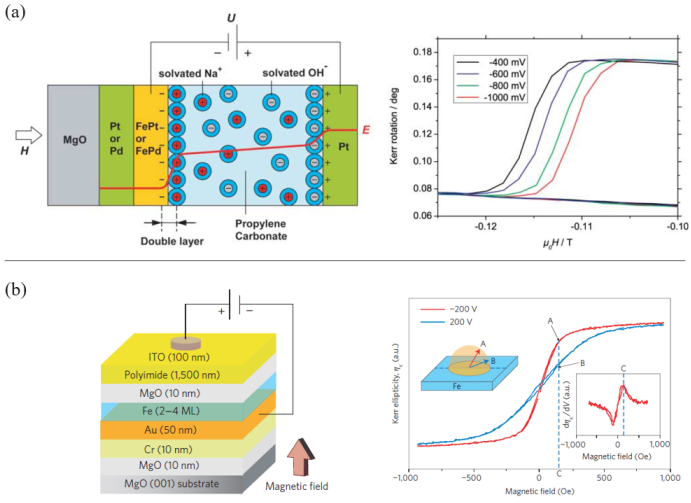

Figure 2.6: *First experimental observation of the VCMA effect. (a) A change in the coercive field of the immersed FePt (FePd) system is observed through gating the liquid electrolyte solution. (b) An all-solid-state system compatible with MRAM application shows a change in magnetic anisotropy upon voltage application. Reproduced from Refs. [58, 71]*

To date, studies have identified various mechanisms that can lead to the modulation of magnetic anisotropy upon voltage applications. Microscopically,

VCMA phenomena can be classified into electronic based and ionic based. Electronic based VCMA effects refer to any mechanism without ionic motions, whereas ionic based VCMA effects involve ionic motions such as diffusion and reduction-oxidation (redox) reaction. In the following sections, we will briefly review the different mechanisms.

2.4.1 Electronic VCMA

Pure Electronic VCMA

The pure electronic VCMA can be explained by the two mechanisms corresponding to the two terms we have introduced in Section 2.3.2: the orbital magnetic moment mechanism and the magnetic dipole (electric quadrupole) mechanism [105, 106]. A schematic of the orbital mechanism is sketched in Figure 2.7. As 3*d* electron orbits have different density of states in the vicinity of the Fermi level, selective charge doping to the orbits by an applied voltage induces a change in the total orbital magnetic moment, and thus modulates the interfacial anisotropy. Such effect is fundamentally based on Bruno's model.

The second mechanism is related to the electric quadrupole. As we discussed in Section 2.3.2, the atomically inhomogeneous electric field at the dielectric/metal interface that is coupled to the electric quadrupole leads to an anisotropic charge distribution, and it induces interfacial anisotropy. An external applied electric field can also couple to the electric quadrupole to cause additional redistribution of the spin moment, as illustrated in Figure 2.7(b) and (c). Since the electric quadrupole is correlated with the magnetic dipole operator, redistribution of the orbital occupancy modulates the interfacial anisotropy energy [91].

In simple words, the pure electronic VCMA is related to the charge doping and redistribution at the interface upon applying a voltage. Theoretical [91, 107] and experimental [108, 109] studies have been performed to validate the mechanisms. Experiments conducting ferromagnetic resonance (FMR) indicate an instant VCMA response upon voltage application [110, 111, 112], which enables high speed and low power operation of MTJ devices for MRAM applications [20, 113]. In this thesis, we will discuss in Chapters 3-6 how to use pure electronic VCMA as the MRAM writing mechanisms. In addition, a potential indication about either the orbital mechanism or quadrupole mechanism dominates the VCMA effect in our MRAM system will be discussed in Chapter 5.

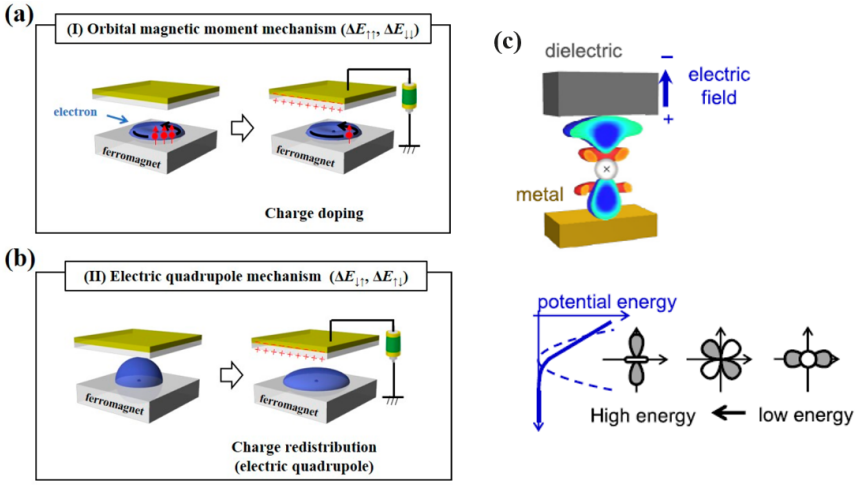

Figure 2.7: *Microscopic origin of the electronic VCMA effect. (a) Orbital magnetic moment mechanism. When a voltage is applied, electrons accumulate (deplete) at the interface. Selective doping to the 3d orbitals leads to a change in orbital magnetic moments, and thus the interfacial anisotropy is modulated. (b) Magnetic dipole (electric quadrupole) mechanism. Interface under applied voltage induces charge redistribution. Such redistribution of 5d orbitals produces the electric quadrupole and varies the magnetic dipole operator, which modulates the interfacial anisotropy. (c) Sectional view of the voltage induced charge density shift in 5d shell of a Pt atom. The electric quadrupole in an atom can be modulated intensively by redistributing the orbital occupancy under an applied voltage. Reprinted from Refs. [105, 106]*

Piezoelectric VCMA

As we discussed in Section 2.3.4, lattice distortion can induce additional contribution to the magnetic anisotropy. Based on this mechanism, if the lattice distortion can be varied upon voltage application, another VCMA mechanism can be realized. Experimentally this has been testified by combing ferromagnetic materials with a piezoelectric actuator [114] or a piezoelectric material [115]. It is therefore called the piezoelectric VCMA effect. Reversible easy axis transition has been demonstrated using a FeNi/piezoelectric actuator hybrid structure [114], as shown in Figure 2.8. However, the piezoelectric response time typically falls in the range of kHz [115], which does not give too much research interest for high speed MRAM applications.

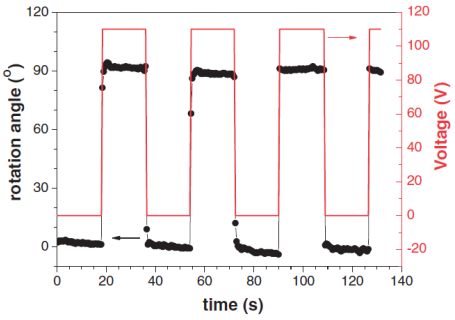

Figure 2.8: *Piezoelectric VCMA response for a FeNi/piezoelectric actuator hybrid structure. The magnetization rotation angle is detected by the real-time magneto-optical Kerr effect (MOKE). The easy axis shows an in-plane to perpendicular transition during a voltage application. Reprinted from Ref. [114]*

Other Electronic Based VCMA Mechanisms

There are yet other types of electronic based VCMA mechanisms. An example is the voltage induced change of Curie temperature in ferromagnetic semiconductors [104, 116]. The ferromagnetic semiconductor Mn-doped InAs [(In,Mn)As] was incorporated as the channel layer in a MOSFET. Application of a gate voltage was observed to modify the ferromagnetic-paramagnetic transition temperature (Curie temperature) of the [In,Mn]As layer through altering the hole-concentration. However, the Curie temperatures of ferromagnetic semiconductors are typically much lower than room temperature (< 50K), which limits the applications.

As another example, a voltage control of exchange bias in FM/AFM structures was also reported [117, 118]. The sign of the exchange bias was reversed upon voltage application such that the magnetization of the FM could be switched thereupon. K. Toyaki suggested the reversal was dominated by AFM domain wall (DW) propagation [119]. However, the transition time depended on the domain wall propagation speed which is in the order of microseconds [119]. In addition, this mechanism requires a certain electric field at the FM/AFM layers, which is unlikely realized in MTJ stacks, since the voltage drop mainly occurs in the vicinity of the MgO barrier.

Despite having drawbacks in these approaches, it is nevertheless interesting to recognize different types of VCMA effects. After all, research never ends, and any mechanisms may have to be revisited in the future.

2.4.2 Ionic VCMA

Another class of VCMA effects relies on the ionic motions such as ion diffusion and redox reaction. The key structure requires an oxide with high O^{2-} mobility in conjunction with a ferromagnetic film whose magnetism can be altered upon oxidation/reduction. C. Bi et al. have studied Co/GdO_x layers and showed that the magnetic anisotropy of Co could be reversibly manipulated from perpendicular to in-plane by reduction of CoO_x to Co [120]. U. Bauer et al. studied a similar Co/GdO_x but focused on the formation/elimination of the Gd metallic thin film in between Co and GdO_x [121]. Magnetic anisotropy of the Co layer could be altered from perpendicular to in-plane depending on the thickness of the Gd layer. This type of ionic VCMA was shown to be ten to hundred times stronger than that of electronic based VCMA. For example, these studies on Co/GdO_x have coefficients of 11600 fJ/Vm [120] or 5000 fJ/Vm [121], while the electronic based VCMA typically ranges in the order of few tens to few hundreds of fJ/Vm. However, despite having super good coefficients, devices utilizing ionic motions suffer from ultra-low speed and poor cycling endurance. To saturate the VCMA response, it often requires a few minutes [120, 121] or even hours [122]. In addition, a recent study reported a limited endurance (2000 cycles) even after improving the system by using H^+ pumping instead of O^{2-} diffusion [123]. At the current stage, these drawbacks make ionic VCMA effects unsuitable for MRAM technologies, and therefore they will no longer be considered in this thesis.

2.5 Magnetic Energy and Magnetization Dynamics

In this section, we introduce how to calculate the magnetic energy and the magnetization dynamics. These are important basis to understand this thesis work. The simulations tools that we regularly apply to solve these properties and assist understanding of the experimental data are also introduced. There are two conditions for the simulation tools: macro-spin and micro-magnetic.

2.5.1 Magnetic Energy Calculation

As an axiomatic concept of thermodynamics, the magnetization of the ferromagnet tends to relax toward the equilibrium states. At equilibrium, there is net zero force acting on the magnetization, and the system is said to be at the local energy minimum. Modeling the energy of the magnetization not only allows us to extract useful parameters from the experimental data, but

also enables prediction of the magnetization of a system under given conditions. The total magnetic energy is constituted by several contributions, including the relevant anisotropy energies introduced in Section 2.3, the exchange interaction between the magnetic moments, and the Zeeman energy:

$$E_{total} = E_{mc} + E_i + E_d + E_{me} + E_{ex} + E_Z \quad [J] \tag{2.14}$$

By its sequence, these are magnetic crystalline anisotropy energy (E_{mc}), interfacial anisotropy energy (E_i), demagnetization energy (E_d), exchange energy (E_{ex}), and Zeeman energy (E_Z).

2.5.2 Magnetization Dynamics

In a ferromagnet, the magnetization $\vec{M}$ varies in time before relaxation because of the magnetic fields or torques acting on it. Such dynamic motion is described by the so-called Landau–Lifshitz–Gilbert (LLG) equation [124]:

$$\frac{d\vec{M}}{dt} = -|\gamma|\vec{M} \times \vec{B}_{eff} + \frac{\alpha}{M_S}\vec{M} \times \frac{d\vec{M}}{dt} \tag{2.15}$$

The first term on the right side of Equation 2.15 describes the precessional motion around the effective field at equilibrium $\vec{B}_{eff}^{eq}$ with a frequency determined by the gyromagnetic ratio γ, where $\vec{B}_{eff}$ includes the effective magnetic anisotropy field, external magnetic field and thermal fluctuation:

$$\vec{B}_{eff} = \vec{B}_{k,eff} + \vec{B}_{ext} + \vec{B}_{thermal} \tag{2.16}$$

The magnetization trajectory can be solved by integration of the LLG equation. Figure 2.9(a) illustrates the trajectory considering only the precession term at 0K (no thermal fluctuation). In fact, for most of the oscillatory systems in reality, the energy dissipates in time resulting in the damping motion. It describes the attenuation of the oscillatory amplitude, making the systems relax toward the equilibrium state. Such damping motion for the magnetization is described by the second term in Equation 2.15, with α the dimensionless Gilbert damping constant. The complete spin dynamic is shown in Figure 2.9(b). One can further include a thermal fluctuation term in the effective field to imitate the dynamic at finite temperature, as illustrated in Figure 2.9(c).

2.5.3 Macro-Spin Simulation

In macro-spin (MS) assumption, the magnetization within a ferromagnet is considered as spatially uniform. It can therefore be seen as a single domain

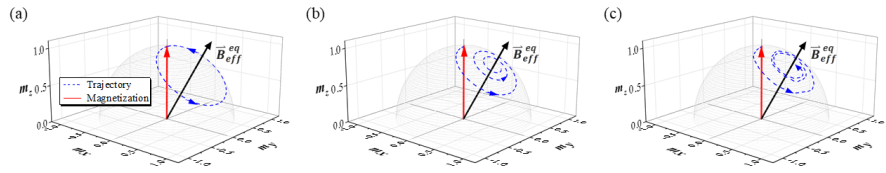

Figure 2.9: *Illustration of the magnetization dynamic including (a) only precession term (0K), (b) precession and damping terms (0K), and (c) precession, damping and thermal terms (300K).*

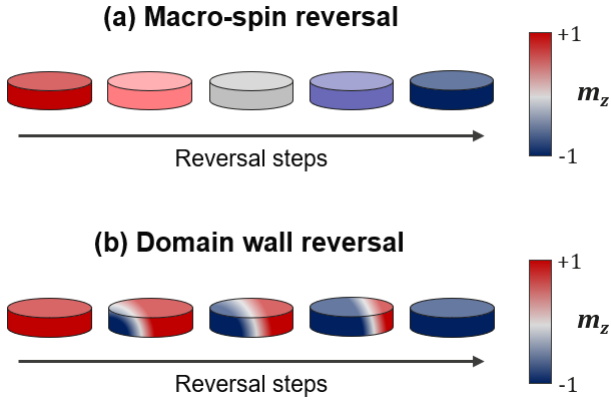

Figure 2.10: *Illustration of the magnetization reversal process under the macro-spin assumption, with m_z being the out-of-plane component of the magnetization.*

ferromagnet with $|\vec{M}| = M_S$. A typical example for the magnetization reversal process in a uniform ferromagnetic thin film is illustrated in Figure 2.10(a). Under this circumstance, solving the problem regarding the magnetization behaviors in both energy and time domains is relatively simple, as demonstrated in the following.

Solving Magnetic Energy

We consider a simple system compatible with the FL in pMTJ stacks, e.g. MgO/CoFeB/Ta, as an example. The indispensable terms to be taken into account are the magnetic anisotropy energy (E_{anis}), demagnetization energy (E_d) and the Zeeman energy (E_Z). Here, we consider the perpendicular anisotropy energy contribution from the interface. The Zeeman energy is

added in the existence of an external magnetic field. The exchange interaction is irrelevant since the FL is seen as a single domain. These energies are associated with the direction of the magnetization. We use the standard spherical coordinate system [Figure 2.11(a)] to express the x, y, z components of the magnetization. The total magnetic energy density (E_{total}/V) is calculated as:

$$E_{total}/V = [E_{anis} + E_d + E_Z]/V \quad [J/m^3] \tag{2.17}$$

$$= \frac{K_i}{t_{FL}} sin^2\theta + K_d cos^2\theta - \vec{M} \cdot \vec{B}_{ext} \tag{2.18}$$

$$= \frac{K_i}{t_{FL}} sin^2\theta + \frac{1}{2}\mu_0 M_S^2 (D_z - D_{x,y}) cos^2\theta - $$

$$- M_S B_x sin\theta cos\varphi - M_S B_y sin\theta sin\varphi - M_S B_z cos\theta \tag{2.19}$$

where $\vec{B}_{ext}$ denotes the external magnetic field and $B_{x,y,z}$ are its components along x, y, and z directions. Figure 2.11(b) shows an example of the total energy as functions of m_z and azimuthal angle φ under the given conditions. The equilibrium direction of the magnetization is reached when the net force is zero, i.e. the first derivative $\partial E_{total}/\partial M$ equals zero, and the energy has a local minimum. This energy minimum (E_{min}) is indicated in the figure in dark blue.

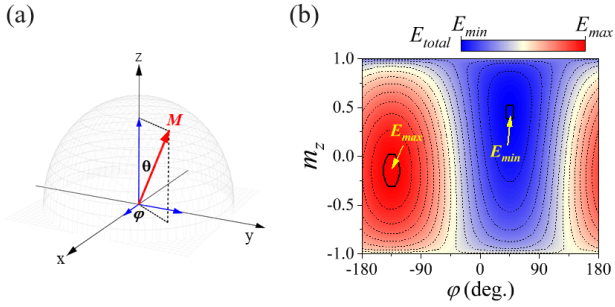

Conditions	Values
Dimension (nm)	[100, 100, 1.7]
M_S (emu/cm^3)	850
K_i (μJ/m^2)	730
[B_x, B_y, B_z] (mT)	[30, 30, 10]

Figure 2.11: *(a) The spherical coordinate system. (b) Illustration of the total magnetic energy as functions of m_z and azimuthal angle φ. The calculation conditions are given in the table.*

Solving Magnetization Dynamics

Under the macro-spin condition, the magnetic dynamic can be solved using programming languages such as Python. In the following, a procedure to

solve the LLG equation is presented. Equation 2.15 is first transformed into a compatible form:

$$\frac{d\vec{m}}{dt} = -\frac{|\gamma|}{(1+\alpha^2)}\vec{m} \times \vec{B}_{eff} - \frac{|\gamma|\alpha}{(1+\alpha^2)}\vec{m} \times (\vec{m} \times \vec{B}_{eff}) \tag{2.20}$$

where $\vec{m}$ ($= \vec{M}/M_S$) is the normalized vector of the magnetization. Here, $\vec{B}_{eff}$ is a vector summation of various field contributions, including the externally applied magnetic field (B_{ext}), the demagnetizing field (B_{demag}), the anisotropy field (B_k), and the thermal fluctuation field (B_{th}).

$$\vec{B}_{eff} = \vec{B}_{ext} + \vec{B}_{demag} + \vec{B}_k + \vec{B}_{th} \tag{2.21}$$

The demagnetizing field is expressed as:

$$\vec{B}_{demag} = -\mu_0 M_S(\vec{D} \cdot \vec{m}) \tag{2.22}$$

where $\vec{D} = (D_x, D_y, D_z)$ is the demagnetizing factor depending on the geometry of the magnetic material, with $D_x + D_y + D_z = 1$. The thermal fluctuation field is a random fluctuating field which can be expressed as [125, 126]:

$$\vec{B}_{th} = (\sigma_x, \sigma_y, \sigma_z)\sqrt{\frac{2\alpha k_B T}{\gamma(1+\alpha^2)\mu_0 M_S V_{FM}(dt)}} \tag{2.23}$$

where $(\sigma_x, \sigma_y, \sigma_z)$ is the 3D isotropic Gaussian distribution, k_B is the Boltzmann constant, T is the ambient temperature in Kelvin, V_{FM} is the volume of the ferromagnet and dt is the time interval for calculating the evolution.

Assuming the unit vectors along x, y and z directions of the Cartesian coordinate system are $\hat{i}$, $\hat{j}$ and $\hat{k}$, the effective field can be concisely expressed as:

$$\vec{B}_{eff} = A_x\hat{i} + A_y\hat{j} + A_z\hat{k} \tag{2.24}$$

with

$$A_x = B_x - \mu_0 M_S D_x m_x + \sigma_x|B_{th}| \tag{2.25}$$

$$A_y = B_y - \mu_0 M_S D_y m_y + \sigma_y|B_{th}| \tag{2.26}$$

$$A_z = B_z - \mu_0 M_S D_z m_z + \frac{2K_i}{\mu_0 M_S t_{FM}} m_z + \sigma_z|B_{th}| \tag{2.27}$$

Because the system has a uni-axial anisotropy, provided by the interfacial perpendicular anisotropy, the anisotropy field is added only to the $\hat{k}$ component.

Now, it is ready to solve Equation 2.20. First, Equation 2.20 can be re-written as:

$$\begin{aligned} d\vec{m} &= \frac{-|\gamma||\vec{B}_{eff}|dt}{(1+\alpha^2)}\vec{m}\times\vec{b}_{eff} + \frac{-|\gamma|\alpha|\vec{B}_{eff}|dt}{(1+\alpha^2)}\vec{m}\times(\vec{m}\times\vec{b}_{eff}) \\ &= \frac{-|\gamma||\vec{B}_{eff}|dt}{(1+\alpha^2)}\vec{m}\times\vec{b}_{eff} + \frac{-|\gamma|\alpha|\vec{B}_{eff}||\vec{N}_{eff}|dt}{(1+\alpha^2)}\vec{m}\times\vec{n}_{eff} \end{aligned} \tag{2.28}$$

where $\vec{b}_{eff}$ is the unit vector of $\vec{B}_{eff}$. $|\vec{N}_{eff}|$ and $\vec{n}_{eff}$ are the amplitude and the unit vector of the resultant vector cross product $\vec{m}\times\vec{b}_{eff}$, respectively.

$$\vec{b}_{eff} = (b_x, b_y, b_z) = \frac{1}{|\vec{B}_{eff}|}(B_x, B_y, B_z) \tag{2.29}$$

$$\vec{m}\times\vec{b}_{eff} = \vec{N}_{eff} = |\vec{N}_{eff}|\vec{d}_{eff} = |\vec{N}_{eff}|(n_x, n_y, n_z) \tag{2.30}$$

Here, Equation 2.28 indicates that the angle of precession (θ_p) within dt is $\frac{-2\pi|\gamma||\vec{B}_{eff}|dt}{(1+\alpha^2)}$ (rad), for which the axis of rotation is along $\vec{b}_{eff}$. Likewise, the angle of damping (θ_d) within dt is $\frac{-2\pi|\gamma|\alpha|\vec{B}_{eff}||\vec{N}_{eff}|dt}{(1+\alpha^2)}$ (rad), for which the rotation axis is $\vec{n}_{eff}$.

Now it becomes a vector rotation problem, which can be solved by applying the vector rotation matrix. An example of the rotation matrix for the precession term is given by:

$$R(\theta_p, \vec{b}_{eff}) = \begin{bmatrix} c_p + b_x^2(1-c_p) & b_xb_y(1-c_p) - b_zs_p & b_xb_z(1-c_p) + b_ys_p \\ b_yb_z(1-c_p) + b_zs_p & c_p + b_y^2(1-c_p) & b_yb_z(1-c_p)b_xs_p \\ b_zb_x(1-c_p) - b_ys_p & b_zb_y(1-c_p) + b_zs_p & c_p + b_z^2(1-c_p) \end{bmatrix} \tag{2.31}$$

where $c_p = cos\theta_p$ and $s_p = sin\theta_p$.

Finally, one can calculate the magnetization evolution with consecutive rotation matrices. For a magnetization with an initial direction $\vec{m}(t)$, it's final direction at $\vec{m}(t+dt)$ can be derived as:

$$\vec{m}(t+dt) = R(\theta_d, \vec{n}_{eff})R(\theta_p, \vec{b}_{eff})\vec{m}(t) \tag{2.32}$$

To ensure the accuracy of the calculation, the time interval should be kept much shorter than the time scales of the magnetization dynamic (usually in the range of GHz), e.g. $dt \leq 10^{-12}s$.

2.5.4 Micro-Magnetic Simulation

In reality, a uniform magnetization appears only in small media. Instead, the exchange interaction between individual magnetic moments must be considered to imitate the real situations. Magnetization switching processes in large media are rather mediated by domain wall motions, as illustrated in Figure 2.10(b). This leads to the area of micro-magnetic simulation. Gratefully, the National Institute of Standards and Technology (NIST) develops and provides an open-source project "Object-Oriented Micro-Magnetic Framework (OOMMF)" [127], allowing users to perform micro-magnetic simulation at will. OOMMF supports MinDriver and TimeDriver to compute energy minimization and magnetization dynamics, respectively. In addition, users can define the layers, shapes, energies, magnetic fields, and even temperature through specifying the relevant built-in modules.

2.6 Precessional Switching of Magnetization

Switching of the magnetization at high speed and low power is a fascinating task for the MRAM community. Before the discovery of VCMA, intensive works have been carried out to seek the lowest switching field for magnetic field switch MRAM. Among several ideas, such as antiparallel field, canted field, and hard-axis field, the concept of 'precessional switching', which directly makes use of the intrinsic magnetic precession phenomenon, induced by hard-axis field pulse demonstrated sub-nanosecond switching speeds [128, 129, 130, 131]. We will see later in Chapter 3 that the conventional type VCMA write mechanism much resembles this precessional switching concept but in a different operation technique. Therefore, it is worth reviewing the pulsed field-induced precessional switching first before going to the experimental chapters. Depending on the field magnitude, there can be three operation regimes: high field, moderate field, and low field. In the following, we review the simulation/experimental works regarding the switching behavior in these regimes. To discuss the precession behavior, the simplest scenario is considered [132]: a large extended thin film magnet with $D_x = D_y = 0$ and $D_z = 1$, the magneto-crystalline anisotropy H_k is in x-direction, and the system is loss-free ($\alpha = 0$). The pulsed magnetic field (H_y) is applied in the in-plane hard-axis, i.e. y-direction.

High Field Regime

The high field regime is defined by $H_y \geq H_k$. In this regime, the magnetization has an equilibrium direction along y during the pulse application. Application of

a fast rising H_y will initiate a large angle precession around this axis, which can be used to reverse the magnetization [133]. Figure 2.12 shows the projection of switching trajectories on the x-z plane for different anisotropy field amplitudes. h_y and h_k indicate the reduced quantity, e.g. $h_y = H_y/M_S$. At $h_y = h_k = 0.01$, the high field regime, the switching trajectory has a stadium shape. Maximum m_z is reached when $m_x = 0$. The switching speed can then be defined by cutting the field at half precession period, i.e. after 180° rotation. Further extending the pulsed-field duration leads to a non-switch.

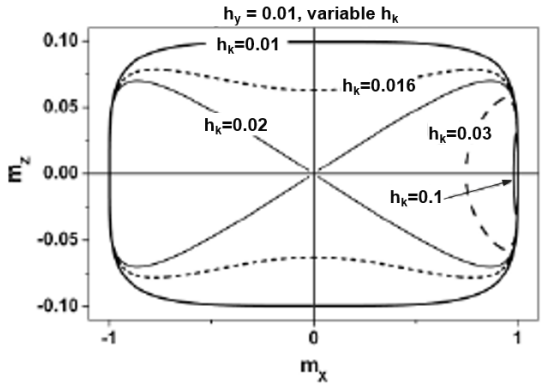

Figure 2.12: *Magnetization trajectory of a uniaxial nonlossy macrospin. Reproduced from Ref. [132].*

Experimentally, this switching trajectory has been proven using a metallic spin valve shown in Figure 2.13(a) [134, 135]. The FL has an in-plane H_k of 7mT. Figure 2.13(b) [135] demonstrates the change in giant magnetoresistance (GMR) as a function of field pulse duration. The switching is observed when pulse duration $t_{pulse} \approx (n + \frac{1}{2}t_{prec})$, where n is a integer defining the order of switching process and t_{prec} is the time for one precession period. This is shown at 140ps, 350ps, 590ps, and 800ps. In the contrary, pulses with $t_{pulse} \approx nt_{prec}$ result in non-reversal. Characterization of the switching probability over a range of H_y and t_{pulse} is shown in Figure 2.14 for both experiment and simulation [135]. The white colored area indicates switching with probability > 0.8, and black colored area indicates non-switch with switching probability < 0.1. It is clearly seen that for $H_y > 70$ Oe (7mT), switching is periodic.

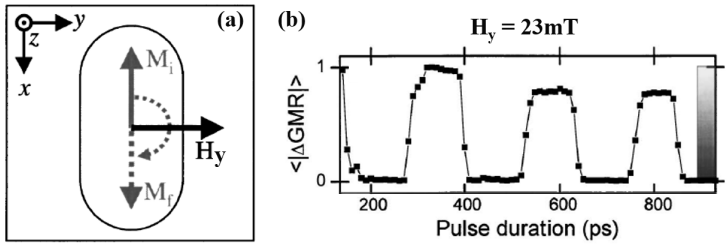

Figure 2.13: *Schematic of the configuration for pulsed field induced precessional switching. M_i and M_f denote the initial and final magnetization, respectively. Reproduced from Ref. [134].*

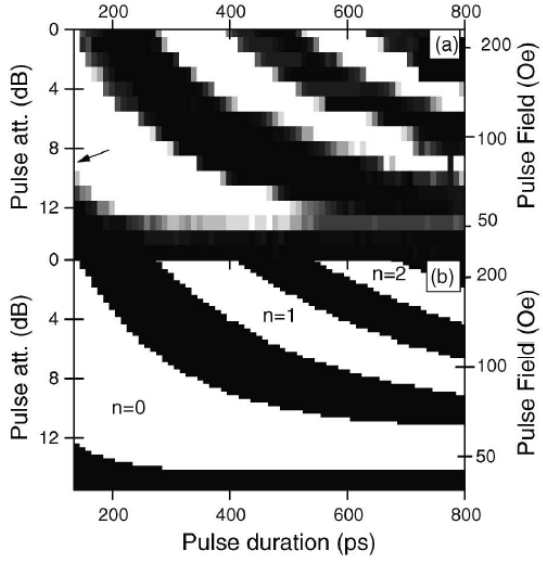

Figure 2.14: *Pulse field dependence of the precessional switching. (a) Experimental results. (b) Macro-spin simulation with H_k = 70 Oe = 7mT and α = 0.03. White: Switching with probability > 0.8. Black: Non-switch with switching probability < 0.1. n indicates the order of switching process. Reprinted from Ref. [135].*

Moderate Field Regime

The field condition for the moderate field regime is $h_k > h_y > h_k/2$. In this regime, the applied field competes with the anisotropy field. The energy

landscape has a saddle point at $m_y = 1$ and two energy minimum, one at $m_x > 0$ and another one at $m_x < 0$. The initial energy is above the energy at the saddle point, and the switching trajectory is deformed. This is shown in Figure 2.12 for the cases $h_k = 0.02$ and 0.016. During precession, m_z reaches the maximum before m_x going to 0, leading to a bone-shape trajectory. It can be seen as if the magnetization rotates alternatively around the two attractors. With finite damping, e.g. $\alpha = 0.03$, the magnetization may precess only half of a period and fall into the energy minima before oscillating back across the in-plane hard axis. This leads to switching independent of t_{pulse}, as shown in Figure 2.14(b) [135] for 70 Oe $> H_y >$ 35 Oe. Experimentally, one can roughly observe the similar behavior but much less reliable. This can be attributed to the thermal agitation that leads to a stochastic switching. Besides, a real system more likely has a micromagnetic structure instead of a macro-spin behavior, and the inhomogeneity of the parameters within a device can be sufficient to inhibit the reversal process.

Low Field Regime

When the applied field is further reduce to below $h_k/2$, the precession amplitude is too weak and reversal in inhibit. As shown in Figure 2.12 at $h_k = 0.03$ and 0.1. The magnetization can never cross the hard-axis. This is also shown in Figure 2.14 for $H_y <$ 35 Oe (3.5mT).

2.6.1 Precessional Switching with VCMA effect

Above we have introduced the precessional switching induced by magnetic field pulses. It is shown that the operation regimes are defined by the relative amplitude of the applied field and the anisotropy field, where the control parameter is the applied field amplitude. With VCMA effect, it is possible to tune the anisotropy field under a fixed magnetic field to implement the different operation regimes. Because the typical switching time for the precessional reversal is typically in the range of sub-nanosecond, it requires correspondingly a fast response of VCMA to fulfill such a switching mechanism. Among different VCMA effects, only the pure electronic VCMA has high speed response at the typical operating temperature range. Coincidentally, the use of MTJ makes it possible, due to the fact that the voltage drops mainly at the MgO layer, and the electric field across the MgO layer can induce the pure electronic VCMA effect which allows us to directly control the anisotropy of the FL. This is what we will study next and we will leave the VCMA write mechanisms for the next chapters.

2.7 Summary

In this chapter, the basis for understanding the relevant magnetic phenomena in this thesis work was reviewed. The magnetic moment in an atom is induced by the electron orbital and spin angular momentum. Together with exchange interaction and spin-orbit coupling, various magnetic anisotropy contributions are comprised in ferromagnetic materials. An externally applied voltage (electric field) can control specific anisotropy through corresponding mechanisms such as electron doping/redistribution, piezoelectric distortion, and ionic motions. From the aspects of speed and reliability, the pure electronic VCMA best suits the MRAM requirements. We also introduce the concept of precessional switching, the knowledge gained from the preceding works will help understand the experimental results shown in VCMA switching. In the following chapters, we will further discuss how pure electronic VCMA effect to improve MRAM writing performance.

Chapter 3

VCMA Write Mechanism: Conventional Scheme

3.1 Introduction

In view of performance and process compatibility, magnetic random access memory (MRAM) has great potential to be introduced as cache/main memories in the advanced technology nodes as it is compatible to complementary metal-oxide-semiconductor (CMOS) process and it shows good scalability [136, 137, 138]. The non-volatile feature enables reduction of the static power in comparison with dynamic RAMs. In the past decades, the spin-transfer-torque (STT) effect, as current-driven write mechanism, has been extensively studied. The STT perpendicularly magnetized magnetic tunnel junction (pMTJ) devices have achieved reliable writing time down to few ns [139, 140]. However, the required switching current is dramatically increased for GHz operation, causing degradation and reliability issues in the MgO tunnel barrier [141].

The pure electronic voltage control of magnetic anisotropy (VCMA) effect allows instant modification of interfacial anisotropy by selective charge doping and electron redistribution at the MgO/free-layer interface upon voltage application[86, 107], as introduced in Chapter 2. Such effect enables a voltage-driven magnetization switching mechanism [58, 59, 142]. Not only the tunnel current is not required, but also the energy consumption can be much suppressed [73]. In this chapter, we will first discuss the mechanism of conventional type VCMA-induced switching. Then, we use imec's standard VCMA devices to study the switching properties. Finally, the merits and challenges for conventional

VCMA switching are pointed out, and the solutions to these challenges will be proposed and discussed in Chapter 4.

Results shown in this chapter were partially published in **Y. C. Wu et al., 64th MMM Conference, EG-11 (2019)** [143] and **Y. C. Wu et al., AIP Adv. 10, 035123 (2020)** [144].

3.2 Conventional VCMA Write Mechanism

The 'Conventional VCMA write' refers to the VCMA-induced switching mechanism proposed by T. Maruyama et al. [58]. The term 'Conventional' is specified to distinguish with our new concept 'Deterministic VCMA write' which will be discussed in Chapter 4. This section introduces the conventional VCMA write mechanism for switching the free-layer (FL) in the perpendicular magnetic tunnel junction (pMTJ) devices.

To explain the mechanism, we have to first recall the LLG equations (Equation 2.15 and 2.16), but with a modified form:

$$\frac{d\vec{M}}{dt} = -|\gamma|\vec{M} \times \vec{B}_{eff}(EF) + \frac{\alpha}{M_S}\vec{M} \times \frac{d\vec{M}}{dt} \tag{3.1}$$

where $\vec{B}_{eff}(EF)$ replaces the ordinary $\vec{B}_{eff}$ to illustrate the voltage controllability. Here, the electric pulses are preferably expressed in the form of electric-field across the MgO barrier ($EF = V/t_{MgO}$), since the VCMA effect is independent of the MgO thickness (t_{MgO}) if the MgO/FL interface properties remain the same. This can be seen in most of the reports where VCMA is termed as 'Electric-field-controlled magnetic anisotropy' [145, 146, 147, 148].

Similar as Equation 2.21, $\vec{B}_{eff}(EF)$ can be expressed as:

$$\begin{aligned}\vec{B}_{eff}(EF) &= \vec{B}_{k,eff}(EF) + \vec{B}_{ext} + \vec{B}_{thermal} \\ &= \left[\vec{B}_{k,eff}(0) + \frac{\partial \vec{B}_{k,eff}}{\partial EF} * EF\right] + \vec{B}_{ext} + \vec{B}_{thermal}\end{aligned} \tag{3.2}$$

As the EF controls the magnitude of the PMA, $\vec{B}_{k,eff}(EF)$ is evaluated as the sum of the anisotropy field at zero bias $\vec{B}_{k,eff}(0)$ and the linear dependent term $\frac{\partial \vec{B}_{k,eff}}{\partial EF} * EF$. We refer to the parameter $\frac{\partial \vec{B}_{k,eff}}{\partial EF}$ as 'VCMA slope' in this thesis.

The conventional writing scheme has a fundamental requirement: P and AP states are approximately symmetric, i.e. $B^{P}_{k,eff}(0) = B^{AP}_{k,eff}(0)$. To achieve

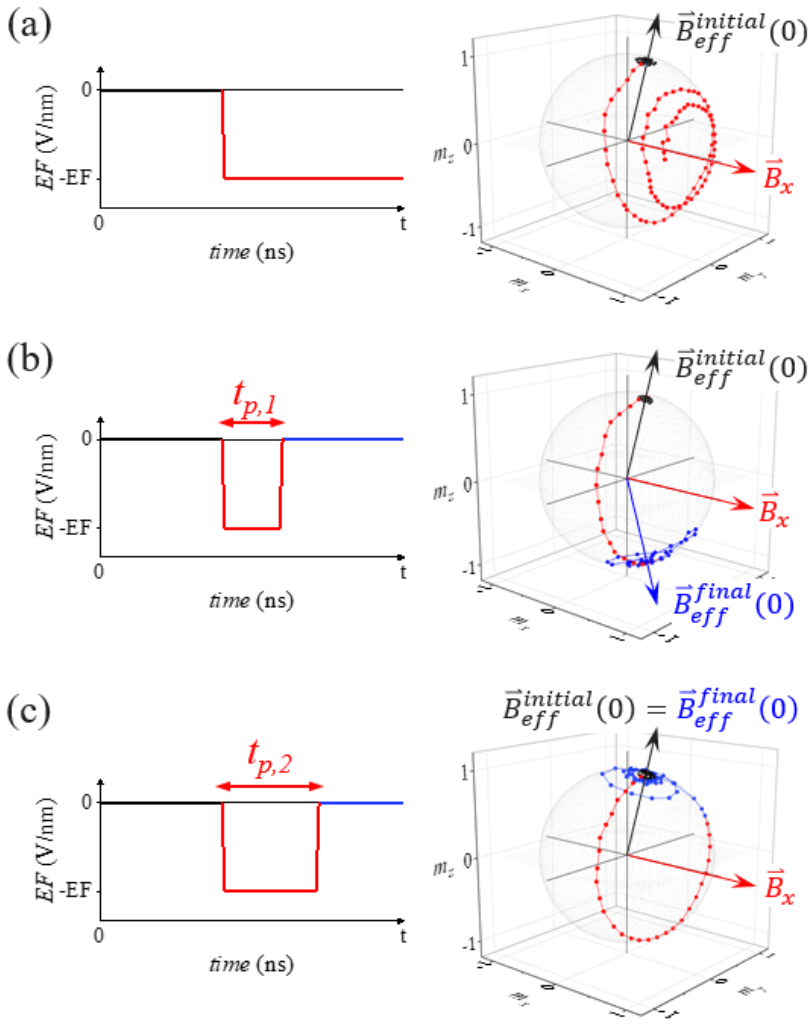

Figure 3.1: *Illustration of the VCMA-induced magnetization precession. (a) Continuous precession for long t_p. (b) $t_{p,1}$ approximately corresponds to a half precession period, resulting in a successful switch. (c) $t_{p,2}$ approximately corresponds to a full precession period. The magnetization rotates back to the initial state causing a failed switch. $\vec{B}_{eff}^{initial}(0)$ and $\vec{B}_{eff}^{final}(0)$ indicate the effective field directions at equilibrium for the initial state and final state, respectively.*

such a condition, the stray field (B_{stray}) from the reference-layer (RL) and the synthetic anti-ferromagnet (SAF) must be compensated by the external out-of-plane magnetic field (B_z) such that the FL experiences effectively zero z-field, i.e. $B_{z,eff} \equiv |B_z - B_{stray}| = 0$. As a consequence, $\vec{B}_{ext}$ can be reduced to $\vec{B}_{x,y}$. For simplicity, we assign the in-plane magnetic field as B_x since any in-plane directions are equivalent for the disk-shaped FL:

$$\vec{B}_{eff}(EF) = \left[\vec{B}_{k,eff}(0) + \frac{\partial \vec{B}_{k,eff}}{\partial EF} * EF\right] + \vec{B}_x + \vec{B}_{thermal} \tag{3.3}$$

We have now introduced the essential variables. Next, the voltage-induced magnetization switching is demonstrated by macro-spin simulation in the time domain. At the initial stage without EF, the magnetization points in the leading z-direction. A hard-axis field B_x is applied to define the axis of precession when $B_{k,eff}$ is removed. While the EF is applied, the magnetization continuously precesses roughly about $\vec{B}_x$, as shown in Figure 3.1(a). One can see that the z-component of the magnetization (m_z) oscillates in time. Therefore, a successful magnetization reversal is achieved by controlling the pulse duration (t_p). When t_p is approximately equal to half-integer of the precession period (t_{prec}), i.e. $t_p = \left(n + \frac{1}{2}\right) t_{prec}$, the sign of the m_z is opposite to the initial state, resulting in a 'switch' [Figure 3.1(b)]. Here, n = 0, 1, 2... denotes the order of the switching events. On the other hand, if t_p is extended to integer of the period, i.e. $t_p = nt_{prec}$, the magnetization rotates back to the same direction as the initial state, leading to a 'non-switch' [Figure 3.1(c)].

This type of precessional switching due to the instant change in the effective magnetic field has been widely discussed by fast-rising magnetic field pulses along the hard-axis [135, 134, 149]. Depending on the magnitude of hard-axis field (B_{hard}) and the anisotropy field (B_k), the switching trajectory can be categorized into three regimes. In Ref. [132], these regimes are classified by $B_{hard} > B_k$ (high field), $B_k > B_{hard} > 0.5B_k$ (moderate field), and $B_{hard} < 0.5B_k$ (low field). VCMA induced precessional reversal resembles field pulsed switching in several perspectives, yet in a different manner.The difference between VCMA switching and pulse magnetic field switching is the field parameter which each mechanism is controlling. We can intuitively recognize that VCMA switching controls B_k to enter the three regimes, where as the field pulse case controls B_{hard}. We will come back with more discussion in Section 3.4.4.

To this point, the basis of conventional VCMA switch mechanism is presented. In the following sections, we study the switching characteristics more in detail using our standard VCMA pMTJ devices.

3.3 MTJ Properties

3.3.1 MTJ Device Preparation

The MTJs used in this study are bottom-pinned perpendicularly magnetized stacks sputter deposited on 300 mm thermally oxidized Si(100) wafers using a Canon-Anelva EC7800 cluster tool. The material stack is shown in Figure 3.2. From the bottom, a $[Co/Pt]_x$ multilayer serves as the lower hard-layer (HL), and the $[Co/Pt]_x$/Co/Ir/Co forms the reduced SAF structure. The RL is ferromagnetically coupled to the SAF structure through an RL spacer. Next, two samples are prepared with different MgO thicknesses (t_{MgO}): 1.1nm and 1.5nm. These two thicknesses target the resistance-area (RA) products at 100 $\Omega{\cdot}\mu m^2$ and 1000 $\Omega{\cdot}\mu m^2$, respectively. We will discuss the impacts of MgO thickness in the following context not only on the write properties but also on the measurement techniques. Then, a 1.7nm CoFeB is deposited as the free-layer (FL). Such thickness is chosen to meet the required perpendicular magnetic anisotropy (PMA) for switching studies. Before capping layers Ta/Ru being deposited, a thin Mg sacrificial layer covers the FL to protect it from sputtering damage during heavy element (Ta) deposition [150]. After all depositions, the films are annealed at 400°C for 30 minutes in vacuum in a 2T out-of-plane magnetic field. Finally, the stack is patterned into circular pillars using 193nm immersion lithography and ion beam etch (IBE), and integrated into devices with top and bottom electrodes.

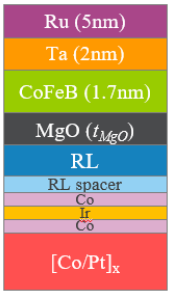

Figure 3.2: *The MTJ stack for voltage-controlled switching experiments in this chapter.*

3.3.2 Saturation Magnetization

The magnetic moments (m) of the magnetic layers are measured by a vibrating sample magnetometer (VSM) using 8*8mm^2 samples before patterning into devices. The out-of-plane magnetic field is swept between $\pm$2T, and the magnetic moments are recorded every 50mT. Figure 3.3(a) plots the area magnetization ($M^{area} = m/area$) as a function of B_z. Steep changes in the curves indicate the reversals of the magnetic layers, and labels 1-8 represent the measuring sequence and the distinct magnetization configurations at different magnetic field ranges [see Figure 3.3(b)]. At Stage 1, all magnetic layers are saturated in the $+z$ direction, which gives the total magnetic moment. From Stage 1 to 2, the RL is reversed as it is anti-ferromagnetically coupled to the HL. The coupling strength is around 700mT, similar to the values reported on an Ir spacer [151]. As the FL has the weakest PMA among the three magnetic layers, it is reversed by the smallest field (Stage 2 to 3). From Stage 3 to 4, the RL and HL reverse simultaneously as a collective behavior of the anti-ferromagnetically coupled layers. Next, from Stage 4 to 5, the magnetic field exceeds the coupling field to reverse the RL and saturates the stack in the $-z$ direction. Finally, Stages 5-8 and back to Stage 1 follow the similar procedure as discussed for Stages 1-5.

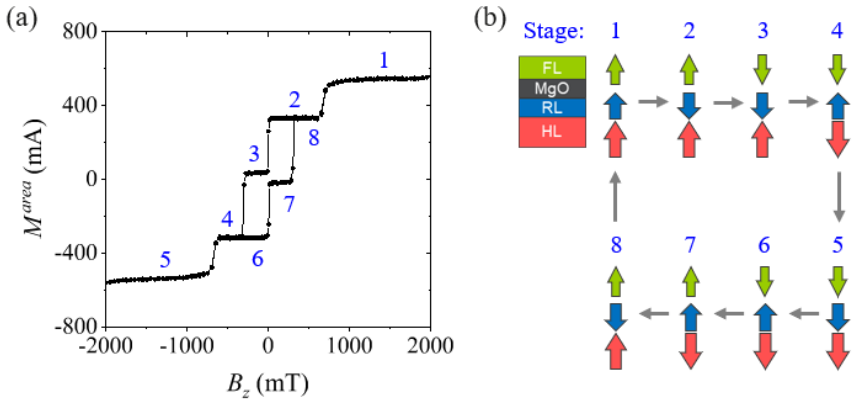

Figure 3.3: *(a) Major loop for the area magnetization as a function of out-of-plane magnetic field for the pMTJ stack. Labels 1-8 indicate the measuring sequence and different magnetic field stages. (b) Schematics of the magnetization configurations at different magnetic field stages.*

From different stages, the area magnetization of the FL, RL, and HL can be calculated:

$$M_1^{area} = M_{HL}^{area} + M_{RL}^{area} + M_{FL}^{area} \tag{3.4}$$

$$M_2^{area} = M_{HL}^{area} - M_{RL}^{area} + M_{FL}^{area} \tag{3.5}$$

$$M_3^{area} = M_{HL}^{area} - M_{RL}^{area} - M_{FL}^{area} \tag{3.6}$$

We obtain $M_{FL}^{area} = 145$mA, $M_{RL}^{area} = 105$mA, and $M_{HL}^{area} = 295$mA.

Magnetic Dead Layer (MDL)

To evaluate the saturation magnetization, one needs to take into account that not the entire volume of the magnetic layer contributes to the total magnetic moment. At the oxide/ferromagnet and/or ferromagnet/metal interfaces, thin layers which contain magnetic elements may not exhibit magnetic properties, so-called the magnetic dead layer (MDL). Generally, MDLs may originate due to local amorphisation/oxidation [152, 153, 154] and inter-diffusion [155, 156]. In the typical MgO/CoFeB/Ta films, it has been reported that MDL mainly forms at the CoFeB/Ta interface because the Ta layer acts as a boron sink and the interface remains amorphous after annealing processes [157, 158].

To estimate the thickness of the MDL (t_{MDL}), samples with different FL thicknesses are prepared with the exact same process conditions. We measure the VSM minor loops to obtain the magnetic moments of the FL, as shown in Figure 3.4(a). Figure 3.4(b) summarizes the area magnetization as a function of FL thickness. By linear extrapolation to zero magnetization, a 0.7nm MDL is estimated. Then, the saturation magnetization of the FL ($M_{S,FL}$) can be calculated as $M_{S,FL} = M_{FL}^{area}/t_{eff} = 1450$ kA/m, with $t_{eff} = t_{FL} - t_{MDL}$. Such a dead layer thickness is comparable to the value obtained from the similar stack [25].

3.3.3 Device Electrical Dimension

Due to the etching damages, the periphery of the patterned devices is magnetically dead and the resistance can be assumed as infinity [159]. Hence, the effective device size, so-called electrical critical dimension (eCD), is smaller than the physical dimension. The resistance-area (RA) product is a parameter to characterize the eCD of a device, where the resistance is the parallel resistance (R_P) of the patterned devices. Typically, RA is estimated by large devices since the damage zone is minor compared to the working zone, and the physical

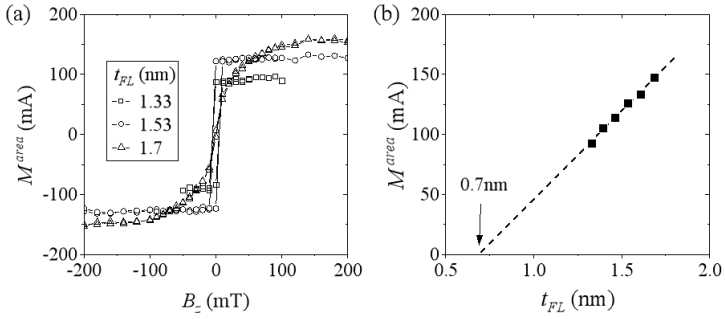

Figure 3.4: *(a) VSM measurements of the area magnetization for different FL thicknesses. (b) Area magnetization as a function of FL thickness. Dashed line shows linear fitting of the data, and the intercept on the x-axis indicates the thickness of the magnetic dead layer (0.7nm).*

dimension represents the eCD. Figure 3.5 shows a transmission electron microscopy (TEM) image of our largest device. A diameter of 129nm is taken to quantify the RAs of $t_{MgO} = 1.1$nm and $t_{MgO} = 1.5$nm as $80\Omega{\cdot}\mu m^2$ and $880\Omega{\cdot}\mu m^2$, respectively. Then, the eCDs of other devices with smaller sizes are derived by $eCD = [\frac{4}{\pi}(RA/R_P)]^{0.5}$. In the rest of this dissertation, the device size refers to eCD unless specified.

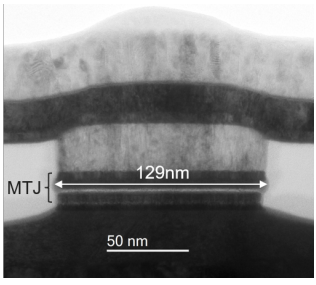

Figure 3.5: *TEM image of a device with a 129nm physical size.*

3.3.4 Tunneling Magneto-Resistance and Coercive Field

The tunneling magneto-resistance ratio (TMR) and coercive field (B_C) of 105nm devices are investigated as a function of out-of-plane magnetic field. Figure 3.6 shows the representative TMR loops for both MgO thicknesses. We observe

TMR is significantly increased by a thicker MgO, with TMR = 200% for t_{MgO} = 1.1nm and TMR = 250% for t_{MgO} = 1.5nm. Such enhancement in TMR is similar to the previous report [160], which can be attributed to the increasing spin-filtering effect for thicker MgO [50, 51, 52]. As discussed in Section 1.2.2, for BCC textured CoFeB/MgO/CoFeB systems, the electrons with different band symmetries have different tunneling probabilities and decay rates. Specifically, electrons with Δ_1 symmetry, which is responsible for high TMR, has the slowest decay rate compared to other symmetries, resulting in very high spin-selectivity and TMR for thicker MgO barriers [51].

On the other hand, B_C for both devices is consistent, indicating the magnetic anisotropy is not impacted by the MgO thickness in the studied range. A similar observation has been reported for MgO thickness ranging from 0.6nm to 1.6nm [161], which suggests that both the crystallinity and magnetic anisotropy of the CoFeB FL can be stabilized with a minimum of 0.6nm MgO. Further increase in MgO thickness does not improve the crystallinity and interface properties.

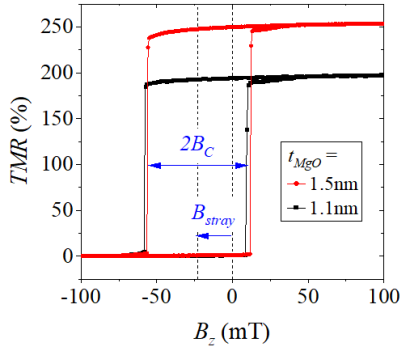

Figure 3.6: *TMR loops as a function of out-of-plane magnetic field for 105nm devices with different MgO thicknesses.*

In addition, we observe a consistent hysteresis loop shift of 23mT in both stacks, which originates from the uncompensated magnetic moments in the RL and HL. In the previous section, we quantified $M_{S,HL} > M_{S,RL}$. The uncompensated magnetization leads to a net B_{stray} in $+z$ direction promoting the anti-parallel (AP) state. Therefore, it requires a stronger B_z to switch the FL from AP to P state.

3.3.5 Perpendicular Magnetic Anisotropy and Thermal Stability Factor

The perpendicular magnetic anisotropy field ($B_{k,eff}$) and the thermal stability factor (Δ) are estimated using the 'sweep-rate dependent switching field distribution' method, a method derived by X. Feng et al. [162]. The MTJ device is placed in a sweeping magnetic field, and a small bias (~20mV) is applied to the device in order to record the resistance and to collect the switching fields. Then, the cumulative switching probability curves for the FL are fitted with the following equation [140, 162]:

$$P_{sw}(B_z) = 1 - exp\{\frac{-B_{k,eff} f_0 \sqrt{\pi}}{2R\sqrt{\Delta}} erfc\left[\sqrt{\Delta}\left(1 - \frac{B_z - B_{stray}}{B_{k,eff}}\right)\right]\} \quad (3.7)$$

where f_0 is the attempt frequency (1GHz) and R is the sweep rate of the magnetic field. Figure 3.7(a) and (b), respectively, show the representative measurements for the repetitive TMR loops of a 105nm device and the switching probability curves collected from 500 events. We obtain $B_{k,eff} = 72mT$ and $\Delta = 51$ through the fitting.

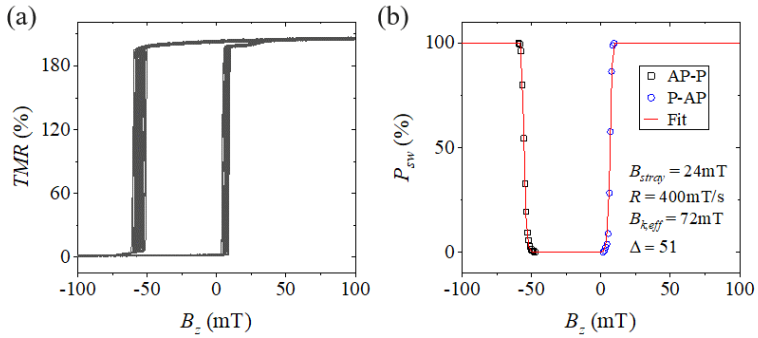

Figure 3.7: *(a) Repetitive TMR measurements as a function of B_z for a 105nm device. (b) Switching probability curves as a function of B_z measured by a sweep rate of 400mT/s.*

Here, $B_{k,eff}$ is well quantified. However, estimation of Δ suffers from the constrain of the fitting model. Feng's method is based on the macro-spin assumption, the Δ obtained from the fitting takes the magnetic domain nucleation area instead of the whole device area. The domain nucleation

width (d_w) is characterized as [161, 163, 164]:

$$d_w = \pi\sqrt{\frac{A_{ex}}{K_{eff}}} \quad [m] \tag{3.8}$$

where A_{ex} is the exchange stiffness. Typical A_{ex} of Co, Fe, and CoFeB materials fall in the range of 10-30 pJ/m [164, 165, 166, 167]. As a result, calculation of the energy barrier and Δ [Equation 1.5 and 1.6] now becomes:

$$\Delta = \frac{E_b}{k_B T} = \frac{K_{eff}\pi(d_w/2)^2 t_{FL}}{k_B T} = \frac{\pi^3 A_{ex} t_{FL}}{4k_B T} \tag{3.9}$$

By considering $\Delta = 51$ and $t_{eff} = 1$nm, A_{ex} is evaluated as 25pJ/m. Previous studies have also reported 23pJ/m from a 2nm CoFeB film [166] and 31pJ/m from a 1.3nm CoFeB film [163].

In addition, using $M_{S,FL} = 1450$ kA/m from the VSM measurements and $B_{k,eff} = 72$mT from the fitting results, we obtain $d_w \sim 72$nm. This d_w value indicates that for devices with their sizes exceeding 72nm, the estimated Δ is constant. As shown in Figure 3.8(a), the experimental Δs are around 50-55 for $eCD > 72$nm, and it decreases at smaller sizes following the calculation from the macro-spin model. Similar results have been reported previously [44, 164, 167]. On the other hand, $B_{k,eff}$ increases for smaller devices, which stems from the reduction in the demagnetization factors of the shape anisotropy [Equation 2.11]. The $[D_z - D_{x,y}]$ term decreases with device size; therefore, for a constant interfacial anisotropy (K_i) the effective perpendicular anisotropy is stronger in scaled devices.

3.3.6 VCMA Coefficient Estimation

The pure electronic VCMA effect modulates the interfacial anisotropy (K_i) by voltage application. By definition and its mechanism, the VCMA coefficient is evaluated as:

$$\xi = \frac{\partial K_i}{\partial EF} \quad [fJ/Vm] \tag{3.10}$$

where EF is the electric-field across the MgO barrier. Combining Equation 3.10 with 2.12 leads to an equivalent expression:

$$\xi = \frac{\partial K_i}{\partial EF} = \frac{\partial K_{eff}}{\partial EF} = \frac{M_{S,FL} t_{FL} t_{MgO}}{2} \frac{\partial B_{k,eff}}{\partial V} \quad [fJ/Vm] \tag{3.11}$$

where V is the applied voltage.

Next, we use the similar method as for the estimation of $B_{k,eff}$ to quantify the VCMA coefficient. The device under test (DUT) is again placed in a sweeping

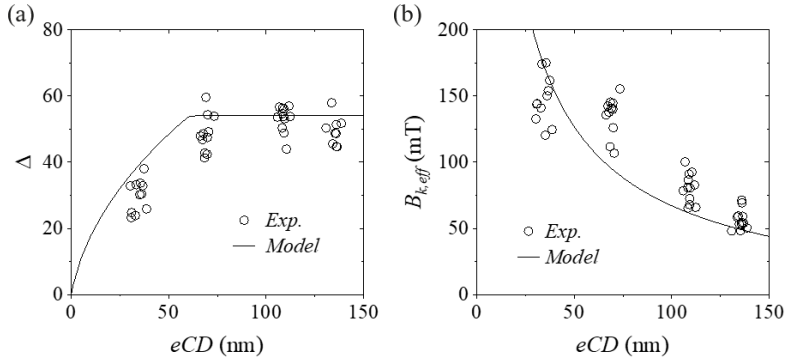

Figure 3.8: *Dependence of device size on (a) Δ and (b) $B_{k,eff}$ for both experiments and model.*

magnetic field. In addition to the small direct-current (DC) bias, the switching probability curves are measured under various bias conditions. A representative measurement is shown in Figure 3.9(a). These curves are subsequently fitted by Equation 3.7. Instead of fitting these curves separately, we adapt the common parameters to all curves simultaneously. The procedure is described in Figure 3.9(b). In the first step, three universal parameters are established: $B^0_{k,eff}$, Δ, and $\partial B_{k,eff}/\partial V$. For each DC current condition (I_n), the corresponding voltages applied on the MTJ device are $V_n^P = I_n R_P$ and $V_n^{AP} = I_n R_{AP}$ (The prober system design company restricts the measurements to a constant current mode. The applied voltages on the AP and P states are therefore different. Otherwise, this step can be simplified to a constant voltage regardless of the MTJ states.). Next, the $B_{k,eff}$ during magnetic field sweep is calculated as:

$$B^P_{k,eff} = B^0_{k,eff} + \frac{\partial B_{k,eff}}{\partial V} \times V_n^P \tag{3.12}$$

$$B^{AP}_{k,eff} = B^0_{k,eff} + \frac{\partial B_{k,eff}}{\partial V} \times V_n^{AP} \tag{3.13}$$

The $B^P_{k,eff}$, $B^{AP}_{k,eff}$, and a common Δ are then applied to all the probability curves simultaneously. Fitting adopts the least square error by modulating those three universal parameters. Finally, it results in a VCMA slope of 39mT/V for devices with $t_{MgO} = 1.5$nm, corresponding to a VCMA coefficient of 42.5fJ/Vm.

Our method is based on two assumptions. First, we assume Δ is independent of bias conditions. This is valid when d_w stays smaller than eCD under any applied

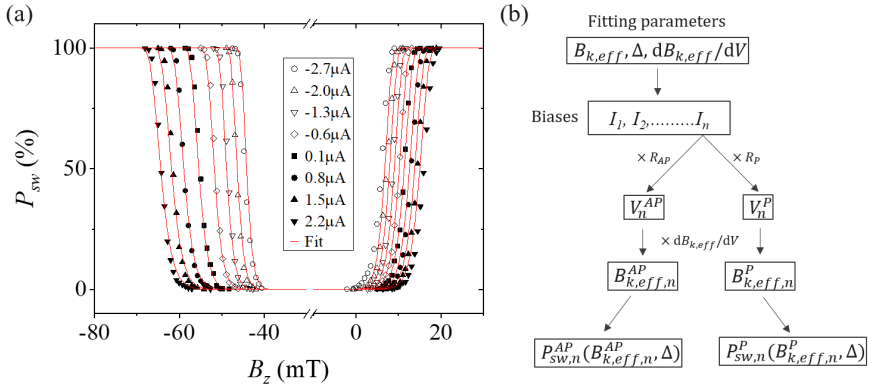

Figure 3.9: *(a) Magnetic field switching probability curves under different bias conditions. (b) Fitting procedure to obtain* $B_{k,eff}$, Δ, *and* $dB_{k,eff}/dV$

voltages. Secondly, the VCMA effect is assumed to be linear, meaning the VCMA slope $dB_{k,eff}/dV$ remains as a constant regardless of the bias conditions. From the literature, the VCMA effects reported in similar MgO/CoFeB/Ta systems have linear responses [145, 146, 168, 169]. The primitive reason for it is due to the small effect. Indeed, the non-linear responses such as V-shape (PMA is increased by both voltage polarities) or ∧-shape (PMA is decreased by both voltage polarities) are mostly reported in systems with a large VCMA effect (ξ > 200 fJ/Vm) [107, 170, 171, 172].

This VCMA coefficient estimation technique is time-efficient. However, it is physically constrained to devices with high RA, typically requires a few hundred $\Omega{\cdot}\mu m^2$ [73, 144, 173]. As discussed in Section 1.2.4, there is a critical current to excite the magnetization dynamics through STT effect. Since our technique applies the bias through the same path as STT, the DC tunneling current in low RA devices can reach the critical STT current, which shields the VCMA effects. Figure 3.10(a)-(c) show representative examples regarding devices with different RAs. For the device with RA = $880\Omega{\cdot}\mu m^2$, the VCMA effect dominates over the STT effect. A positive (negative) voltage enhances (reduces) PMA leading to an expansion (minification) in the switching field B_{sw}. On the contrary, for the typical STT device that has $RA < 10\Omega{\cdot}\mu m^2$, the STT effect dominates over the VCMA effect. A positive (negative) DC bias favors AP-P (P-AP) transition, the switching field is therefore strongly shifted accordingly. Based on these characteristics, for devices with intermediate $RA = 80\Omega{\cdot}\mu m^2$, both VCMA and STT effects are comparable. For any bias conditions, both VCMA and STT are compensated for the AP-P switching direction, whereas the P-AP switching

direction is assisted. As a consequence, this technique is not applicable to low RA devices. Nevertheless, we will discuss another method to confirm the VCMA coefficient in these devices in Section 3.4.3.

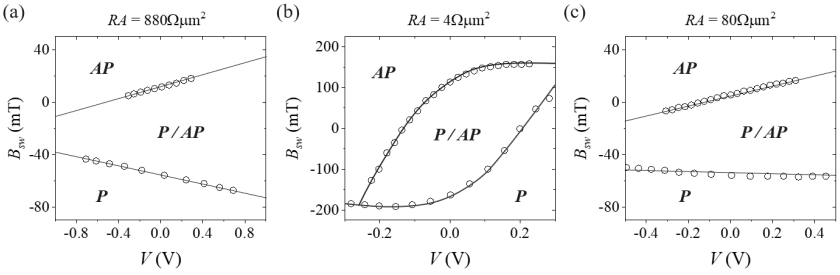

Figure 3.10: *Switching diagrams of switching field versus DC voltage for devices with (a) RA = 880Ω·μm², (b) RA = 4Ω·μm², and (c) RA = 80Ω·μm².*

Device Selection

Judging from the resultant $B_{k,eff}$ and VCMA slope, it is required to select the functional devices. To avoid device breakdown, the maximum affordable EF is limited to 1.4V/nm. For devices with eCD <100nm, $B_{k,eff}$ becomes too strong to be removed by voltage pulses, and VCMA-induced FL switching can never occur. On the other hand, although $B_{k,eff}$ of the 130nm devices can be easily removed, these devices are prone to thermal disturbance compared to 105nm devices. Therefore, our studies will focus on 105nm devices.

3.4 Switching Studies

3.4.1 Electrical Setup

To perform pulse switching studies, the MTJ device is connected to an electrical setup shown in Figure 3.11(a). The top electrode is connected to a bias-tee. The AC port has a pulse generator PG connected, which has a 50Ω impedance. On the DC port, a Keithley 2400 source measure unit (SMU) and a digitized multimeter (DMM) are attached. In addition, this prober system has two individual controls to generate B_x and B_z separately. During the pulse measurements, the magnetic fields are constantly applied to the device, where B_z is applied to compensate B_{stray}, and B_x defines the precession axis for switching. Figure

3.11(b) shows the configuration of the pulses. The writing pulse is generated by the pulse generator, and the pulse duration (t_p) is defined as the total width including a 100ps risetime and a 100ps falltime. After the writing pulse, the SMU sends a small DC current for the DMM to read the resistance of the device.

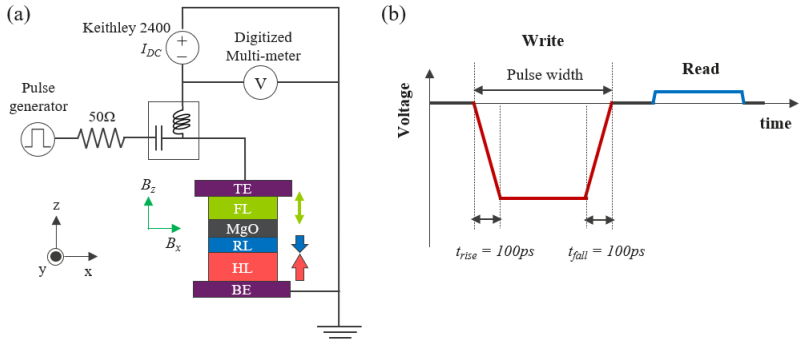

Figure 3.11: *(a) Schematic of the electrical setup for the pulse voltage control magnetization switching measurements. (b) Configuration of the pulses for the switching experiments.*

3.4.2 Measurements and Analyses

Switching Probability

Switching probability (P_{sw}) is tested by sending repeating pulses with fixed amplitude and pulse duration several times (here we test 2000 events per condition), as exemplified in Figure 3.12(a). If the resistance state is changed after pulse, it is counted as a successful switch. P_{sw} for AP-P and P-AP are distinguished by the resistance read before and after the writing pulse. Figure 3.12(b) shows a representative example under the following conditions: $EF = -1.3V/nm$, $B_x = 20mT$, and $B_z = -B_{stray}$. Such VCMA-induced switching has some interesting features:

- ***P_{sw}* curves are mostly identical for both directions**: Because B_{stray} is compensated by B_z in the conventional switching scheme, the AP and P state are equally stable. Both AP-P and P-AP switching follows the same dynamics (Equation 3.1).

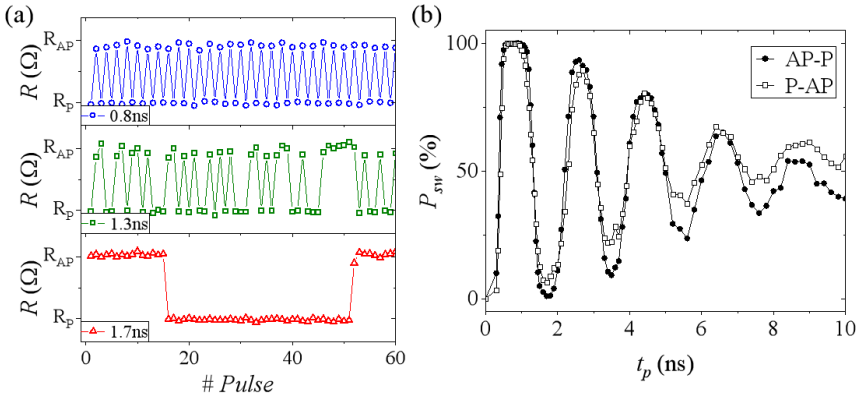

Figure 3.12: *(a) Representative measurements of voltage pulse induced magnetization switch at different pulse durations. (b) Switching probability as a function of pulse duration.*

- **Oscillatory P_{sw}**: As explained in Section 3.2, FL rotates around B_x during voltage application, the switching probability depends on the time where the voltage is cut. For t_p = half-integer periods, P_{sw} is high, whereas t_p = integer periods leads to low P_{sw}.
- **P_{sw} converges toward 50% at longer t_p**: Due to the damping motion, m_z attenuates from ± 1 to 0. Therefore, P_{sw} decreases in time, and typically only the first peak reaches high probability. When $m_z \sim 0$ at long t_p, cutting the voltage results in 50% P or AP regardless of the initial state.

Determination of Switching Speed

Using the P_{sw} curves, we try to obtain the VCMA switching speed (f_s). It is termed as speed to illustrate how fast the VCMA device is written. To systematically assess f_p, we apply a periodic function, i.e. $-Mcos(2\pi t_p/t_{prec})$, to fit the first period, where t_{prec} indicates the precession period. Figure 3.13 shows a representative example. The maximum (M) of the fitting equation is a floating value which can be greater than 100, implying that m_z does not necessarily be one to achieve 100% probability. The fitting error is minor and has a negligible impact on t_{prec}, since t_{prec} is mainly determined by the first two minimum in probability, which corresponding to the initial state and the first order of switching process n = 1. The inverse of t_{prec} represents the average precession speed of the first cycle (f_p). Since the maximum P_{sw} occurs

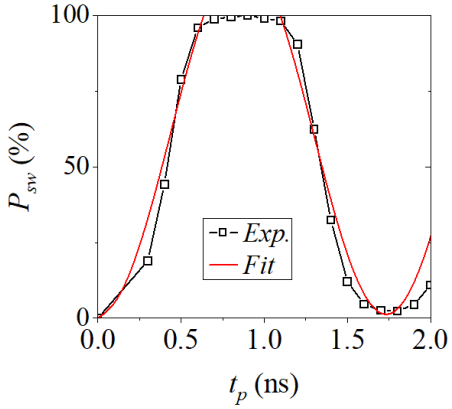

Figure 3.13: *Demonstration of modeling the switching speed. Open symbols are the experimental data, and the red line indicates a cosine function with the precession frequency as the fitting parameter.*

approximately at half of a period, we define the switching speed (f_s) as two times the average precession speed: $f_s = 2f_p$.

3.4.3 Impact of MgO thickness

In Section 3.3.4 and 3.3.5, we have observed that changing the MgO thickness does not impact B_C and PMA of the FL. However, we were not able to confirm whether the VCMA coefficient is independent of the MgO thickness using the DC measurement technique discussed in Section 3.3.6. Nevertheless, we can test the consistency of the switching probability curves between the two MgO conditions. This method is possible thanks to the fundamental characteristics of the STT effect. The required STT current to induce FL switching is dramatically increased for t_p below few nanoseconds [138, 174]. Typically, for devices with RA larger than few tens of $\Omega{\cdot}\mu m^2$, the STT effect becomes negligible and has no impact on the spin dynamics in the precessional switching regime (below few nanoseconds) [59, 74]. Fortunately, the period of the VCMA-induced precession is often in the range of sub-nanoseconds to nanoseconds. Therefore, any magnetization reversal must be induced purely by the VCMA effect.

In Figure 3.14, we observe that when EF is similar, the P_{sw} curves and the fitted speeds are comparable for devices with different t_{MgO}, confirming that the VCMA coefficient is not impacted by the MgO thickness, both samples have $\xi = \sim$42.5 fJ/Vm. This feature also allows one to design the stack to

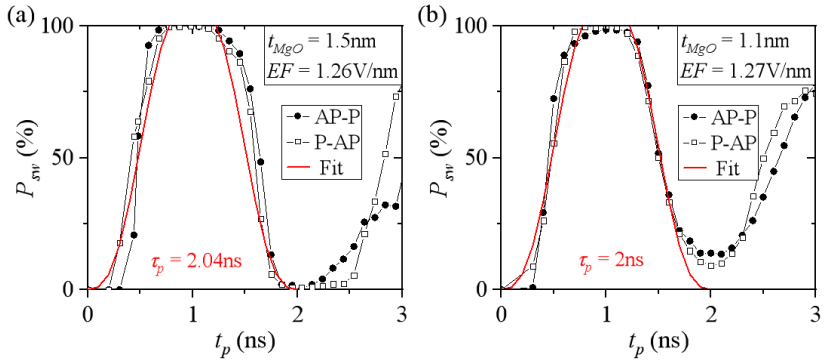

Figure 3.14: *Switching probability as a function of pulse duration for (a) $t_{MgO} = 1.5nm$ and $EF = -1.26V/nm$ ($V_{pulse} = 1.9V$), and (b) $t_{MgO} = 1.1nm$ and $EF = -1.27V/nm$ ($V_{pulse} = 1.4V$). Red curves indicate the fitting results, showing similar t_{prec} for both devices.*

significantly reduce the switching energy (E_{sw}) by simply increasing the MgO thickness to suppress the tunnel current. In these given examples, E_{sw} is 36fJ for device with $t_{MgO} = 1.5$nm and 196fJ for device with $t_{MgO} = 1.1$nm.

3.4.4 Impact of Pulse Amplitude

In this section, we study the impact of pulse amplitude on the switching properties. To get more insights, we study the characteristics with both simulations and experiments. On the simulation side, we will focus on modeling the magnetic energy, whereas experimentally we will study the variation in speed in order to correlate with the simulation results.

Operation Regimes Identification

The magnetic energy of the FL is modeled based on macro-spin assumption using the parameters obtained in Section 3.3, as listed in Table 3.1. The energy diagrams under different EF are investigated in order to characterize the operation regimes. Figure 3.15(a) shows the definition of the magnetization angle. Here, we specifically consider two energy terms: the excess energy (E_{ex}) and the energy barrier (E_b). E_{ex} is defined as the difference between the energy along 90 degree (x-direction) at a given EF (denoted as $E_{90,EF}$) and the initial equilibrium energy (E_i) without bias, which describes the energy that allows

Table 3.1: *Simulation parameters for magnetic energy calculation.*

Parameter	Value
Junction Size	105 nm
FL thickness	1 nm
Mesh Size	$2 \times 2 \times 1$ nm^3
Saturation magnetization	1450 kA/m^3
Interfacial anisotropy	1310 µJ/m^2
Exchange stiffness	25 pJ/m
VCMA coefficient	40 fJ/Vm

the FL to precess across the horizontal plane.

$$E_{ex} = E_{90,EF} - E_i \tag{3.14}$$

On the other hand, E_b is the energy difference between $E_{90,EF}$ and the equilibrium energy at EF (denoted as $E_{eq,EF}$), which is the barrier that prevents the FL from switching if the system is relaxed.

$$E_b = E_{90,EF} - E_{eq,EF} \tag{3.15}$$

We then further derive the expressions for E_{ex} and E_b. Here, we consider a scheme shown in Figure 3.15(a), where the FL experience a external field in the in-plane direction. Notice that because we are considering a magnetic disk, therefore the in-plane directions are equilibrium. For simplicity, we use B_x to represents the total external in-plane field. Starting from Equation 2.17:

$$E = E_d + E_{anis} + E_Z$$

the total magnetic energy density of the system at the given EF and angle $[E(EF, \theta)]$ is calculated by the sum of the demagnetizing energy, interfacial perpendicular anisotropy energy and Zeeman energy:

$$E(EF, \theta) = \frac{1}{2}\mu_0 M_S^2 cos^2\theta + \frac{K_i + \xi * EF}{t_{eff}} sin^2\theta - M_S B_x sin\theta \tag{3.16}$$

Here, because any in-plane axis is equilibrium for a disk-like FL, and the external field is applied in x-direction, the Zeeman energy term can be simplified to $M_S B_x sin\theta$. Then,

$$E_{ex} = E(EF, 90^\circ) - E_i = \frac{K_i + \xi * EF}{t_{eff}} - M_S B_x - E_{min}(0, \theta) \tag{3.17}$$

$$E_b = E(EF, 90°) - E_{eq,EF} = \frac{K_i + \xi * EF}{t_{eff}} - M_S B_x - E_{min}(EF, \theta) \quad (3.18)$$

where $E_i = E_{min}(0, \theta)$ and $E_{eq,EF} = E_{min}(EF, \theta)$ indicate the minimum energy at given EF and θ. One can find these minimum conditions by calculating first derivative $\partial E/\partial\theta = 0$, as derived by the Stoner-Wohlfarth model [175].

$$\partial E_{min}(0,\theta)/\partial\theta = -\frac{1}{2}\mu_0 M_S^2 sin2\theta + \frac{K_i}{t_{eff}} sin2\theta - M_S B_x cos\theta \quad (3.19)$$

$$= K_{eff} sin2\theta - M_S B_x cos\theta = 0 \quad (3.20)$$

By expressing K_{eff} as $M_S B_{k,eff}/2$, we can further derive the initial magnetization angle by:

$$\frac{M_S B_{k,eff}}{2} sin2\theta = M_S B_x cos\theta \quad (3.21)$$

$$B_{k,eff} sin\theta cos\theta = B_x cos\theta \quad (3.22)$$

$$sin\theta = \frac{B_x}{B_{k,eff}} \quad (3.23)$$

Similarly, for $\partial E_{min}(0,\theta)/\partial\theta$ we obtain:

$$sin\theta = \frac{M_S B_x}{2(K_{eff} + \frac{\xi * EF}{t_{eff}})} \quad (3.24)$$

Finally, by substituting Equations 3.23 and 3.24 to Equations 3.17 and 3.18, respectively, one can obtain the full expression for E_{ex} and E_b as:

$$E_{ex} = \frac{K_i + \xi * EF}{t_{eff}} - M_S B_x - \frac{1}{2}\mu_0 M_S^2 \left(1 - \frac{B_x^2}{B_{k,eff}^2}\right) - \frac{K_i B_x^2}{t_{eff} B_{k,eff}^2} + \frac{M_S B_x^2}{B_{k,eff}} \quad (3.25)$$

$$E_b = \frac{K_i + \xi * EF}{t_{eff}} - M_S B_x - \frac{1}{2}\mu_0 M_S^2 \left[1 - \left(\frac{M_S B_x}{2(K_{eff} + \frac{\xi * EF}{t_{eff}})}\right)^2\right] - \frac{K_i}{t_{eff}} \left(\frac{M_S B_x}{2(K_{eff} + \frac{\xi * EF}{t_{eff}})}\right)^2 + M_S B_x \frac{M_S B_x}{2(K_{eff} + \frac{\xi * EF}{t_{eff}})} \quad (3.26)$$

Figure 3.15(b) exemplifies E_{ex} and E_b as a function of EF at $B_x = 22$mT. Depending on the signs of E_{ex} and E_b, we define the operation Regimes 1-3,

where the boundary conditions are $E_{ex} = 0$ and $E_b = 0$. Figure 3.15(c)-(e) shows the representative energy diagrams at each regime, where $|EF_1| < |EF_2| < |EF_3|$.

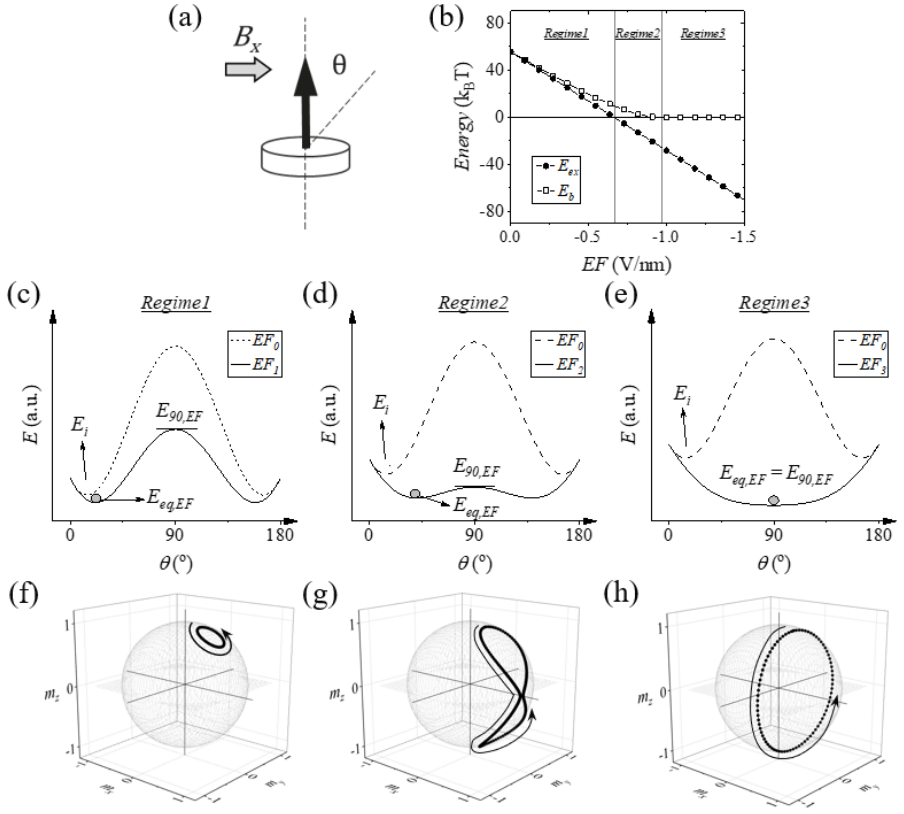

Figure 3.15: *(a) The simulation scheme for energy calculation. (b) Calculated excess energy (E_{ex}) and energy barrier (E_b) as a function of EF at $B_x = 22mT$. (c-e) Illustration of the energy diagrams for Regime 1-3. (f-h) Simulation of switching trajectories for Regimes 1-3.*

In the following, we discuss the switching trajectories in these regimes. The trajectories are simulated using LLG equation, with the damping constant being assumed as 0. In Regime1, since both E_{ex} and E_b are positive, the FL cannot switch over the barrier. The z component of the magnetization (m_z) therefore remains the same sign as the initial state during the EF pulse, as shown in Figure 3.15(f). From the switching trajectory, although we can estimate the precession period, we define the switching speed as 0 since the final state is

always in the same direction as the initial state regardless of the pulse duration. When increasing EF to reduce the PMA and barrier, E_{ex} firstly becomes negative in Regime2. The energy diagram shows that there still exists two equilibrium magnetization positions, resembling the one moderate field regime pointed out in Ref. [132]. Although E_b remains positive, $E_{ex} < 0$ indicates there exists sufficient excess energy for the FL to precess through the barrier. The switching trajectory is shown in Figure 3.15(g). Qualitatively, the trajectory rotates alternatively around the two attractors at the two equilibrium positions $m_z > 0$ and $m_z < 0$. Indeed, it is possible to change the sign of m_z under this condition. Hence, $E_{ex} = 0$ defines the lower switching boundary. When the EF is further enhanced, removing E_b enters Regime3. The energy diagram shows a monostable equilibrium magnetization position pointing along B_x. The magnetization trajectory is stadium-liked, as shown in Figure 3.15(h) for a energy loss-free case. In this regime, switching should be induced in any system, since there is no barrier to prevent switching. For instance, in the real systems, there is finite damping which causes energy dissipation. While it results in the relaxation of the FL toward the equilibrium states, the precessional switching characteristics can still be properly observed. Accordingly, the upper boundary can be defined as $E_b = 0$.

Experimental Observation

After recognizing the operation regimes, the switching characteristics are investigated experimentally. The switching probability curves at different pulse amplitudes are measured, and their switching speeds are subsequently assessed. Figure 3.16(a) summarizes f_s as a function of EF with $B_x = 22$mT for devices with different MgO thicknesses. Again, we observe consistent EF dependence in the two stacks which confirms the same VCMA coefficient. In this figure, f_s is characterized into two phases. First, for f_s below 0.5 GHz, f_s cannot be deduced because there is no oscillation observed in the P_{sw} curves; hence, f_s is zero. Secondly, there is an acceleration phase above 0.5 GHz, where f_s is increased by EF.

Next, we discuss why there are only two phases observed in the experiments. We also compare with the simulation switching speed obtained for different damping constants. The three operation regimes are labeled. From the energy calculation results, the three operation regimes are distinguished by EF = -0.67Vnm and -0.97V/nm. Without a doubt, f_s is zero in Regime1 because no switching is induced. As shown in Figure 3.16(b), P_{sw} is zero for EF = -0.6V/nm regardless of the pulse duration. In Regime2, although some switchings occur at EF = -0.85V/nm, f_s cannot be deduced because there is no clear oscillation. This can be attributed to the thermal fluctuation effect dominating over the precessional

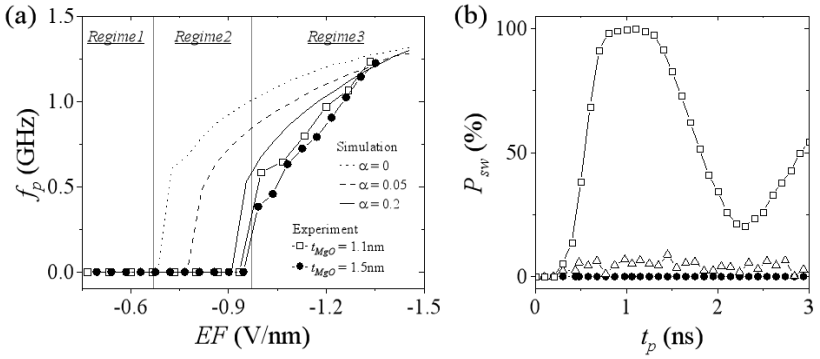

Figure 3.16: *(a) Switching speed as a function of pulse amplitude for two different MgO thicknesses with B_x = 22mT. The operation regimes are labeled. Dotted, dashed, and solid curves indicate the switching speed obtained from macro-spin simulation under different damping conditions. (b) Representative switching probability curves in different operation regimes.*

switching characteristics. When EF is further increased up to Regime3, E_{ex} is large enough to overcome the thermal fluctuation, and the oscillatory features become clear. Here, we observe that higher EF increases f_s progressively. We then use macro-spin simulation based on the device parameters trying to reproduce the trend. We find that above EF = -0.67V, a system with $\alpha = 0$ shows proper precessional switching, and above the threshold the speed increases progressively. However, the simulation speed is far from the experiments. We then add the damping term in the calculation, and we find that with increasing α, f_s at the same EF decreases gradually. This is because damping represents the rate of energy dissipation. In addition, it also need extra cost of energy to induce switching, which reflects the needs of stronger EF to reach the threshold conditions. We find that $\alpha = 0.2$ fits quantitatively well with the threshold EF and f_s of experiments, despite that such α is 1-2 orders of magnitude larger than the typical values obtained from the experiments [176]. Previous reports have also shown that they needed α = 0.1-0.2 to reach the same switching probability patterns and write error rates as their experiments [177, 178]. This is probably attributed to several reasons such as non-uniform distribution of the stray field, nucleation reversal and pinning of magnetization at the MTJ pillar edge, which results in decoherence of magnetization dynamics. After all, macro-spin behavior is too ideal compared to the real devices. In addition, the finite pulse rise time also causes a delay in the magnetization evolution, which imposes additional discrepancy to the simulation results.

Correlation between Simulation and Experiment

Regarding the discussions above, we correlate the results from simulations and experiments. E_{ex} is calculated and plotted as functions of EF and B_x, as shown in Figure 3.17. The operation regimes are distinguished by the two boundaries conditions $E_{ex} = 0$ (solid curve) and $E_b = 0$ (dashed line). The measured data (open symbols), whose speeds can be deduced, is attached in the same plot for comparison. We observe that all the measured data points are situating in Regime3, reflecting that certain amount of overdrive is required to overcome the thermal fluctuation for any B_x conditions. It also indicates that it is rather difficult to realize precessional switching in the moderate field regime for a real system at finite temperature due to the high noise-sensitivity. These experimental results show good agreements from the perspective of magnetic energies.

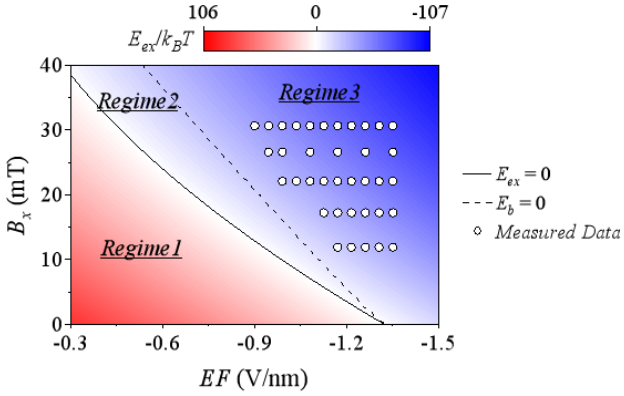

Figure 3.17: *Simulated E_{ex} landscape in the unit of k_BT as functions of EF and B_x. Red (blue) area indicates a positive (negative) E_{ex}. Regimes 1-3 and the corresponding areas are distinguished by $E_{ex} = 0$ (solid curve) and $E_b = 0$ (dashed line). Open symbols represent the data points whose speeds can be deduced.*

3.4.5 Impact of In-plane Magnetic Field

B_x is an indispensable component to induce switching. In this section, we discuss the impacts of B_x on the fundamental and switching properties.

First of all, since B_x is applied along the hard axis of the FL, it reduces the energy barrier between the two states. Figure 3.18(a) shows the simulation results for the energy diagram of the FL under different B_x, showing that the barrier height is lowered by stronger fields. As a consequence, the required voltage to remove the remaining barrier is also reduced. This phenomenon can be observed in Figure 3.17 where the boundary conditions are achieved at lower EF in the cases of higher B_x.

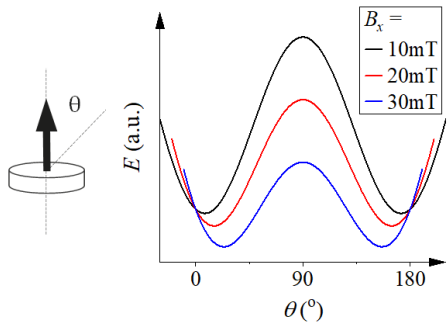

Figure 3.18: *OOMMF simulation of energy diagrams under various B_x conditions.*

Secondly, under the same pulse amplitude, stronger B_x accelerates the magnetization reversal. One can qualitatively see it from the ferromagnetic resonance frequency that $f \sim \gamma\sqrt{B_x(B_x - B_{k,eff})}$ [179]. Here, we introduce the term 'characteristic writing speed (f_c)'. f_c describes the speed at which $B_{k,eff} = 0$. This condition occurs when the energy barrier is removed purely by the applied voltage. From the estimation of $B_{k,eff}$ and $\partial B_{k,eff}/\partial V$, it is possible to calculate the corresponding 'characteristic voltage (V_c)' or 'characteristic electric field (EF_c)':

$$V_c = B_{k,eff}/(\frac{\partial B_{k,eff}}{\partial V}) \tag{3.27}$$

At V_c, the equilibrium magnetization direction is defined by the sum of $\vec{B}_x$ and $\vec{B}_{thermal}$. If $\vec{B}_x$ is large to dominate over $\vec{B}_{thermal}$, then it can be further reduced to B_x. From the above equation, we calculate that EF_c is -1.35V/nm for the studied device. Figure 3.19 shows the experimental f_s obtained at various B_x. Again, we compare them with the simulation speeds. Similar to the previous section, the experimental results deviate from the ideal system with $\alpha = 0$, but they can be well reproduced with $\alpha = 0.2$.

Finally, as the energy barrier is decreased by B_x, the energy barrier and Δ are lowered. Figure 3.20(a) presents the experimental Δ as a function of B_x. It is

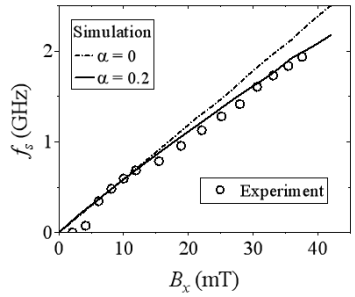

Figure 3.19: *Switching speed as a function of B_x obtained from experiments (open symbols) and simulations at different α, showing good agreements for α = 0.2.*

monotonically reduced by B_x. Despite faster switching speed, losing retention can cause an increase in write errors. In Figure 3.20(b), we show that the minimum write error rate (WER) first decreases monotonically with increasing B_x, and it increases for $B_x > 30$mT. This phenomenon reveals the competition between the thermal fluctuation during the voltage pulse and before/after the voltage pulse. In the lower B_x region, the reduction of WER can be explained by the reducing impact of the thermal fluctuation field during the precession [177, 180]. On the other hand, an increase in WER in the strong B_x region is caused by the random phase fluctuation before and after pulse [180]. It is therefore crucial to apply adequate B_x to improve writing speed and WER while preserving low thermal disturbance during rest.

3.5 Merits and Challenges

Above we have discussed switching properties of conventional VCMA-induced magnetization switching, the last section in this chapter gives an overview of its merits and challenges.

3.5.1 Merits

Compared to STT-MRAM, VCMA-MRAM is fascinating as it outperforms in many aspects:

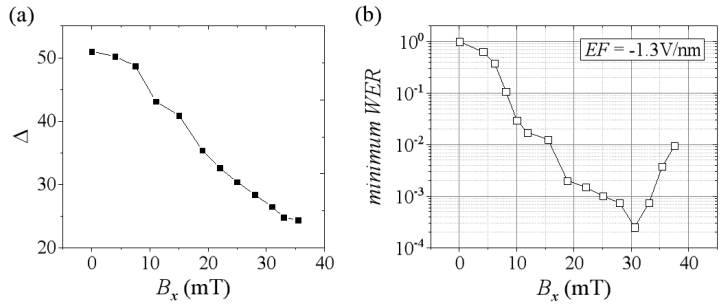

Figure 3.20: *(a) Δ as a function of B_x. (b) Minimum write error rate as a function of B_x. Decrease in WER on the lower B_x side is attributed to the less thermal disturbance during the pulse, whereas increase in WER on the higher B_x side stems from random phase fluctuation before/after the pulse due to the loss of anisotropy.*

- ***High TMR***: A high TMR ensures a sufficient read margin for MRAM applications. Thanks to the better spin-filtering effect in thicker MgO, TMR of the VCMA-MRAM is superior to STT-MRAM. We report in this dissertation an over 250% TMR, whereas the state-of-the-art STT-MRAMs are reported with 200% [18, 181].

- ***Ultra-fast Write***: Differing from STT-MRAM, the speed of VCMA-MRAM can be controlled by the magnitude of the in-plane magnetic field. Typically, the VCMA switching speed falls in the range of sub-ns to a maximum of 2ns, whereas STT switching speed is limited to above few nanoseconds due to the long incubation delay [182]. As a result, VCMA-MRAM is 10x faster than STT-MRAM.

- ***Ultra-low Energy Consumption***: As the tunnel current is minimized, the VCMA switching energy can be suppressed up to two orders lower than that of STT switch even at 10x speed. In addition, the characteristic switching voltage is independent of the programming speed. Figure 3.21(a) and (b) show the typical switching voltages (normalized to the lowest) as a function of pulse duration for STT- and VCMA-MRAM. The voltage increases drastically for faster STT operation while it remains as a constant for VCMA operation. Figure 3.21(c) compares the device performance between them.

- ***Good Scalability***: Similar to STT-MRAM, VCMA-MRAM has a shared read/write path, making it possible to be integrated into a 1-transistor/1-MTJ crossbars structure with a minimum cell size of 6-8F^2 [148], where

F is the feature size of the technology node. Moreover, the unipolar voltage-driven writing process enables a 1-diode selector/1-MTJ structure [183, 184] which can further scale it down to the densest possible $4F^2$.

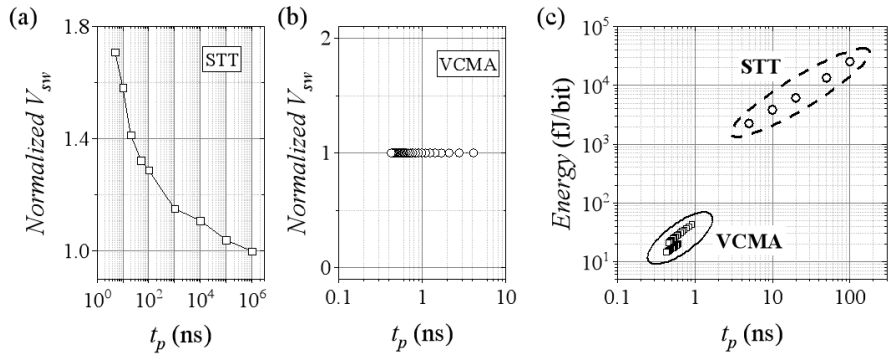

Figure 3.21: *Normalized switching voltage as a function of pulse duration for (a) STT-MRAM and (b) VCMA-MRAM. (c) Write energy as a function of pulse duration. VCMA-MRAM functioning region shows a 10x faster speed and a 100x lower energy compared to typical STT-MRAM.*

3.5.2 Challenges

Despite the merits mentioned above, there exist several challenges before VCMA-MRAM can become applicable:

- ***Magnetic Field Generator***: According to the switching mechanism, the in-plane magnetic field is an indispensable element for VCMA writing of pMTJ devices as it controls the FL precession axis and frequency. However, implementation of a field generator makes memory integration more difficult. Recently, some process friendly concepts were being proposed [185, 186], but it has not yet been studied on VCMA-MRAM. In Chapter 4, we will address this challenge using a novel magnetic-hark-mask (MHM) integration.
- ***Pre-Read Operation***: Since the VCMA effect is unipolar, and P/AP states are equally stable in the conventional writing scheme, a pre-read is needed to decide if writing is required to ensure a desired final state [20]. For pure voltage control, the pMTJ device typically has a high resistance, which slows the sensing time. This sequential read-write

operation significantly increases the write duty cycle. In Chapter 4, we will propose and discuss a new writing scheme that can solve the requirement of pre-read operation to realize genuine ns-scale writing speed.

- ***VCMA Coefficient***: As discussed in Section 3.3.5 and 3.3.6, a VCMA effect of around 40fJ/Vm allows operation of the device with its size down to 100nm. Below it, either the magnetic anisotropy becomes too strong to be removed or the retention of data storage is lost. To allow further scaling of device size, 1000fJ/Vm is required for 30nm devices [106, 187]. Figure 3.22 shows the development map since 2008. Although there is still a gap remaining between first principle simulations and experimental results, recent progress showed a bright future approaching this target. Improving the VCMA effect is beyond the scope of this dissertation; however, it is worth mentioning that both material dusting at the MgO/FL interface [168, 171, 172] and high-k dielectric may path the way to high VCMA efficiency [188, 189, 190].

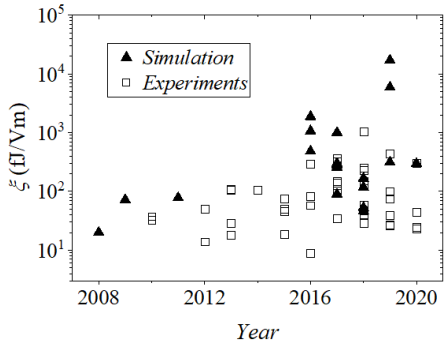

Figure 3.22: *History of VCMA coefficient development for both first principle simulation and experimental results.*

3.6 Summary

In this chapter, we have introduced the conventional VCMA write mechanism. Such mechanism was testified on our standard VCMA pMTJ devices. Before moving to the switching studies, the techniques to quantify the pMTJ fundamental properties including M_S, eCD, PMA and VCMA coefficient were discussed. In the switching studies, we researched the impact of MgO thickness, pulse amplitude, and B_x magnitude on the switching properties. We observed

mostly identical switching properties for devices with different MgO thicknesses (1.1nm and 1.5ns), as long as the electric-field remains the same. By simulation of the magnetic energies, three operation regimes were specified by the two boundary conditions: $E_{ex} = 0$ and $E_b = 0$. Experimental results regarding the variation of switching speeds at different EF could be well explained by the simulation results. Moreover, we defined the characteristic switching speed from the macro-spin calculation, and we validated it experimentally. Finally, the merits and challenges of the conventional VCMA write mechanism were highlighted. It manifests great potential to be the next MRAM generation for high speed and lower power applications after addressing the challenges.

Chapter 4

External-Field-Free and Deterministic Solutions to Conventional VCMA Write

4.1 Introduction

As discussed in Chapter 3 Section 3.5.2, some challenges remain to be solved in order to make VCMA-MRAM more suitable for practical applications. In this chapter, we aim at addressing the two fundamental challenges. The first section discusses the solutions to **Challenge 1: External-Field-Free Operation**, and later in the second section we propose a new writing concept to implement **Challenge 2: Pre-Read-Free Operation**.

Results shown in this chapter were partially published in **Y. C. Wu et al., IEEE Symp. VLSI Tech., TMFS.4 (2020)** [113] and **K. Garello et al., IEEE Symp. VLSI Tech., T194-T195 (2019)** [185] (co-authored).

4.2 External-Field-Free Operation

To achieve external-field-free writing of MTJ devices using the conventional VCMA scheme, the free-layer (FL) must be subjected to a hard-axis field. For perpendicular magnetic tunnel junction (pMTJ) devices, an in-plane magnetic field (B_x) is indispensable as it controls the precessional axis and the frequency

of the FL. Such field generator should be integrated as a component in the memory cell [185, 186], but it has not yet been studied and demonstrated on VCMA devices. In this section, we discuss the methods to achieve the requirement and apply to the integrated devices.

4.2.1 In-Plane Magnetic Field Generator

A simple way to build a constant magnetic field on the FL is to place a magnetic component in the MTJ cell. Here, we discuss two types of magnetic field generator and their properties by micro-magnetic simulation.

In-Plane Polarizer (IPP)

The concept of a polarizer was firstly proposed for spin-transfer torque (STT)-MRAM [191, 192, 193]. For the in-plane magnetized MTJs, placing a perpendicular fixed layer in the MTJ stack could tilt the FL away from the in-plane easy axes. The main purposes were to reduce the incubation time and to improve the switching speed since the spin torque is effectively zero if the angle between the FL and the RL is 0° or 180° (STT $\propto \vec{m}_{FL} \times (\vec{m}_{FL} \times \vec{m}_{RL})$, where $\vec{m}_{FL}$ and $\vec{m}_{RL}$ are the normalized magnetization of the FL and the RL, respectively).

A similar concept can be applied to the perpendicular MTJs to serve as the in-plane magnetic field generator. As shown in Figure 4.1, by adding an in-plane magnetized layer in the pMTJ cell, a built-in in-plane polarizer (IPP) is integrated intrinsically in the pillar.

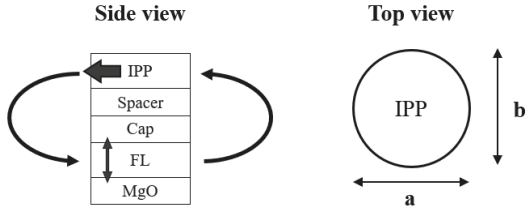

Figure 4.1: *Concept of in-plane polarizer as the in-plane magnetic field generator.*

First, we discuss the case where the MTJ pillar is circular (a = b = 80nm). The magnetic field generated by the IPP on the FL is calculated using OOMMF micro-

magnetic simulation. The simulation model is simplified to a FL/Spacer/IPP stack. The spacer here represents the capping layers plus any dummy layers between the FL and IPP, which also defines the distance between them. The properties of the FL are kept the same as we discussed in Chapter 3 (t_{eff} = 1 nm, K_i = 1310 µJ/m^2, $M_{S,FL}$ = 1450 kA/m, and VCMA = 40 fJ/Vm), whereas the saturation magnetization of the IPP is assumed as $M_{S,IPP}$ = 1300 kA/m. Figure 4.2 shows the in-plane field imposed on the FL generated by the IPP ($B_{x,IPP}$) as functions of spacer thickness (t_{Spacer}) and IPP thickness (t_{IPP}). With increasing t_{IPP}, $B_{x,IPP}$ becomes stronger. In the contrary, $B_{x,IPP}$ decreases as the spacer thickness is increased.

Given in Figure 3.20 that an adequate range of B_x = 20-35mT is required to achieve lower write error rates, we pick 4nm spacer and 2nm IPP which corresponds to $B_{x,IPP}$ = 26mT to simulate VCMA switching.

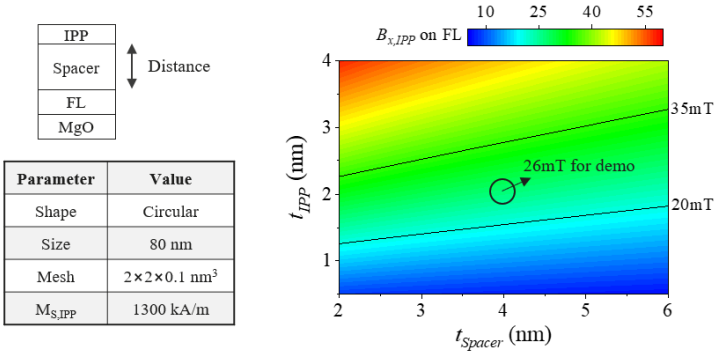

Parameter	Value
Shape	Circular
Size	80 nm
Mesh	2×2×0.1 nm^3
$M_{S,IPP}$	1300 kA/m

Figure 4.2: *Micro-magnetic simulation of the in-plane field generated by the in-plane polarizer imposed on the FL as functions of the thickness (t_{IPP}) and distance.*

Figure 4.3 shows the simulation results assuming zero temperature effect. The initial magnetization of the FL is set to $+z$ direction, while that for the IPP is set to $-x$ direction. The first 2ns (time = -2ns to 0ns) is taken as the relaxation time, and after which an electric-field (EF) of -1.4V/nm is applied to the cell. This corresponds to the change in interfacial perpendicular anisotropy (K_i) from 1310 µJ/m^2 to 1254 µJ/m^2. In Figure 4.3(c) and (d), we compare the trajectories of the z-component of the FL ($m_{z,FL}$) without and with IPP, respectively. The cell without IPP is subjected to an externally applied static B_x of 26mT, whereas the cell with IPP is subjected to a $B_{x,IPP}$ of 26mT. It is shown that precessional VCMA switch occurs only in the cell with a static external field. The FL of the IPP cell relaxes directly to the in-plane direction

after pulse.

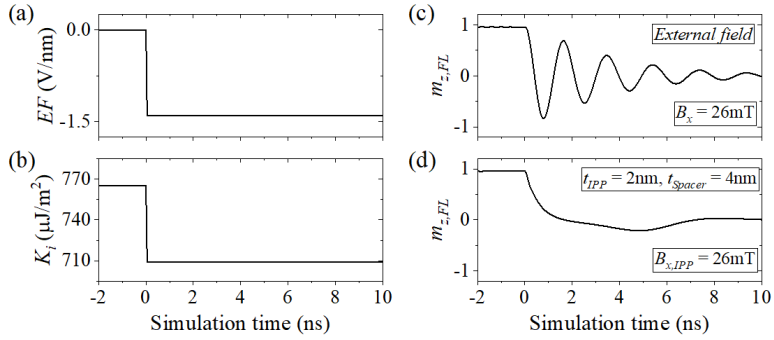

Figure 4.3: *(a) Applied electric-field (EF) and (b) interfacial perpendicular anisotropy (K_i) as a function of simulation time. (c) Simulation of VCMA switch using externally applied in-plane magnetic field. (d) Simulation of VCMA switch using circular in-plane polarizer, with t_{IPP} = 2nm and t_{Spacer} = 4nm.*

The FL of the IPP cell fails to precess normally as what behaves within the static external field, and such direct relaxation of the FL would cause uncertainty in the final magnetization state, as it leads to a 50% switching probability. To investigate the reason causing failure of precession in the IPP cell, the magnetization of the IPP is investigated by recording its time-dependent direction during switching. We find out that the failure is attributed to an unstable IPP. While IPP imposes an in-plane field on the FL, the FL also imposes a perpendicular field on the IPP. Simulation suggests that with a 4nm spacer, a 30mT perpendicular field generated by the FL ($B_{z,FL}$) is applied on the IPP, as shown in Figure 4.4(a). Such field induces IPP precession during switching. Figure 4.4(b) shows the time-dependent IPP direction. Within 2ns, which is the most crucial time for FL switching, IPP rotates almost half cycle. Without a stable in-plane field, FL can not steadily precess, and therefore the FL has a relaxation-like trajectory after pulse.

In order to address the unstable IPP issue, we introduce shape anisotropy to the cell by making the pillar elliptical. Then, IPP no longer has an easy plane anisotropy. Instead, it has an in-plane easy (hard) axis along the major (minor) axis of the ellipse. On the other hand, the anisotropy of the FL remains perpendicular, since the interfacial anisotropy remains sufficiently strong to overcome the shape anisotropy regardless of the plane geometry.

In Figure 4.5, we study the trajectories during VCMA switch for both FL and IPP under different **a**/**b** ratios of the cell. The major axis **a** is kept as 80nm, while the minor axis **b** is reduced from 80nm (circular) to 50nm (elliptical).

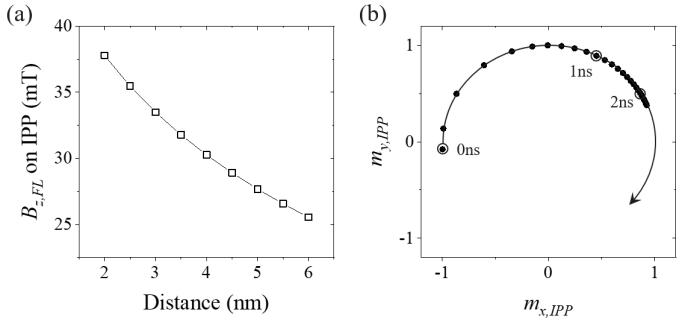

Figure 4.4: *(a) Free-layer generated z field on the IPP as a function of the distance between the FL and the IPP. (b) IPP precession due to an imposed z field generated by the FL.*

From $\mathbf{b} = 80$nm to 70nm, the in-plane shape anisotropy is insufficient to suppress IPP precession after applying the pulse, and the conventional VCMA switch does not occur. Starting from $\mathbf{b} = 60$nm, we observe that IPP becomes more stable. Although a small oscillation is still induced immediately after applying a pulse, it does not strongly disturb the FL and the conventional precession characteristic is restored. By further increasing the aspect ratio of the ellipse to $\mathbf{a}/\mathbf{b} = 80\text{nm}/50\text{nm}$, IPP becomes more stable and its oscillation is negligible.

From these simulation results, we sum up the potential IPP solution to achieve external-field-free VCMA writing of pMTJ devices. An elliptical pillar with $\mathbf{a}/\mathbf{b}$ ratio larger than 1.3 is required to stabilize the magnetization of the IPP. With a robust IPP, the ordinary VCMA switch can be triggered.

Magnetic-Hard-Mask (MHM)

Another option to integrate a field generator is to use the magnetic-hard-mask (MHM), proposed firstly by K. Garello for spin-orbit torque (SOT)-MRAM usages [185]. The concept is shown in Figure 4.6. The MTJ hard-mask (HM) is used for shaping the MTJ pillar, whereas the HM (typically TiN) on the top is used to establish the metal line below the MTJ to connect the MTJ to the bottom electrodes (BE). In his novel concept, a Co-MHM is deposited prior to the ordinary TiN-HM. Since the shape of the bottom metal line is conventionally rectangular, the Co-MHM has an in-plane shape anisotropy by default. This novel idea is not only applicable to SOT-MRAM, but also to STT-MRAM for incubation time reduction and to VCMA-MRAM for external-field-free control.

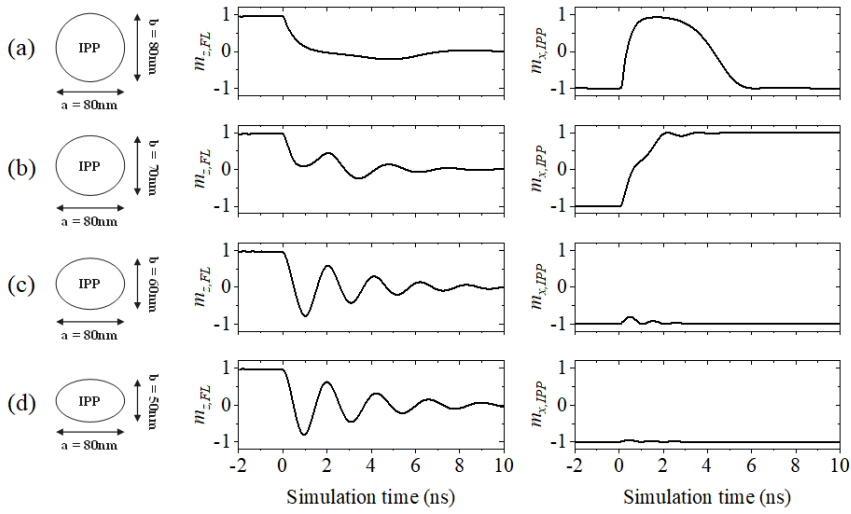

Figure 4.5: *Simulation of VCMA switch using ellipsoidal perpendicular magnetic tunnel junction and in-plane polarizer. The plane dimension of the ellipsoidal pillar is (a) a/b = 80nm/80nm, (b) a/b = 80nm/70nm, (c) a/b = 80nm/60nm, and (d) a/b = 80nm/50nm, with t_{IPP} = 2nm and distance = 4nm. The middle panel shows the z-component of the FL and the right panel show the x-component of the IPP.*

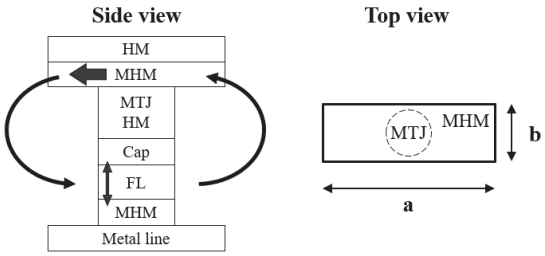

Figure 4.6: *Concept of magnetic-hard-mask as the in-plane magnetic field generator.*

In the following, the magnetic properties of the MHM are studied using OOMMF simulation. We build a 5*5 MHM array and take energy minimization criteria to investigate their magnetizations. The material is assumed to have $M_{S,MHM}$ = 1300 kA/m. Figure 4.7(a) shows the result of an array consisting of 390*120*50nm^3 (length*width*thickness) MHMs, with the pitch = 540*260nm^2.

The colors identify the x-component of the magnetization. We observe that the center MHM has relatively uniform magnetization, while the peripheral MHMs show inhomogeneity. The simulation results here indicate that the neighboring MHMs are important to stabilize the center one through the magneto-static coupling, and the inhomogeneity in the peripheral MHMs can be attributed to lack of neighboring MHMs.

In fact, since the inhomogeneity is ascribed to the energy minimization through forming multi-domain structures, scaling down the MHM size can effectively ease the issue. Figure 4.7(b) shows the result of a 5*5 array consisting of 100*50*25 nm^3 MHMs, with pitch = 150*100 nm^2. By simply reducing the size of the MHM, the magnetization becomes more uniform even for the peripheral ones. This also brings benefits to device size miniaturizing for the advanced technology nodes.

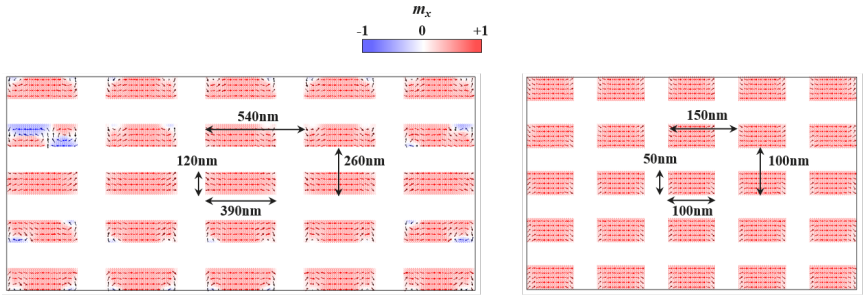

Figure 4.7: *Simulation of the magnetization for a 5*5 MHM arrays. (a) MHM dimension is 390*120*50 nm^3 (length, width, thickness) and pitch is 540*260 nm^2. (b) MHM dimension is 100*50*25 nm^3 and pitch is 150*100 nm^2.*

Next, we discuss the in-plane field generated by a 5*5 array of 390*120*50nm^3 MHMs ($B_{x,MHM}$). The magnetization of the MHM array is first relaxed to the minimum energy, and the in-plane field is recorded for the FL located at the center of the MHM array. Figure 4.8(a) shows the simulation results for different MHM thickness at various distances. Here, the distance is the total thickness between the FL and the MHM on top of it, which includes the thickness of the capping layers and the MTJ HM. Similar to the IPP results, a thicker MHM generates a stronger $B_{x,MHM}$, while increasing the distance lowers it. The shadow area indicates the typical distance (60-80nm) in our integrated devices. As mentioned, for our current VCMA devices, a B_x of 20-35mT is the

most suitable range for VCMA switching. Hence, it is shown that a t_{MHM} of 40-50nm is required.

In addition to a sufficient $B_{x,MHM}$, it is also important that the FL experiences a spatially uniform $B_{x,MHM}$ such that the precession frequency within a FL is also consistent. We perform simulations to record the magnetic field profile with a resolution of 10*10 nm^2. Figure 4.8(b) shows an example of [x,y] map for $B_{x,MHM}$ profile with t_{MHM} = 50nm at a distance of 70nm. The square and circular areas denote the MHM and MTJ pillar locations, respectively. Results show that $B_{x,MHM}$ is highly uniform not only at the MTJ position (60nm in diameter), but also for an area up to 120*120 nm^2. The $B_{x,MHM}$ gradient becomes significant only starting at 100nm away from the center. Furthermore, since the distance between the FL and the MHM is typically several tens of nanometers, $B_{z,FL}$ on MHM is negligible. These results suggest that MHM is an appropriate solution to serve as the in-plane field generator.

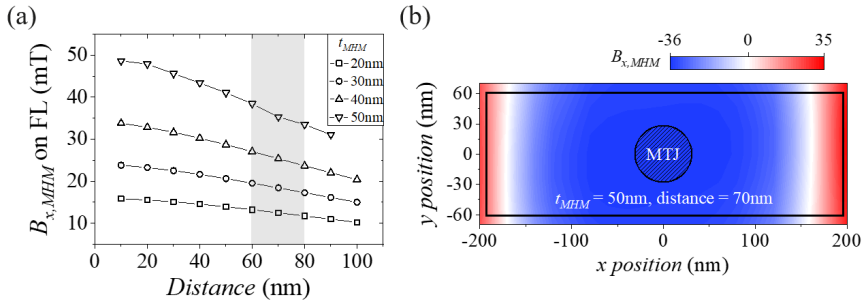

Figure 4.8: *Simulation of the in-plane field on the free-layer generated by a 5*5 array of 390*120*50nm^3 MHMs ($B_{x,MHM}$). (a) $B_{x,MHM}$ as a function of the distance between the FL and the MHM for different MHM thicknesses. Shadow area indicates the typical distance in integrated devices, which is the total thickness of capping layers and MTJ HM. (b) $B_{x,MHM}$ profile at the distance of 70nm for 50nm thick MHM. Black square indicates the area of the MHM. Circular area denotes the location of the MTJ pillar.*

4.2.2 Discussion

Above we have studied two types of field generator that can be integrated in the memory cell: in-plane polarizer (IPP) and magnetic-hard-mask (MHM). Both of them can provide a steady in-plane field to the FL under specific designs. However, MHM is believed to be more suitable not only from the application point of view but also from the perspective of stack design. In fact,

the major driving forces that pushed MRAM evolving from in-plane technology to perpendicular technology were to lower the write energy (for STT-MRAM) and increase the array density. The IPP cell requires an elliptical shape to stabilize the magnetization of the IPP, which limits the bit size scaling and array density. Moreover, the distance between the FL and IPP is short such that these magnetic layers are magneto-statically coupled. Increasing the distance is not an ideal solution since a large height/diameter ratio is unfavorable for the etching process. Therefore, the MHM concept can be more compatible than IPP for the advanced technology nodes.

4.2.3 First Demonstration of Field-Free Conventional Switch (FFCS)

After proving the feasibility of the MHM concept and the first demonstration on SOT-MRAM [185], we attempt to apply it on the VCMA devices. According to the simulation results (Figure 4.8), a 45nm Co-MHM is chosen to generate a sufficient $B_{x,MHM}$ for in-plane-field-free control. Figure 4.9 shows the cross-sectional TEM image of the Co-MHM integrated VCMA-pMTJ cell. The pMTJ used is the same as that in Chapter 3, with $t_{MgO} = 1.5$nm. Below the MTJ is the metal line having the shape defined by the MHM, which connects to a bottom electrode (BE). Above the MTJ, a TiN MTJ HM shapes the device pillar, and next a 45nm Co-MHM is deposited prior to the conventional TiN HM. Finally, a Cu interconnect forms the top electrode (TE). The MHM is magnetized in $-x$ direction, and it generates a $+B_{x,MHM}$ at the FL position.

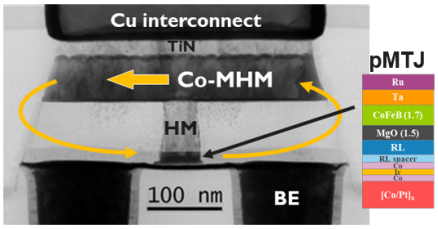

Figure 4.9: *Cross-sectional TEM image of the Co-MHM integrated VCMA-pMTJ cell. The distance from the Co-MHM to the FL is approximately 70nm. Arrows indicate the magnetization of the Co-MHM and the generated magnetic field direction.*

Field Calibration

To estimate how large is the $B_{x,MHM}$ imposed on the FL, K. Garello et al. [185] made use of the SOT switching characteristics, where the FL can only be switched in a certain range of $B_{x,eff}$ ($= |B_{x,MHM} - B_x|$). This method is, however, not applicable to our VCMA devices. Here, we provide another technique which is more suitable and straightforward for devices with lower PMA.

Instead of testing the switchability, we measure the TMR under various B_x. Since our device has $B_{k,eff}$ of 70-80mT, a change in $B_{x,eff}$ can effectively tilt the FL (and potentially the RL). The conductance, and accordingly the TMR, of the device depends on the angle between the FL and the RL:

$$G(\theta) = G_{90} + (G_p - G_{90})\, cos\theta \tag{4.1}$$

where θ is the angle between the FL and the RL, G_p is the conductance of the P state, and G_{90} is the conductance of the orthogonal magnetization configuration. In Figure 4.10, B_x is applied in the direction opposite to $B_{x,MHM}$. TMR firstly increases as $B_{x,eff}$ is gradually reduced. When $B_{x,MHM}$ is completely compensated by B_x = -33mT, we measure a maximum TMR of 215%. Further increase in B_x over-compensates $B_{x,MHM}$ such that TMR drops again.

Compared to the standard device without MHM, we measure consistent TMR and coercive field from the MHM device under B_x = -33mT. This indicates that MHM integration does not impact the MTJ properties. It is also worth noting that the experimental $B_{x,MHM}$ is in good agreement with the simulation value.

Field-Free Conventional Switch (FFCS)

Finally, we demonstrate field-free conventional VCMA switching of an 80nm pMTJ device. Figure 4.11 presents the precessional switching of the MHM device in absence of B_x at EF = -1.4V/nm, consistently with the switching of the standard device with B_x applied. A write-error-rate (WER) of 10^5 switching events is measured, with a minimum WER of 2×10^{-4} achieved at 0.87ns. In the standard device, a similar WER is obtained under B_x = 33mT. However, we measure a better WER of 9×10^{-5} for the standard device under B_x = 25mT, indicating that MHM can be further optimized by reducing the Co-MHM thickness to decrease $B_{x,MHM}$.

To sum up, our studies on MHM address the first challenge in VCMA-MRAM: **External-Field-Free Operation**.

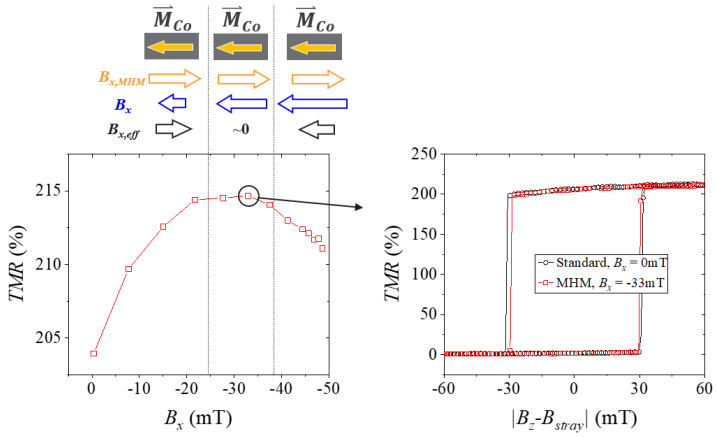

Figure 4.10: *(Left) TMR as a function of B_x, showing maximum TMR at $B_x \sim$ -33mT. Arrows indicate different strength for MHM field ($B_{x,MHM}$), external field (B_x) and effective field ($B_{x,eff}$) applied on the FL. As $B_{x,MHM}$ and B_x are in competition at the FL position, the TMR has a maximum at compensation. (Right) TMR loops comparison between a MHM device at B_x = -33mT (field compensated) and a standard device without MHM and B_x, showing no degradation after MHM integration.*

4.3 Deterministic VCMA Write

In the conventional VCMA write scheme, both P and AP states are equally stable. Since VCMA effect is uni-polar in our device, both P-AP and AP-P transitions share the exact same write pulse. Therefore, to ensure a desired final state, a pre-read is needed to decide if writing is required [20]. For pure voltage control, VCMA devices typically have a higher resistance-area product than the STT devices, which slows down the reading speed. This sequential read-write operation significantly extends the total write duration and increases the write duty cycle. In this section, we propose and discuss a new writing scheme that can get rid of the pre-read operation, in order to realize genuine ns-scale write speed.

4.3.1 Concept

In Figure 4.12, the concept is described in the perspective of energy profiles. The energy diagrams for the conventional and the proposed deterministic VCMA

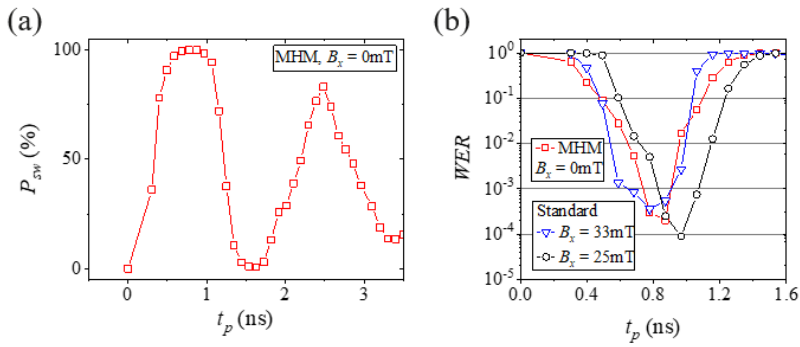

Figure 4.11: *(a) Oscillatory switching probability of an MHM integrated 80nm device for the conventional VCMA switching scheme without external in-plane field applied. (b) Write error rate (WER) assessments for an MHM and standard devices. The WER curve for MHM device is comparable to the standard device under B_x of 33mT, both precession frequency and lowest WER are similar. The standard device under B_x of 25mT shows the best WER.*

write schemes are shown. In the conventional scheme, both AP and P states have the same stability. The required voltage to remove the energy barrier and to induce FL precession is the same for both AP-P and P-AP transitions. To effectively separate the switching voltages, we propose to induce asymmetry in the stabilities. In the presence of an out-of-plane field, one of the states is favored. Here, we discuss the case where the AP state is more stable than the P state. This condition can be achieved by applying an external magnetic field to the free-layer, or simply implemented intrinsically through design of the SAF/RL stray fields. Under this circumstance, the AP-P and P-AP transitions have distinct threshold voltages. At $V = V1$, switching is uni-directional and only P-AP is available. At $V = V2$, the energy barrier is completely removed, Switching should behave similarly as in the conventional scheme, and both P-AP and AP-P transitions are possible.

4.3.2 Switching Probability Differentiation

To study how much is the required out-of-plane field on the FL to enable deterministic write, we investigate the switching probability curves for both transitions using imec's standard VCMA device (Figure 3.2, with $t_{MgO} =$ 1.1nm). The P_{sw} curves as a function of pulse duration (t_p) are measured at $B_x = 33$mT for different effective offset fields. Here, the effective offset field

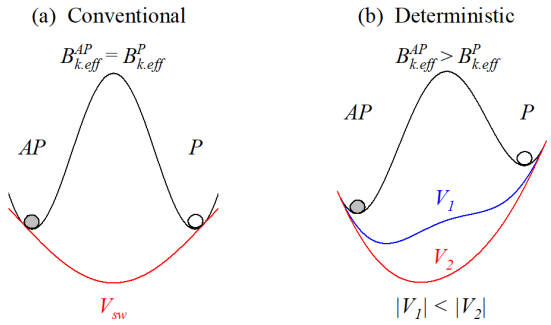

Figure 4.12: *Energy diagrams for the conventional and deterministic VCMA write scheme.*

($B_{z,eff}$) is equivalent to the total z field including the external field and the stray fields from the SAF/RL layers ($B_{z,eff} \equiv |B_z - B_{stray}|$). For each P_{sw} vs. t_p curve, we collect the maximum P_{sw} at half precession period. Figure 4.13(a)-(e) summarizes the maximum P_{sw} as a function of EF for different $B_{z,eff}$. At $B_{z,eff}$ = 0mT, writing is in the conventional mode, hence the maximum P_{sw} vs. EF curves for the two transitions are similar .

When $B_{z,eff}$ is progressively increased, the required EF to achieve 100% P-AP transition is lowered, while that for AP-P transition is higher. The onset of deterministic switching starts when the difference in maximum P_{sw} reaches 100%, i.e. $B_{z,eff} \geqslant$ 5mT. Figure 4.13(f) shows an increasing difference in $P_{sw}^{P-AP} - P_{sw}^{AP-P}$ with stronger $B_{z,eff}$, and a 100% difference is attained at EF = -1V/nm.

4.3.3 Properties at Offset

We have found that $B_{z,eff}$ = 5mT leads to the onset of deterministic mode. In this section, we discuss the corresponding device properties under such condition. In Figure 4.14(a) and (b), the original P_{sw} vs. t_p curves are shown. At EF = -1.0V/nm, we observe that P-AP transition is promoted, while AP-P transition is much suppressed. A uni-directional P-AP switching occurs when t_p is longer than 0.8ns, which can serve as an initialization condition. At EF = -1.4V/nm, both transitions have the ordinary precessional characteristics and the oscillatory switching probability curves are similar as in the conventional writing mode. For the AP-P transition, we measure P_{sw} = 100% at t_p = 0.4ns.

In addition to the difference in switching probability curves, the retentions of the

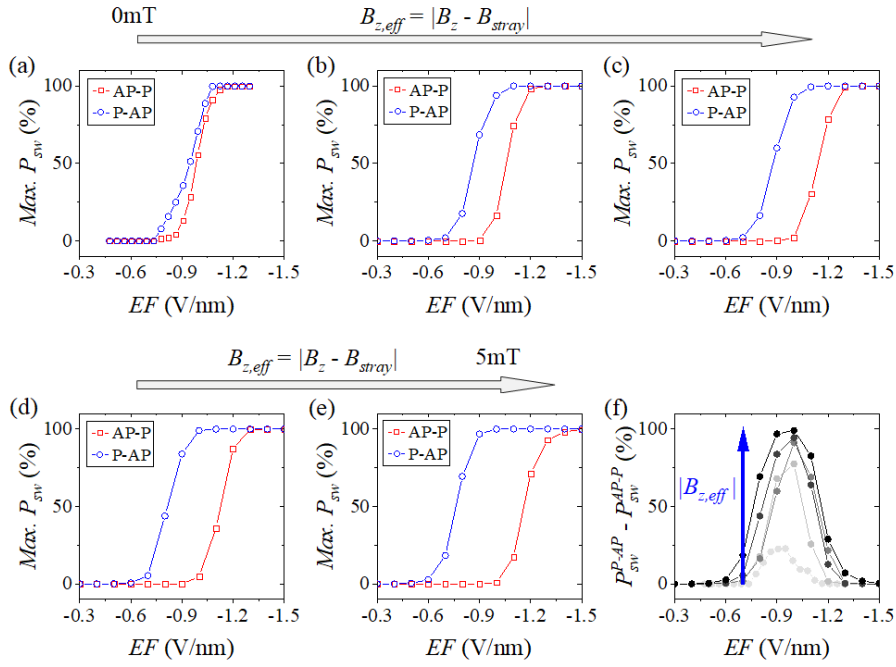

Figure 4.13: *Maximum switching probability under different offset fields. With increasing $B_{z,eff}$, the required EF to reach $P_{sw} = 100\%$ becomes more separated for the two transitions.*

two states are also asymmetric. We use the method discussed in Section 3.3.5 to evaluate the thermal stability factors of the two states, Δ_{AP} and Δ_P. Figure 4.14(c) shows that with increasing $B_{z,eff}$, AP (P) state becomes more (less) stable. The variation of these estimated values follow well with the calculation using the macro-spin model:

$$\Delta = \Delta_i \left(1 \pm \frac{B_{z,eff}}{B_{k,eff}}\right)^2 \tag{4.2}$$

where Δ_i indicates the intrinsic thermal stability at zero offset field. For the conventional mode, Δ is 54 for both states, whereas Δ_{AP} is 61.7 and Δ_P is 47.4 for the deterministic mode at $B_{z,eff} = 5$mT. Although asymmetric retention is somewhat unwanted, it becomes trivial if both Δ_{AP} and Δ_P are doubled. One can realize it with a thicker FL and with an improved VCMA coefficient.

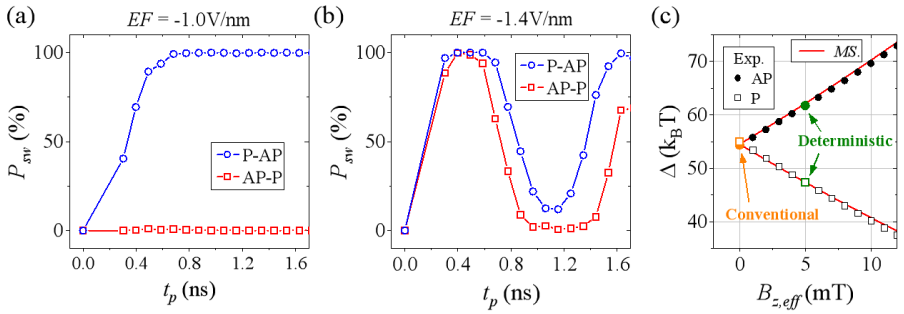

Figure 4.14: *Oscillatory switching probability curves at 5mT effective offset field for (a) EF = -1.0V/nm and (b) EF = -1.4V/nm. (C) Thermal stability factor as a function of the effective offset field. Orange and green labels correspond to the conditions for conventional and deterministic operations, respectively. Red curve is the calculated trend for* Δ *using the macro-spin model.*

4.3.4 Pulse Configuration

Based on the P_{sw} curves obtained in the previous section, we propose the pulse configurations for the deterministic write scheme. Figure 4.15 lists the different configurations for the conventional and the deterministic write schemes. In the conventional scheme, pulse 1 is requested to read the MTJ state, and pulse 2 is sent if a switch is needed. The read operation uses a voltage whose polarity is opposite to the write one, which increases the PMA during reading duration to suppress the potential read disturbance [194]. Both switching directions share the same sequential read-write operation.

In our proposed deterministic scheme, pulse 1 has a lower amplitude and longer duration compared to pulse 2, which initializes the MTJ to the AP state. If an AP state is requested, then pulse 2 is not required; or if the P state is requested, pulse 2 is sent to switch the FL to the P state. To sum up, a **single-pulse** brings the MTJ to the AP state, whereas a **double-pulse** leads to the P state.

4.3.5 Demonstration and Discussion

In Figure 4.14, the best condition for AP-P transition (EF = -1.4V/nm, t_p = 0.4ns) has been identified; however, those curves are measured when the FL is in a steady state. To make deterministic switch reliable, one needs to first understand how the inter-time and second pulse duration impact the switching behavior.

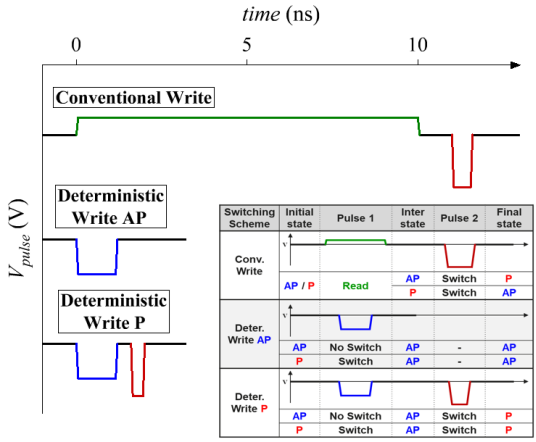

Figure 4.15: *Pulse configurations and the corresponding states for the conventional and deterministic VCMA write schemes.*

To test the double-pulse switching probability, an additional pulse generator is added to the test setup, as shown in Figure 4.16. Both PG1 and PG2 are synchronized and connected through a power combiner before the bias-tee to allow us to test sequential pulses with any defined inter-time (t_{inter}). A B_x of 33mT is applied to the device during the test. We choose EF = -1.0V/nm and t_{p1} = 1.2ns as the single-pulse condition, and we record the switching probability of AP-P transition from 200 events under different combinations of t_{inter} and t_{p2}. The results are presented in Figure 4.17 as a contour map. High (low) probability is expressed in red (blue) color. We observe a double oscillatory behavior on both axes. First, the oscillatory probability in t_{p2} can be understood as the behavior similar to what happens in conventional VCMA write, where $m_{z,FL}$ rotates around the in-plane field. From the 50%-to-50% duration (e.g. time between the two white lines at t_{inter} = 0.2ns), we find that the FL takes approximately 0.55ns to precess a half period. This corresponds to a switching speed f_s of 1.82GHz, which is consistent with the speed observed in the conventional switching mechanism under similar B_x condition (Figure **??**).

On the other hand, the probability also oscillates when changing t_{inter} for a fixed t_{p2}. Experimentally, the observed frequency is about 2.2 GHz. Different from the precession period during switching, the period during the inter-time is related to both the anisotropy field and the external field. Then, for different t_{inter}, m_z changes periodically in time, and therefore the initial torque applied on the magnetization when the second pulse is applied changes also periodically, leading to different t_{p2} to reach maximum probability.

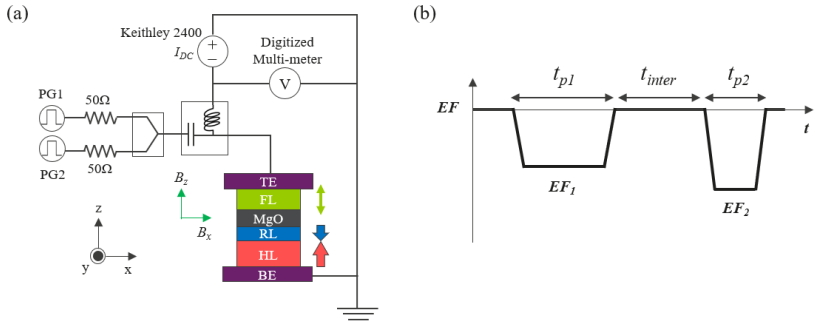

Figure 4.16: *Schematic of the electrical setup and pulse configuration for the deterministic VCMA write test.*

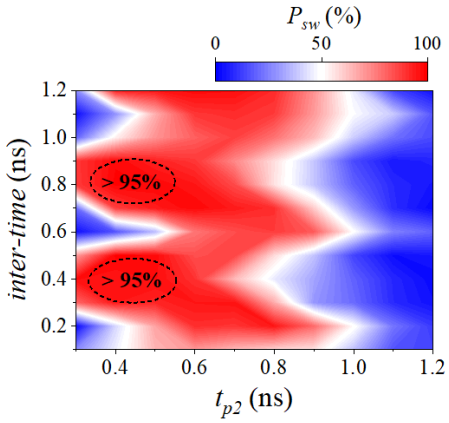

Figure 4.17: *Double-pulse switching probability for AP to P transition as functions of second pulse duration and inter-time. Red (blue) area indicates high (low) switching probability. Conditions for $P_{sw} > 95\%$ are labeled.*

Finally, we use the best P_{sw} condition to demonstrate deterministic writing. Pulse 1 is set as EF = -1.0V/nm and t_{p1} = 1.2ns. We choose t_{inter} = 0.4ns, and pulse 2 is set as EF = -1.4V/nm and t_{p2} = 0.4ns. Figure 4.18(a) demonstrates continuous magnetization switching using alternating single- and double-pulse. We show that single-pulse always switches the FL to the AP state and double-pulse ends in the P state. In addition, the magnetization remains un-switched if a single-pulse is applied to the AP state or a double-pulse is sent to the P state [Figure 4.18(b) and (c)].

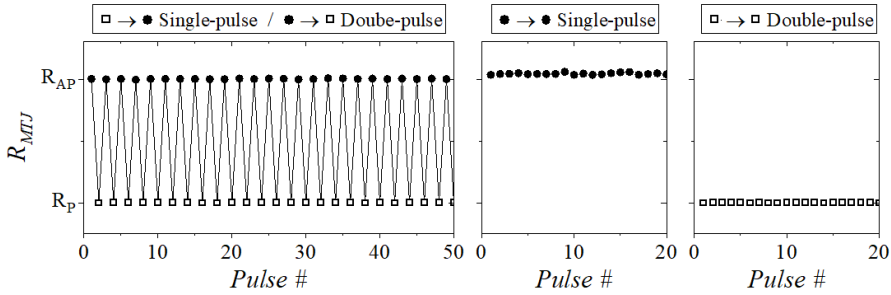

Figure 4.18: *Demonstration of the deterministic VCMA write concept at t_{p2} = 0.4ns and inter-time = 0.4ns. (Left) Continuous magnetization switching using alternating single-pulse and double-pulse, showing single-pulse results in the AP-P transition and double-pulse results in the P-AP transition. (Middle, Right) Magnetization remains un-switched if a single-pulse is applied to the AP state or a double-pulse is applied to the P state.*

To validate our experimental results, we perform macro-spin simulations. The simulation parameters are chosen based on the experiments. Figure 4.19 shows that the single-pulse switches the FL from $m_{z,FL}$ = -1 to +1, representing the P-AP transition. If the FL has an initial $m_{z,FL}$ = +1, the single-pulse only induces a slight oscillation but does not cause any switching. The magnetization relaxed to the equilibrium state soon after the pulse. Next, a double-pulse is applied to the FL, and the magnetization is switched from $m_{z,FL}$ = +1 to -1 (AP-P transition). Finally, if a double-pulse is applied to the P state, the FL is first initialized to the AP state and immediately reversed back to the P state by the second pulse.

4.3.6 Energy Consumption and Benchmark

The energy consumption of the deterministic scheme is compared to the conventional scheme. Figure 4.20(a) shows the write configurations and their energies normalized to the AP-P transition of the conventional write. We estimate comparable energy for a P-AP-P cycle. Moreover, the pre-read operation is not required in the deterministic mode, which makes the write process time-efficient. The total durations demonstrated above were 1.2ns for writing AP state and 2ns for writing P state. In comparison with this, the conventional read-write operation may take a longer time to complete (> 10ns) mainly due to the slow reading speed. Therefore, the proposed deterministic VCMA write scheme can be more suitable for applications such as neuromorphic

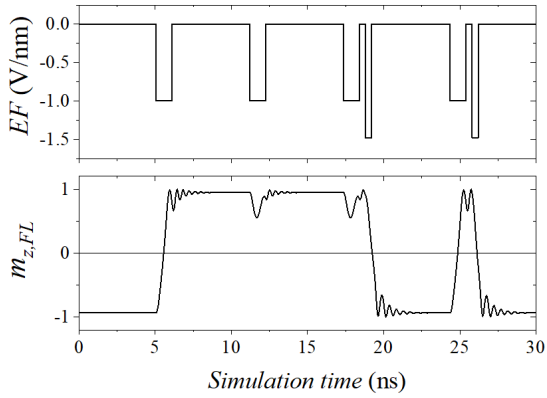

Figure 4.19: *Macro-spin simulation of the deterministic write concept.*

computing and machine learning whose writing is more frequently than reading. Furthermore, it shows 1∼2 orders lower write current density compared to the state-of-the-art STT-MRAMs even at ns speed [Figure 4.20(b)].

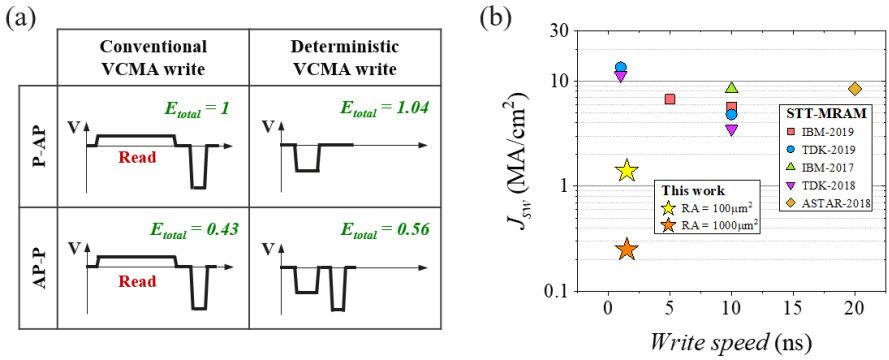

Figure 4.20: *(a) Comparison of the energy consumption between the conventional and the deterministic VCMA write scheme. The total energy of each write configuration is normalized to the P-AP write energy of the conventional scheme. (b) Switching current density as a function of write speed, benchmarking against the state-of-the-art STT-MRAMs. STT-MRAM data obtained from Refs. [138, 174, 195, 196, 197].*

4.4 Summary

In this chapter, the fundamental challenges in the conventional VCMA-MRAM were first pointed out. The first challenge is regarding the integration of an in-plane magnetic field generator, and the second challenge is the required pre-read operation before writing. Both challenges must be addressed to take full advantage of VCMA-MRAM.

To address the field generator challenge, two potential solutions were studied: in-plane polarizer (IPP) and magnetic-hard-mask (MHM). Micro-magnetic simulations suggested that both solutions were able to supply suitable in-plane fields to the free-layer. However, IPP was considered less suitable for the advanced technology node because the MTJ pillar must be patterned into elliptical shape to stabilize the magnetization of the IPP. In addition, the IPP and the FL were coupled due to the short distance between them, which could potentially change the properties of the MTJ stack during stack processing. On the contrary, MHM was recognized as a better solution. On one hand, the typical thickness of the MTJ HM was several tens of nanometers, hence the integration of MHM would not impact the MTJ properties. On the other hand, the MHM defined the shape of the metal line below the MTJ, which intrinsically had a rectangular shape to provide itself with a strong shape anisotropy. Furthermore, scaling down the MHM size could effectively make it more stable. Such MHM concept was then put into practice by combining with imec's standard VCMA cell. Experimental results showed consistent fundamental and switching properties as in non-MHM integrated devices: high tunneling magneto-resistance, precessional switching, and low write error rates. These results suggested that MHM could solve the magnetic field integration challenge.

To tackle the second challenge on the need of a pre-read operation, a new deterministic VCMA writing scheme was proposed. By intentionally introducing asymmetry in the FL stabilities, the two transitions had distinct threshold voltages. Although it simultaneously made one state less favorable, it would be trivial by doubling the stability and VCMA efficiency. In this deterministic writing scheme, a single-pulse which had a lower amplitude and a longer duration was utilized as the initialization pulse to reset to the AP state. A double-pulse consisting of an identical single-pulse, an inter-time, and a second pulse aimed to set to the P state. The inter-time and the second pulse must meet certain combinations to achieve high switching probability. Nevertheless, continuous magnetization switchings were demonstrated using alternating single-pulse and double-pulse. Compared to the conventional mode, deterministic writing did not compromise write energy consumption while removing the need of pre-read. Hence, our proposed method addressed the second challenge of the pre-read

operation, making VCMA-MRAM more suitable for applications.

In conclusion, we have proposed and studied the solutions to the fundamental challenges of the VCMA devices, which could make VCMA-MRAM better than current. Future research needs to focus on improving the reliability of both solutions.

Chapter 5

Operating Temperature: Impact on Magnetic and VCMA Writing Properties

5.1 Introduction

As a fundamental requirement, the memory cell must be able to support a certain range of operating temperatures (T). For example, Intel defines a 0°∼85° (275K∼360K) for commercial devices [198]. Recent studies have revealed that all the magnetic properties, including saturation magnetization [199], magnetic anisotropy [200], and VCMA coefficient [201], are varying with operating temperature. But the temperature dependences of these properties differ with materials and stacks [201, 202]. Further, the operation properties of the magnetic tunnel junction (MTJ) are closely related to these variations, such as the writing voltage and data retention [203, 204]. Understanding of these properties is therefore important to implement VCMA in the MRAM applications.

Figure 5.1 illustrates the diagram of how the operating temperature impacts the magnetic and VCMA writing properties accordingly. In the first level, temperature changes the saturation magnetization (M_S), interfacial anisotropy (K_i), VCMA effect (ξ), and breakdown voltage (V_{BD}). The relative changes in M_S and K_i determine the eventual effective anisotropy K_{eff}, and the corresponding write voltage is defined by K_{eff} and ξ. Finally, the variation in

V_{BD} will decide the write voltage margin. In this chapter, we will sequentially examine these temperature-induced changes using imec's standard VCMA pMTJ devices. The temperature of interest ranges from 300K to 400K.

Results discussed in this chapter were partially published in **Y. C. Wu et al., 65th MMM Conference, L2-05 (2020)** [205] and will be submitted to **Y. C. Wu et al., Appl. Phys. Lett. (2020)** [206].

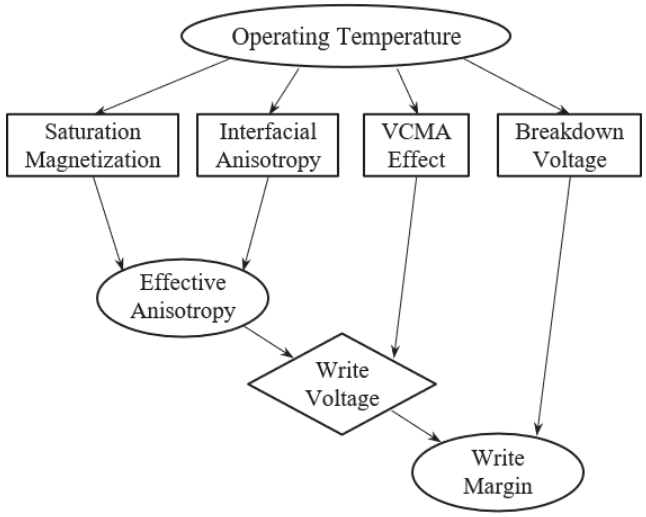

Figure 5.1: *Diagram showing the impact of operating temperature on the MTJ parameters and the device operating properties.*

5.2 Material and MTJ stacks

The material and MTJ stacks used in this chapter are shown in Figure 5.2. Two thicknesses of the CoFeB free-layer (t_{FL}), 1.5nm and 1.7nm, are prepared for different purposes. For MTJ1, t_{FL} is 1.5nm, and it is being used to estimate the variations of the fundamental magnetic properties in a wide range of ambient temperatures because its perpendicular magnetic anisotropy (PMA) is sufficiently strong to withstand temperature above 400K. For MTJ2, t_{FL} is made 1.7nm for VCMA-induced switching experiments, as it offers a moderate PMA range which can be removed within the limitation of breakdown voltage. The purpose of each layer and the deposition conditions have been explained in Section 3.3.1. The MTJ size of interest is 105nm in electrical dimension.

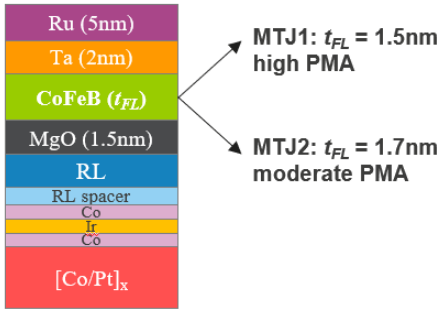

Figure 5.2: *MTJ stacks for investigating the temperature dependences of magnetic and switching properties.*

5.3 Variations of Magnetic Properties on Operating Temperature

In this section, we use MTJ1 to investigate and discuss the temperature dependences of the saturation magnetization, magnetic anisotropy, and VCMA coefficient.

5.3.1 Saturation Magnetization

In the first step, the magnetic moment of the FL is measured by the vibrating sample magnetometer (VSM) using 8*8mm^2 non-patterned samples. Figure 5.3 shows representative out-of-plane minor loops for estimation of the FL-magnetization. One can clearly see a drop in the saturation values at elevated temperatures. Figure 5.3(b) summarizes the FL-magnetization as a function of temperature, where the conversion between the area magnetization and the saturation magnetization is also presented. This conversion takes into account the thickness of the magnetic dead layer (MDL), estimated as 0.7nm in Section 3.3.2, where the effective FL thickness (t_{eff}) is 0.8nm. After subtraction of MDL, the saturation magnetization is $M_{S,FL} = 1447$kA/m at room temperature, and it decreases to 1350kA/m at 400K.

Generally, the temperature dependence of the saturation magnetization fits well with Bloch's law [199]:

$$M_S(T) = M_S(0)\left[1 - \left(\frac{T}{T_C}\right)^{1.5}\right] \tag{5.1}$$

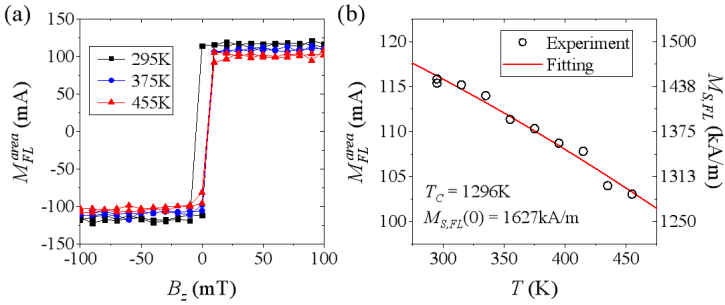

Figure 5.3: *(a) Representative VSM measurements for the free-layer minor loops at different ambient temperatures. (b) Area and saturation magnetization of the free-layer as a function of ambient temperature. Red curve represents the fitting result using Bloch's law equation, showing $M_{S,FL}(0) = 1627kA/m$ and $T_C = 1296K$.*

where $M_S(0)$ is the saturation magnetization at 0K and T_C is the Curie temperature in K (above which the ferromagnetism is vanishing). To obtain a better fitting result, we extend the measurement to 455K. In Figure 5.3(b), we find that the experimental data are fitted well with $M_S(0) = 1627$kA/m and $T_C = 1296$K. In the literature, the $M_S(0)$ and T_C of pure Fe and Co have been reported, with $M_S^{Fe}(0) = 222$emu/g ($\sim$1748kA/m), $T_C^{Fe} = 1043$K, $M_S^{Co}(0) = 164$emu/g ($\sim$1460kA/m, and $T_C^{Co} = 1385$K [202, 207, 208, 209]. Although our measured temperature range (295K$\sim$455K) is relatively narrow compared to T_C, both fitting parameters, $M_S(0)$ and T_C, of our sample are found consistent with these values considering the composition of our CoFeB. Recent studies on CoFeB-based alloys also reported similar values [201, 204].

5.3.2 Tunneling Magneto-Resistance and Coercivity

Moving on to the patterned MTJ, the temperature-dependent properties of the 105nm devices are investigated. The resistance is measured in an out-of-plane magnetic field (B_z), as shown in Figure 5.4(a). The resistance of the parallel state (R_P) is observed to remain unchanged while that for the anti-parallel state (R_{AP}) decreases apparently with increasing temperatures. To interpret the origins of these dependences, one needs to consider both spin-dependent and spin-independent contributions to the resistivity. The spin-dependent component is related to the spin polarization (P), which is reduced at elevated temperatures due to the excitation of magnons and thermally induced magnetic disorder [203, 210]. As the spin polarization is decreased, TMR is also decreased

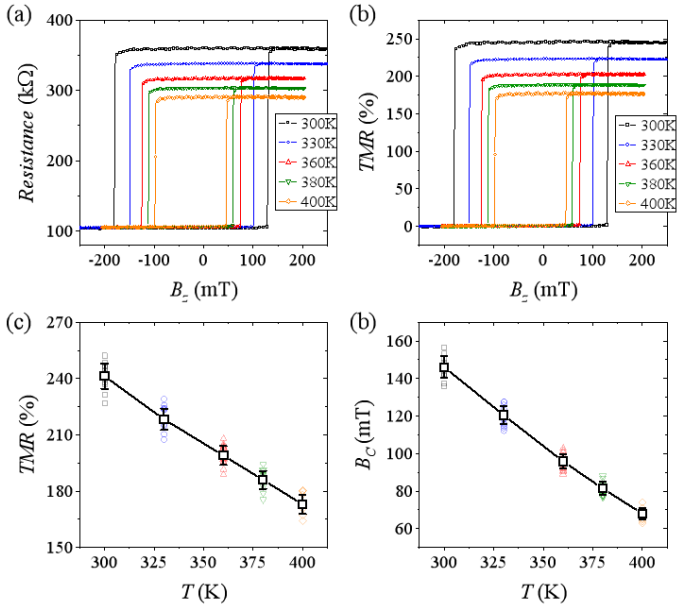

Figure 5.4: *(a) Representative resistance-field hysteresis loops and (b) tunneling magneto-resistance at various ambient temperatures. (c) Tunneling magneto-resistance and (d) coercive fields as a function of ambient temperature for the 105nm devices. Black curves in (c) and (d) show the median values and standard deviation from 15 devices.*

(Equation 1.4: $TMR = \frac{2P^2}{1-P^2}$). For the spin-independent contribution, a electron hopping process via localized states of defects in the tunnel barrier can also lead to a temperature-dependent reduction of the TMR [211].

Besides TMR, the coercive field (B_C) also decreases with increasing temperature, which is resulting from the reduction of anisotropy energy. In the next section, the PMA and thermal stability factors are discussed.

5.3.3 PMA and Thermal Stability Factor

The PMA ($B_{k,eff}$) and thermal stability factor (Δ) are estimated using the magnetic field sweep method (see Section 3.3.5 and Equation 3.7), and their temperature dependences are shown in Figure 5.5. First, the dependence of effective anisotropy field ($B_{k,eff}$) on temperature is mainly attributed to the relative changes in the two contributions: shape anisotropy and interfacial

anisotropy. Equations 5.2 and 5.3 illustrate the calculation of these two terms, with temperature dependences added:

$$K_{eff}(T) = K_d(T) + K_u(T) \tag{5.2}$$

$$\frac{M_S(T)B_{k,eff}(T)}{2} = -\frac{1}{2}\mu_0 M_S^2(T)(D_z - D_{x,y}) + \frac{K_i(T)}{t_{eff}} \tag{5.3}$$

where K_d and K_u are, respectively, the demagnetization energy density and the uni-axial perpendicular anisotropy energy density.

Using the $B_{k,eff}(T)$ obtained from the field sweep method and the $M_S(T)$ obtained from the VSM measurements in the previous section, we calculate the $K_u(T)$ that is induced by both MgO/CoFeB and CoFeB/Ta interfaces ($K_i(T)$). The conversion results are shown in Figure 5.5(b). We observed a median $K_i(25°C)$ of 1186µJ/m^2, in good agreements with the typical MgO/CoFeB/Ta tri-layer systems [83, 212], and it decreases to 979µJ/m^2 at 400K.

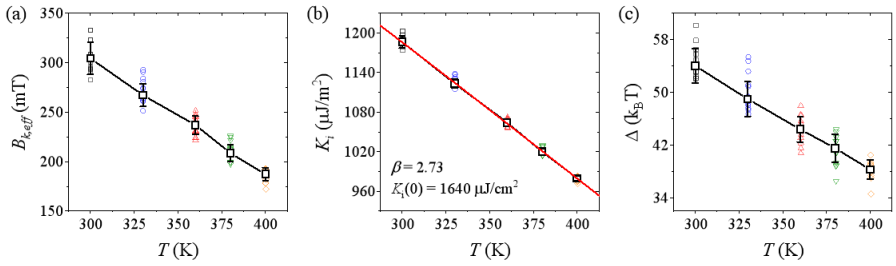

Figure 5.5: *Ambient temperature dependence of the (a) $B_{k,eff}$, (b) K_i, and (c) Δ for the 105nm MTJ1. Black curves show the median values and standard deviation from 15 devices. Red curve indicates the fitting with the empirical power law of $M_S(T)$.*

It has been reported that the dependence of the magnetic properties on temperature can be fitted well with an empirical power law of $M_S(T)$ [201]:

$$\frac{K_i(T)}{K_i(0)} = \left[\frac{M_S(T)}{M_S(0)}\right]^{\beta} = \left[1 - \left(\frac{T}{T_C}\right)^{1.5}\right]^{\beta} \tag{5.4}$$

where the exponent β characterizes the sensitivity of the material parameter to the temperature. Using the T_C obtained from the VSM measurements, we found that the $K_i(T)$ dataset is well fitted with $\beta = 2.73$ and $K_i(0) = 1640$µJ/m^2. Notice that $\beta = 2.73$ is somewhat similar to the prediction from Callen-Callen's theory ($\beta = 3$) for bulk PMA. However, recent studies also

found a leading exponent of $\beta = 2$ in the similar MgO/CoFeB/heavy-metal systems [201, 213, 214]. They all interpreted their experimental observations to the strong degree of spin-orbit interactions. Indeed, the strong SOC also induces PMA when in contact with ferromagnets. In the highly-ordered $L1_0$ phase FePt and CoPt alloys [215, 216], it has been reported with an leading exponent of $\beta = 2$. Because there are still lack of detailed physics regarding the temperature dependence of interfacial anisotropy, we will not further discuss the based on Callen-Callen theory. However, it is worth mentioning that Z. Wen et. al. also pointed out that one may be possible to get some insights to the strength of SOC from the exponent [214]. Perhaps, our FL has a lower strength of SOC owing to the use of Mg sacrificial layer before deposition of the Ta capping layer that suppresses the diffusion of Ta into the CoFeB layer [150], Ta mostly acts as a boron sink to assist CoFeB crystallization during the annealing process [217]. This also reflects on the thermal tolerance of our MTJ that survives 400°C thermal budget, while the magnetic properties in other MgO/CoFeB/Ta systems without sacrificial layers are degrading after annealing at above 300°C [48, 150, 218].

As a second fitting parameter in Equation 3.7, we observe a monotonic decrease in Δ from 54 to 38.3 when the temperature is increased from 300K to 400K. Since the devices under consideration are relatively large compared to the domain nucleation size, a nucleation type reversal is favored such that the temperature dependence of Δ is determined by the exchange stiffness (A_{ex}) and the ambient temperature, i.e. $\Delta(T) \sim \pi^3 A_{ex}(T) t_{eff}/4k_B T$ [44]. Since $A_{ex}(T)$ is found weakly influenced in the temperature range of interest [219], $\Delta(T)$ is mainly governed by the change of ambient temperature.

5.3.4 VCMA Coefficient

Next, the temperature dependence of the VCMA coefficient (ξ) is investigated. We use the magnetic field sweep method at various DC biases to estimate the VCMA slope, i.e. the $\partial B_{k,eff}/\partial V$ parameter. The measurements are exemplified in Figure 5.6. We measure that the $\partial B_{k,eff}/\partial V$ parameter decreases from 40.2mT/V at 300K to 35.6mT/V at 400K. Based on the definition of the VCMA effect, we can convert $\partial B_{k,eff}/\partial V$ to ξ by:

$$\xi(T) = \frac{\mu_0 M_S(T) t_{eff} t_{MgO}}{2} \left[\frac{\partial B_{k,eff}}{\partial V}(T)\right] \tag{5.5}$$

The corresponding reduction in ξ is from 35fJ/Vm to 28.8fJ/Vm. Using $\left[\frac{M_S(T)}{M_S(0)}\right]^{\beta}$ to fit the temperature dependence of the VCMA coefficient, we obtain

a β of 2.88 and a $\xi(0)$ of 49.3fJ/Vm. To interpret such an exponent, we discuss based on the fundamental VCMA mechanisms (Section 2.4.1). The electronic-based VCMA effect has two basic contributions: orbital magnetic moment mechanism (electron doping) and electric quadrupole mechanism (electron re-distribution) [105]. The orbital magnetic moment mechanism is explained by Bruno's model [81], where the magnetic anisotropy originates from the difference between the orbital magnetic moments in the perpendicular direction and the in-plane direction. Electron selective doping to the orbitals changes the moments, thereby contributing to the VCMA effect. On the other hand, the electric quadrupole mechanism is related to the spin-orbit coupling (SOC). When heavy metal is present at the dielectric/ferromagnet interface, the orbital moments are coupled to the spin moments through SOC, and the atomically inhomogeneous electric field causes anisotropic charge distribution and induces an anisotropy in the spin moments. An externally applied electric field can also couple to the electric quadrupole to induce re-distribution of the spin moments, resulting in the second VCMA contribution [91].

Intuitively from the observation of $K_i(T)$, where the interfacial PMA is generated mainly by the MgO/CoFeB interface, we may attribute a major portion of VCMA effect is dominated by the orbital magnetic moment mechanism. This is reasonable since the voltage drops mainly at the MgO barrier, and the electric field only penetrates through the first few layers at the MgO/CoFeB interface, hence the magnetic properties at the MgO/CoFeB interface dominate over the CoFeB/Ta properties to determine the overall temperature dependence of the VCMA effect. Also, because the use of Mg sacrificial layer which suppresses diffusion of Ta atom to the MgO/CoFeB interface, it is likely that the quadrupole mechanism has only minor contribution to the overall VCMA effect. Under these circumstances, we believe that $\beta = 2.88$ is majorly led by the orbital magnetic moment mechanism. In a similar MgO/CoFeB/Ta system, a $\beta = 2.83$ has also been reported [201]. However, a $\beta = 2$ has yet been observed in another MgO/Co2FeAl/Ru system [214]. The actual situation of the VCMA effect and its temperature dependence is rather complex, and more detailed understandings would require *ab* initio calculations.

5.4 Operation Properties

From the above measurements, we found that $\xi(T)$ is more susceptible to temperature variation than $K_i(T)$. As suggested by Ref. [201], this would cause a rise in the switching voltage in order to compensate for the loss in the $\xi(T)/K_i(T)$ figure of merit when the operating temperature is increased. However, we also observe that $B_{k,eff}(T)$ is more vulnerable than the $\frac{\partial B_{k,eff}}{\partial V}(T)$

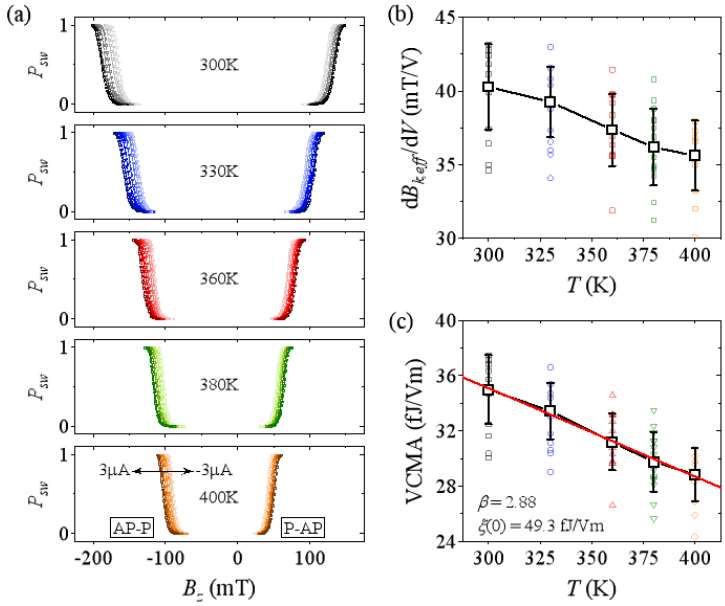

Figure 5.6: *(a) Representative magnetic field switching distributions under various DC gate biases (between 3μA and -3μA) and ambient temperatures. Ambient temperature dependence of the (b) VCMA slope and (c) VCMA coefficient estimated by fitting the distributions in (a). Black curves in (b) and (c) show the median values and standard deviation from 15 devices.*

parameter, which should be reducing the switching voltage with increasing temperature.

To validate how the above temperature dependences are affecting the actual writing properties, we use MTJ2 devices with a 1.7nm FL to perform voltage-induced magnetization reversal, presuming that the temperature-related parameters (β and T_C) are not significantly changed by the FL thickness of interest. The $B_{k,eff}$ and K_i of these devices are estimated as 75mT and 1310μJ/m^2 at 300K.

5.4.1 Critical VCMA Switching Voltage

We investigate the critical switching voltage (V_c). Notice that there always exists discrepancy between the simulation speed and experimental speed, we extract V_c experimentally with a semi-quantitative manner. The procedure to

extract V_c is explained as the following. First, similar to the method explained in Chapter 3-Section 3.4.4, we systematically assess the precession period (t_{prec}) at different temperature and B_x conditions, and we convert the switching period to switching speed ($f_s = 2/t_{prec}$), as shown in Figure 5.7(a) and (b). Here, the switching voltages at $B_x = 20$mT (10mT) are not measurable at above 330K (360K) due to the loss of PMA and retention, which is also constrained by the current VCMA efficiency that devices with stronger PMA could not be switched within the breakdown limit. Nevertheless, it is shown that V_p progressively accelerates f_s.

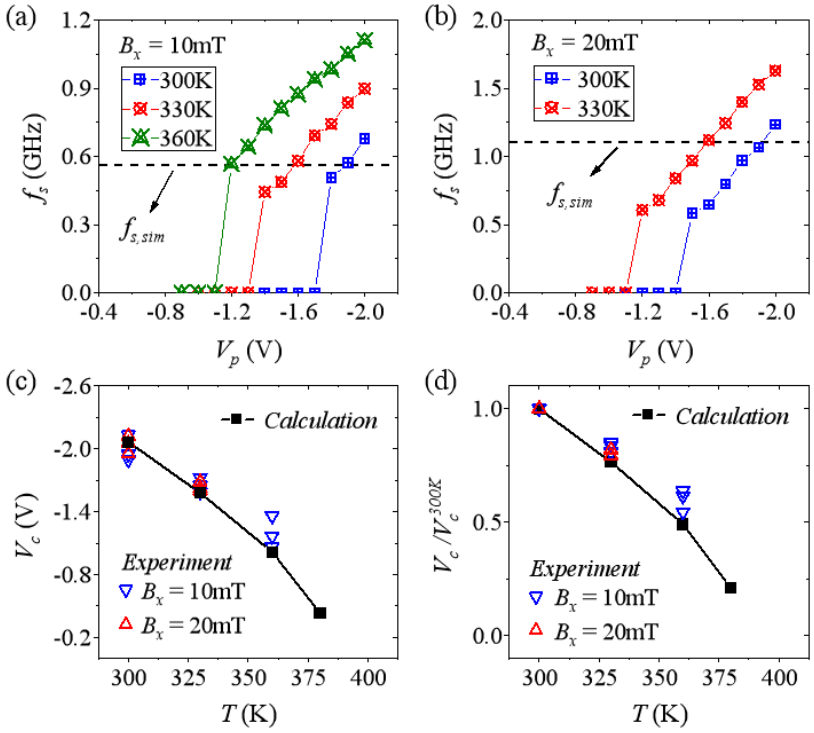

Figure 5.7: *Switching speed (f_s) as a function of pulse voltage (V_p) at various ambient temperatures for MTJ2, with B_x = (a) 10mT and (b) 20mT. Black dashed line indicate the switching speed obtained by simulation. (c) Critical VCMA switching voltage and (d) normalized critical switching voltage as a function of ambient temperature. Black curves show the calculated values using the temperature-related parameters (T_C and βs) obtained from MTJ1.*

Subsequently, to identify V_c, we use macro-spin simulation to predict f_s for

each temperature and B_x, by considering the temperature dependence of K_i and VCMA slope. The damping constant is assumed to be 0.2, as explained in Section 3.4.4. The thermal fluctuation field is not included in the simulation. From the simulation, we estimate the switching frequency as 0.57 GHz and 1.1GHz under B_x = 10mT and B_x = 20mT, respectively, and these are weakly dependent on temperature. We then acquire the intersection between the experimental f_s and simulated $f_{s,sim}$, which correspondingly gives the critical switching voltage. Figure 5.7(c) summarizes V_c as a function of temperature for B_x = 10mT and 20mT. For both B_x conditions, V_c is decreasing with increasing temperature, which we attribute to the faster drop in $B_{k,eff}(T)$ compared to the $\frac{\partial B_{k,eff}}{\partial V}(T)$ parameter. Our results suggest that even though $\xi(T)$ is more susceptible to the temperature variation compared to $K_i(T)$, the actual write voltage is rather determined by $B_{k,eff}(T)$ and $\frac{\partial B_{k,eff}}{\partial V}(T)$ parameters, since $B_{k,eff}$ controls the easy axis of the magnetization and the $\partial B_{k,eff}/\partial V$ parameter determines the required voltage to switch the magnetization between PMA and in-plane anisotropy.

In addition, we apply the temperature-related parameters (T_C and βs) obtained from MTJ1 to calculate the required V_c for MTJ2, and we observe a good agreement with our experimental observations. This supports our hypothesis that β and T_C are consistent in both stacks.

5.4.2 Breakdown Voltage and Write Margin

In the final step, we perform the DC ramped voltage stress (RVS) method with an 80mV/s ramp rate to evaluate the breakdown voltage (V_{BD}) at different temperatures for MTJ2. Figure 5.8 presents the V_{BD} distributions from 80 devices at each temperature. It shows that the 63% V_{BD} decreases from 2.06V to 1.68V, which is due to the temperature acceleration. Recent studies have revealed that current-induced self-heating is negligible in such an MTJ with a high resistance-area product [220]. The lower degradation rate of $V_{BD}(T)$ ($\sim$3.8mV/K) than $V_c(T)$ ($\sim$36.6mV/K) increases the write margin at higher operating temperatures and can mitigate the risk of MTJ degradation.

5.5 Summary

In this chapter, we studied the impact of ambient temperature on the magnetic and switching properties of the voltage-controlled perpendicular magnetic tunnel junction devices. For the magnetic properties, the saturation magnetization (M_S), interfacial anisotropy (K_i), and VCMA coefficient (ξ) were investigated at

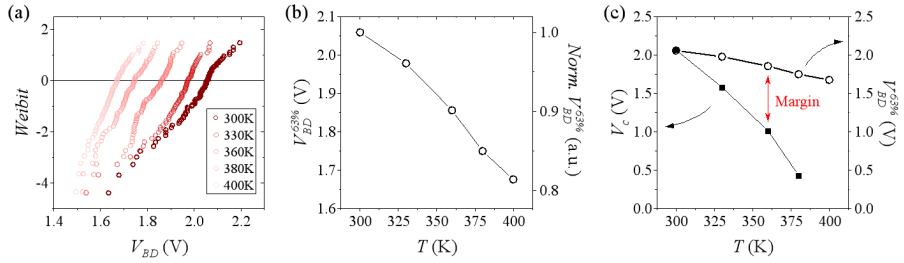

Figure 5.8: *(a) RVS breakdown voltage distributions for different ambient temperatures. (b) 63% breakdown voltage ($V_{BD}^{63\%}$) and its normalized value as a function of ambient temperature. (c) Comparison between $V_{BD}^{63\%}$ and V_c as a function of ambient temperature, showing wider write voltage margins at elevated temperatures.*

different temperatures. From the $M_S(T)$ dependence, we fitted with Bloch's law to obtain $M_S(0) = 1627$ kA/m and $T_C = 1296$K, which were in agreement with earlier reported values. Later, the $K_i(T)$ and $\xi(T)$ were fitted with the power law of $M_S(T)$. We acquired the exponent (β), which represents the temperature sensitivity, for these properties. A $\beta = 2.73$ was observed for $K_i(T)$, which implied a major contribution of perpendicular magnetic anisotropy (PMA) from the MgO/CoFeB interface with a dominant β of 3 and a minor contribution from the CoFeB/Ta interface where the spin-orbit coupling (SOC) mediated PMA has a $\beta = 2$. Similarly, A $\beta = 2.88$ was measured for $\xi(T)$, indicating that the VCMA effect in our devices mostly originated from the orbital magnetic moment mechanism. Indeed, since the electric field dropped at the MgO, only the orbits in the vicinity of the MgO/CoFeB interface could provide a voltage effect. In addition, $\beta = 2.88$ also suggested the absence of Ta at the MgO/CoFeB.

In the second step, we experimentally examined the critical switching voltage (V_c) for VCMA-induced magnetization reversal. We observed an around 50% reduction in V_c when increasing the ambient temperature from 300K to 360K. We attributed this behavior to the relative changes in the effective anisotropy field ($B_{k,eff}$) and the VCMA slope ($\partial B_{k,eff}/\partial V$). On the other hand, the breakdown voltage (V_{BD}) was less susceptible to the temperature variation, with a only 20% drop at 400K compared to 300K, making the write voltage margin larger at elevated temperatures.

These studies showed that VCMA devices could adapt high-temperature operations, and the relatively stable VCMA slope and V_{BD} promised mitigation of degradation issues by a larger write voltage margin at elevated temperatures. Future research and development should focus on stack engineering to boost the

VCMA coefficient, in order to allow for VCMA writing of high PMA devices as well as maintaining the retention.

Chapter 6

Hybrid MRAM: Voltage-Gate assisted Spin-Orbit Torque

6.1 Introduction

Non-volatile memory (NVM) is believed to address the large stand-by power issues in advanced technology nodes. Among proposed candidates, magnetic random access memory (MRAM) is attracting great attention due to its CMOS process compatibility, high density, low power, and relatively fast speed [136]. Recent progress has optimized spin-transfer torque (STT)-MRAM for embedded last-level cache (LLC), micro control unit (MCU), and eFlash applications [18, 181, 197, 221], with first commercial products beginning to appear in the market. Despite its excellent performance, current STT-MRAM technology cannot be implemented in the higher memory hierarchy, such as register and L1/2 cache memory, due to the significant incubation delay and voltage breakdown/speed trade-off, which inhibits reliable programming below 5ns [182].

To solve the limitations in STT switching scheme, two alternative switching mechanisms have been proposed. One is the voltage control of magnetic anisotropy (VCMA) effect. In Chapters 3 and 4, we have studied both the conventional and the new deterministic VCMA writing schemes. These unipolar, voltage-driven, switching schemes manifest ultra-low energy consumption (fJ) at ns-scaled magnetization reversal speeds. The other switching mechanism is called the spin-orbit torque (SOT). In this chapter, we will first review the switching mechanism of SOT, and then the challenges of SOT-MRAM will be stated. To improve the writing scheme, we study a hybrid switching

mechanism, namely ***Voltage-Gate assisted Spin-Orbit Torque (VGSOT)***, by combining the advantages from both VCMA and SOT. We will demonstrate that VGSOT can effectively mitigate the challenges that both VCMA-MRAM and SOT-MRAM facing at the advanced technology nodes: insufficient efficiency. Based on the learning, we also propose multiple criteria to provide the guide for device scaling.

Results discussed in this chapter will be submitted to **Y. C. Wu et al., PRA (2020)** [222].

6.2 SOT Switching and SOT-MRAM

6.2.1 SOT Switching of Perpendicular Magnetization

Spin-orbit torques are the transfer of orbital angular momentum from the lattice to the spin system, which, in general, are mediated by two current-induced spin current sources: ***Spin Hall Effect*** and ***Rashba Effect*** (see also Section 1.2.4 for a brief introduction) [64]. These two phenomena generate a damping-like torque T_{DL} and a field-like torque T_{FL} on the adjacent magnetization. The contributions of the two SOT sources to the two torques are still in the argument in literature [223, 224], but in a simplified scenario one can comprehend as follow: T_{DL} is attributed to spin Hall effect [225] and T_{FL} is attributed to Rashba effect [226]. To date, the SOT-induced magnetization switching is understood as: T_{DL} triggers magnetization reversal and T_{FL} accelerates it [227].

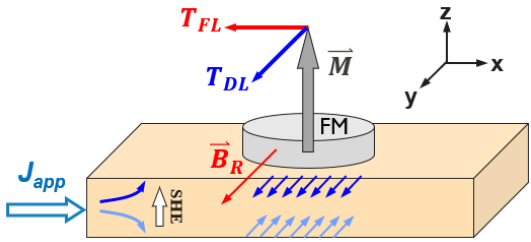

Figure 6.1: *Schematic of the spin-orbit torques applied on the perpendicular magnetization of the adjacent ferromagnet.*

The magnetization dynamics under SOT current injection can be expressed as:

$$\frac{d\vec{m}}{dt} = -\gamma\vec{m} \times \vec{B}_{eff} + \alpha\vec{m} \times \frac{d\vec{m}}{dt} + \gamma T_{DL} + \gamma T_{DL} \tag{6.1}$$

with

$$T_{DL} = \tau_{DL}\vec{m} \times \vec{m} \times \vec{y} \tag{6.2}$$

$$T_{FL} = \gamma\tau_{FL}\vec{m} \times \vec{y} \tag{6.3}$$

The τ_{DL} and τ_{FL} are the longitudinal and transverse component of the spin-orbit torques, respectively. Their amplitudes are expressed as:

$$\tau_{DL} = \frac{\hbar}{2e}\frac{\theta_{SH}}{M_S t_{FL}} J_{app} \tag{6.4}$$

$$\tau_{FL} = \frac{\hbar}{2e}\frac{\theta_{R}}{M_S t_{FL}} J_{app} \tag{6.5}$$

where J_{app} is the applied current density in ±x-direction, θ_{SH} is the spin Hall angle, and θ_R is the Rashba coefficient. When solving Equation 6.1, and only considering the damping-like torque which triggers the switching, one can derive:

$$\frac{d\vec{m}}{dt} = -\frac{\gamma}{1+\alpha^2}\vec{m} \times \left(\vec{B}_{eff} + \alpha\tau_{DL}\hat{y}\right) - \frac{\gamma}{1+\alpha^2}\vec{m} \times \left[\vec{m} \times \left(\alpha\vec{B}_{eff} - \tau_{DL}\hat{y}\right)\right] \tag{6.6}$$

$$= -\frac{\gamma}{1+\alpha^2}\vec{m} \times \left(\vec{B}_k m_z\hat{z} + \vec{B}_{demag} + \vec{B}_x + \alpha\tau_{DL}\hat{y}\right)$$

$$- \frac{\gamma}{1+\alpha^2}\vec{m} \times \left[\vec{m} \times \left(\alpha\vec{B}_k m_z\hat{z} + \alpha\vec{B}_{demag} + \alpha\vec{B}_x - \tau_{DL}\hat{y}\right)\right] \tag{6.7}$$

where $\vec{B}_k$ is the perpendicular anisotropy. The introduction of $\vec{B}_x$ ensures deterministic switching after cutting off the current pulse [223]. The second term on the right-hand side of Equation 6.7 describes the effective damping effect. Here, the intrinsic damping effect is proportional to the perpendicular anisotropy in the ±z-direction ($\alpha\vec{B}_k m_z\hat{z}$), whereas the damping-like torque from the SHE effect is in the ±y-direction. This SOT torque geometry makes SOT switching very efficient because τ_{DL} is not collinear, and does not compete, with $\vec{B}_k\hat{z}$. The initial incubation time for SOT switching is therefore considerably small compared to the conventional STT switching [228] (STT directly competes with the intrinsic damping because the spin-polarized current from the reference-layer is also in the ±z-direction). When performing macro-spin simulations, one can directly see the benefit of SOT switching: the magnetization takes only half of a precession before reversal for SOT switching, while it takes several precessions in the case of STT switching [229], as shown in Figure 6.2.

6.2.2 SOT-MRAM

Based on the scheme of SOT, the three-terminal SOT-MRAM has been proposed as the candidate of the next generation of MRAM. The unit cell consists of a

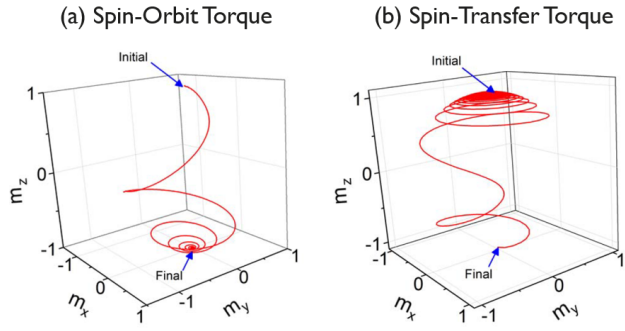

Figure 6.2: *Switching trajectory of the perpendicular magnetization by (a) SOT and (b) STT. Reproduced from Ref. [229].*

SOT track at the bottom, with two bottom electrodes connected on the two sides, and a top-pinned magnetic tunnel junction is sitting on top of the SOT track, as shown in Figure 6.3. By injecting in-plane current in an adjacent SOT layer, the FL magnetization absorbs the spin current and is tilted toward $+y$ or $-y$ depending on the direction of current and the spin Hall angle. To ensure deterministic switching, an in-plane magnetic field (B_x) is applied along the current flowing direction ($+x$ or $-x$) [223]. After turning off the applied current, the FL magnetization will be switched upward or downward depending on the magnetic field direction. This writing mechanism shows energy-efficient and reliable sub-ns writing capabilities [19, 228]. Furthermore, the three-terminal cell structure can separate the read and write path, which improves the endurance of the SOT-MRAM compared to the two-terminal STT-MRAM.

However, SOT-MRAM also presents technological challenges. First, it requires the presence of B_x to ensure deterministic switching. Various credible solutions have been proposed and demonstrated, such as integrating an embedded magnet as a field generator [185, 113], making use of exchange bias by direct coupling with an anti-ferromagnet [230, 231], or assisting reversal with STT [232]. Second, in order to operate such three-terminal devices, two transistors must be incorporated into a unit cell. One transistor is responsible for writing the FL through the SOT line and the other is in charge of reading the memory state through the MTJ. This 2T1MTJ cell structure limits the array density. Third, although the orthogonal spin orientation of SOT allows much shorter writing duration than STT, the SOT write current (density) remains one order of magnitude larger than that for STT-MRAM [229], which imposes a larger transistor to accommodate its write current. Although the required SOT switching current can be scaled by the SOT efficiency, it will become unrealistic

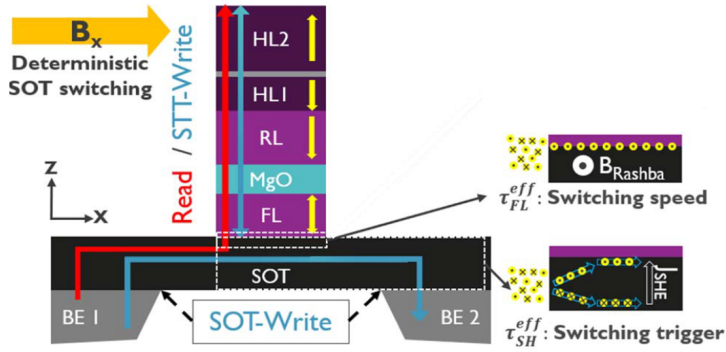

Figure 6.3: *Schematic of the unit SOT-MRAM cell and the SOT write mechanism. Reproduced from Ref. [227].*

when scaling down the MTJ size while maintaining its non-volatility. In the next section, we specifically discuss the challenging efficiencies for both SOT-MRAM and VCMA-MRAM.

6.2.3 Challenging Efficiencies in SOT- and VCMA-MRAM

The volume of the FL is one of the deterministic parameters to define the thermal stability factor (Δ, Equation 1.6) and the retention of an MTJ device. When scaling down the MTJ size, one inevitably has to enhance the anisotropy to maintain its non-volatility feature. The SOT switching current, however, does not scale with the volume of the FL, it rather scales with the cross-section area only (Equation 1.11):

$$\Delta = \frac{M_S B_{k,eff} A_{FL} t_{FL}}{2k_B T} = \frac{\pi M_S B_{k,eff} D_{FL} t_{FL}}{8k_B T} \quad (Eq.\ 1.6)$$

$$I_{c0} = \frac{2e}{\hbar} \frac{M_S t_{FL}}{\theta_{SH}} \left(\frac{B_{k,eff}}{2} - \frac{B_x}{2} \right) t_{SOT} w_{SOT} \quad (Eq.\ 1.11)$$

where $A_{FL} = \pi D^2/4$ is the plane area of the free-layer, with D the MTJ diameter. In Equation 1.11, I_{c0} is proportional to the cross-section area of the FL if the MTJ diameter is the same as the SOT track width (w_{SOT}).

By combining Equations 1.6 and 1.11, we derive the equation that allows for estimation of the SOT current linking to the thermal stability factor and the MTJ size:

$$I_{sw} \sim \frac{8ek_B T}{\pi\hbar} \frac{w_{SOT} t_{SOT} \Delta}{\theta_{SH} D^2} = \frac{8ek_B T}{\pi\hbar} \frac{t_{SOT} \Delta}{\theta_{SH} D} \tag{6.8}$$

On the right side of Equation 6.8, it is possible to further simplify the equation by having a SOT track width (w_{SOT}) that is equal to the MTJ diameter. Further, to calculate the targeted SOT current at a targeted speed, size and Δ, we use the reference values obtained at 1ns from the state-of-the-art SOT-pMTJ: $\Delta^{ref.}(D = 60nm) = 51$, $I_{sw}^{ref.}(@1ns) = 331\mu A$, and $|\theta_{SH}^{ref.}| = 0.32$ (more information see Ref. [19]).

$$\frac{I_{sw}^{tar.}}{I_{sw}^{ref.}} = \frac{\Delta^{tar.}}{\Delta^{ref.}} \frac{\theta_{SH}^{ref.} D^{ref.}}{\theta_{SH}^{tar.} D^{tar.}} \tag{6.9}$$

In Figure 6.4, we target $\Delta^{tar.} = 60$ for all MTJ size to meet the requirement for embedded memory applications. It shows that regardless of the targeted current range (25-130μA), the required $\theta_{SH}^{tar.}$ are too high to be reached, making scaling of SOT-MRAM infeasible. Table 6.1 lists the typical θ_{SH} values from the materials that are commonly used in CMOS technology. Among the common metals, tungsten (W) has the largest reported efficiency of 0.3-0.4 [233, 234]. Note that new exotic materials such as topological insulators (TI), e.g. BiSe and BiSbTe [235, 236], have $\theta_{SH} > 1$, but these materials are to date too complex to be integrated with pMTJs using the CMOS process. For comparison, a recent STT-MRAM has shown a 96µA switching current at 1ns or a 34µA at 10ns, with $\Delta \sim 80$ for the 30nm MTJ [174]. Therefore, additional improvements in SOT writing must be achieved to make SOT-MRAM competitive with STT-MRAM in terms of size and current.

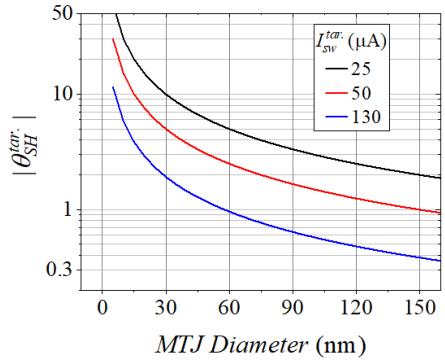

Figure 6.4: *SOT efficiency as a function of MTJ diameter for different targeting switching currents.*

For the VCMA-MRAM, similarly, large VCMA coefficients (ξ) are also mandatory to avoid compromising the data retention in scaled MTJ. By

Table 6.1: *The spin Hall angle of different materials.*

Material	θ_{SH}	Reference
W	0.3-0.4	[233, 234]
Pt	0.08-0.12	[237, 238]
Ta	0.15	[57]
Pd	0.008-0.01	[239, 240]
IrMn	0.06	[241, 242]
PtMn	0.24	[243]
TI	1.4-4.25	[235, 236]

combining the macro-spin estimation equations for Δ (Equation 1.6) and ξ (Equation 3.11), we obtain an equivalent equation for prediction of the targeting VCMA coefficient ($\xi^{tar.}$) at different MTJ sizes:

$$\xi^{tar.} = \frac{M_{S,FL} t_{FL} t_{MgO}}{2} \frac{\partial B_{k,eff}}{\partial V} \quad (Eq.\ 3.11)$$

$$\xi^{tar.} = \frac{4 k_B T}{\pi} \frac{t_{MgO} \Delta}{D^2 V_{max}} \tag{6.10}$$

where V_{max} is the maximum supply voltage depending on the technology nodes. For example, V_{max} at the 10nm node is 0.7V for the embedded memory applications or 1.2V for the stand-alone memory applications [244]. As shown in Figure 6.5(a), a $\xi > 8000$fJ/Vm is required for sub-30nm MTJ, if the supplied voltage is limited to 0.7V. Further, while the in-plane field is mandatory for the precessional switching, it reduces the stability of the FL at the same time. Hence, an enhancement in PMA is necessary to avoid compensating Δ, thereby increasing the required VCMA coefficient, as exemplified in Figure 6.5(b) for the 30nm MTJ.

Although there are reports showing $\xi > 1000$fJ/Vm both experimentally and theoretically, those are either slow ionic effects [121, 122] or combined with oxides other than MgO [188, 189]. Typical values in pMTJs are to date 30-70fJ/Vm at the device level [147].

6.3 VGSOT-MRAM

To overcome those challenges in SOT-MRAM and VCMA-MRAM, a hybrid device combining the advantages of VCMA and SOT was proposed [70, 173],

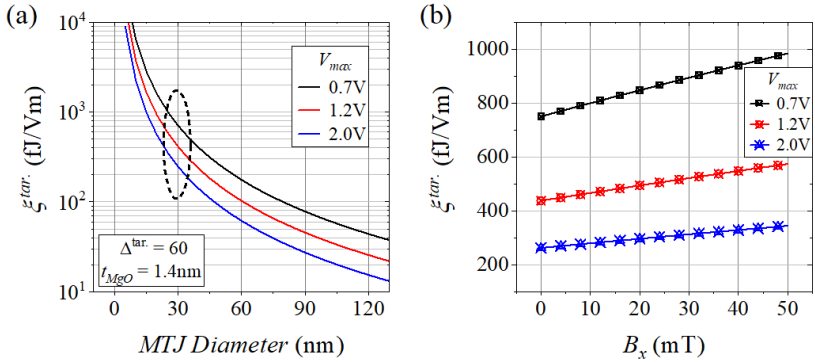

Figure 6.5: *(a) VCMA coefficient requirement as a function of MTJ diameter for a targeted $\Delta = 60$ and $t_{MgO} = 1.4$nm. (b) VCMA coefficient requirement as a function of in-plane field for the 30nm MTJ. Calculations for both figures are based on the macro-spin assumption.*

namely voltage-gate assisted spin-orbit torque (VGSOT)-MRAM. The cell structure is shown in Figure 6.6.

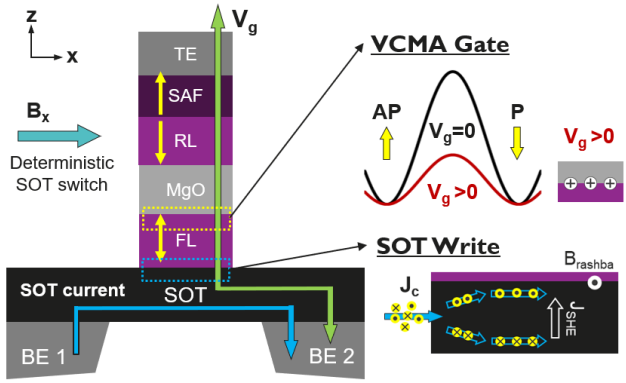

Figure 6.6: *Illustration of the VGSOT writing scheme. A positive VCMA top gate induces electron accumulation at the FL/MgO interface, which lowers the PMA of the FL and results in SOT switching with reduced current. The VCMA gate also enables bit-cell selectivity in a multi-pillar structure (See Figure 6.7).*

6.3.1 Concept, Purpose, and Benefit

In the VGSOT cell concept, VCMA acts as an assisting effect, while SOT is responsible for switching the FL magnetization. The main difference between the conventional SOT cell and the VGSOT cell is the MgO thickness. In order to make use of the VCMA effect, the MgO barrier (and the resistance-area product) of the VGSOT cell is made thicker than that of the conventional SOT cell, which suppresses current tunneling through MTJ, and thereby reducing the STT effect. This hybrid switching mechanism brings the following new features and benefits to SOT-MRAMs.

SOT Switching Current Reduction

The VCMA effect instantly modifies the perpendicular magnetic anisotropy field ($B_{k,eff}$) of the FL when a voltage is applied across the MTJ, and the SOT switching current can be re-calculated as:

$$I_{sw} \sim \frac{2eM_S t_{FL}}{\hbar\theta_{SH}} \left(\frac{B_{k,eff}}{2} - \frac{\xi V_g}{M_S t_{FL} t_{MgO}} - \frac{B_x}{\sqrt{2}} \right) w_{SOT} t_{SOT} \tag{6.11}$$

In the case of a normal VCMA effect ($\xi > 0$), a positive top gate voltage ($V_g > 0$) induces electron accumulation at the FL/MgO interface to reduce the PMA, thereby reducing the SOT switching current.

Bit-Cell Selectivity and Cell-Size Reduction

The conventional SOT-MRAM has a three-terminal structure, where the unit cell is made up of two transistors and one MTJ. One transistor is connected to the SOT track to supply the SOT switching current, and another transistor located on top of the MTJ is being used to read the MTJ state [Figure 6.7(a)]. Such 2T1MTJ structure limits the array density.

Applying a VCMA gate can enable a multi-pillar structure. As shown in Figure 6.7(b), multiple MTJs share a single SOT line, and the effective cell structure becomes (n+1)TnMTJ. The ideal cell size can be optimized to $8F^2$, similar to that of the cross-bar STT-MRAM. The gate voltage then acts as a cell selector, and only the selected cell can be switched with a reduced SOT current. Here, we define the selectivity (i_{sw}) as:

$$i_{sw} = \frac{I_{sw}(V_g > 0)}{I_{sw}(V_g = 0)} = \frac{\frac{B_{k,eff}}{2} - \frac{\xi V_g}{M_S t_{FL} t_{MgO}} - \frac{B_x}{\sqrt{2}}}{\frac{B_{k,eff}}{2} - \frac{B_x}{\sqrt{2}}} < 1 \tag{6.12}$$

where a smaller i_{sw} ensures good selectivity along a SOT line.

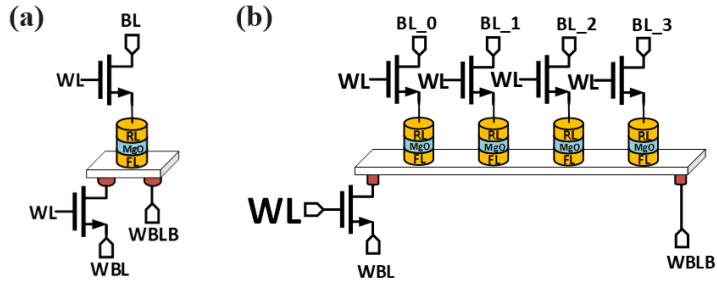

Figure 6.7: *Schematics of (a) the single-cell SOT-MRAM and (b) the multi-pillar VGSOT-MRAM with 4 MTJs on one SOT track (courtesy of M. Gupta and M. Perumkunnil).*

Disturbance-Free Reading

Thanks to the uni-polar VCMA effect, the VGSOT cell can achieve high-speed reading without read-disturbance. For $V_g < 0$, the FL-PMA is enhanced such that it is more stable against thermal agitation or potential STT disturbance. Figure 6.8 exemplifies a read-disturbance simulation [194]. The read error rapidly rises and converges to 50% at positive biases due to the loss of PMA and data retention. Oppositely, it is largely suppressed by negative biases.

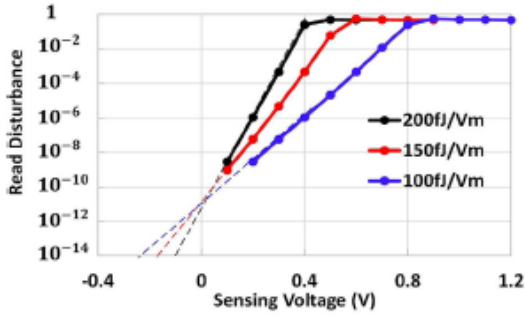

Figure 6.8: *Reduction of reading disturbance using a negative sensing voltage. Reprinted from [194].*

6.3.2 Status of VGSOT-MRAM

VGSOT-MTJ proof of concept has been firstly established in the industry with an in-plane MTJ [70], where switching current reduction has been demonstrated [70, 173]. The claim of a high VCMA effect in in-plane technologies continues the interests in in-plane devices. Indeed, the experimental records on high VCMA coefficients were reported using a high-strained in-plane free-layer, with ξ over 1000fJ/Vm [170]. However, strain control remains crucial to the VCMA properties and may not necessarily bring benefit to the VCMA coefficient improvement [245]. Further, in-plane MTJ technology will eventually face issues regarding size scaling and array density. Only until recently, the first demonstration of VGSOT switching on perpendicularly magnetized free-layer was reported using a tri-layer Hall-bar structure in the laboratory [231]. Not only the switching current reduction was demonstrated, but also the feasibility of combining field-free switching using the in-plane exchange bias provided by the IrMn SOT track.

Table 6.2: *Recent progress on VGSOT development.*

Year	Orientation	Structure/ Size	SOT layer	θ_{SH}^{eff}	VCMA (fJ/Vm)	TMR (%)	Ref.
2016	In-Plane	MTJ Device 80*240nm^2	Ta	0.13	30	138	[70]
2017	In-Plane	MTJ Device 85*255nm^2	Ta	0.18	30	130	[173]
2019	In-Plane	MTJ Device 51*71nm^2	-	-	9	65	[245]
2019	Perpendicular	Tri-layer Hall-bar	IrMn	0.25	35	-	[231]

All the above-mentioned studies are resumed in Table 6.2. To date, a full study of VGSOT writing of integrated pMTJ devices has not yet been performed with 300mm CMOS compatible processes. This is what we will examine and discuss in this chapter.

6.4 VGSOT Study on 300mm Integrated pMTJ

6.4.1 MTJ Preparation and Experimental Setup

To conduct the study, a 300°C annealed top-pinned pMTJ is integrated with imec's 300mm SOT-MRAM platform [19]. Figure 6.9(a) shows the transmission electron microscopy (TEM) image of the standard SOT cell and the pMTJ materials stack for the VGSOT studies. From the bottom, a tungsten (W) SOT track connects the two sides with two bottom electrodes (BE). On top of it is a top-pinned pMTJ, with a 1nm CoFeB free-layer (FL). The MgO tunnel barrier is 1.7nm thick with a resistance-area (RA) products of $\sim$5k$\Omega\cdot\mu m^2$, aiming to suppress the STT effect through the MTJ stack. The reference-layer (RL) is CoFeB, which is ferromagnetically coupled to the lower synthetic anti-ferromagnet (SAF) through an RL-spacer. Then the RL multilayer is anti-ferromagnetically coupled to the $[Co/Pt]_x$ multilayer-based upper synthetic anti-ferromagnet (SAF) by a Ru spacer. Finally, the MTJ is capped with Ta/Ru capping layers. After deposition, the stack is annealed at 300°C for 30 minutes in vacuum in a 2T out-of-plane magnetic field. Then, the MTJ is patterned into circular pillars using 193nm immersion lithography and ion beam etch (IBE), with a specific etch-stop condition to leave the W intact. In the end, the W-SOT track is etched into 190nm in width, and its resistivity is 120$\mu\Omega\cdot$cm resulting in a $\sim$320Ω SOT track resistance.

To characterize the patterned devices, we set up an electrical test scheme shown in Figure 6.9(b), which allows DC and pulsed measurements for SOT and gate channels with controllable voltages (V_{SOT} & V_g), durations ($t_{p,SOT}$ & $t_{p,g}$), and delays. The Labview program used to control this electrical setup automatically add $0.5V_{SOT}$ to the gate voltage before communicating with the pulse generator, so FL experiences a constant V_g for all V_{SOT} at any desired V_g.

6.4.2 Device Fundamental Properties

In Figure 6.10, the fundamental properties of the devices are measured as a function of the electrical dimension (eCD), ranging from 80nm to 150nm. We estimate a median tunneling magneto-resistance (TMR) of 120%, and a coercive field (B_C) of 40mT that decreases to 25mT in the smallest devices. Surprisingly, compared to imec's reference devices in the previous works [185], we notice that simply increasing the MgO barrier thickness lowers B_C. This can potentially be attributed to the MgO deposition conditions, and it can be resolved by stack engineering. Using the magnetic field switching distribution method [140], as exemplified in Figure 6.10(d), we estimate a median PMA field ($B_{k,eff}$) of

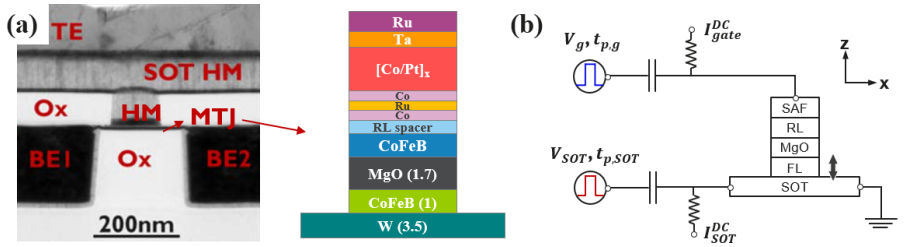

Figure 6.9: *(a) Cross-section TEM image of the imec 300mm SOT-MRAM platform (reproduced from Ref. [19]) and the schematic of the pMTJ stack used in this chapter. (b) Schematic of the electrical setup for VGSOT measurements. Both SOT and gate channels have controllable DC/pulsed voltages (V_{SOT} & V_g), durations ($t_{p,SOT}$ & $t_{p,g}$), and delays.*

70mT, independent of eCD, and a thermal stability factor (Δ) increasing with eCD from 35 to 50 k_BT.

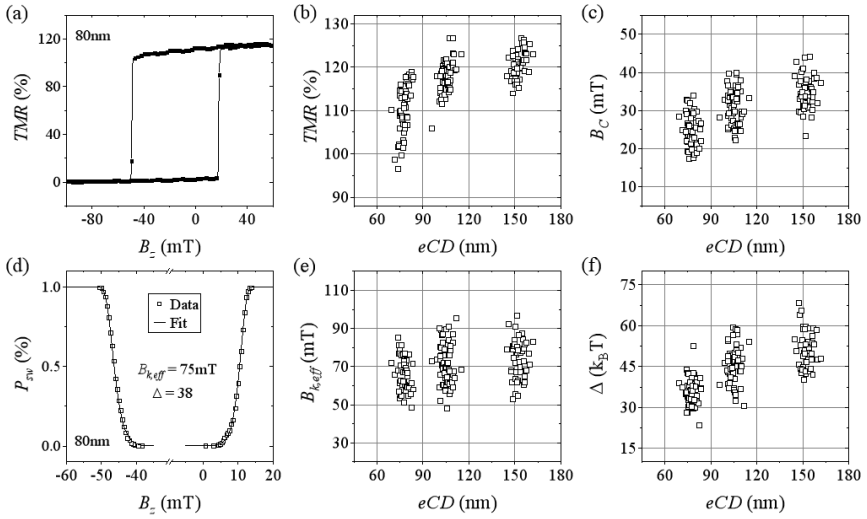

Figure 6.10: *(a) Representative TMR hysteresis loop of an 80nm pMTJ device. (b,c) TMR and coercive field (B_C) as a function of the electrical dimension (eCD). (d) Representative magnetic field switching probability curve to estimate effective anisotropy field ($B_{k,eff}$) and thermal stability factor (Δ) for an 80nm device. (e,f) $B_{k,eff}$ and Δ as a function of eCD.*

6.4.3 SOT Switching

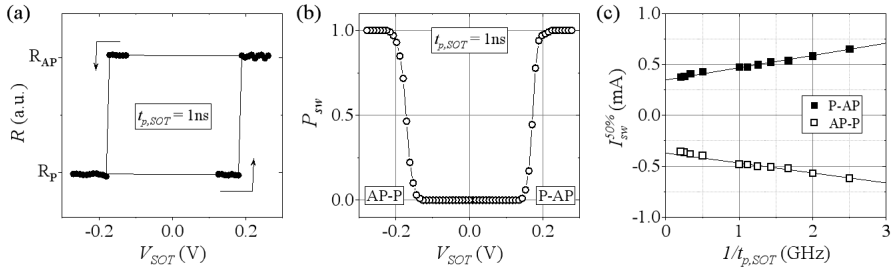

Figure 6.11: *(a) MTJ resistance and (b) switching probability as a function of SOT voltage, with a pulse duration of 1ns. (c) Critical SOT switching current at P_{sw} = 50% as a function of $1/t_{p,SOT}$, showing typical linear scaling.*

In the following, we discuss the switching results obtained from devices with eCD $\sim$ 80nm sitting on top of 190nm wide SOT tracks, with the SOT resistance $R_{SOT} \sim 320\Omega$. All measurements are performed at B_x = 10mT. The RL/SAF stray field is compensated by an external z-field ($\sim$ -15mT). Figure 6.11(a) and (b) show the typical SOT switching and probability curve as a function of SOT pulsed voltage (V_{SOT}) at $t_{p,SOT}$ = 1ns. We define the critical switching voltage at P_{sw} = 50% and convert it to SOT switching current ($I_{sw}^{50\%}$). When plotting $I_{sw}^{50\%}$ as a function of $1/t_{p,SOT}$, we remark a typical linear scaling in the GHz regime [Figure 6.11(c)] [246]. The intercept at 0 GHz indicates the intrinsic critical switching current (I_{c0}). The slope q is the effective charge parameter which represents the number of electrons needed to be pumped into the system before a reversal occurring, which describes the efficiency of angular momentum transferring from the current to the spin system [246]. The relationship of the SOT current can therefore be expressed as:

$$I_{sw} = I_{c0} + \frac{q}{t_p} \tag{6.13}$$

Here, we obtain an average intrinsic critical switching current (I_{c0}^{avg}) of the two switching directions I_{c0}^{avg} = 0.32mA, and $q^{avg} = 1.35 \times 10^{-13}$C.

6.4.4 VGSOT Switching

In the second step, we apply V_g and investigate the SOT switching current. Figure 6.12(a) shows the representative switching probability curves at $t_{p,SOT}$ = 0.4ns for different V_g values. It shows a clear decrease (increase) of V_{SOT}

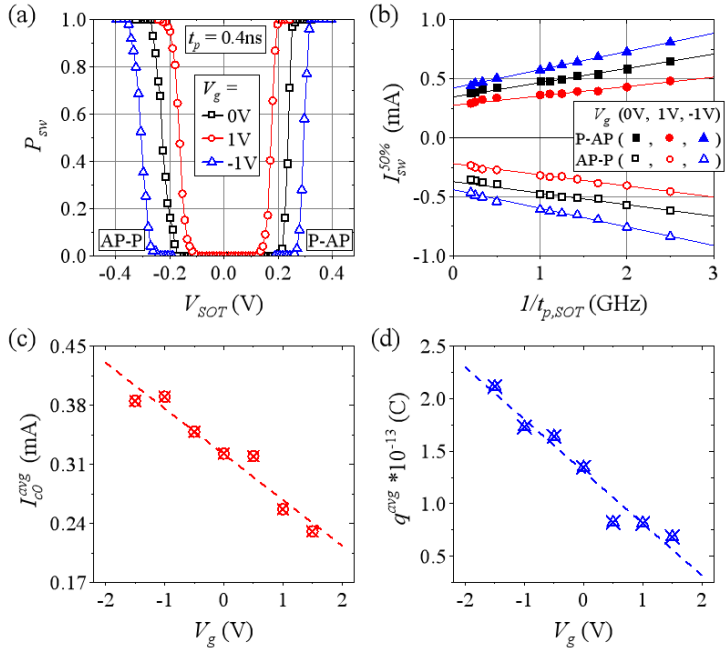

Figure 6.12: *(a) Classical switching probability distribution (P_{sw}) as a function of SOT pulse voltage under different gate amplitudes at t_p = 0.4ns. (b) Critical SOT switching current at P_{sw} = 50% as a function of $1/t_{p,SOT}$, showing typical linear scaling for all gate amplitudes. (c) I_{c0}^{avg} as a function of gate voltage. (d) q^{avg} parameter as a function of gate voltage.*

under V_g of 1V (-1V) for both AP-P and P-AP transitions. We then plot $I_{sw}^{50\%}$ as a function of $1/t_{p,SOT}$ [Figure 6.12(b)]. Similarly, we observe linear scaling in the sub-ns regime for all gate values, implying that V_g does not modify the SOT switching mechanisms but mostly assists the reversal.

Figure 6.12(c) and (d) summarize I_{c0}^{avg} and q^{avg} as a function of gate voltage. Both quantities are found to reduce (enhance) for $V_g > 0$ (< 0). The variation of I_{c0}^{avg} can be interpreted as the direct modification of the PMA upon gate voltage application. Further, the linear dependence of q^{avg} on V_g reflects the change of the nucleation energy for magnetization reversal.

VCMA Coefficient

Next, we quantify the VCMA coefficient with two different methods. For the first method, since the SOT switching current is proportional to $B_{k,eff}$, the average SOT switching current I_{sw}^{avg} should vary linearly with V_g, which we observe for all $t_{p,SOT}$ as shown in Figure 6.13(a). As expected from the VCMA effect, I_{sw}^{avg} reduces (enhances) for $V_g > 0$ (< 0) due to electron accumulation (depletion) at the FL/MgO interface. Consequently, we can estimate the VCMA coefficient (labeled as ξ_I to be distinguished from magnetic field sweep method) by [228]:

$$J_{sw} = \frac{I_{sw}}{w_{SOT} t_{SOT}} \sim \frac{2eM_S t_{FL}}{\hbar \theta_{SH}} \left(\frac{B_{k,eff}}{2} - \frac{B_x}{\sqrt{2}} \right) \tag{6.14}$$

$$\frac{\partial J_{sw}}{\partial V_g} = \frac{eM_S t_{FL}}{\hbar \theta_{SH}} \frac{\partial B_{k,eff}}{\partial V_g} \tag{6.15}$$

$$\xi_I \sim \frac{M_S t_{FL} t_{MgO}}{2} \frac{B_{k,eff}(0)}{J_{sw}(0)} \frac{\partial J_{sw}}{\partial V_g} \tag{6.16}$$

We obtain $\xi_I \sim 15$fJ/Vm from the VGSOT switching scheme.

Secondly, we evaluate the VCMA effect using the magnetic field sweep method described in Section 3.3.6. The VCMA slope $\partial B_{k,eff}/\partial V$ is estimated as 20mT/V, which corresponds to a VCMA coefficient ($\xi_B = \frac{M_S t_{FL} t_{MgO}}{2} \frac{\partial B_{k,eff}}{\partial V}$) of 15fJ/Vm, in good agreement with ξ_I. Moreover, we find that ξ_I is independent of t_p, proving that the VCMA effect in our VGSOT devices is a pure electronic-based and instantaneous effect.

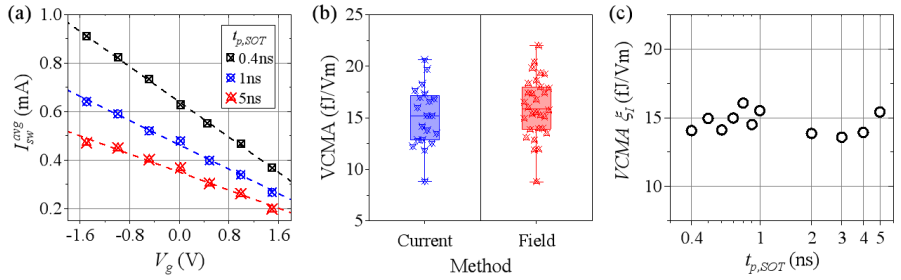

Figure 6.13: *(a) Average SOT switching current as a function of gate voltage for different pulse widths ($t_{p,SOT}$). (b) Comparison of the estimated VCMA coefficient between VGSOT switching current method and magnetic field switch method, showing consistent values. (c) VCMA coefficient, estimated from VGSOT switching current method, as a function of $t_{p,SOT}$.*

Selectivity

In Figure 6.14(a), we examine the selectivity of multiple devices. We observe that the average switching current at $P_{sw} = 50\%$ for $V_g = 1$V is mostly separated from that for $V_g = 0$V. However, to achieve a full selectivity, a larger difference in switching current will be needed. Further, we investigate the write error rate (WER) distributions. Figure 6.14(b) shows the write error rate (WER) of 10^5 events at $t_{p,SOT} = 0.4$ns and 1ns, and V_g = -1, 0 and 1V. It is shown that with the current VCMA efficiency, it is insufficient to achieve a full selectivity a V_g = 1V , where the single-cell WER at $V_g = 1$V still overlaps with the WER at $V_g = 0$V. Based on our results, we further predict that a full selectivity of a single cell for the present devices would require $\xi \sim 40$fJ/Vm at a maximum V_g of 1V, as exemplified with the green curves. This corresponds to a SOT switching current ratio (i_{sw}) of 0.5. Note that the steepness of the WER curves can typically be improved by enhancing Δ and $B_{k,eff}$ [247].

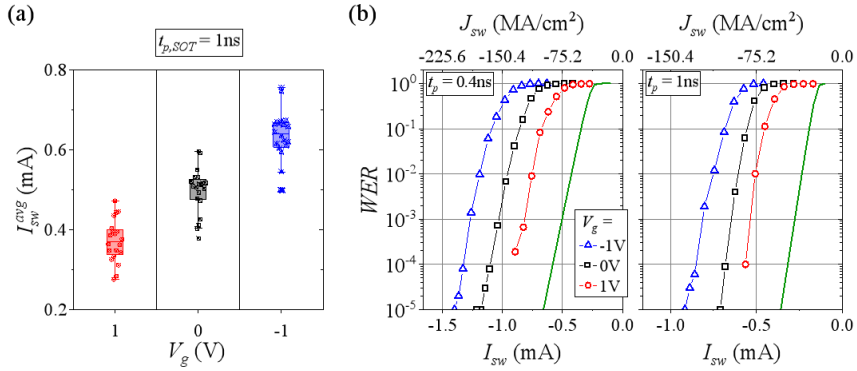

Figure 6.14: *(a) Average SOT current distribution at 1ns under different gate voltages, estimated from 20 similar devices. (b) Single device write error rate (WER) of* 10^5 *events for the AP-P transition at* $t_{p,SOT} = 0.4$ *and 1ns. Green curves predict the WER for* $\xi = 40$*fJ/Vm at* $V_g = 1$*V, required to achieve single device full selectivity.*

Endurance

One of the benefits of three-terminal devices is the endurance. To prove this, we test its endurance at an intensive write stress that is higher than the required value at WER $< 10^{-5}$. Figure 6.15 demonstrates that both the unselected cell ($V_g = 0$V) and the selected cell ($V_g = 1$V) are able to sustain 10^{12} cycles under

J_{sw} = 200MA/cm^2 and t_p = 0.4ns at a repetition rate of 50MHz. All MTJ and SOT resistances

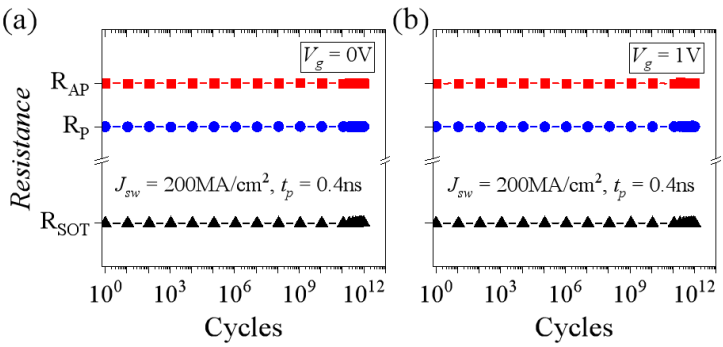

Figure 6.15: *Endurance tests of* 10^{12} *cycles under* J_{SOT} = *200MA/cm*^{2} *and* t_p = *0.4ns with (a)* V_g = *0V and (b)* V_g = *1V at 50MHz repetition rate.*

6.4.5 Study of Pulse Configuration

Next, we study how the gate duration and timing are modifying I_{sw}^{avg} at $t_{p,SOT}$ = 5ns and V_g = 1V. We investigate the gate coverage, where SOT and gate pulses are synchronized, and $t_{p,g}$ is varied from 0ns to 5ns, as shown in Figure 6.16(a). We observe that I_{sw}^{avg} decreases progressively with increasing $t_{p,g}$, reaching a maximum reduction of 25% when $t_{p,g} \sim 0.8t_{p,SOT}$. We interpret this as a decrease of nucleation energy which results in a reduction of nucleation delay time [228]. On the other hand, we extend the gate duration prior-to or subsequent-to the SOT pulse in addition to the primitive 5ns, respectively in Figure 6.16(b) and (c). It demonstrates that both pre-SOT and post-SOT gate do not influence I_{sw}^{avg}. Similar results are also obtained for $t_{p,SOT}$ = 1ns. These results suggest that one can moderately increase the gate duration to ensure sufficient margin for SOT write while maintaining the bit selectivity.

6.4.6 Energy Consumption

The total switching energy (E_{total}) is evaluated using an equivalent circuit shown in Figure 6.17(a). The SOT line is separated into two resistors, each has a resistance of $0.5R_{SOT}$. The gate channel resistance has the MTJ resistance

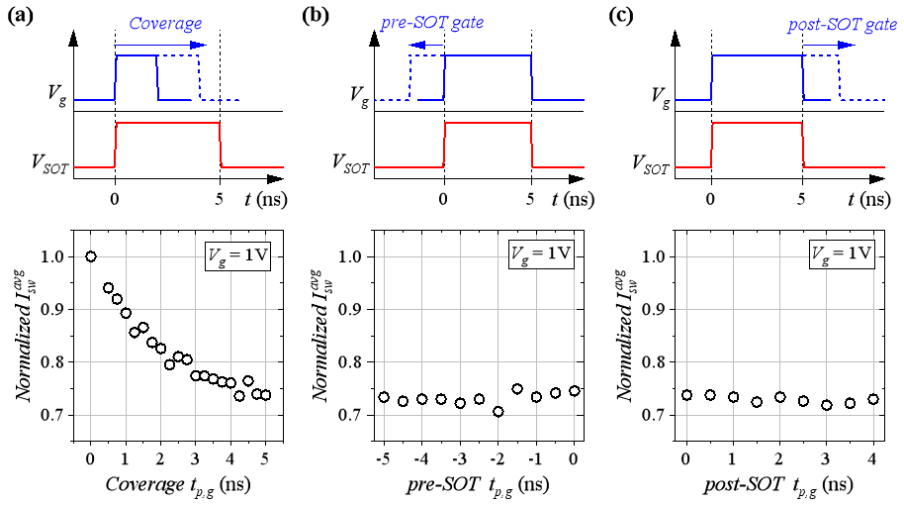

Figure 6.16: *(a) Normalized switching current density as a function of gate duration with V_g = 1V. SOT and gate pulses are synchronized, and $t_{p,SOT}$ = 5ns. $t_{p,g}$ is progressively increased from 0ns to 5ns. Normalized switching current density as a function of additional $t_{p,g}$ prior-to (b) or subsequent-to (c) the primitive 5ns coverage of the SOT pulse.*

and half SOT resistance connected in series. E_{total} is therefore expressed as:

$$E_{total} = E_{SOT} + E_{gate} \tag{6.17}$$

$$= I_{SOT}^2 R_{SOT} t_p + I_{gate}^2 [R_p + 0.5 R_{SOT}] t_p \tag{6.18}$$

We use the parallel resistance as R_{MTJ} to calculate the worst energy consumption in gate channel in order to illustrate the benefit of gate assistance. Figure 6.17(b) and (c) presents the values of E_{SOT}, E_{gate}, and E_{total} at t_p = 1ns and 0.4ns. Since gate energy (E_{gate}) is negligible due to high MTJ resistance, the main energy dissipation comes from E_{SOT}. This demonstrates the benefit of the gate assistance to SOT writing, with a E_{total} reduced by 45% at V_g = 1V to 41fJ and 30fJ for t_p = 1ns and 0.4ns, respectively.

6.5 Criteria and Outlook for Scaled VGSOT-MRAM

Although we have shown the benefits of the VGSOT writing scheme, several criteria must be obeyed when scaling VGSOT-pMTJ devices to 30nm in diameter,

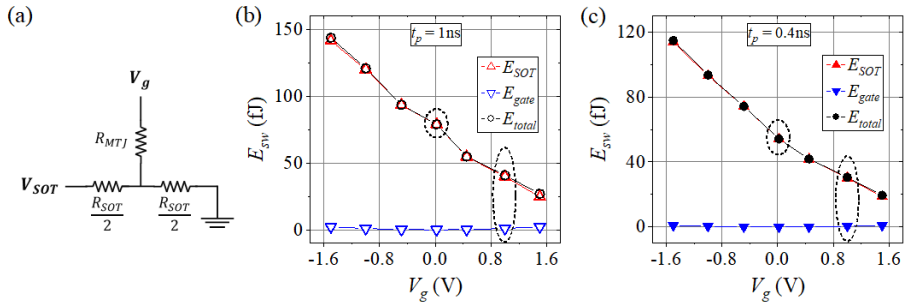

Figure 6.17: *(a) Schematic of the equivalent circuit used to estimate the VGSOT switching energy. Switching energies (E_{sw}) as a function of gate voltage at (b) t_p = 1ns and (c) t_p = 0.4ns.*

in order to take full advantages for high-speed memory applications. These criteria are:

- ***MgO thickness reduction***
- ***Low SOT Switching Current***
- ***Retention at*** V_g
- ***Bit Selectivity***

MgO thickness reduction

First, the MgO thickness and the RA product must be optimized to improve the reading speed, while preserving the benefits of gate effects. When reducing the MgO thickness, the STT effect inevitably becomes more significant. A hypothetical relationship between the magnitude of STT and VCMA is shown in Figure 6.18(a), where the efficiency describes the amount of PMA that can be switched by a given applied voltage (0.7V). The STT efficiency is calculated based on the recent experimental values where the best switching properties are demonstrated (see Ref. [174]). We assume the spin polarization parameter remains as a constant when varying the MgO thickness.

When reducing the MgO thickness, the resistance decreases logarithmically. Therefore, the STT current increases exponentially. However, the electric-field, which is responsible for the VCMA effect, scales linearly with the MgO thickness. Hence, there exists an inverse point that one of the STT and VCMA effects

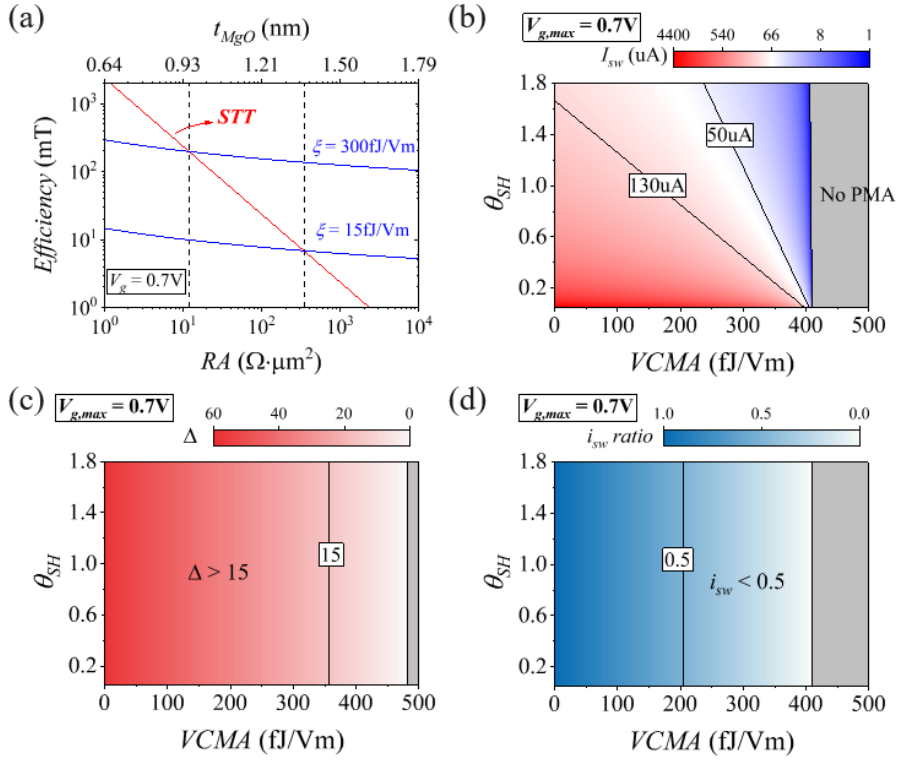

Figure 6.18: *Prediction of device parameters required at 30nm MTJ diameter based on different criteria: (a) relative efficiencies of STT and VCMA effects for MgO thickness reduction, (b) targeting SOT switching current, (c) free-layer retention at V_g, and (d) bit selectivity.*

dominates over the other. For example, our present devices with $\xi = 15$fJ/Vm would require a RA product of few hundreds $\Omega{\cdot}\mu m^2$ to suppress the STT current to below the VCMA efficiency. In order to improve the read performance of the VGSOT-MRAM to that comparable to the STT-MRAM, one should first improve the VCMA effect to 300fJ/Vm, according to our calculation. In fact, recent study has also shown pure VCMA switching characteristics in a device with RA = $14\Omega{\cdot}\mu m^2$, even though their VCMA coefficient was in the typical range of 30-40fJ/Vm [74]. Perhaps the use of a single CoFeB free-layer [43, 83] increases the damping constant which suppresses the STT efficiency. Overall, we predict that the MgO thickness can be reduced down to ∼1nm, corresponding to a RA ∼ 10-$20\Omega{\cdot}\mu m^2$. Furthermore, one can still apply the reversed-bias

method to enhance the PMA for reading and to reduce the chance of reading error [194, 248].

Low SOT Switching Current at $\mathbf{V_g}$ ($I_{sw}(V_g)$)

The second criterion is the low SOT switching current. This criterion is not only to fit the transistor's specifications but also to reduce the switching energy to achieve real low power applications. In Figure 6.18(b), we predict the required SOT current at 1ns writing speed for a 30nm MTJ device with $\Delta = 60$. We calculate it based on the performance obtained in our previous work [19] by varying the SOT and VCMA efficiencies. The color codes indicate high (red) and low (blue) SOT switching currents. Here, we consider a fixed gate voltage of 0.7V, which fits the maximum supply voltage of the transistor at the 10nm node for the embedded memory applications. Two targeted SOT currents are indicated: 130µA and 50µA. For a given SOT efficiency, increasing the VCMA coefficient can further reduce the switching current. However, it is also shown that VCMA > 410fJ/Vm is not desired, as it would enter the pure VCMA-induced magnetization switching regimes.

Retention at $\mathbf{V_g}$ ($\Delta(V_g)$)

The third criterion is regarding the retention during gate applied. In Section 6.4.5, we found that a full gate coverage is needed to achieve maximum reduction in SOT current. In order to compensate for the potential delay in the arrival time of the SOT current due to the long SOT track, one may need to moderately extend the gate duration to provide sufficient margin for SOT write. Both pre-SOT and post-SOT gate do not influence I_{sw}; however, they would potentially cause random magnetization reversal as the PMA and Δ are reduced. Here, we hypothetically suggest that a $\Delta > 15$ is mandatory within the time scales of the gate duration (sub-ns $\sim$ ns), where $\Delta = 15$ maintains a typical lifetime of few milliseconds. The calculation of $\Delta(V_g)$ is shown in Figure 6.18(c), when V_g is fixed at 0.7V, ξ should not exceed 360fJ/Vm.

Bit Selectivity (i_{sw})

The final criterion concerns the bit selectivity. Our present devices require $i_{sw} < 0.5$ to achieve full selectivity at WER $< 10^{-5}$. As shown in Figure 6.18(d), to accomplish such a requirement, a ξ of >200fJ/Vm is mandatory.

6.5.1 SOT and VCMA Parameter Selection

Based on the above-cited criteria, we summarize the essential SOT and VCMA parameters. In Figure 6.19, all requirements are assembled. Black outlined area defines the I_{sw} targets at 50µA(dashed line) and 130µA(dashed-dotted line), red outlined area determines $\Delta(V_g) > 15$, blue outlined area indicates selectivity $i_{sw} < 0.5$, and the shadow area illustrates the available θ_{SH} and ξ efficiencies to meet the targets. Within the typical materials in CMOS technologies, we find that θ_{SH}

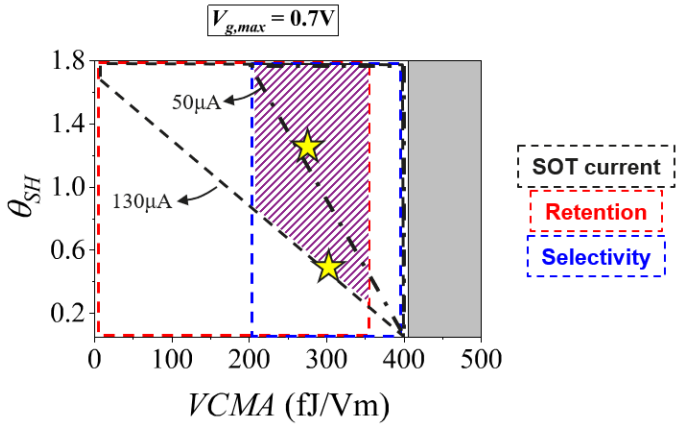

Figure 6.19: *SOT and VCMA parameter selection to meet the VGSOT criteria. Black outlined area defines the I_{sw} targets at 50µA(dashed-dotted line) and 130µA(dashed-dotted line), red outlined area determines $\Delta(V_g) > 15$, blue outlined area indicates selectivity $i_{sw} < 0.5$, and the shadow area illustrates the available θ_{SH} and ξ efficiencies to meet the requirements.*

$= 0.45$ and $\xi = 300$fJ/Vm can fulfill the $I_{sw}(V_g)$ target at 130µA. A recent report has demonstrated that $\theta_{SH} = 0.45$ is achievable by engineering the W-based SOT track [227]. On the other hand, recent studies using dusting layers, such as Cr and Ir, at the FL/MgO interface demonstrate significant improvements in VCMA coefficient to above 300fJ/Vm [172, 249]. Since SOT and VCMA occur at different interfaces, these effects may be optimized individually.

Further reduction of I_{sw} to 50µA target will need the TI-based SOT track. For example, BiSe shows a $\theta_{SH} > 1.4$ [235]. Increasing SOT efficiency can also mitigate the VCMA demand. Therefore, besides searching for new exotic materials, future research should also focus on the process conditions to implement TI-base materials in CMOS technology.

6.5.2 Design-to-Technology Co-Optimization (DTCO)

Finally, by performing design-to-technology co-optimization (DTCO) analysis (courtesy of M. Gupta and M. Perumkunnil), we benchmark VGSOT against other embedded memory technologies such as SRAM, STT-MRAM, and SOT-MRAM at 5nm technology node, as shown in Table 6.3. The performance values for SRAM high-density (HD) and high-performance (HP) are estimated based on the data from imec and different foundries [250, 251, 252, 253]. The Contact Poly Pitch (CPP) and Metal Pitch (MP) numbers are estimated accordingly with CPP = 45nm and MP = 30nm based on imec's technology and models [254]. The architectures of STT-MRAM [254] and SOT-MRAM [255] used to estimate their performance are described in the references. For VGSOT-MRAM, the 2 and 4 MTJ variants represent the number of pillars on a single SOT line. Optimization of the VGSOT performance follows the similar procedure as for SOT-MRAM [255], but taking additional variables such as number of MTJ, SOT track length/resistance, spin Hall angle, and VCMA coefficient. We show that the VGSOT-4MTJ design can much reduce the effective area of the conventional SOT-MRAM, making it comparable to the STT-MRAM and less than 50% of the high-density SRAM at minimal performance degradation.

Table 6.3: *DTCO analysis (courtesy of M. Gupta and M. Perumkunnil) of performances for different embedded memory technologies at the 5nm node, including SRAM, STT-MRAM, SOT-MRAM and VGSOT-MRAM technologies. Projected values for VGSOT are calculated with improved MTJ properties (see Table 6.4 Target 2) and assuming a SOT channel resistivity of 160μΩ·cm.*

Spec	**Bit-Cell Type**						
	SRAM		**STT**	**SOT**	**VGSOT**		
	HD	HP			2MTJ	4MTJ	Projected
Area (μm^2)	0.021	0.028	0.0084	0.016	0.0122	0.009	0.009
Read Power (nW)	7.28	18.7	6.20	25.5	3.16	2.96	5.8
Write Power (nW)	9.85	25.7	24.4	31.4	47.5	46.5	4.6
Read Latency (ns)	∼1.5	∼0.8	∼3.75	∼1	∼10	∼10	∼3-5
Write Latency (ns)	∼1.5	∼0.8	∼20	∼2	∼1	∼1	∼1
V_{DD} (V)	∼0.7	∼0.7	∼0.7	∼0.7	∼0.7	∼0.7	∼0.7
Retention	-	-	> 10yrs	> 10yrs	> 10yrs	> 10yrs	> 10yrs
Endurance	10^{16}	10^{16}	10^{9}	10^{14}	10^{14}	10^{14}	10^{14}

However, based on our present VGSOT device properties, the read performance will be limited to 10ns due to the large MTJ resistance. Furthermore, the write

power of VGSOT-4MTJ cell becomes larger than the conventional SOT devices because of the longer SOT line which increases the resistance. To prove that the VGSOT concept is promising, we further project the write/read performance using the improved pMTJ properties that described in the previous section, i.e. RA = 20Ω·µm^2, ξ = 300fJ/Vm, and θ_{SH} = 0.45. It is shown that the read latency can be comparable to the STT devices, and both the write power and write latency are outperforming the STT devices. In addition, due to the separated read/write paths, the VGSOT option also significantly improves the endurance cycle compared to STT-MRAM. These results suggest that, among the MRAM cell types, VGSOT-MRAM is more suitable for embedded applications at the advanced technology nodes.

6.6 Summary

To sum up, in this chapter we presented voltage-gate assisted spin-orbit torque (VGOST) writing of pMTJ devices using CMOS-compatible processes. We demonstrated VGSOT writing to be energy efficient, offering reliable sub-ns switching and resilience against large write/read stress. Properties obtained in this work are summarized in Table 6.4 again, where the target values desired at 30nm MTJ diameter are also listed. We highlighted that the VGSOT scheme can ease the requirements of challenging VCMA and SOT parameters. For example, while a $\xi >$ 800fJ/Vm is requested for VCMA-MRAM or a $\theta_{SH} > 2$ (5) is mandatory for SOT-MRAM at 130µA (50µA) target, the VGSOT cell needs only $\xi <$ 300fJ/Vm and $\theta_{SH} < 0.45$ (1.3) to accomplish the targeted currents. With these assumptions, we projected that VGSOT-MRAM is suitable for both high-density and high-performance memory designs while maintaining the advantage of low-power and inherent non-volatility.

Table 6.4: *MTJ properties and performance of this work and the future targets for the 30nm devices. The target performances are calculated based on the improved MTJ properties to meet application requirements.*

	Current Status		**Target 1**	**Target 2**
eCD (nm)	80		30	30
t_{MgO} (nm)	1.7		1	1
w_{SOT} (nm)	190		30	30
TMR (%)	110		150	150
$\|\theta_{SH}\|$	0.32		0.45	1.3
VCMA (fJ/Vm)	10-20		300	300
Δ	35		60	60
t_p (ns)	0.4	1	1	1
V_g (V)	0 / 1	0 / 1	0 / 0.7	0 / 0.7
$I_{SOT}(V_g)$ (µA)	684 / 510	521 / 370	486 / 130	168 / 45
$J_{SOT}(V_g)$ (MA/cm^2)	103 / 77	78 / 56	463 / 124	160 / 43
$E_{total}(V_g)$ (fJ)	54 / 30	79 / 41	481 / 54	76 / 25
Endurance	$> 10^{12}$		$> 10^{12}$	$> 10^{12}$

Chapter 7

Conclusion and Outlook

This final chapter summarizes the main results obtained in each chapter, and the outlook for future MRAM development is given.

7.1 Conclusion

Magnetic random access memory has been attractive since the late 1990s, as it is believed to address the large standby-power issues in the fully non-volatile memory hierarchy. Extensive engineering works have been carried out to finally make the prototype spin-transfer torque (STT)-MRAMs come to reality [256]. For us researchers, we continued seeking alternative operation mechanisms that perform beyond STT. The desire for high speed and low energy writing has led us to study voltage control of magnetic anisotropy (VCMA) effect for voltage-controlled, or voltage-assisted, magnetic tunnel junction devices. Below, the main contributions of this thesis are reviewed again; afterward, how this thesis works improve the present MTJ/MRAM devices are evaluated.

Chapter 3 investigated the conventional VCMA-controlled magnetization switching mechanism. We have explored the impacts of MgO thickness, electric field amplitude, and in-plane field magnitude on the switching properties. MgO thickness was found not affecting the VCMA properties such as coefficient and switching speed, under the basis of negligible STT effect. For increasing electric field amplitude, not only the switching probability gets improved but also the speed is accelerated. Such acceleration can also be accomplished by stronger in-plane field magnitudes, which allows for constant voltage writing at various

switching speeds. These properties are also in good agreement with model predictions. From these experiments, we have learned that VCMA imposes several benefits on pMTJ devices. First, it promises low power writing, with the tunnel current 10-100x lower than the typical STT devices. Second, it offers an ultra-fast switching mechanism, where the magnetization reversal frequency determined by the intrinsic gyromagnetic ratio and the in-plane field is typically in the GHz regime. These two characteristics already make VCMA switching 100-1000x lower energy at 10x faster speed than typical STT writing. Furthermore, the uni-polar characteristic of the VCMA effect ensures a disturbance-free read using an opposite bias. However, to take full advantage of VCMA, we also stated the challenges remaining to be addressed: integration of the magnetic field generator and removal of pre-read operation. The solutions to these challenges are discussed in Chapter 4.

Chapter 4 focused on solving the challenges raised in the conventional VCMA writing scheme. First, the magnetic field integration methods are proposed and discussed. One is the in-plane polarizer (IPP) and the other one is the magnetic-hard-mask (MHM). With micro-magnetic simulations, we find that IPP required an elliptical MTJ for stabilization, making it less promising for device size scaling. Besides, IPP is not completely compartmented from the MTJ, which could impose variations on the MTJ properties. Conversely, the MHM proposed in Ref. [185] can be served for shaping the metal line below the MTJ, which intrinsically has a rectangular shape for maintaining its stability. In addition, the MHM is a fully separated component in the cell, which is ideal for individual optimization. Then, we demonstrate in-plane field-free VCMA switching with MHM integration. The tunneling magneto-resistance, switching speed, and write error rate of the MHM devices are found consistent with the standard devices in external fields. Based on the results, we believe MHM could be a novel and integration-friendly method. In the second part, we propose a new switching scheme to overcome the need for a pre-read operation. The pre-read operation is necessary in the conventional scheme due to the same switching voltage polarity and duration for both P-AP and AP-P directions. This, however, elongates the total writing duration since the high resistance-area product of VCMA devices would slow down the reading speed. We propose a deterministic writing scheme under an asymmetric P/AP stability. The switching at a lower electric field is uni-directional, which is deterministic and can also serve as an initialization. We demonstrate the deterministic P-AP (AP-P) switching with a single-pulse (double-pulse), and the magnetization dynamics are confirmed with macro-spin simulations. Both solutions discussed in this chapter path the way for VCMA device advancements for practical applications.

Chapter 5 tested the VCMA device properties under ambient temperature

variations. We observe that all the magnetic properties, such as saturation magnetization (M_S), interfacial perpendicular magnetic anisotropy (K_i), and VCMA coefficient (ξ), are decreasing with increasing operating temperature. These temperature-dependent variations can be modeled and explained well with Callen-Callen's theory and the power law of $M_S(T)$. Further, we validate experimentally for the first time that the critical VCMA switching voltage (V_c) drops by 50% when increasing operating temperature from 25°C to 85°C. Such dependence can also be explained and reproduced based on the observations in $M_S(T)$, $K_i(T)$, and $\xi(T)$. These characteristics draw interests from the viewpoint of implementing VCMA in MRAM applications.

Chapter 6 analyzed a hybrid switching mechanism utilizing VCMA and spin-orbit torque (SOT) effects, namely voltage-gate assisted spin-orbit torque (VGSOT). The need for a hybrid mechanism was initiated from the device scaling perspective. For pure VCMA operation, the required VCMA coefficient ξ to avoid compensating retention is predicted to be $\xi > 1000$fJ/Vm for the sub-30nm pMTJ devices. Although $\xi > 1000$fJ/Vm has been reported experimentally, it is currently limited to the molecular beam epitaxy (MBE) deposited stacks rather than the typical sputtered systems. Similar in the SOT-pMTJ, a spin Hall angle (θ_{SH}) > 2 is needed to target a 130µA SOT switching current at sub-30nm pMTJ. To date, the highest $\theta_{SH} = 4.25$ has been reported in topological insulators, but they are too complicated to be integrated in CMOS process. The combination of VCMA and SOT can significantly mitigate both requirements down to $\xi = 300$fJ/Vm and $\theta_{SH} = 0.45$ while maintaining the non-volatile feature in scaled MTJ sizes. Besides VCMA/SOT parameter mitigation, we also demonstrate VGSOT to be energy efficient (few tens of fJ), offering reliable writing at GHz speeds. We also initiate the design scopes for the scaled VGSOT devices based on several criteria and specifications. With the design-to-technology co-optimization (DTCO) analysis, we finally project that VGSOT-MRAM is suitable for both high-density and high-performance memory designs for embedded applications beyond 10nm technology nodes.

7.1.1 Evaluation of VCMA and VGSOT

In this additional section, we briefly evaluate how the results of this thesis works are improving the MRAM performance metrics compared to the typical STT-MRAMs. This evaluation does not aim to specify which MRAM type is the best for the future, but it highlights the importance or the potential tradeoffs with VCMA and VGSOT techniques.

- ***Write Speed***: Compared to the state-of-the-art STT-MRAMs, which typically write the MTJ with 5-20ns speeds, both VCMA and VGSOT

schemes are offering 10x faster speeds. For VCMA, increasing the applied voltage does not monotonically improve the switching probability at a given speed, but one must tune the pulse duration accordingly. This also implies a more strictly defined process uniformity to minimize the inhomogeneity in arrays. For VGSOT, a higher SOT current can typically switch the free-layer faster and with lower errors. Also, thanks to the VCMA gate which reduces the perpendicular magnetic anisotropy, VGSOT writing can be more reliable than pure SOT at given pulse conditions.

- ***Write Power/Energy***: For a given MTJ size, the write power for STT and SOT are in the same order (see Table 6.3). In VGSOT devices, because only the selected cells with reduced PMA are switched, its write power can be one order less than that for STT or SOT devices. The VCMA devices also have the write power one order less than the STT/SOT devices because of the higher resistance and lower current. Energy-wise, both VGSOT and VCMA switch the MTJ 10x faster than STT, therefore the total energy can be 2-3 orders of magnitude lower than the STT devices.

- ***Read Performance***: Read speed in the present VCMA and VGSOT devices are limited because of the high resistance-area products which are used to suppress the tunneling STT current through the MTJ channel. This can be addressed by reducing the MgO barrier thickness along with the improved VCMA coefficients. Besides MgO thickness reduction, VGSOT devices have one more parameter released: the damping constant. Because SOT is not collinear with the intrinsic damping effect, increasing the damping constant will not impact the SOT switching current. Conversely, higher damping constant makes STT less efficient. Therefore, higher damping constant allows a higher read current while suppressing the STT efficiency. As for VCMA devices, the damping constant is related to the write error rate, as it may reduce the effective z-component after precession [178]. It is therefore not recommended to increase damping constant for reading speed improvement.

- ***Retention***: The VCMA and SOT effects do not directly impact the retention of the MTJ device. However, their magnitudes determine the minimum device size for targeted retention. For example, to target $\Delta(RT) = 60$, the minimum diameter for VCMA-MTJ is approximately 75nm, assuming a 1.4nm MgO thickness, a writing voltage of 1.5V, and a VCMA coefficient of 50fJ/Vm.

- ***Endurance***: In STT-MRAMs, the write and read operation shares the same path. The large current injection through the MTJ would gradually degrade the MgO barrier, which limits the endurance. For VCMA devices,

despite having the same write/read path, the current passing through the MTJ is much suppressed, both joule heating and electromigration issues are therefore much less pronounced. On the other hand, VGSOT devices have a separated write/read path, hence the SOT write current does not directly impact the MTJ endurance. The VCMA gate stress is not significant either, since the gate voltage, e.g. 0.7V, is much lower than the typical breakdown voltage (∼1.6V for 1ns pulse) for the 1nm MgO. Ideally, both VCMA- and VGSOT-MRAM can have much better endurance ($> 10^{14}$) than STT-MRAMs.

7.2 Outlook

The introduction of VCMA into the MRAM fields indeed promises some more energy-efficient ways for MRAM writing. Personally, I would expect the prototypes of both VCMA-MRAM and VGSOT-MRAM to appear in the industry in the late 2020s. Needless to say, challenges are there, as already cited in this thesis. For the future of VCMA, there are three aspects that I would emphasize: the VCMA coefficient improvement techniques, the implementation of high VCMA in MRAM cells, and MRAM beyond memory application.

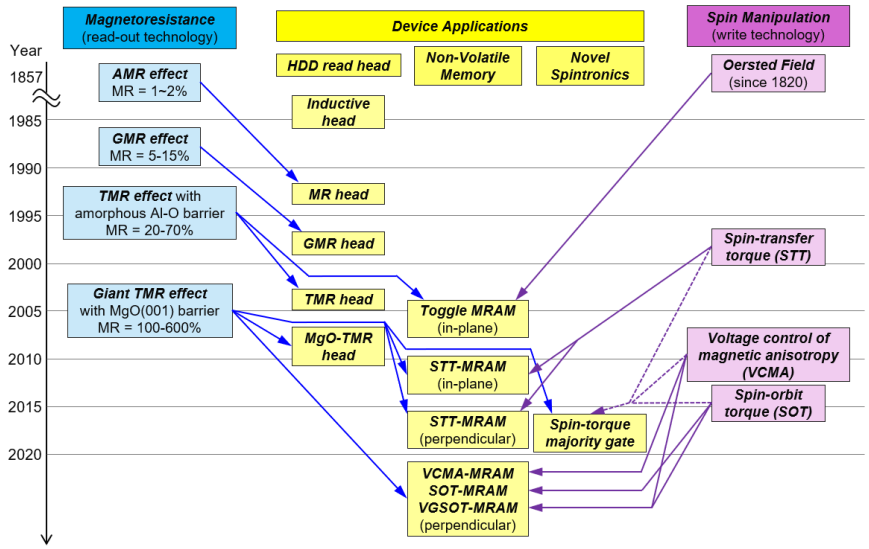

Figure 7.1: *History and future perspectives on basic physical phenomena of spintronics and their device applications. Reproduced from Refs. [257, 258].*

VCMA Coefficient Improvement Techniques

Just before the finish of this PhD research, the physics to describe the pure electronic-based VCMA effect has been basically established [86, 105]. Recognizing the electron doping and redistribution components of the VCMA effect surely paves the way for designing the simulation/experimental conditions to achieve high coefficients. Indeed, the recent simulation reports have shown sufficiently high coefficients (see Figure 3.22). However, realizing those concepts in experiments is challenging. Nevertheless, as proof of concepts, several techniques have been carried out. A typical example that proves the electron doping component is the introduction of high-k dielectric, such as crystalline $SrTiO_3$ (STO). The higher dielectric constant imposes more electron accumulation at the free-layer(FL)/STO interface, boosting the VCMA effect significantly to more than 10x larger than the conventional MgO systems [188, 189]. On the other hand, several experiments using dusting layers in the FL/dust/MgO structures have been performed to confirm the electron redistribution component of the VCMA effect. Those experiments are mostly carried out with MBE deposition to allow more precise control for the interface conditions, and they have also validated the concept. The next step would be implementing these studies in the sputtered systems, as sputter deposition is still the most commonly used method for CMOS process and mass production.

Implementation of High VCMA in MRAM Cells

Although several studies have demonstrated good VCMA efficiencies, they were mostly done on either simplified systems such as tri-layer stacks or large scaled hall bar structures. The ready-to-use VCMA effects in integrated magnetic tunnel junctions (MTJs) remain in the range of 30-70fJ/Vm only. The gap between simplified systems and integrated MTJs may be attributed to the complexity of the MTJ stacks, the deposition methods, the material compatibility, and even the process conditions. For example, although high-k STO generates high VCMA coefficients, it showed TMR only smaller than 20% [259, 260]. A potential way to overcome such a limitation may be using a hybrid free-layer structure STO/free-layer(FL)/MgO, where the FL/MgO component is responsible for MTJ reading and the high-k dielectric/FL part takes charge of FL writing. In the VGSOT design, this is however not possible, as one side of the FL must be in contact with the SOT layer. Therefore, more engineering efforts must be taken to optimize both SOT/FL and FL/MgO interface conditions.

MRAM Beyond Memory Application

Neuromorphic Computing: Besides the memory applications, recently MRAM has also received more attention for neuromorphic computing. Neuromorphic computing is a computational method using electronic devices to create artificial neural systems that mimic the human brain and nervous systems. MRAM technologies are possible to simulate synapse-like neuro systems as they use stochastic switching, meaning the writing probability increases with longer write durations. The typical requirements for these systems are low energy and fast computation. These properties already impose interests on VCMA- [261] and SOT-MTJ devices [262]. VGSOT-MTJ can even be more suitable than the conventional SOT-MTJ, in the sense that the VGSOT scheme makes the arrays denser and lower power.

Bibliography

[1] Lillian Hoddeson. The discovery of the point-contact transistor. *Historical Studies in the Physical Sciences*, 12(1):41–76, 1981.

[2] Kahng Dawon. Electric field controlled semiconductor device. *US Patent*, US3206670A, 1960.

[3] Golden E. Moore. Cramming More Components onto Integrated Circuits. *Proceedings of the IEEE*, 86(1):82–85, 1998.

[4] John van Neumann. First Draft of a Report on the EDVAC. *IEEE Annals of the History of Computing*, 15(4):27–75, 1993.

[5] H.-S. Philip Wong and Sayeef Salahuddin. Memory leads the way to better computing. *Nature Technology*, 10:191–194, 2015.

[6] Shinichiro Shiratake. STT-MRAM Design and device requirement. *IEEE International Electron Devices Meeting (IEDM)*, 2015.

[7] Tetsuo Endoh, Hiroki Koike, Shoji Ikeda, Takahiro Hanyu, and Hideo Ohno. An Overview of Nonvolatile Emerging Memories - Spintronics for Working Memories. *IEEE Journal on Emerging and Selected Topics in Circuits and Systems*, 6(2):109–119, 2016.

[8] Jagan Singh Meena, Simon Min Sze, Umesh Chand, and Tseung-Yuen Tseng. Overview of emerging nonvolatile memory technologies. *Nanoscale Research Letters*, 9(526), 2014.

[9] J. Joshua Yang, Dmitri B. Strukov, and Duncan R. Stewart. Memristive devices for computing. *Nature Nanotechnology*, 8(1):13–24, 2013.

[10] Shimeng Yu and Pai-Yu Chen. Emerging Memory Technologies: Recent Trends and Prospects. *IEEE Solid-State Circuits Magzine*, 8:43–56, 2016.

[11] T. Kawahara, K. Ito, R. Takemura, and H. Ohno. Spin-transfer torque MRAM technology: Review and prospect. *Microelectronics Reliability*, 52:613–627, 2012.

[12] Eric Karl, Yih Wang, Yong-Gee Ng, Zheng Guo, Fatih Hamzaoglu, Uddalak Bhattacharya, Kevin Zhang, Kaized Mistry, and Mark Bohr. A 4.6 GHz 162Mb SRAM Design in 22nm Tri-Gate CMOS Technology with Integrated Active V_{MIN}-Enhancing Assist Circuitry. *IEEE International Solid-State Circuits Conference (ISSCC)*, 2012.

[13] Eric Pop. Energy Dissipation and Transport in Nanoscale Devices. *Nano Research*, 3(3):147–169, 2010.

[14] Rainer Waser, Regina Dittmann, Georgo Staikov, and Kristof Szot. Redox-Based Resistive Switching Memories - Nanoionic Mechanisms, Prospects, and Challenges. *Advanced Materials*, 21:2632–2663, 2009.

[15] H.-S. Philip Wong, Heng-Yuan Lee, Shimeng Yu, Yu-Sheng CHen, Yi Wu, Pang-Shiu Chen, Byoungil Lee, Frederick T. Chen, and Ming-Jinn Tsai. Metal-Oxide RRAM. *Proceedings of IEEE*, 100:1951–1970, 2012.

[16] Xiaoxin Xu, Hangbing Lv, Hongtao Liu, Qing Luo, Tiancheng Gong, Ming Wang, Guoming Wang, Meiyun Zhang, Yang Li, Qi Liu, Shibing Long, and Ming Liu. Investigation of LRS dependence on the retention of HRS in CBRAM. *Nanoscale Research Letters*, 10(61), 2015.

[17] Thomas Mikolajick, Stefan Slesazeck, Min Hyuk Park, and Uwe Schroeder. Ferroelectric hafnium oxide for ferroelectric random-access memories and ferroelectric fi eld-effect transistors . *MRS Bulletin*, 43(5):340–346, 2018.

[18] V. B. Naik, K. Lee, K. Yamane, R. Chao, J. Kwon, N. Thiyagarajah, N. L. Chung, S. H. Huang, B. Behin-Aein, J. H. Lim, T. Y. Lee, W. P. Neo, H. Dixit, S. K. L. C. Goh, T. Ling, J. Hwang, D. Zeng, J. W. Ting, E. H. Toh, L. Zhang, R. Low, N. Balasankaran, L. Y. Zhang, K. W. Gan, L. Y. Hau, J. Mueller, B. Pfefferling, O. Kallensee, S. L. Tan, C. S. Seet, Y. S. You, S. T. Woo, E. Quek, S. Y. Siah, and J. Pellerin. Manufacturable 22nm FD-SOI Embedded MRAM Technology for Industrial-grade MCU and IOT Applications. *IEEE International Electron Devices Meeting (IEDM)*, pages 2.3.1–2.3.4, 2019.

[19] K. Garello, F. Yasin, S. Couet, L. Souriau, J. Swerts, S. Rao, S. Van Beek, W. Kim, E. Liu, S. Kundu, D. Tsvetanova, N. Jossart, K. Croes, E. Grimaldi, M. Baumgartner, D. Crotti, A. Furnemont, P. Gambardella, and G. S. Kar. SOT-MRAM 300mm integration for low power and ultrafast embedded memories. *IEEE Symposium on VLSI Circuits*, pages C81–C82, 2018.

[20] Hiroki Noguchi, Kazutaka Ikegami, Keiko Abe, Shinobu Fujita, Yoichi Shiota, Takayuki Nozaki, Shinji Yuasa, and Yoshishige Suzuki. Novel Voltage Controlled MRAM (VCM) with Fast Read/Write Circuits for Ultra Large Last Level Cache. *IEEE International Electron Devices Meeting (IEDM)*, pages 27.5.1–27.5.4, 2016.

[21] Andrew D. Kent and Daniel C. Worledge. A new spin on magnetic memories. *Proceedings of the IEEE*, 10:187–191, 2015.

[22] Stuart A. Wolf, Jiwei Lu, Mircea R. Stan, Eugene Chen, and Daryl M. Treger. The Promise of Nanomagnetics and Spintronics for Future Logic and Universal Memory. *Nature Nanotechnology*, 98(12):2155–2168, 2010.

[23] M. Julliere. Tunneling Between Ferromagnetic Films. *Physics Letters*, 54A(3):225–226, 1975.

[24] Jyotirmoy Chatterjee, Taiebeh Tahmasebi, Sofie Mertens, Gouri Sankar Kar, Tai Min, and Jo De Broek. Seed Layer Effect on the Magnetic Properties of Ultrathin Co/Pt Multilayers With Perpendicular Magnetic Anisotropy. *IEEE Transactions on Magnetics*, 50(11), 2014.

[25] Kyota Watanabe, Shunsuke Fukami, Hideo Sato, Fumihiro Matsukura, and Hideo Ohno. Magnetic Properties of CoFeB-MgO Stacks with Different Buffer-Layer Materials (Ta or Mo). *IEEE Transactions on Magnetics*, 52(7), 2016.

[26] Jyotirmoy Chatterjee, Taiebeh Tahmasebi adn Johan Swerts, Gouri Sankar Kar, Tai Min, and Jo De Broek. Impact of seed layer on post-annealing behavior of transport and magnetic properties of Co/Pt multilayer-based bottom-pinned perpendicular magnetic tunnel junctions. *Applied Physics Express*, 8:063002, 2015.

[27] Witold Skowronski, Takayuki Nozaki, Duong D. Lam, Yoichi Shiota, Kay Yakushiji, Hitoshi Kubota, Akio Fukushima, Shinji Yuasa, and Yoshishige Suzuki. Underlayer material influence on electric-field controlled perpendicular magnetic anisotropy in CoFeB/MgO magnetic tunnel junctions. *Physical Review B*, 91:184410, 2015.

[28] Yasutaka Takemura, Du-Yeong Lee, Seung-Eun Lee, and Jea-Gun Park. Dependency of tunneling magnetoresistance ratio on Pt seed-layer thickness for double MgO perpendicular magnetic tunnel junction spin-valves with a top $Co_2Fe_6B_2$ free layer *ex-situ* annealed at 400°C. *Nanotechnology*, 27:485203, 2016.

[29] S. Bandiera, R. C. Sousa, S. Auffret, B. Rodmacq, and B. Dieny. Enhancement of perpendicular magnetic anisotropy thanks to Pt insertions in synthetic antiferromagnets. *Applied Physics Letters*, 101:072410, 2012.

[30] Kay Yakushiji, Akio Fukushima, Hitoshi Kubota, Makoto Konoto, and Shinji Yuasa. Ultralow-Voltage Spin Transfer Switching in Perpendicularly Magnetized Magnetic Tunnel Junctions with Synthetic Antiferromagnetic Reference Layer. *Applied Physics Express*, 6:113006, 2013.

[31] S. Ishikawa, H. Sato, M. Yamanouchi, S. Ikeda, S. Fukami, F. Matsukura, and H. Ohno. Magnetic properties of MgO-[Co/Pt] multilayers with a CoFeB insertion layer. *Journal of Applied Physics*, 113:17C721, 2013.

[32] Kyo-Suk Chae, Tae-Hun Shim, and Jea-Gun Park. Dependency of anti-ferro-magnetic coupling strength on Ru spacer thickness of $[Co/Pd]_n$-synthetic-anti-ferro-magnetic layer in perpendicular magnetic-tunnel-junctions fabricated on 12-inch TiN electrode wafer. *Journal of Applied Physics*, 116:033904, 2014.

[33] Huadong Gan, Roger Malmhall, Zihui Wang, Bing K Yen, Jing Zhang, Xiaobin Wang, Yuchen Zhou, Xiaojie Hao, Dongha Jung, Kimihiro Satoh, and Yiming Huai. Perpendicular magnetic tunnel junction with thin CoFeB/Ta/Co/Pd/Co reference layer. *Applied Physics Letters*, 105:192403, 2014.

[34] Seung-Eun Lee, Tae-Hun Shim, and Jea-Gun Park. $Co_2Fe_6B_2$/MgO-based perpendicular spin-transfer-torque magnetic-tunnel-junction spin-valve without $[Co/Pt]_n$ lower synthetic-antiferromagnetic layer. *Nanotechnology*, 26(47), 2015.

[35] Zhitao Diao, Dmytro Apalkov, Mahendra Pakala, Yunfei Ding, Alex Panchula, and Yiming Huai. Spin transfer switching and spin polarization in magnetic tunnel junction with MgO and AlO_x barriers. *Applied Physics Letters*, 87:232502, 2005.

[36] Fei Guo, Zhiming Wu, Ting Chen, Yaping Wu, Guanzhi Cai, and Junyong Kang. Effect of boron in Fe/MgO interface on structure stability and state coupling. *Computational Materials Science*, 101:138–142, 2015.

[37] David D. Djayaprawira, Koji Tsunekawa, Motonobu Nagai, Hiroki Maehara, Shinji Yamagata, and Naoki Watanabe. 230% room-temperature magnetoresistance in CoFeB/MgO/CoFeB magnetic tunnel junctions. *Applied Physics Letters*, 86:092502, 2005.

[38] Shinji Yuasa, Taro Nagahama, Akio Fukushima, Yoshishige Suzuki, and Koji Ando. Giant room-temperature magnetoresistance in single-crystal Fe/MgO/Fe magnetic tunnel junctions. *Nature Materials*, 3:868–871, 2004.

[39] Zhiyong Qiu, Jiaxiang Shang, Xiaofang Bi, Shengkai Gong, and Huibin Xu. Study of electronic structure in $Co/Al_2O_3/Co$ heterojunctions from first principles. *Acta Materialia*, 52:533–537, 2004.

[40] Dexin Wang, Cathy Nordman, James M. Daughton, Zhenghong Qian, and Jonathon Fink. 70% TMR at Room Temperature for SDT Sandwich Junctions with CoFeB as Free and Reference Layers. *IEEE Transactions on Magnetics*, 40(4), 2004.

[41] S. Ikeda, J.Hayakawa, Y. Ashizawa, Y. M. Lee, K. Miura, H. Hasegawa, M. Tsunoda, F. Matsukura, and H. Ohno. Tunnel magnetoresistance of 604% at 300K by suppression of Ta diffusion in CoFeB/MgO/CoFeB pseudo-spin-valves annealed at high temperature. *Applied Physics Letters*, 93:082508, 2008.

[42] Mathias Bersweiler, Hideo Sato, and Hideo Ohno. Magnetic and Free-Layer Properties of MgO/(Co)FeB/MgO Structure: Dependence on CoFeB Composition. *IEEE Magnetics Letters*, 8:3109003, 2017.

[43] H. Sato, M. Yamanouchi, S. Ikeda, S. Fukami, F. Matsukura, and H. Ohno. Perpendicular-anisotropy CoFeB-MgO magnetic tunnel junctions with a MgO/CoFeB/Ta/CoFeB/MgO recording structure. *Applied Physics Letters*, 101:022414, 2012.

[44] H. Sato, E. C. I. Enobio, M. Yamanouchi, S. Ikeda, S. Fukami, F. Matsukura, and H. Ohno. Properties of magnetic tunnel junctions with a MgO/CoFeB/Ta/CoFeB/MgO recording structure down to junction diameter of 11nm. *Applied Physics Letters*, 105:062403, 2014.

[45] Gwang-Guk An, Ja-Bin Lee, Seung-Mo Yang, Jae-Hong Kim, Woo-Seong Chung, and Jin-Pyo Hong. Highly stable perpendicular magnetic anisotropies of CoFeB/MgO frames employing W buffer and capping layers. *Acta Materialia*, 87:259–265, 2015.

[46] Makoto Konoto, Hiroshi Imamura, Tomohiro Taniguchi, Kay Yajushiji, Hitoshi Kubota, Akio Fukushima, Koji Ando, and Shinhi Yuasa. Effect of MgO Cap Layer on Gilbert Damping of FeB Electrode Layer in MgO-Based Magnetic Tunnel Junctions. *Applied Physics Express*, 6:073002, 2013.

[47] Chih-Wei Cheng, Wuwei Feng, G. Chern, C. M. Lee, and Te ho Wu. Effect of cap layer thickness on the perpendicular magnetic anisotropy in top MgO/CoFeB/Ta structures. *Journal of Applied Physics*, 110:033916, 2011.

[48] B. Fang, X. Zhang, B. S. Zhang, Z. M. Zeng, and J. W. Cai. Tunnel magnetoresistance in thermally robust Mo/CoFeB/MgO tunnel junction with perpendicular magnetic anisotropy. *AIP Advances*, 5:067116, 2015.

[49] Claude Chappert, Albert Fert, and Frederic Nguyen Van Dau. The emergence of spin electronics in data storage. *Nature Materials*, 6:813–823, 2007.

[50] W. H. Butler, X.-G. Zhang, T. C. Schulthess, and J. M. MacLaren. Spin-dependent tunneling conductance of Fe|MgO|Fe sandwiches. *Physical Review B*, 63:054416, 2001.

[51] William H. Butler. Tunneling magnetoresistance from a symmetry filtering effect. *Science and Technology of Advanced Materials*, 9:014106, 2008.

[52] A. V. Khvalkovskiy, D. Apalkov, S. Watts, R. Chepulskii, R. S. Beach, A. Ong, X. Tang, A. Driskill-Smith, W. H. Butler, P. B. Visscher, D. Lottis, E. Chen, V. Nikitin, and M. Krounbi. Basic principles of STT-MRAM cell operation in memory arrays. *Journal of Physics D: Applied Physics*, 46(1pp):074001, 2013.

[53] R. Sbiaa, H. Meng, and S. N. Piramanayagam. Materials with perpendicular magnetic anisotropy for magnetic random access memory. *Physica status solidi RRL*, 5(12):413–419, 2011.

[54] W. Zhao, E. Belhaire, Q. Mistral, C. Chappert, V. Javerliac, B. Dieny, and E. Nicolle. Macro-model of Spin-Transfer Torque based Magnetic Tunnel Junction device for hybrid Magnetic-CMOS design. *IEEE International Behavioral Modeling and Simulation Workshop*, pages 40–43, 2006.

[55] J. C. Slonczewski. Current-driven excitation of magnetic multilayers. *Journal of Magnetism and Magnetic Materials*, 159:L1–L7, 1996.

[56] L. Berger. Emission of spin waves by a magnetic multilayer traversed by a current. *Physical Review B*, 54(13), 1996.

[57] Luqiao Liu, Chi-Feng Pai, Y. Li, H. W. Tseng, D. C. Ralph, and R. A. Buhrman. Spin-Torque Switching with the Giant Spin Hall Effect of Tantalum. *Science*, 366:555–558, 2012.

[58] T. Maruyama, Y. Shiota, T. Nozaki, K. Ohta, N. Toda, M. Mizuguchi, A. A. Tulapurkar, T. Shinjo, M. Shiraishi, S. Mizukami, Y. Ando, and Y. Suzuki. Large voltage-induced magnetic anisotropy change in a few atomic layers of iron. *Nature Nanotechnology*, 4:158–161, 2009.

[59] Yoichi Shiota, Takayuki Nozaki, Freferic Bonell, Shinichi Murakami, Teruya Shinjo, and Yoshishige Suzuki. Induction of coherent magnetization switching in a few atomic layers of FeCo using voltage pulses. *Nature Materials*, 11:39–43, 2012.

[60] J. C. Slonczewski. *Physical Review B*, Currents, torques, and polarization factors in magnetic tunnel junctions(024411), 2005.

[61] Sabpreet Bhatti, Rachid Sbiaa, Atsufumi Hirohata, Hideo Ohno, Shunsuke Fukami, and S.N. Piramanayagam. Spintronics based random access memory: a review. *Materials Today*, 00(00), 2017.

[62] Paul Bouquin, Siddharth Rao, Gouri Sankar Kar, and Thibaut Devolder. Size dependence of spin-transfer torque switching in perpendicular magnetic tunnel junctions. *Applied Physics Letters*, 113(222408), 2018.

[63] Jongyeon Kim, Bill Tuohy, Cong Ma, Won Ho Choi, Ibrahim Ahmed, David Lilja, and Chris H. Kim. Spin-Hall Effect MRAM Based Cache Memory: A Feasibility Study. *73rd Annual Device Research Conference (DRC)*, 2015.

[64] A. Manchon, J. Zelezny, I. M. Miron, T. Jungwirth, J. Sinova, A. Thiaville, K. Garello, and P. Gambardella. Current-induced spin-orbit torques in ferromagnetic and antiferromagnetic systems. *Reviews of Modern Physics*, 91(035004), 2019.

[65] M. I. Dyakonov and V. I. Perel. Current-induced spin orientation of electrons in semiconductors. *Physics Letters*, 35A(6):459–460, 1971.

[66] J. E. Hirsch. Spin Hall Effect. *Physical Review Letters*, 83(9):1834–1837, 1999.

[67] Ki-Seung Lee, Seo-Won Lee, Byoung-Chul Min, and Kyung-Jin Lee. Threshold current for switching of a perpendicular magnetic layer induced by spin Hall effect. *Applied Physics Letters*, 102:112410, 2013.

[68] Pietro Gambardella. Introduction to spin torques and spin-orbit torques in metal layers. *[Online]*, Available: https://ethz.ch/content/specialinterest/matl/intermag/en/publications/talks.html, 2015.

[69] Stewart E. Barnes, Jun'ichi Ieda, and Sadamichi Maekawa. Rashba Spin-Orbit Anisotropy and the Electric Field Control of Magnetism. *Scientific Reports*, 4:4105, 2014.

[70] H. Yoda, N. Shimomura, Y. Ohsawa, S. Shirotori, Y.Kato, T. Inokuchi, Y. Kamiguchi, B. Altansargai, Y. Saito, K. Koi, H. Sugiyama, S. Oikawa, M. Shimizu, M. Ishikawa, K. Ikegami, and A. Kurobe. Voltage-Control Spintronics Memory (VoCSM) Having Potentials of Ultra-Low Energy. *IEEE International Electron Devices Meeting*, pages 27.6.1–27.6.4, 2016.

[71] Martin Weisheit, Sebastian Fähler, Alain Marty, Yves Souche, Christiane Poinsignon, and Dominique Givord. Electric Field-Induced Modification of Magnetism in Thin-Film Ferromagnets. *Science*, 315(5810):349–351, 2007.

[72] Yoichi Shiota, Takuto Maruyama, Takayuki Nozaki, Teruya Shinjo, Masashi Shiraichi, and Yoshishige Suzuki. Voltage-Assisted Magnetization Switching in Ultrathin $Fe_{80}Co_{20}$ Alloy Layers. *Applied Physics Express*, 2:063001, 2009.

[73] C. Grezes, F. Ebrahimi, J. G. Alzate, X. Cai, J. A. Katine, J. Langer, B. Ocker, P. Khalili Amiri, and K. L. Wang. Ultra-low switching energy and scaling in electric-field-controlled nanoscale magnetic tunnel junctions with high-resistance-area product. *Applied Physics Letters*, 108:012403, 2016.

[74] S. Kanai, Y. Nakatani, M. Yamanouchi, S. Ikeda, H. Sato, F. Matsukura, and H. Ohno. Magnetization switching in a CoFeB/MgO magnetic tunnel junction by combining spin-transfer torque and electric field-effect. *Applied Physics Letters*, 104:212406, 2014.

[75] Joachim Stöhr and Hans Christoph Siegmann. *Magnetism: From Fundamentals to Nanoscale Dynamics*, volume 152. Springer, 2006.

[76] Chunhui Du, Hailong Wang, Fengyuan Yang, and P. Chris Hammel. Systematic variation of spin-orbit coupling with d-orbital filling: Large inverse spin Hall effect in $3d$ transition metals. *Physical Review B*, 90(140407(R)), 2014.

[77] Henri Alloul. *Introduction to the Physics of Electrons in Solids*. Springer, 2011.

[78] Robert M. White. *Quantum Theory of Magnetism*. Springer, 2007.

[79] J. H. Van Vleck. On the Anisotropy of Cubic Ferromagnetic Crystals. *Physical Review*, 52:1178–1198, 1937.

[80] G. H. O. Daalderop, P. J. Kelly, and M. F. H. Schuurmans. First-principles calculation of the magnetocrystalline anisotropy energy of iron, cobalt, and nickel. *Physical Review B*, 41(17):11919–11937, 1990.

[81] Patrick Bruno. Tight-binding approach to the orbital magnetic moment and magnetocrystalline anisotropy of transition-metal monolayers. *Physical Review B*, 39(1):865–868, 1989.

[82] G. H. O. Daalderop, P. J. Kelly, and M. F. H. Schuurmans. Magnetocrystalline anisotropy and orbital moments in transition-metal compounds. *Physical Review B*, 44(21):12054–12057, 1991.

[83] S. Ikeda, K. Miura, H. Yamamoto, K. Mizunuma, H. D. Gan, M. Endo, S. Kanai, J. Hayakawa, F. Matsukura, and H. Ohno. A perpendicular-anisotropy CoFeB–MgO magnetic tunnel junction. *Nature Materials*, 9:721–724, 2010.

[84] Louis Néel. Superficial magnetic anisotropy and orientation substructures. *J. Phys. Radium*, 15(4):225–239, 1954.

[85] P. Bruno and J.-P. Renard. Magnetic Surface Anisotropy of Transition Metal Ultrathin Films. *Applied Physics A*, 49:499–506, 1989.

[86] Yoshishige Suzuki and Shinhi Miwa. Magnetic anisotropy of ferromagnetic metal in low-symmetry systems. *Physics Letters A*, 383:1203–1206, 2019.

[87] Gerrit van der Laan. Microscopic origin of magnetocrystalline anisotropy in transition metal thin films. *Journal of Physics: Condensed Matter*, 10(14), 1998.

[88] J. Stöhr. Exploring the microscopic origin of magnetic anisotropies with X-ray magnetic circular dichroism (XMCD) spectroscopy. *Journal of Magnetism and Magnetic Materials*, 200:470–497, 1999.

[89] Ding sheng Wang, Ruqian Wu, and A. J. Freeman. Magnetocrystalline anisotropy of interfaces: first-principles theory for Co-Cu interface and interpretation by an effective ligand interaction model. *Journal of Magnetism and Magnetic Materials*, 129:237–258, 1994.

[90] C. ANdersson, B. Sanyal, O. Eriksson, L. Nordström, O. Karis, D. Arvanitis, T. Konishi, E. Holub-Krappe, and J. Hunter Dunn. Influence of Ligand States on the Relationship between Orbital Moment and Magnetocrystalline Anisotropy. *Physical Review Letters*, 99:177207, 2007.

[91] Shinji Miwa, Motohiro Suzuki, Masahito Tsujikawa, Kensho Matsuda, Takayuki Nozaki, Kazuhito Tanaka, Takuya Tsukahara, Kohei Nawaoka, Minori Goto, Yoshinori Kotani, Tadakatsu Ohkubo, Frederic Bonell, Eiiti Tamura, Kazuhiro Hono, Tetsuya Nakamura, Masafumi Shirai, Shinji Yuasa, and Yoshishige Suzuki. Voltage controlled interfacial mechanism through platinum orbits. *Nature Communications*, 8(15848), 2017.

[92] K. H. He, J. S. Chen, and Y. P. Feng. First principles study of the electric field effect on magnetization and magnetic anisotropy of FeCo/MgO(001) thin film. *Applied Physics Letters*, 99:072503, 2011.

[93] Bin Shao, Wu-Jun Shi, Min Feng, and Xu Zuo. Large perpendicular magnetic anisotropy of single Co atom on MgO monolayer: A first-principles study. *Journal of Applied Physics*, 117:17B316, 2015.

[94] N. Nakajima, T. Koide, T. Shidara, H. Miyauchi, H. Fukutani, A. Fujimori, K. Iio, T. Katayama, M. Nývlt, and Y. Suzuki. Large Magnetic Anisotropy Caused by Interfacial Hybridization via Enhanced Orbital Moment in Co/Pt Multilayers: Magnetic Circular X-Ray Dichroism Study. *Physical Review Letters*, 81(23), 1998.

[95] J. A. Osborn. Demagnetizing Factors of the General Ellipsoid. *Physical Review*, 67(11,12):351–357, 1945.

[96] Du-Xing Chen, Enric Pardo, and Alvaro Sanchez. Demagnetizing Factors of Rectangular Prisms and Ellipsoid. *IEEE Transactions on Magnetics*, 38(4):1742–1752, 2002.

[97] Masanori Kobayashi. Surface Magnetic Charge Distribution and Demagnetizing Factors of Circular Cylinders. *IEEE Transactions on Magnetics*, 28(3):1810–1814, 1992.

[98] C. Chappert and P. Bruno. Magnetic anisotropy in metallic ultrathin films and related experiments on cobalt films. *Journal of Applied Physics*, 64(10):5736–5741, 1988.

[99] M. T. Johnson, P. J. H. Bloeman, F. J. A. den Broeder, and J. J. de Vries. Magnetic anisotropy in metallic multilayers. *Reports on Progress in Physics*, 59(11), 1996.

[100] Q. L. Ma, S. Iihama, T. Kubota, X. M. Zhang, S. Mizukami, Y. Ando, and T. Miyazaki. Effect of Mg interlayer on perpendicular magnetic anisotropy of CoFeB films in MgO/Mg/CoFeB/Ta structure. *Applied Physics Letters*, 101:122414, 2012.

[101] W. H. Meiklejohn and C. P. Bean. New Magnetic Anisotropy. *Physical Review*, 105(3):904–913, 1956.

[102] W. H. Meiklejohn and C. P. Bean. New Magnetic Anisotropy. *Physical Review*, 102(5):1413–1414, 1957.

[103] H. S. Jeong, G. T. Jeong, G. H. Koh, I. H. Song, W. J. Park, T. W. Kim, S. J. Jeong, Y. N. Hwang, S. J. Ahn, H. J. Kim, J. S. Hong, W. C. Jeong,

S. H. Lee, J. H. Park, W. Y. Cho, J. S. Kim, S. H. Song, H. J. Kim, S. O. Park, U. I. Jeong, and Kinam Kim. Fully Integrated 64Kb MRAM with Novel Reference Cell Scheme. *IEEE International Electron Devices Meeting (IEDM)*, pages 21.5.1–21.5.4, 2002.

[104] H. Ohno, D. Chiba, F. Matsukura, T. Omiya, E. Abe, T. Dietl, Y. Ohno, and K. Ohtani. Electric-field control of ferromagnetism. *Nature*, 408:944–946, 2000.

[105] Shinji Miwa, Motohiro Suzuki, Masahito Tsujikawa, Takayuki Nozaki, Tetsuya Nakamura, Masafumi Shirai, Shinji Yuasa, and Yoshishige Suzuki. Perpendicular magnetic anisotropy and its electric-field-induced change at metal-dielectric interfaces. *Journal of Physics D: Applied Physics*, 52(6), 2019.

[106] Takayuki Nozaki, Tatsuya Yamamoto, Shinji Miwa, Masahito Tsujikawa, Masafumi Shirai, Shinji Yuasa, and Yoshishige Suzuki. Recent Progress in the Voltage-Controlled Magnetic Anisotropy Effect and the Challenges Faced in Developing Voltage-Torque MRAM. *Micromachines*, 10(327), 2019.

[107] Jia Zhang, Pavel V. Lukashev, Sitaram S. Jaswal, and Evgeny Y. Tsymbal. Model of orbital populations for voltage-controlled magnetic anisotorpy in transition-metal thin films. *Physical Review B*, 96(014435), 2017.

[108] Shinji Miwa, Kensho Matsuda, Kazuhito Tanaka, Yoshinori Kotani, Minori Goto, Tetsuya Nakamura, and Yoshishige Suzuki. Voltage-controlled magnetic anisotropy in Fe|MgO tunnel junctions studied by x-ray absorption spectroscopy. *Applied Physics Letters*, 107(162402), 2015.

[109] Motohiro Suzuki, Takuya Tsukahara, Risa Miyakaze, Taishi Furuta, Koki Shimose, Minori Goto, Takayuki Nozaki, Shinji Yuasa, Yoshishige Suzuki, and Shinji Miwa. Extended X-ray absorption fine structure analysis of voltage-induced effects in the interfacial atomic structure of Fe/Pt/MgO. *Applied Physics Express*, 10(6), 2017.

[110] T. Nozaki, Y. Shiota, M. Shiraishi, T. Shinjo, and Y. Suzuki. Voltage-induced perpendicular magnetic anisotropy change in magnetic tunnel junctions. *Applied Physics Letters*, 96:022506, 2010.

[111] Takayuki Nozaki, Yoichi Shiota, Shinji Miwa, Shinichi Murakami, Frederic Bonell, Shota Ishibashi, Hitoshi Kubota, Kay Yakushiji, Takeshi Saruya, Akio Fukushima, Shinji Yuasa, Teruya Shinjo, and Yoshishige Suzuki. Electric-field-induced ferromagnetic resonance excitation in an ultrathin ferromagnetic metal layer. *Nature Physics*, 8:491–496, 2012.

[112] Takayuki Nozaki, Hiroko Arai, Kay Yakushiji, Shingo Tamaru, Hitoshi Kubota, Hiroshi Imamura, Akio Fukushima, and Shinju Yuasa. Magnetization switching assisted by high-frequency-voltage induced ferromagnetic resonance. *Applied Physics Express*, 7(073002), 2014.

[113] Y. C. Wu, W. Kim, K. Garello, F. Yasin, G. Jayakumar, S. Couet, R. Carpenter, S. Kundu, S. Rao, D. Crotti, J. Van Houdt, G. Groeseneken, and G. S. Kar. Deterministic and field-free voltage-controlled MRAM for high performance and low power application. *IEEE Symposium on VLSI Technology*, TMFS.4, 2020.

[114] Li Xi, Xiaobin Guo, Zhen Wang, Yue Li, Yuelin Yao, Yalu Zuo, and Desheng Xue. Voltage-Driven In-Plane Magnetization Easy Axis Switching in FeNi/Piezoelectric Actuator Hybrid Structure. *Applied Physics Express*, 6:015804, 2013.

[115] V. B. Naik, H. Meng, J. X. Xiao, R. S. Liu, A. Kumar, K. Y. Zeng, P. Luo, and S. Yap. Effect of electric-field on the perpendicular magnetic anisotropy and strain properties in CoFeB/MgO magnetic tunnel junctions. *Applied Physics Letters*, 105:052403, 2014.

[116] D. Chiba, M. Yamanouchi, F. Matsukura, and H. Ohno. Electrical Manipulation of Magnetization Reversal in a Ferromagnetic Semiconductor. *Science*, 301(5635):943–945, 2003.

[117] Pavel Borisov, Andreas Hochstrat, Xi Chen, Wolfgang Kleemann, and Christian Binek. Magnetoelectric Switching of Exchange Bias. *Physical Review Letters*, 94:117203, 2005.

[118] Xi Chen, Andeas Hochstrat, Pavel Borisov, and Wolfgang Kleemann. Magnetoelectric exchange bias systems in spintronics. *Applied Physics Letters*, 89:202508, 2006.

[119] Kentaro Toyoki, Yu Shiratsuchi, Atsushi Kobane, Chiharu Mitsumata, Yoshinori Kotani, Tetsuya Nakamura, and Ryoichi Nakatani. Magnetoelectric switching of perpendicular exchange bias in Pt/Co/α-Cr_2O_3/Pt stacked films. *Applied Physics Letters*, 106(162404), 2015.

[120] Chong Bi, Yaohua Liu, T. Newhouse-Illige, M. Xu, M. Rosales, J. W. Freeland, Oleg Mryasoc, Shifeng Zhang, S. G. E. te Velthuis, and W. G. Wang. Magnetoelectric switching of perpendicular exchange bias in Pt/Co/α-Cr_2O_3/Pt stacked films. *Applied Physics Letters*, 106(162404), 2015.

[121] Uwe Bauer, Lide Yao, Aik Jun Tan, Parnika Agrawal, Satoru Emori, Harry L. Tuller, Sebastiaan van Dijken, and Geoffrey S. D. Beach.

Magneto-ionic control of interfacial magnetism. *Nature Materials*, 14:174–181, 2015.

[122] A. Rajanikanth, T. Hauet, F. Montaigne, S. Mangin, and S. Andrieu. Magnetic anisotropy modified by electric field in V/Fe/MgO(001)/Fe epitaxial magnetic tunnel junction. *Applied Physics Letters*, 103:062402, 2013.

[123] Aik Jun Tan, Mantao Huang, Can Onur Avci, Felix Büttner, Maxwell Mann, Wen Hu, Claudio Mazzoli, Stuart Wilkins, Harry L. Tuller, and Geoffrey S. D. Beach. Magneto-ionic control of magnetism using a solid-state proton pump. *Nature Materials*, 18:35–41, 2019.

[124] Thomas L. Gilbert. A Phenomenological Theory of Damping in Ferromagnetic Materials. *IEEE Transactions on Magnetics*, 40(6), 2004.

[125] William Fuller Brown. Thermal Fluctuation of a Single-Domain Particle. *Physical Review*, 130(5):1677–1686, 1963.

[126] H. Akimoto, H. Kanai, Y. Uehara, T. Ishizuka, and S. Kameyama. Analysis of thermal magnetic noise in spin-valve GMR heads by using micromagnetic simulation. *Journal of Applied Physics*, 97:10N705, 2005.

[127] M. J. Donahue and D. G. Porter. "OOMMF User's Guide, Version 1.0." Interagency Report NISTIR 6376, National Institude of Standards and Technology, Gaithersburg, MD (Sep 1999), see http://math.nist.gov.oommf/.

[128] C. H. Back, D. Weller, J. Heidmann, D. Mauri, D. Guarisco, E. L. Garwin, and H. C. Siegmann. *Physical Review Letters*, Magnetization Reversal in Ultrashort Magnetic Field Pulses(15), 1998.

[129] C. H. Back, R. Allenspach, W. Weber, S. S. Parkin, D. Weller, E. L. Garwin, and H. C. Siegmann. *Science*, Minimum Field Strength in Precessional Magnetization Reversal(864), 1999.

[130] M. Bauer, R. Lopusnik, J. Fassbender, and B. Hillebrands. *Journal of Magnetism and Magnetic Materials*, Magnetization reversal in ultrashort magnetic "eld pulses:165–176, 2000.

[131] B. Hillebrands and K. Ounadjela. *Topics of Applied Physics*, Spin Dynamics in Confined Magnetic Structures I:1–34, 2002.

[132] Burkard Hillebrands and Andre Thiaville. Spin Dynamics in Confined Magnetic Structures III, 2006.

[133] T. M. Crawforda, T. J. Silva, C. W. Teplin, and C. T. Rogers. *Applied Physics Letters*, Subnanosecond magnetization dynamics measured by the second-harmonic magneto-optic Kerr effect(55), 1999.

[134] H. W. Schumacher, C. Chappert, R. C. Sousa, P. P. Freitas, and J. Miltat. Quasiballistic Magnetization Reversal. *Physical Review Letters*, 90(017204), 2003.

[135] H. W. Schumacher, C. Chappert, P. Crozat, R. C. Sousa, P. P. Freitas, J. Miltat, J. Fassbender, and B. Hillebrands. Phase Coherent Precessional Magnetization Reversal in Microscopic Spin Valve Elements. *Physical Review Letters*, 90(017201), 2003.

[136] B. Dieny, I. L. Prejbeanu, K. Garello, P. Gambardella, P. Freitas, R. Lehndorff, W. Raberg, U. Ebels, S. O. Demokritov, J. Akerman, A. Deac, P. Pirro, C. Adelmann, A. Anane, A. V. Chumak, A. Hirohata, S. Mangin, Sergio O. Valenzuela, M. Cengiz Onbaşlı, M. d'Aquino, G. Prenat, G. Finocchio, L. Lopez-Diaz, R. Chantrell, O. Chubykalo-Fesenko, and P. Bortolotti. Oppotunities and challenges for spintronics in the microelectronics industry. *Nature Electronics*, 3:446–459, 2020.

[137] Arne Brataas, Andrew D. Kent, and Hideo Ohno. Current-induced torques in magnetic materials. *Nature Materials*, 11:372381, 2012.

[138] L. Thomas, G. Jan, S. Serrano-Guisan, H. Liu, J. Zhu, Y. Lee, S. Le, J. Iwata-Harms, R. Tong, S. Patel, V. Sundar, D. Shen, Y. Yang, R. He, J. Haq, Z. Teng, V. Lam, P. Liu, Y. Wang, T. Zhong, H. Fukuzawa, , and P. Wang. STT-MRAM devices with low damping and moment optimized for LLC applications at 0x nodes. *IEEE International Electron Devices Meeting (IEDM)*, pages 27.3.1–27.3.4, 2018.

[139] H. Sato, H. Honjo, T. Watanabe, M. Niwa, H. Koike, S. Miura, T. Saito, H. Inoue, T. Nasuno, T. Tanigawa, Y. Noguchi, T. Yoshiduka, M. Yasuhira, S. Ikeda, S.-Y. Kang, T. Kubo, K. Yamashita, Y. Yagi, R. Tamura, and T. Endoh. 14ns write speed 128Mb density Embedded STT-MRAM with endurance $> 10^{10}$ and 10yrs retention @ 85°C using novel low damage MTJ integration process. *IEEE International Electron Devices Meeting (IEDM)*, pages 27.2.1–27.2.4, 2018.

[140] L. Thomas, G. Jan, J. Zhu, H. Liu, Y. J. Lee, S. Le, R. Y. Tong, K. Pi, Y. J. Wang, D. Shen, R. He, J. Haq, J. Teng, V. Lam, K. Huang, T. Zhong, T. Torng, and P. K. Wang. Perpendicular spin transfer torque magnetic random access memories with high spin torque efficiency and thermal stability for embedded applications (invited). *Journal of Applied Physics*, 115(172615), 2014.

[141] W. S. Zhao, Y. Zhang, T. Devolder, J. O. Klein, D. Ravelosona, C. Chappert, , and P. Mazoyer. Failure and reliability analysis of STT-MRAM. *Microelectronics Reliability*, 52:1848–1852, 2012.

[142] S. Kanai, M. Yamanouchi, S. Ikeda, Y. Nakatani, F. Matsukura, and H. Ohno. Electric-field-induced magnetization reversal in a perpendicular-anisotropy CoFeB-MgO magnetic tunnel junction. *Applied Physics Letters*, 101(122403), 2012.

[143] Y. C. Wu, W. Kim, S. Couet, K. Garello, S. Rao, B. F. Vermeulen, S. Van Beek, S. Kundu, S. Houshmand Sharifi, F. Yasin, J. Swerts, D. Crotti, J. Van Houdt, G. Groeseneken, and G. S. Kar. Study of GHz Precessional Switching Speed in BEOL-Compatible Perpendicular MTJ. *64^{th} Annual Conference on Magnetism and Mangetic Materials (MMM)*, pages EG–11, 2019.

[144] Y. C. Wu, W. Kim, S. Couet, K. Garello, S. Rao, S. Van Beek, S. Kundu, S. Houshmand Sharifi, D. Crotti, J. Van Houdt, G. Groeseneken, and G. S. Kar. Study of precessional switching speed control in voltage-controlled perpendicular magnetic tunnel junction. *AIP Advances*, 10(035123), 2020.

[145] C. Grezes, A. Rojas Rozas, F. Ebrahimi, J. G. Alzate, X. Cai, J. A. Katine, J. Langer, B. Ocker, P. Khalili Amiri, and K. L. Wang. In-plane magnetic field effect on switching voltage and thermal stability in electric-field-controlled perpendicular magnetic tunnel junctions. *AIP Advances*, 6(075014), 2016.

[146] J. Huang, C. H. Sim, V. B. Naik, M. Tran, S. T. Lim, A. Huang, Q. J. Yap, and G. Han. Electric field effect on a double MgO CoFeB-based free layer. *Journal of Magnetism and Magnetic Materials*, 401:1150–1154, 2016.

[147] C. Grezes, H. Lee, A. Lee, S. Wang, F. Ebrahimi, X. Li, K. Wong, J. A. Katine, B. Ocker, J. Langer, P. Gupta, P. Khalili Amiri, and K. L. Wang. Write Error Rate and Read Disburbance in Electric-Field-Controlled Magnetic Random-Access Memory. *IEEE Magnetics Letters*, 8(3102705), 2017.

[148] P. K. Amiri, J. G. Alzate, X. Q. Cai, F. Ebrahimi, Q. Hu, K. Wong, C. Grezes, H. Lee, G. Yu, X. Li, M. Akyol, Q. Shao, J. A. Katine, J. Langer, B. Ocker, and K. L. Wang. Electric-Field-Controlled Magnetoelectric RAM: Progress, Challenges, and Scaling. *IEEE Transactions on Magnetics*, 51(11), 2015.

[149] Th. Gerrits, H. A. M. van den Berg, J. Hohlfeld, L. Bar, and Th. Rasing. Ultrafast precessional magnetization reversal by picosecond magnetic field pulse shaping. *Nature*, 418:509–511, 2002.

[150] J. Swerts, S. Mertens, T. Lin, S. Couet, T. Tomczak, K. Sankaran, G. Pourtois, W. Kim, J. Meersschaut, L. Souriau, D. Radisic, S. Van Elshocht, G. Kar, and A. Furnemont. BEOL compatible high tunnel magneto resistance perpendicular magnetic tunnel junctions using a sacrificial Mg free layer cap. *Applied Physics Letters*, 106(262407), 2015.

[151] Kay Yakushiji, Atsushi Sugihara, Akio Fukushima, Hitoshi Kubota, and Shinji Yuasa. Very strong antiferromagnetic interlayer exchange coupling with iridium spacer layer for perpendicular magnetic tunnel junction. *Applied Physics Letters*, 110(092406), 2017.

[152] E. Y. Tsymbal, K. D. Belashchenko, J. P. Velev, S. S. Jaswal, M. van Schilfgaarde, I. I. Oleynik c, and D. A. Stewart. Interface effects in spin-dependent tunneling. *Progress in Materials Science*, 52:401–420, 2007.

[153] Shiro Entani, Manabu Kiguchi, Susumu Ikeda, and Koichiro Saiki. Magnetic properties of ultrathin cobalt films on SiO_2 substrates. *Thin Solid Films*, 493:221–225, 2005.

[154] Soo Young Jang, Chun-Yeol You, S. H. Lim, and S. R. Lee. Annealing effects on the magnetic dead layer and saturation magnetization in unit structures relevant to a synthetic ferrimagnetic free structure. *Journal of Applied Physics*, 109(013901), 2011.

[155] K. Oguz, P. Jivrajka, M. Venkatesan, G. Feng, and J. M. D. Coey. Magnetic dead layers in sputtered $Co_{40}Fe_{40}B_{20}$ films. *Journal of Applied Physics*, 103(07B526), 2008.

[156] Jaivardhan Sinha, Masamitsu Hayashi, Andrew J. Kellock, Shunsuke Fukami, Michihiko Yamanouchi, Hideo Sato, Shoji Ikeda, Seiji Mitani, See hun Yang, Stuart S. P. Parkin, and Hideo Ohno. Enhanced interface perpendicular magnetic anisotorpy in Ta|CoFeB|MgO using nitrogen doped Ta underlayers. *Applied Physics Letters*, 102(242405), 2013.

[157] S. V. Karthik, Y. K. Takahashi, T. Ohkubo, K. Hono, S. Ikeda, and H. Ohno. Transmission electron microscopy investigation of CoFeB/MgO/CoFeB pseudospin valves annealed at different temperatures. *Journal of Applied Physics*, 106(023920), 2009.

[158] Toyoo Miyajima, Takahiro Ibusuki, Shinjiro Umehara, Masashige Sato, Shin Eguchi, Mineharu Tsukada, and Yuji Kataoka. Transmission

electron microscopy study on the crystallization and boron distribution of CoFeB/MgO/CoFeB magnetic tunnel junctions with various capping layers. *Applied Physics Letters*, 94(122501), 2009.

[159] J. H. Jeong and T. Endoh. Improvement of electric and magnetic properties of patterned magnetic tunnel junctions by recovery of damaged layer using oxygen showering post-treatment process. *Journal of Applied Physics*, 117(17D906), 2015.

[160] Jun Hayakawa, Shoji Ikeda, Fumihiro Matsukura, Hiromasa Takahashi, and Hideo Ohno. Dependence of Giant Magnetoresistance of Sputtered CoFeB/MgO/CoFeB Magnetic Tunnel Junctions on MgO Barrier Thickness and Annealing Temperature. *Japanese Journal of Applied Physics*, 44(19):L587–L589, 2005.

[161] M. Yamanouchi, R. Koizumi, S. Ikeda, H. Sato, K. Mizunuma, K. Miura, H. D. Gan, F. Matsukura, and H. Ohno. Dependence of magnetic anisotropy on MgO thickness and buffer layer in $Co_{20}Fe_{60}B_{20}$-MgO structure. *Journal of Applied Physics*, 109(07C712), 2011.

[162] Xuebing Feng and P. B. Visscher. Sweep-rate-dependent coercivity simulation of FePt particle arrays. *Journal of Applied Physics*, 95(7043), 2004.

[163] M. Yamanouchi, A. Jander, P. Dhagat, S. Ikeda, F. Matsukura, and H. Ohno. Domain Structure in CoFeB Thin Films With Perpendicular Magnetic Anisotropy. *IEEE Magnetics Letters*, 2(3000304), 2011.

[164] H. Sato, M. Yamanouchi, K. Miura, S. Ikeda, H. D. Gan, K. Mizunuma, R. Koizumi, F. Matsukura, and H. Ohno. Junction size effect on switching current and the thermal stability in CoFeB/MgO perpendicular magnetic tunnel junctions. *Applied Physics Letters*, 99(042501), 2011.

[165] T. Devolder, J.-V. Kim, L. Nistor, R. Sousa, B. Rodmacq, and B. Dieny. Exchange stiffness in ultrathin perpendicularly magnetized CoFeB layers determined using the spectroscopy of electrically excited spin waves. *Journal of Applied Physics*, 120(183902), 2016.

[166] T. Devolder, L. Bianchini, K. Miura, K. Ito, Joo-Von Kim, P. Crozat, V. Morin, A. Helmer, C. Chappert, S. Ikeda, and H. Ohno. Spin-torque switching window, thermal stability, and material parameters of MgO tunnel junctions. *Applied Physics Letters*, 98(162502), 2011.

[167] H. Sato, M. Yamanouchi, K. Miura, S. Ikeda, R. Koizumi, F. Matsukura, and H. Ohno. CoFeB Thickness Dependence of Thermal Stability Factor in CoFeB/MgO Perpendicular Magnetic Tunnel Junctions. *IEEE Magnetics Letters*, 3(3000204), 2012.

[168] X. Li, K. Fitzell, S. Wu, C. Ty Karaba, A. Buditama, G. Yu, K. L. Wong, N. Altieri, C. Grezes, N. Kioussis, S. Tolbert, Z. Zhang, J. P. Chang, P. K. Amiri, and K. L. Wang. Enhancement of voltage-controlled magnetic anisotropy through precise control of Mg insetion thickness at CoFeB|MgO interface. *Applied Physics Letters*, 110(052401), 2017.

[169] J. Zhu, J. A. Katine, G. E. Rowlands, Y. J. Chen, Z. Duan, J. G. Alzate, P. Upadhyaya, J. Langer, P. K. Amiri, K. L. Wang, and I. N. Krivorotov. Voltage-Induced Ferromagnetic Resonance in Magnetic Tunnel Junctions. *Physical Review Letters*, 108(197203), 2012.

[170] Y. Kato, H. Yoda, Y. Saito, S. Oikawa, K. Fujii, M. Yoshiki, K. Koi, H. Sugiyama, M. Ishikawa, T. Inokuchi, N. Shimomura, M. Shimizu, S. Shirotori, B. Altansargai, Y. Ohsawa, K. Ikegami, A. Tiwari, and A. Kurobe. Giant voltage-controlled magnetic anisotropy effect in a crystallographically strained CoFeB system. *Applied Physics Express*, 11(053007), 2018.

[171] T. Nozaki, A. Koziol Rachwal, W. Skowronski, V. Zayets, Y. Shiota, S. Tamaru, H. Kubota, A. Fukushima, S. Yuasa, and Y. Suzuki. Large Voltage-Induced Changes in the Perpendicular Magnetic Anisotropy of an MgO-Based Tunnel Junction with an Ultrathin Fe Layer. *Physical Review Applied*, 5(044006), 2016.

[172] A. Koziol Rachwal, T. Nozaki, K. Freindl, J. Korecki, S. Yuasa, and Y. Suzuki. Enhancement of perpendicular magnetic anisotropy and its electric field-induced change through interface engineering in Cr/Fe/MgO. *Scientific Reports*, 7(5993), 2017.

[173] H. Yoda, N. Shimomura, T. Inokuchi, Y.Kato, Y. Ohsawa, K. Abe, N. Shimomura, Y. Saito, S. Shirotori, K. Koi, B. Altansargai, S. Oikawa, M. Shimizu, M. Ishikawa, K. Ikegami, Y. Kamiguchi, S. Fujita, and A. Kurobe. High-Speed Voltage-Control Spintronics Memory (High-Speed VoCSM). *IEEE International Memory Workshop (IMW)*, pages 1–5, 2017.

[174] J. M. Iwata-Harms, G. Jan, S. Serrano-Guisan, L. Thomas, H. Liu, J. Zhu, Y.-J. Lee, S. Le, R.-Y. Tong, S. Patel, V. Sundar, D. Shen, Y. Yang, R. He, J. Haq, Z. Teng, V. Lam, P. Liu, Y.-J. Wang, T. Zhong, H. Fukuzawa, and P.-K. Wang. Ultrathin perpendicular magnetic anisotropy CoFeB free layers for highly efficient, high speed writing in spin-transfer-torque magnetic random access memory. *Scientific Reports*, 9(19407), 2019.

[175] C. Tannous and J. Gieraltowski. The Stoner-Wohlfarth model of ferromagnetism. *European Journal of Physics*, 29:475–487, 2008.

[176] T. Devolder, P.-H. Ducrot, J.-P. Adam, I. Barisic, N. Vernier, Joo-Von Kim, B. Ockert, and D. Ravelosona. Damping of $Co_xFe_{80-x}B_{20}$ ultrathin films with perpendicular magnetic anisotropy. *Applied Physics Letters*, 102(022407), 2013.

[177] S. Kanai, Y. Nakatani, M. Yamanouchi, S. Ikeda, F. Matsukura, and H. Ohno. In-plane magnetic field dependence of electric field-induced magnetization switching. *Applied Physics Letters*, 103(072408), 2013.

[178] Yoichi Shiota, Takayuki Nozaki, Shingo Tamaru, Kay Yakushiji, Hitoshi Kubota, Akio Fukushima, Shinji Yuasa, and Yoshishige Suzuki. Evaluation of write error rate for voltage-driven dynamic magnetization switching in magnetic tunnel junctions with perpendicular magnetization. *Applied Physics Express*, 9(013001), 2016.

[179] A. K. Shukla, M. Goto, X. Xu, K. Nawaoka, J. Suwardy, T. Ohkubo, K. Hono, S. Miwa, and Y. Suzuki. *Scientific Reports*, Voltage-Controlled Magnetic Anisotropy in $Fe_{1-x}Co_x$/Pd/MgO system(10362), 2018.

[180] T. Yamamoto, T. Nozaki, Y. Shiota, H. Imamura, S. Tamaru, K. Yakushiji, H. Kubota, A. Fukushima, Y. Suzuki, and S. Yuasa. Thermally Induced Presession-Orbit Transition of Magnetization in Voltage-Driven Magnetization Switching. *Physical Review Applied*, 10(024004), 2018.

[181] K. Lee, J. H. Bak, Y. J. Kim, C. K. Kim, A. Antonyan, D. H. Chang, S. H. Hwang, G. W. Lee, N. Y. Ji, W. J. Kim, J. H. Lee, B. J. Bae, J. H. Park, I. H. Kim, B. Y. Seo, S. H. Han, Y. Ji, H. T. Jung, S. O. Park, O. I. Kwon, J. W. Kye, Y. D. Kim, S. W. Pae, Y. J. Song, G. T. Jeong, K. H. Hwang, G. H. Koh, H. K. Kang, and E. S. Jung. 1Gbit High Density Embedded STT-MRAM in 28nm FDSOI Technology. *IEEE International Electron Devices Meeting (IEDM)*, pages 2.2.1–2.2.4, 2019.

[182] T. Devolder, J. Hayakawa, K. Ito, H. Takahashi, S. Ikeda, P. Crozat, N. Zerounian, Joo-Von Kim, C. Chappert, and H. Ohno. Single-Shot Time-Resolved Measurements of Nanosecond-Scale Spin-Transfer Induced Switching: Stochastic Versus Deterministic Aspects. *Physical Review Letters*, 10(057206), 2008.

[183] Richard Dorrance, Juan G. Alzate, Sergiy S. Cherepov abd Pramey Upadhyaya, Ilya N. Krivorotov, Hordan A. Katine, Juergen Langer, Kang L. Wang, Pedram Khalili Amiri, and Dejan Markovic. Diode-MTJ Crossbar Memory Cell Using Voltage-Induced Unipolar Switching for High-Density MRAM. *IEEE Electron Device Letters*, 34(06), 2013.

[184] Pedram Khalili Amiri and Kang. L. Wang. Systems and Methods for Implementing Magnetoelectric Junctions. *U.S. Patent*, 8 841 739, 2015.

[185] K. Garello, F. Yasin, H. Hody, S. Couet, L. Souriau, S. H. Sharifi, J. Swerts, R. Carpenter, S. Rao, W. Kim, J. Wu, K. K. Vudya Sethu, M. Pak, N. Jossart, D. Crotti, A. Furnemont, and G. S. Kar. Manufacturable 300mm platform solution for Field-Free Switching SOT-MRAM. *IEEE Symposium on VLSI Technology*, pages T194–T195, 2019.

[186] Q. Hu. Systems and Methods for Implementing Magnetoelectric Junctions Including Integrated Magnetization Components. *U.S. Patent*, 15/222871, 2017.

[187] Cecile Grezes, Xiang Li, Kin L. Wong, Farbod Ebrahimi, Pedram Khalili Amiri, and Kang L. Wang. Voltage-controlled magnetic tunnel junctions with synthetic ferromagnet free layer sandwiched by asymmetric double MgO barriers. *Journal of Physics D: Applied Physics*, 53(014006), 2020.

[188] Bart Vermeulen. The Giant VCMA Effect for Novel MRAM Applications, 2019.

[189] S. Nakazawa, A. Obinata, D. Chiba, and K. Ueno. Electric field control of magnetic anisotropy in a Co/Pt bolayer deposited on a high-k $SrTiO_3$. *Applied Physics Letters*, 110(062406), 2017.

[190] Shouzhong Peng, Sai Li, Wang Kang, Jiaqi Zhou, Na Lei, Youguang Zhang, Hongxin Yang, Xiang Li, Pedram Khalili Amiri, Kang L. Wang, and Weisheng Zhao. Large voltage-controlled magnetic anisotropy in the $SrTiO_3$/Fe/Cu structure. *Applied Physics Letters*, 111(152403), 2017.

[191] Ching-Ming Lee, Jyh-Shinn Yang, and Te-Ho Wu. Micromagnetic Simulation for Spin-Transfer Switching With a Tilted Spin Polarizer. *IEEE Transaction on Magnetics*, 47(3), 2011.

[192] B. Lacoste, M. Marins de Castro, R. C. Sousa, I. L. Prejbeanu, L. D. Buda-Prejbeanu, S. Auffret, U. Ebels, B. Rodmacq, B. Dieny, T. Devolder, and C. Ducruet. Micromagnetic Simulation for Spin-Transfer Switching With a Tilted Spin Polarizer. *IEEE 8th International Memory Workshop (IMW)*, pages 1–4, 2016.

[193] Rachid Sbiaa and S. N. Piramanayagam. Recent Developments in Spin Transfer Torque MRAM. *Physica Status Solidi (RRL)*, 11(12), 2017.

[194] Hochul Lee, Cecile Grezes, Shaodi Wang, Farbod Ebrahimi, Puneet Gupta, Pedram Khalili Amiri, and Kang L. Wang. Source Line Sensing in Magneto-Electric Random-Access Memory to Reduce Read Disturbance and Improve Sensing Margin. *IEEE Magnetics Letters*, 7(31034054), 2016.

[195] G. Hu, J. J. Nowak, G. Lauer, J. H. Lee, J. Z. Sun, J. Harms, A. Annunziata, S. Brown, W. Chen, Y. H. Kim, N. Marchack, S. Murthy, C. Kothandaraman, E. J. O'Sullivan, J. H. Park, M. Reuter, R. P. Robertazzi, P. L. Trouilloud, Y. Zhu, and D. C. Worledge. Low-Current Spin Transfer Torque MRAM. *International Symposium on VLSI Technology, Systems and Application (VLSI-TSA)*, pages 1–2, 2017.

[196] James Lourembam, Bingjin Chen, Aihong Huang, Salauddeen Allauddin, and Sze Ter Lim. A non-collinear double MgO based perpendicular magnetic tunnel junction. *Applied Physics Letters*, 113(022403), 2018.

[197] Guohan Hu, Janusz J. Nowak, Matthias G. Gottwald, Jonathan Z. Sun, Dimitri Houssameddine, Junghoon Bak, Stephen L. Brown, Pouya Hashemi, Qing He, Juhyun Kim, Chandrasekharan Kothandaraman, Gen Lauer, Hyun Koo Lee, Thitima Suwannasiri, Philip L. Trouilloud, and Daniel C. Worledge. Reliable Five-Nanosecond Writing of Spin-Transfer Torque Magnetic Random-Access Memory. *IEEE Magnetics Letters*, 10(4504304), 2019.

[198] See Intel website. `https://www.intel.com/content/www/us/en/products/programmable/temperature.html`. Accessed: 16-07-2020.

[199] N. W. Ashcroft and N. D. Mermin. Solid State Physics, Saunders College, 1976.

[200] H. B. Callen and E. Callen. The present status of the temperature dependence of magnetocrystalline anisotropy, and the $l(l+1)/2$ power law. *Journal of Physics and Chemistry of Solids*, 27:1271–1285, 1966.

[201] Juan G. Alzate, Pedram Khalili Amiri, Guoqiang Yu, Pramey Upadhyaya, Jordan A. Katine, Juergen Langer, Berthold Ocker, Ilya N. Krivorotov, and Kang L. Wang. Temperature dependence of the voltage-controlled perpendicular anisotropy in nanoscale MgO|CoFeB|Ta magnetic tunnel junctions. *Applied Physics Letters*, 104(112410), 2014.

[202] M. D. Kuz'min. Shape of Temperature Dependence of Spontaneous Magnetization of Ferromagnets: Quantitative Analysis. *Physical Review Letters*, 94(107204), 2005.

[203] C. Park, J. J. Kan, C. Ching, J. Ahn, L. Xue, R. Wang, A. Kontos, S. Liang, M. Bangar, H. Chen, S. Hassan, S. Kim, M. Pakala, and S. H. Kang. Temperature Dependence of Critical Device Parameters in 1 Gb Perpendicular Magnetic Tunnel Junction Arrays for STT-MRAM. *IEEE Transactions on Magnetics*, 153(2), 2017.

[204] Y. C. Wu, W. Kim, S. Rao, K. Garello, S. Van Beek, S. Couet, E. Liu, J. Swerts, S. Kundu, L. Souriau, F. Yasin, D. Crotti, J. K. Jochum, M. J. Van Bael, J. Van Houdt, G. Groeseneken, and G. S. Kar. Impact of operating temperature on the electrical and magnetic properties of the bottom-pinned perpendicular magnetic tunnel junctions. *Applied Physics Letters*, 113(142405), 2018.

[205] Y. C. Wu, W. Kim, S. Van Beek, S. Couet, R. Carpenter, S. Rao, S. Kundu, J. Van Houdt, G. Groeseneken, D. Crotti, and G. S. Kar. Impact of Ambient Temperature on the Switching Behavior of Voltage-Controlled Perpendicular Magnetic Tunnel Junction. *65th Annual Conference on Magnetism and Mangetic Materials (MMM)*, pages L2–05, 2020.

[206] Y. C. Wu, W. Kim, S. Van Beek, S. Couet, R. Carpenter, S. Rao, S. Kundu, J. Van Houdt, G. Groeseneken, D. Crotti, and G.S. Kar. Impact of Ambient Temperature on the Switching of Perpendicular Magnetic Tunnel Junctions by Voltage-Controlled Magnetic Anisotropy. *Applied Physics Letters*, pending.

[207] J. Crangle and G. M. Goodman. The magnetization of pure iron and nickel. *Proceedings of the Royal Society A*, 321(477), 1971.

[208] R. Pauthenet. Experimental verification of spin-wave theory in high fields (invited). *Journal of Applied Physics*, 53(11), 1982.

[209] P. Mohn and E. P. Wohlfarth. The Curie temperature of the ferromagnetic transition metals and their compounds. *Journal of Physics F: Metal Physics*, 17(12), 1987.

[210] U. Rudiger, R. Calarco, U. May, K. Samm, J. Hauch, H. Kittur, M. Sperlich, and G. Guntherodt. Temperature dependent resistance of magnetic tunnel junctions as a quality proof of the barrier. *Journal of Applied Physics*, 89(11), 2001.

[211] C. H. Shang, J. Nowak, R. Jansen, and J. S. Moodera. Temperature dependence of magnetoresistance and surface magnetization in ferromagnetic tunnel junctions. *Physical Review B*, 58(R2917), 1998.

[212] A. Okada S. Kanai M. Yamanouchi S. Ikeda F. Matsukura and H. Ohno. Electric-field effects on magnetic anisotropy and damping constant in Ta/CoFeB/MgO investigated by ferromagnetic resonance. *Applied Physics Letters*, 105(052415), 2014.

[213] Yu Fu, I. Barsukov, Jing Li, A. M. Gonc¸alves, C. C. Kuo, M. Farle, and I. N. Krivorotov. Temperature dependence of perpendicular magnetic anisotropy in CoFeB thin films. *Applied Physics Letters*, 108(142403), 2016.

[214] Zhenchao Wen, Hiroaki Sukegawa, Takeshi Seki, Takahide Kubota, Koki Takanashi, and Seiji Mitani. Voltage control of magnetic anisotropy in epitaxial Ru/Co2FeAl/MgO heterostructures. *Scientific Reports*, 7(45026), 2017.

[215] R. Skomski, A. Kashyap, and D. J. Sellmyer. Finite-Temperature Anisotropy of PtCo Magnets. *IEEE Transactions on Magnetics*, 39(5), 2003.

[216] J. B. Staunton, S. Ostanin, S. S. A. Razee, B. L. Gyorffy, L. Szunyogh, B. Ginatempo, and Ezio Bruno. Temperature Dependent Magnetic Anisotropy in Metallic Magnets from an *Ab Initio* Electronic Structure Theory: $L1_0$-Ordered FePt. *Physical Review Letters*, 93(257204), 2003.

[217] Kyota Watanabe, Shinya Ishikawa, Hideo Sato, Shoji Ikeda, Michihiko Yamanouchi, Shunsuke Fukami, Fumihiro Matsukura, and Hideo Ohno. Dependence of magnetic properties of MgO/CoFeB/Ta stacks on CoFeB and Ta thicknesses. *Japanese Journal of Applied Physics*, 54(04DM04), 2015.

[218] T. Liu, Y. Zhang, J. W. Cai, and H. Y. Pan. Thermally robust Mo/CoFeB/MgO trilayers with strong perpendicular magnetic anisotropy. *Scientific Reports*, 4(5895), 2014.

[219] Kodai Niitsu. Temperature dependence of magnetic exchange stiffness in iron and nickel. *Journal of Applied Physics D: Applied Physics*, 53(39LT01), 2020.

[220] S. Van Beek, B. J. O'Sullivan, P. J. Roussel, R. Degraeve, E. Bury, J. Swerts, S. Couet, L. Souriau, S. Kundu, S. Rao, W. Kim, F. Yasin, D. Crotti, D. Linten, and G. Kar. Impact of self-heating on reliability predictions in STT-MRAM. *IEEE International Electron Devices Meeting (IEDM)*, pages 25.2.1–25.2.4, 2018.

[221] J. G. Alzate, U. Arslan, P. Bai, J. Brockman, Y. J. Chen, N. Das, K. Fischer, T. Ghani, P. Heil, P. Hentges, R. Jahan, A. Littlejohn, M. Mainuddin, D. Ouellette, J. Pellegren, C. Puls T. Pramanik, P. Quintero, T. Rahman, M. Sekhar, B. Sell, M. Seth, A. J. Smith, A. K. Smith, L. Wei, C. Wiegand, O. Golonzka, and F. Hamzaoglu. 2MB Array-Level Demonstration of STT-MRAM Process and Performance Towards L4 Cache Applications. *IEEE International Electron Devices Meeting (IEDM)*, pages 2.4.1–2.4.4, 2019.

[222] Y. C. Wu, K. Garello, W. Kim, M. Gupta, M. Perumkunnil, S. Van Beek, S. Couet, R. Carpenter, S. Rao, F. Yasin, H. Hody, G. Jayakumar, J. Van

Houdt, G. Groeseneken, D. Crotti, and G. S. Kar. Voltage-Gate Assisted SOT-pMRAM for Low Power Embedded Applications. *Physical Review Applied*, pending.

[223] Ioan Mihai Miron, Kevin Garello, Gilles Gaudin, Pierre-Jean Zermatten, Marius V. Costache, Stephane Auffret, Sebastien Bandiera, Bernard Rodmacq, Alain Schuhl, and Pietro Gambardella. Perpendicular switching of a single ferromagnetic layer induced by in-plane current injection. *Nature*, 476:189–193, 2011.

[224] V. P. Amin and M. D. Stiles. Spin transport at interfaces with spin-orbit coupling: Phenomenology. *Physical Review B*, 94(104420), 2016.

[225] K. Ando, S. Takahashi, K. Harii, K. Sasage, J. Ieda, S. Maekawa, and E. Saitoh. Electric Manipulation of Spin Relaxation Using the Spin Hall Effect. *Physical Review Letters*, 101(036601), 2008.

[226] A. Manchon, H. C. Koo, J. Nitta, S. M. Frolov, and R. A. Duine. New perspectives for Rashba spin–orbit coupling. *Nature Materials*, 14:871–882, 2015.

[227] Kevin Garello, Farrukh Yasin, and Gouri Sankar Kar. Spin-Orbit Torque MRAM for ultrafast embedded memories: from fundamentals to large scale technology integration. *IEEE International Memory Workshop (IMW)*, pages 101–104, 2019.

[228] E. Grimaldi, V. Krizakova, G. Sala, F. Yasin, S. Couet, G. S. Kar, K. Garello, and P. Gambardella. Single-shot dynamics of spin-orbit torque and spin transfer torque switching in three-terminal magnetic tunnel junctions. *Nature Nanotechnology*, 15:111–117, 2020.

[229] Seo-Won Lee and Kyung-Jin Lee. Emerging Three-Terminal Magnetic Memory Devices. *Proceedings of the IEEE*, 104(10), 2016.

[230] S. Fukami, C. Zhang, S. DuttaGupta, A. Kurenkov, and H. Ohno. Magnetization switching by spin-orbit torque in an antiferromagnet-ferromagnet bilayer system. *Nature Materials*, 15:535–541, 2016.

[231] S. Z. Peng, J. Q. Lu, W. X. Li, L. Z. Wang, H. Zhang, X. Li, K. L. Wang, and W. S. Zhao. Field-Free Switching of Perpendicular Magnetization through Voltage-Gated Spin-Orbit Torque. *IEEE International Electron Devices Meeting (IEDM)*, pages 28.6.1–28.6.4, 2019.

[232] M. Wang, W. Cai, D. Zhu, Z. Wang, J. Kan, Z. Zhao, K. Cao, Z. Wang, Y. Zhang, C. Park, J. P. Wang, A. Fert, and W. Zhao. Field-free switching of a perpendicular magnetic tunnel junction through interplay of spin-orbit and spin-transfer torques. *Nature Electronics*, 1:582–588, 2018.

[233] Qiang Hao and Gang Xiao. Giant Spin Hall Effect and Switching Induced by Spin-Transfer Torque in a $W/Co_{40}Fe_{40}B_{20}/MgO$ Structure with Perpendicular Magnetic Anisotropy. *Physical Review Applied*, 3(034009), 2015.

[234] Luqiao Liu, Chi-Feng Pai, Y. Li, H. W. Tseng, D. C. Ralph, and R. A. Buhrman. Enhancement of perpendicular magnetic anisotropy and transmission of spin-Hall-effect-induced spin currents by a Hf spacer layer in W/Hf/CoFeB/MgO layer structures. *Applied Physics Letters*, 104(082407), 2014.

[235] A. R. Mellnik, J. S. Lee, A. Richardella, J.L.Grab, P. J. Mintun, M. H. Fischer, A.Vaezi, A. Manchon, E.-A.Kim, N. Samarth, and D. C. Ralph. Spin-transfer torque generated by a topological insulator. *Nature*, 511:449–451, 2014.

[236] Yabin Fan, Pramey Upadhyaya, Xufeng Kou, Murong Lang, So Takei, ZhenxingWang, Jianshi Tang, Liang He1, Li-Te Chang, Mohammad Montazeri, Guoqiang Yu, Wanjun Jiang, Tianxiao Nie, Robert N. Schwartz, Yaroslav Tserkovnyak, and Kang L.Wang. Magnetization switching through giant spin-orbit torque in a magnetically doped topological insulator heterostructure. *Nature Materials*, 13:699–704, 2014.

[237] A. Azevedo, L. H. Vilela-Leao, R. L. Rodriguez-Suarez, A. F. Lacerda Santos, and S. M. Rezende. Spin pumping and anisotropic magnetoresistance voltages in magnetic bilayers: Theory and experiment. *Physical Review B*, 83(144402), 2011.

[238] Z. Feng, J. Hu, L. Sun, B. You, D. Wu, J. Du, W. Zhang, A. Hu, Y. Yang, D. M. Tang, B. S. Zhang, and H. F. Ding. Spin Hall angle quantification from spin pumping and microwave photoresistance. *Physical Review B*, 85(214423), 2012.

[239] Kouta Kondou, Hiroaki Sukegawa, Seiji Mitani, Kazuhito Tsukagoshi, and Shinya Kasai. Evaluation of Spin Hall Angle and Spin Diffusion Length by Using Spin Current-Induced Ferromagnetic Resonance. *Applied Physics Express*, 5(073002), 2012.

[240] Zhenyao Tang, Yuta Kitamura, Eiji Shikoh, Yuichiro Ando, Teruya Shinjo, and Masashi Shiraishi. Temperature Dependence of Spin Hall Angle of Palladium. *Applied Physics Express*, 6(083001), 2013.

[241] V. Tshitoyan, C. Ciccarelli, A. P. Mihai, M. Ali, A. C. Irvine, T. A. Moore, T. Jungwirth, and A. J. Ferguson. Electrical manipulation of ferromagnetic NiFe by antiferromagnetic IrMn. *Physical Review B*, 92(214406), 2015.

[242] Di Wu, Guoqiang Yu, Ching-Tzu Chen, Seyed Armin Razavi, Qiming Shao, Xiang Li, Bingcheng Zhao, Kin L. Wong, Congli He, Zongzhi Zhang, Pedram Khalili Amiri, and Kang L. Wang. Spin-orbit torques in perpendicularly magnetized $Ir_{22}Mn_{78}/Co_{20}Fe_{60}B_{20}/MgO$ multilayer. *Applied Physics Letters*, 109(222401), 2016.

[243] Yongxi Ou, Shengjie Shi, D. C. Ralph, and R. A. Buhrman. Strong spin Hall effect in the antiferromagnet PtMn. *Physical Review B*, 93(220405(R)), 2016.

[244] Etienne Sicard. Introducing 7-nm FinFET technology in Microwind. hal-01558775, 2017.

[245] Y. Ohsawa, H. Yoda, S. Shirotori, M. Shimizu, B. Altansargai, H. Sugiyama, N. Shimomura, K. Koi, Y. Kato, S. Oikawa, T. Inokuchi, and A. Kurobe. Voltage-control spintronics memory (VoCSM) toward development of a $4F^2$-cell with strained in-plane-MTJ. *Electron Devices Technology and Manufacturing Conference (EDTM)*, pages 145–147, 2019.

[246] Kevin Garello, Can Onur Avci, Ioan Mihai Miron, Manuel Baumgartner, Abhijit Ghosh, Stephane Auffret, Olivier Boulle, Gilles Gaudin, and Pietro Gambardella. Ultrafast magnetization switching by spin-orbit torques. *Applied Physics Letters*, 105(212402), 2014.

[247] Zhitao Diao, Zhanjie Li, Shengyuang Wang, Yunfei Ding, Alex Panchula, Eugene Chen, Lien-Chang Wang, and Yiming Huai. Spin-transfer torque switching in magnetic tunnel junctions and spin-transfer torque random access memory. *Journal of Physics: Condensed Matter*, 19(165209), 2007.

[248] T. Ikeura, T. Nozaki, Y. Shiota, T. Yamamoto, H. Imamura, H. Kubota, A. Fukushima, Y. Suzuki, and S. Yuasa. Reduction in the write error rate of voltage-induced dynamic magnetization switching using the reverse bias method. *Japaneses Journal of Applied Physics*, 57(040311), 2018.

[249] Sohee Kwon, Qilong Sun, Farzad Mahfouzi, Kang L. Wang, Pedram Khalili Amiri, and Nicholas Kioussis. Voltage-Controlled Magnetic Anisotropy in Heterostructures with Atomically Thin Heavy Metals. *Physical Review Applied*, 12(044075), 2019.

[250] J. Chang, Y.-H. Chen, W.-M. Chan, S. P. Singh, H. C, H. Fujiwara, J.-Y. Lin, K.-C. Lin, J. Hung, R. Lee, H.-J. Liao, J.-J. Liaw, Q. Li, C.-Y. Lin, M.-C. Chiang, and S.-Y. Wu. A 7nm 256Mb SRAM in High-K Metal-Gate FinFET Technology with Write-Assist Circuitry for Low-V_{MIN} Applications. *IEEE International Solid-State Circuits Conference (ISSCC)*, pages 206–207, 2017.

[251] M. Clinton, R. Singh, M. Tsai, S. Zhang, B. Sheffield, and J. Chang. A 5GHz 7nm L1 cache memory compiler for high-speed computing and mobile applications. *IEEE International Solid-State Circuits Conference (ISSCC)*, pages 200–201, 2018.

[252] J. Chang, Y.-H. Chen, G. Chan, H. Cheng, P.-S. Wang, Y. Lin, H. Fujiwara, R. Lee, H.-J. Liao, P.-W. Wang, G. Yeap, and Q. Li. A 5nm 135Mb SRAM in EUV and High-Mobility-Channel FinFET Technology with Metal Coupling and Charge-Sharing Write-Assist Circuitry Schemes for High-Density and Low-VV_{MIN} Applications. *IEEE International Solid-State Circuits Conference (ISSCC)*, pages 238–240, 2020.

[253] M. K. Gupta, P. Weckx, S. Cosemans, P. Schuddinck, R. Baert, D. Yakimets, D. Jang, Y. Sherazi, P. Raghavan, A. Spessot, A. Mocuta, and W. Dehaene. Device circuit and technology co-optimisation for FinFET based 6T SRAM cells beyond N7. *European Solid-State Device Research Conference (ESSDERC)*, pages 256–259, 2017.

[254] S. Sakhare, M. Perumkunnil, T. Huynh Bao, S. Rao, W. Kim, D. Crotti, F. Yasin, S. Couet, J. Swerts, S. Kundu, D. Yakimets, R. Baert, HR. Oh, A. Spessot, A. Mocuta, G. S. Kar, and A. Furnemont. Enablement of STT-MRAM as last level cache for the high performance computing domain at the 5nm node. *IEEE International Electron Devices Meeting (IEDM)*, pages 18.3.1–18.3.4, 2018.

[255] M. Gupta, M. Perumkunnil, K. Garello, S. Rao, F. Yasin, G. S. Kar, and A. Furnemont. High-density SOT-MRAM technology and design specifications for the embedded domain at 5nm node. *IEEE International Electron Devices Meeting (IEDM)*, pages 24.5.1–24.5.4, 2020.

[256] See website. `https://www.mram-info.com/stt-mram`. Accessed: 20-10-2020.

[257] S. Yuasa, A. Fukushima, K. Yakushiji, T. Nozaki, M. Konoto, H. Maehara, H. Kubota, T. Taniguchi, H. Arai, H. Imamura, K. Ando, Y. Shiota, F. Bonell, Y. Suzuki, N. Shimomura, E. Kitagawa, J. Ito, S. Fujita, K. Abe, K. Nomura, H. Noguchi, and H. Yoda. Future Prospects of MRAM Technologies. *IEEE International Electron Devices Meeting (IEDM)*, pages 3.1.1–3.1.4, 2013.

[258] Enlong Liu. Materials and designs of magnetic tunnel junctions with perpendicular magnetic anisotropy for high-density memory applications, 2018.

[259] J. Hayakawa, S. Kokado, K. Ito, M. Sugiyama, H. Asano, M. Matsui, A. Sakuma, and M. Ichimura. Bias Voltage

Dependence of Tunnel Magnetoresistance Effect in Spin-Valve Type MnIr/NiFe/$Co_{90}Fe_{10}$/$SrTiO_3$/$La_{0.7}Sr_{0.3}MnO_3$ Tunnel Junctions. *Japanese Journal of Applied Physics*, 41:1340–1342, 2002.

[260] E. M. J. Hassen, B. Viala, M. C. Cyrille, M. Cartier, O. Redon, P. Lima, B. Belhadji, H. X. Yang, J. Velev, and M. Chshiev. Room temperature magnetoresistance in CoFeB/$SrTiO_3$/CoFeB magnetic tunnel junctions deposited by ion beam sputtering. *Journal of Applied Physics*, 111(07C727), 2012.

[261] Jialin Cai, Bin Fang, Like Zhang, Wenxing Lv, Baoshun Zhang, Tiejun Zhou, Giovanni Finocchio, and Zhongming Zeng. Voltage-Controlled Spintronic Stochastic Neuron Based on a Magnetic Tunnel Junction. *Physical Review Applied*, 11(034015), 2019.

[262] J. Doevenspeck, K. Garello, B. Verhoef, R. Degraeve, S. Van Beek, D. Crotti, F. Yasin, S. Couet, G. Jayakumar, I. A Papistas, P. Debacker, R. Lauwereins, W. Dehaene, G.S. Kar, S. Cosemans, A. Mallik1, and D. Verkest. SOT-MRAM based Analog in-Memory Computing for DNN inference. *IEEE Symposium on VLSI*, page JFS4, 2019.

List of publications

International Conferences (First-authored)

1. **Y. C. Wu**, W. Kim, S. Rao, K. Garello, S. Couet, E. Liu, J. Swerts, S. Kundu, L. Souriau, F. Yasin, D. Crotti, G. S. Kar, J. Jochum, M. Van Bael, J. Van Houdt, and G. Groeseneken. "Impact of temperature on the switching behavior of scaled perpendicular magnetic tunnel junctions", 62$^{\text{nd}}$ Annual Conference on Magnetism and Magnetic Materials, Pittsburgh, BE-11 (2017)

2. **Y. C. Wu**, W. Kim, S. Couet, K. Garello, S. Rao, B. Vermeulen, S. Van Beek, S. Kundu, S. Houshmand Sharifi, F. Yasin, J. Swerts, D. Crotti, J. Van Houdt, G. Groeseneken, and G. S. Kar. "Study of GHz VCMA precessional switching speed in BEOL compatible perpendicular MTJ", 64$^{\text{th}}$ Annual Conference on Magnetism and Magnetic Materials, Las Vegas, EG-11 (2019)

3. **Y. C. Wu**, W. Kim, K. Garello, F. Yasin, G. Jayakumar, S. Couet, R. Carpenter, S. Kundu, S. Rao, D. Crotti, J. Van Houdt, G. Groeseneken, and G. S. Kar. "Deterministic and field-free voltage-controlled MRAM for high performance and low power applications", 40$^{\text{th}}$ Symposia on VLSI Technology and Circuits, TMFS.4 (2020)

4. **Y. C. Wu**, W. Kim, S. Van Beek, S. Couet, R. Carpenter, S. Rao, S. Kundu, J. Van Houdt, G. Groeseneken, D. Crotti, and G. S. Kar. "Impact of Ambient Temperature on the Switching Behavior of Voltage-Controlled Perpendicular Magnetic Tunnel Junction", 65$^{\text{th}}$ Annual Conference on Magnetism and Magnetic Materials, L2-05 (2020)

Peer Reviewed Journals (First-authored)

1. **Y. C. Wu**, W. Kim, S. Rao, K. Garello, S. Couet, E. Liu, J. Swerts, S. Kundu, L. Souriau, F. Yasin, D. Crotti, J. Jochum, M. Van Bael, J. Van Houdt, G. Groeseneken, and G. S. Kar. "Impact of operating temperature on the electrical and magnetic properties of the bottom-pinned perpendicular magnetic tunnel junctions", Applied Physics Letters 113, 142405 (2018)

2. **Y. C. Wu**, W. Kim, S. Couet, K. Garello, S. Rao, S. Van Beek, S. Kundu, S. Houshmand Sharifi, D. Crotti, J. Van Houdt, G. Groeseneken, and G. S. Kar. "Study of Precessional Switching Speed Control in Voltage-Controlled Perpendicular Magnetic Tunnel Junction", AIP Advances 10, 035123 (2020)

3. **Y. C. Wu**, W. Kim, F. Yasin, G. Jayakumar, S. Couet, R. Carpenter, S. Kundu, S. Rao, D. Crotti, J. Van Houdt, G. Groeseneken, and G. S. Kar. "Impact of Ambient Temperature on the Switching of Voltage-Controlled Perpendicular Magnetic Tunnel Junction", Applied Physics Letters, (Pending)

4. **Y. C. Wu**, W. Kim, K. Garello, F. Yasin, G. Jayakumar, S. Couet, R. Carpenter, S. Kundu, S. Rao, D. Crotti, J. Van Houdt, G. Groeseneken, and G. S. Kar. "Voltage-Gate Assisted SOT-pMRAM for Low Power Embedded Applications", Physical Review Applied, (Pending)

5. **Y. C. Wu**, W. Kim, K. Garello, F. Yasin, G. Jayakumar, S. Couet, R. Carpenter, S. Kundu, S. Rao, D. Crotti, J. Van Houdt, G. Groeseneken, and G. S. Kar. "Deterministic Voltage-Controlled Magnetic RAM for Advanced Ultralow Power Memory", Electron Device Letters, (Pending)

Patent filed

1. **Y. C. Wu**, W. Kim, S. Cosemans, and G. S. Kar. "Systems and Methods for Deterministic Writing of Voltage-Controlled Magnetic Memory Device", submitted (2020)

Co-Authored Contributions

1. B. Vermeulen, **J. Wu**, J. Swerts, S. Mertens, S. Couet, Y. Tomczak, J. Meersschaut, D. Linten, I. Radu, G. Rampelberg, C. Detavernier, A. Thean, J. Jochum, M. Van Bael, K. Temst, G. Groeseneken, K. Martens, A. Shukla, S. Hatanaka, K. Tanaka, K. Matsuda, K. Nawaoka, M. Goto, S. Miwa, E. Tamura, and Y. Suzuki. "The giant VCMA effect for novel MRAM applications", International Nanotechnology Conference on Communication and Cooperation, Leuven, Belgium (2016)

2. B. Vermeulen, **J. Wu**, J. Swerts, S. Mertens, S. Couet, Y. Tomczak, J. Meersschaut, D. Linten, I. Radu, G. Rampelberg, C. Detavernier, A. Thean, J. Jochum, M. Van Bael, K. Temst, G. Groeseneken, K. Martens, A. Shukla, S. Hatanaka, K. Tanaka, K. Matsuda, K. Nawaoka, M. Goto, S. Miwa, E. Tamura, and Y. Suzuki. "Perpendicular magnetic anisotropy of CoFeB\Ta bilayers on ALD HfO_2", 9th International Symposium on Magnetic Multilayers, Uppsala, Sweden (2016)

3. B. Vermeulen, **J. Wu**, J. Swerts, S. Mertens, S. Couet, Y. Tomczak, J. Meersschaut, D. Linten, I. Radu, G. Rampelberg, C. Detavernier, A. Thean, J. Jochum, M. Van Bael, K. Temst, G. Groeseneken, K. Martens, and K. Sankaran. "The Giant VCMA effect for novel MRAM applications ", General Scientific Meeting of the Belgian Physical Society, Gent, Belgium (2016)

4. E. Liu, J. Swert, **J. Wu**, A. Vaysset, S. Couet, S. Mertens, S. Rao, W. Kim, S. Van Elshocht, J. De Broek, and G. S. Kar. "Top-pinned STT-MRAM devices with high thermal stability hybrid free layers for high density memory applications", IEEE International Magnetic Conference, Singapore, Singapore (2018)

5. K. Garello, F. Yasin, H. Hody, S. Couet, L. Souriau, S. Houshmand Sharifi, J. Swerts, R. Carpenter, S. Rao, W. Kim, **J. Wu**, K. Vudya Sethu, M. Pak, N. Jossart, D. Crotti, A. Furnemont, and G. S. Kar. "Manufacturable 300mm platform solution for Field-Free Switching SOT-MRAM", Symposia on VLSI Technology and Circuits, pp. T194-T195, Kyoto, Japan (2019)

6. S. Van Beek, R. Carpenter, S. Kundu, S. Couet, J. Swerts, S. Rao, W. Kim, **J. Wu**, S. Houshmand Sharifi, F. Yasin, B. Vermeulen, and G. S. Kar. "The magneto-optical Kerr effect for efficient characterization of thermal stability in dense arrays of pMTJs", 64^{th} Annual Conference on Magnetism and Magnetic Materials, Las Vegas, USA (2019)

7. S. Van Beek, K. Martens, P. Roussel, **J. Wu**, W. Kim, S. Rao, J. Swerts, D. Crotti, D. Linten, G. S. Kar, and G. Groeseneken. "Thermal stability analysis and modelling of advanced perpendicular magnetic tunnel junctions", AIP Advances 8, 055909 (2018)

8. E. Liu, J. Swerts, **Y. C. Wu**, A. Vaysset, S. Couet, S. Mertens, S. Rao, W. Kim, S. Van Elshocht, J. De Broek, and G. S. Kar. "Top-pinned STT-MRAM devices with high thermal stability hybrid free layers for high density memory applications", IEEE Transactions on Magnetics 54(11), 3401805 (2018)

9. E. Liu, **Y. C. Wu**, S. Couet, S. Mertens, S. Rao, W. Kim, K. Garello, D. Crotti, S. Van Elshocht, J. De Broek, G. S. Kar, and J. Swerts. "Synthetic ferromagnet pinning layers enabling top-pinned magnetic tunnel junctions for high density embedded MRAM applications", Physical Review Applied 10, 054054 (2018)

Curriculum Vitae

Yueh Chang (Jackson) Wu was born in 1992 in Taipei, Taiwan. He received his Bachelor degree in Material Science and Engineering from National Chiao Tung University (NCTU), Hsinchu, Taiwan in 2014, and Master degree in Nanoscience, Nanotechnology and Nanoengineering from Katholieke Universiteit Leuven (KULeuven), Leuven, Belgium in 2016. During master thesis, he joined the Device Reliability and Electrical Characterization (DRE) group at imec to study the voltage control of magnetic anisotropy effect.

In November 2016, he started pursuing the Ph.D degree in Electrical Engineering at KULeuven in collaboration with Memory Device Design (MDD) group at imec. His research focused on alternative and exploratory writing mechanisms for the future generations of magnetic random access memory (MRAM) technologies, under the guidance of Prof. Guido Groeseneken and Prof. Jan Van Houdt.

FACULTY OF ENGINEERING SCIENCE
DEPARTMENT OF ELECTRICAL ENGINEERING
MICAS
Kasteelpark Arenberg 10
B-3001 Leuven
Jackson.Wu@imec.be
https://www.esat.kuleuven.be